STRUCTURAL SYSTEMS

RESEARCH PROJECT

Report No.
SSRP–2001/01

SEISMIC PERFORMANCE OF CIRCULAR HOLLOW COLUMNS SUBJECTED TO HIGH SHEAR

By

GIULIO RANZO
M.J. N. PRIESTLEY

Final Report Submitted to Caltrans under Contract No. 59A0051

March 2001

Department of Structural Engineering
University of California, San Diego
La Jolla, California 92093-0085

University of California, San Diego
Department of Structural Engineering
Structural Systems Research Project

Report No. SSRP-2001/01

Seismic Performance Of Circular Hollow Columns Subjected To High Shear

By

GIULIO RANZO
Graduate Student Researcher

M.J. N. PRIESTLEY
Professor of Structural Engineering

Final Report Submitted to Caltrans under Contract No. 59A0051

Department of Structural Engineering
University of California, San Diego
La Jolla, California 92093-0085

March 2001

Technical Report Documentation Page

1. Report No.	2. Government Accession No.	3. Recipient's Catalog No.
SSRP 2001-01		

4. Title and Subtitle	5. Report Date
Seismic Performance of Circular Hollow Columns Subjected To High Shear	Jan 2000
	6. Performing Organization Code
7. Author(s) Dr. Giulio Ranzo, PhD Prof. M.J. Nigel Priestley	8. Performing Organization Report No. UCSD / SSRP-2001/01
9. Performing Organization Name and Address Department of Structural Engineering School of Engineering University of California, San Diego La Jolla, California 92093-0085	10. Work Unit No. (TRAIS)
	11. Contract or Grant No.
12. Sponsoring Agency Name and Address California Department of Transportation Engineering Service Center 1801 30th St., West Building MS-9 Sacramento, California 95807	13. Type of Report and Period Covered Final Report -
	14. Sponsoring Agency Code

15. Supplementary Notes

Prepared in cooperation with the State of California Department of Transportation.

16. Abstract

The purpose of this research program is to investigate the shear strength of thin-wall circular hollow columns. This type of structural member presents several advantages when compared to solid columns due to the reduced mass per unit length afforded by the reduced section area. Disadvantages depend upon the possibility to ensure appropriate concrete confinement while keeping simple construction procedures. In fact, in the past hollow columns were typically designed with two coaxial layers of longitudinal reinforcement (placed near the inside and the outside faces) linked by a large number of crossties. As recent studies from Japan have demonstrated, this type of members show extremely ductile behavior, but require significant construction effort and cost.

The purpose of the present work is to develop simple (i.e. easy to build, with only one layer of reinforcement), cost-effective structural members to be used for large highway bridges. Shear tests were conducted as a part of the research program on hollow columns, to show that appropriate design details can ensure good performance also when these members are subjected to high shear demand.

The main results of the experimental studies conducted on three large size specimens are reported herein. The test units, designed with only one layer of longitudinal and spiral reinforcement near the outside face, were subjected to constant compressive axial force and cyclically varying lateral load. Theoretical aspects of the shear strength degradation with increasing lateral displacement are approached with recently developed shear strength models and with the Modified Compression Field Theory. Predictions of the behavior and of the failure mode are compared with the experimental results, showing good agreement.

The first unit failed in flexure in a ductile fashion, while the second and the third failed in shear in a ductile and brittle fashion respectively. In all tested units concrete spalled off in the inside face, causing rapid strength degradation. Results indicate that a ductile performance is obtained with relatively low levels of longitudinal reinforcement and axial load. The shear strength enhancement due to the effect of the axial load appears to be less significant than in solid members.

17. Key Words	18. Distribution Statement
Shear strength, hollow columns, confinement	Unlimited

19. Security Classification (of this report)	20. Security Classification (of this page)	21. No. of Pages	22. Price
Unclassified	Unclassified	~203	

Form DOT F 1700.7 (8-72) Reproduction of completed page authorized

This Page Left Blank

ABSTRACT

The purpose of this research program is to investigate the shear strength of thin-wall circular hollow columns. This type of structural member presents several advantages when compared to solid columns due to the reduced mass per unit length afforded by the reduced section area. Disadvantages depend upon the possibility to ensure appropriate concrete confinement while keeping simple construction procedures. In fact, the past hollow columns were typically designed with two layers of longitudinal reinforcement (placed near the inside and the outside faces) linked by a large number of crossties. As recent studies from Japan have demonstrated, this type of members show extremely ductile behavior, but require significant construction effort and cost.

The purpose of the present work is to develop simple (i.e. easy to build, with only one layer of reinforcement), cost-effective structural members to be used for large highway bridges. Shear tests were conducted as a part of the research program on hollow columns, to show that appropriate design details can ensure good performance also when these members are subjected to high shear demand.

The main results of the experimental studies conducted on three large size specimens are reported herein. The test units, designed with only one layer of longitudinal and spiral reinforcement near the outside face, were subjected to constant compressive axial force and cyclically varying lateral load. Theoretical aspects of the shear strength degradation with increasing lateral displacement are approached with recently developed shear strength models and with the Modified Compression Field Theory. Predictions of the behavior and of the failure mode are compared with the experimental results, showing good agreement.

The first unit failed in flexure in a ductile fashion, while the second and the third failed in shear in a ductile and brittle fashion respectively. In all tested units concrete spalled off in the inside face, causing rapid strength degradation. Results indicate that a ductile performance is obtained with relatively low levels of longitudinal reinforcement and axial load. The shear strength enhancement due to the effect of the axial load appears to be less significant than in solid members.

TABLE OF CONTENTS

ABSTRACT ..... **II**

TABLE OF CONTENTS ..... **II**

NOTATION ..... **V**

LIST OF FIGURES ..... **VII**

LIST OF TABLES ..... **XII**

1 INTRODUCTION **1**

2 DESIGN CONSIDERATIONS AND ANALYTICAL MODELS **3**

2.1 SHEAR STRENGTH 3
2.1.1 UCSD Models 3
2.1.2 ATC 32 Model 11
2.1.3 Caltrans MEMO 20-4 Model 12
2.2 FORCE-DISPLACEMENT ENVELOPE RESPONSE 13
2.2.1 Elastic Flexural Displacement 14
2.2.2 Plastic Flexural Displacement 15
2.2.3 Shear Displacement 17

3 TEST SPECIMENS **20**

3.1 TEST SETUP AND LOADING SCHEMES 24
3.2 INSTRUMENTATION 26

4 EXPERIMENTAL RESULTS **29**

4.1 SPECIMEN HS1 29
4.1.1 Predicted Response 29
4.1.1.1 Force-Displacement Predicted Response 29
4.1.1.2 Shear Behavior 33
4.1.2 General Observations 35
4.1.2.1 Elastic Cycles 35
4.1.2.2 Inelastic Cycles 38
4.1.3 Hysteretic Response 44
4.1.3.1 Force-Displacement 44
4.1.3.2 Moment-Curvature 46
4.1.3.3 Axial Load 47
4.1.3.4 Shear Deformation 48
4.1.4 Envelope Response 52
4.1.4.1 Displacement Components 52
4.1.4.2 Plastic Hinge Length 55
4.1.5 Profiles At Load (or Displacement) Peak Level 55

4.1.5.1 Flexural and Shear Deformation Components 56
4.1.5.2 Curvatures 59
4.1.5.3 Longitudinal Reinforcement Strains 62
4.1.5.4 Transverse Reinforcement Strains 65
4.1.5.5 Section Longitudinal Strain Profiles 69
4.1.5.6 Section Transverse Strain Profiles 77
4.1.6 Discussion 82
4.2 SPECIMEN HS2 86
4.2.1 Predicted Response 86
4.2.1.1 Force –Displacement Predicted Response 87
4.2.1.2 Shear Behavior 91
4.2.2 General Observations 94
4.2.2.1 Elastic Cycles 94
4.2.2.2 Inelastic Cycles 97
4.2.3 Hysteretic Response 102
4.2.3.1 Force-Displacement 102
4.2.3.2 Moment-Curvature 103
4.2.3.3 Axial-Load 105
4.2.3.4 Shear Deformation 106
4.2.4 Envelope Response 111
4.2.4.1 Displacement Components 111
4.2.4.2 Plastic Hinge Length 114
4.2.5 Profiles at Peak Load (or Displacement) Levels 114
4.2.5.1 Flexural and Shear Deformation Components 114
4.2.5.2 Curvatures 118
4.2.5.3 Longitudinal Reinforcement Strains 121
4.2.5.4 Transverse Reinforcement Strains 124
4.2.5.5 Section Longitudinal Strain Profiles 127
4.2.5.6 Section Transverse Strain Profiles 135
4.2.6 Discussion 139
4.3 SPECIMEN HS3 142
4.3.1 Predicted Response 142
4.3.1.1 Force –displacement Predicted Response 143
4.3.1.2 Shear Behavior 147
4.3.2 General Observations 150
4.3.2.1 Elastic Cycles 150
4.3.2.2 Inelastic Cycles 154
4.3.3 Hysteretic Response 157
4.3.3.1 Force-Displacement 157
4.3.3.2 Moment-Curvature 159
4.3.3.3 Axial-Load 160
4.3.3.4 Shear Deformation 161
4.3.4 Envelope Response 166
4.3.4.1 Displacement Components 166
4.3.4.2 Plastic Hinge Length 169
4.3.5 Profiles at Peak Load (or Displacement) Levels 169

4.3.5.1 Flexural and Shear Deformation Components 170
4.3.5.2 Curvatures 173
4.3.5.3 Longitudinal Reinforcement Strains 176
4.3.5.4 Transverse Reinforcement Strains 179
4.3.5.5 Section Longitudinal Strain Profiles 182
4.3.5.6 Section Transverse Strain Profiles 189
4.3.5.7 Section Shear Deformation Profiles 194
4.3.6 Discussion 198

5 SUMMARY AND CONCLUSIONS 200

REFERENCES 202

NOTATION

A_g	Gross section area
A_h	Spiral area
A_n	Net section area
A_{st}	Total area of the longitudinal reinforcement
D	External diameter of the section
D_i	Internal diameter of the section
D_{long}	Longitudinal reinforcement diameter
E_c	Concrete elastic modulus
E_s	Steel elastic modulus
F_{va}	Average capacity of the spirals
F_1	Factor in Caltrans M20-4 shear model dependent of ductility level
F_2	Factor in Caltrans M20-4 shear model dependent of axial load level
G	Shear modulus
H	Column height
I_Z	Moment of inertia
J_T	Elastic energy due to shear
L_P	Plastic hinge length
M	Applied moment
$N_{spirals}$	Number of spiral
P	Axial load
R'	Radius of the spiral
V	Applied shear
V_n	Nominal shear strength of circular hollow column
V_c	Shear strength of concrete component
V_s	Shear strength of transverse reinforcement component
V_p	Shear strength of axial load component
V_y'	Lateral force at first yield
c_0	Cover concrete
c_{yield}	Neutral axis depth at ideal flexural capacity
c_{ult}	Neutral axis depth
k_1	Coefficient in ATC 32 shear model (compressive load)
k_2	Coefficient in ATC 32 shear model (tensile load)
f_c'	Concrete compressive strength
f_{yh}	Yield strength for spiral
f_{yv}	Yield strength for longitudinal reinforcement
f_t	Concrete tensile strength
f_u	Ultimate strength for longitudinal reinforcement
r_1	Internal radii of section
r_2	External radii of section
s	Spiral spacing
α	Factor for the column aspect ratio
β	Factor for longitudinal reinforcement ratio

ε_c	Concrete strain (0.004)
ε_s	Steel strain (0.015)
ε_{if}	Concrete strain near inside face
ε_u	Ultimate longitudinal reinforcement strain
φ	Curvature
φ'	Curvature at first yield
γ	Factor for strength reduction of concrete component
γ_{xy}	Shear strain
μ_Δ	Displacement ductility level
ν	Poisson ratio
ν_{xy}	Shear Stress
θ	Angle of shear crack
ρ	Volumetric transverse reinforcement ratio
ξ	Ratio of the section shear area to gross area
?	Column top displacement
? $_{EF}$	Column top displacement due to elastic flexure
? $'_{EF}$	Elastic flexural displacement at first yield
? $_{pF}$	Column top displacement due to plastic flexure
? $_{S}$	Column top displacement due to shear
? $_{sc}$	Column top displacement due to concrete shear deformation
? $_{ss}$	Column top displacement due to transverse reinforcement shear
? $_{y}$	Column top yield displacement

LIST OF FIGURES

Figure 2.1 Neutral Axis Positions for Hollow Circular Columns 4
Figure 2.2 Reduction of Concrete Shear Component (8) with Curvature Ductility 5
Figure 2.3 Definition of Circular Section Shear Parameters 6
Figure 2.4 Shear Strength Reduction as Function of Radii Ratios 8
Figure 2.5 Axial Load Component of Shear Strength 10
Figure 2.6 Elastic Flexural Displacement 14
Figure 2.7 Plastic Flexural Displacement 16
Figure 2.8 Shear Displacement 17
Figure 3.1 Section Geometry and Reinforcement 22
Figure 3.2 Unit HS2 – Reinforcing Cage 23
Figure 3.3 Unit HS2 Before Casting 24
Figure 3.4 Unit HS2 After Casting 24
Figure 3.5 Test Setup 25
Figure 3.6 Lateral Loading Protocol 26
Figure 3.7 North Side of Unit HS2 28
Figure 3.8 West Side of Unit HS2 28
Figure 4.1 Comparison of Predicted Force-Displacement Response of Unit HS1 with Different Shear Strength Models 31
Figure 4.2 Predicted Lateral Displacment/Sprial Strain Relationship for HS1 34
Figure 4.3 Predicted Force/Spiral Strain Relationship for HS1 34
Figure 4.4 Photo at 700kN – from NW 38
Figure 4.5 Unit HS1 Condition After 1 Cycle to μ_Δ = 1. (Side View) 39
Figure 4.6 Unit HS1 Condition After 1 Cycle to μ_Δ = 1. (Front View) 40
Figure 4.7 Unit HS1 Condition After 1 cycle to μ_Δ = 3 (Side View) 42
Figure 4.8 Unit HS1 Compression Zone and Bar Buckling on First Cycle to μ_Δ = 6 43
Figure 4.9 Unit HS1 – Composite Photo of Inside Face Spalling After 3 Cycles to μ_Δ = 6 44
Figure 4.10 Unit HS1 Lateral Force-Displacement Response 45
Figure 4.11 Unit HS1 Base Section Moment-Curvature Response 46
Figure 4.12 Unit HS1 – Variation of Applied Axial Load with Displacement 48
Figure 4.13 Unit HS1 – Lateral Force/Shear Distortion From Gross Column Measurements 50
Figure 4.14 Unit HS1 – Lateral Force/Shear Strain from Small Shear Panels 51
Figure 4.15 Unit HS1 Shear and Flexural Components of Total Displacement 52
Figure 4.16 HS1 Displacement Components vs. Total Top Displacement 54
Figure 4.17 Unit HS1 Lateral Force/Displacement-Component Response 54
Figure 4.18 Unit HS1 Shear Displacement Profiles at Different Ductility Levels 57
Figure 4.19 Unit HS1 Flexural Displacement Profiles at Different Ductility Levels 58
Figure 4.20 Unit HS1 Curvature Profile at Different Ductility Levels – Strain Penetration Ignored 60
Figure 4.21 Unit HS1 Curvature Profile at Different Ductility Levels – Strain Penetration Included 61

Figure 4.22 Unit HS1 Profile of Longitudinal Rebar Strain at Extreme North Tension Location (Push Loading) 63
Figure 4.23 Unit HS1 Profile of Longitudinal Rebar Strain at Extreme South Tension Location (Pull Loading) 64
Figure 4.24 Unit HS1 Vertical Profiles of Spiral Strain on West Side 67
Figure 4.25 Unit HS1 Vertical Profiles of Spiral Strain on East Side 68
Figure 4.26 Unit HS1 Section Longitudinal Bar Strain Profiles, 102 mm Below Base Section, Push Loading 71
Figure 4.27 Unit HS1 Section Longitudinal Bar Strain Profiles, 102 mm Below Base Section, Pull Loading 72
Figure 4.28 Unit HS1 Section Longitudinal Bar Strain Profiles, 156 mm Above Base Section, Push Loading 73
Figure 4.29 Unit HS1 Section Longitudinal Bar Strain Profiles, 156 mm Above Base Section, Pull Loading 74
Figure 4.30 Unit HS1 Section Longitudinal Bar Strain Profiles, 609 mm Above Base Section, Push Loading 75
Figure 4.31 Unit HS1 Section Longitudinal Bar Strain Profiles, 609 mm Above Base Section, Pull Loading 76
Figure 4.32 Unit HS1 Section Transverse Bar Strain Profiles 280 mm Above Base Section 79
Figure 4.33 Unit HS1 Section Transverse Bar Strain Profiles 840 mm Above Base Section 80
Figure 4.34 Unit HS1 Section Transverse Bar Strain Profiles 1400 mm Above Base Section 81
Figure 4.35 Unit HS1 Development of Spiral Strain with Increasing Top Displacement 85
Figure 4.36 Unit HS1 Development of Spiral Strain with Increasing Lateral Load 85
Figure 4.37 Unit HS2 Refined Force-Displacement Response Predictions 88
Figure 4.38 Unit HS2 Predicted Displacement/Spiral Strain Relationship 93
Figure 4.39 Unit HS2 Predicted Force/Spiral Strain Relationship 93
Figure 4.40 Unit HS2 Crack Pattern at 75% of First Yield (Side View) 96
Figure 4.41 Unit HS2 Crack Pattern at Ductility 1 (Side View) 98
Figure 4.42 Unit HS2 Concrete Spalling on Compression Zone, Outside Surface at μ_Δ = 2.0 99
Figure 4.43 Unit HS2 Spalling of Inside Surface of Compression Zone at $\mu_?$ = 3.0, First Cycle 100
Figure 4.44 Unit HS2 Spalling and Crusing of Compression Zone, and Rebar Buckling, at $\mu_?$ = 3.0, Second Cycle 100
Figure 4.45 Unit HS2 Shear Failure, with Spiral Fracture, at $\mu_?$ = 3.5 101
Figure 4.46 Unit HS2 Buckling of Longitudinal Bars and Fracture of Spirals in Compression Zone at $\mu_?$ = 3.5 102
Figure 4.47 Unit HS2 Compression of Theoretical and Experimental Force-Displacement Response 103
Figure 4.48 Unit HS2 Base Moment/Curvature Experimental Response 104
Figure 4.49 Unit HS2 Lateral Displacement/Axial Load Relationship 105
Figure 4.50 Unit HS2 Lateral Force/Shear Distortion from Gross Column Measurements 107

Figure 4.51 HS2 Lateral Force/Shear Strain from Small Shear Panels (West Side of Column) 109
Figure 4.52 Unit HS2 Lateral Force/Shear Strain from Small Shear Panels (East Side of Column) 110
Figure 4.53 Unit HS2 Shear and Flexural Components of Total Displacement..... 111
Figure 4.54 Unit HS2 Displacement Components vs Total Top Displacement 113
Figure 4.55 Unit HS2 Lateral Force/Displacement-Component Response 113
Figure 4.56 Unit HS2 Shear Displacement Profiles at Different Ductilities 116
Figure 4.57 Unit HS2 Flexural Displacement Profiles at Different Ductilities 117
Figure 4.58 Unit HS2 Curvature Profiles at Different Ductilities – Strain Penetration Ignored 119
Figure 4.59 Unit HS2 Curvature Profiles at Different Ductilities – Strain Penetration Included..... 120
Figure 4.60 Unit HS2 Profiles of Longitudinal Rebar Strain at Extreme North Tension Location (Push Loading)..... 122
Figure 4.61 Unit HS2 Profiles of Longitudinal Rebar Strain at Extreme South Tension Location (Pull Loading) 123
Figure 4.62 Unit HS2 Vertical Profiles of Spiral Strain on West Side 125
Figure 4.63 Unit HS2 Vertical Profiles of Spiral Strain on West Side 126
Figure 4.64 Unit HS2 Section Longitudinal Bar Strain Profiles 102 mm Below Base Section, Push Loading 129
Figure 4.65 Unit HS2 Section Longitudinal Bar Strain Profiles 102 mm Below Base Section, Pull Loading..... 130
Figure 4.66 Unit HS2 Section Longitudinal Bar Strain Profiles 152 mm Above Base Section, Push Loading 131
Figure 4.67 Unit HS2 Section Longitudinal Bar Strain Profiles 102 mm Below Base Section, Pull Loading..... 132
Figure 4.68 Unit HS2 Section Longitudinal Bar Strain Profiles 609 mm Above Base Section, Push Loading 133
Figure 4.69 Unit HS2 Section Longitudinal Bar Strain Profiles 609 mm Above Base Section, Pull Loading..... 134
Figure 4.70 Unit HS2 Section Transverse Bar Strain Profiles 350 mm Above Base Section..... 136
Figure 4.71 Unit HS2 Section Transverse Bar Strain Profiles 876 mm Above Base Section..... 137
Figure 4.72 Unit HS2 Section Transverse Bar Strain Profiles 1397 mm Above Base Section..... 138
Figure 4.73 Unit HS2 Development of Spiral Strain with Increasing Top Development 141
Figure 4.74 Unit HS2 Development of Spiral Strain with Increasing Lateral Load..... 141
Figure 4.75 Unit HS3 Refined Force-Displacement Response Predictions 144
Figure 4.76 Unit HS3 Predicted Displacement/Spiral Strain Relationship 148
Figure 4.77 Unit HS3 Predicted Displacement/Spiral Strain Relationship 149
Figure 4.78 Unit HS3 Crack Pattern at 75% of First Yield (Side View)..... 152
Figure 4.79 Unit HS3 Crack Pattern at First Yield (Side View) 153
Figure 4.80 Unit HS3 Crack Pattern at Ductility 1 (Side View) 155

Figure 4.81 Unit HS3 Spiral Bar Fracture at Ductility 2 156
Figure 4.82 Unit HS3 Failure of Compression Zone at Ductility 2 157
Figure 4.83 Unit HS3 Comparison of Theoretical and Experimental Force-Displacement Response 158
Figure 4.84 Unit HS3 Base Moment-Curvature Experimental Response 160
Figure 4.85 Unit HS3 Lateral Displacement/Axial Load Relationship 161
Figure 4.86 Unit HS3 Lateral Force/Shear Distortion from Gross Column Measurements 163
Figure 4.87 Unit HS3 Lateral Force/Shear Strain Forces Small Shear Panels (West Side of Column) 164
Figure 4.88 Unit HS3 Lateral Force/Shear Strain Forces Small Shear Panels (East Side of Column) 165
Figure 4.89 Unit HS3 Shear and Flexural Components of Total Displacement..... 168
Figure 4.90 Unit HS3 Displacement Components vs Total Top Displacement 168
Figure 4.91 Unit HS3 Lateral Force/Displacement-Component Response 169
Figure 4.92 Unit HS3 Shear Displacement Profiles at Different Ductilities 171
Figure 4.93 Unit HS3 Flexural Displacement Profiles at Different Ductilities 172
Figure 4.94 Unit HS3 Curvature Profiles at Different Ductilities – Strain Penetration Ignored 174
Figure 4.95 Unit HS3 Curvature Profiles at Different Ductilities – Strain Penetration Included..... 175
Figure 4.96 Unit HS3 Profiles of Longitudinal Rebar Strain at Extreme North Tension Location (Push Loading)..... 177
Figure 4.97 Unit HS3 Profiles of Longitudinal Rebar Strain at Extreme South Tension Location (Pull Loading) 178
Figure 4.98 Unit HS3 Vertical Profiles of Spiral Strain on West Side 180
Figure 4.99 Unit HS3 Vertical Profiles of Spiral Strain on East Side 181
Figure 4.100 Unit HS3 Section Longitudinal Bar Strain Profiles 102 mm Below Base Section, Push Loading 183
Figure 4.101 Unit HS3 Section Longitudinal Bar Strain Profiles 102 mm Below Base Section, Pull Loading..... 184
Figure 4.102 Unit HS3 Section Longitudinal Bar Strain Profiles 152 mm Above Base Section, Push Loading 185
Figure 4.103 Unit HS3 Section Longitudinal Bar Strain Profiles 152 mm Above Base Section, Pull Loading..... 186
Figure 4.104 Unit HS3 Section Longitudinal Bar Strain Profiles 609 mm Above Base Section, Push Loading 187
Figure 4.105 Unit HS3 Section Longitudinal Bar Strain Profiles 609 mm Above Base Section, Pull Loading..... 188
Figure 4.106 Unit HS3 Section Transverse Bar Strain Profiles 280 mm Above Base Section..... 191
Figure 4.107 Unit HS3 Section Transverse Bar Strain Profiles 700 mm Above Base Section..... 192
Figure 4.108 Unit HS3 Section Transverse Bar Strain Profiles 1260 mm Above Base Section..... 193
Figure 4.109 Crack Pattern in Small Instrumental Shear Panels 195

Figure 4.110 Unit HS3 Shear Deformation Measured by Small Shear Panels 987 mm Above Base Section 196
Figure 4.111 Unit HS3 Shear Deformation Measured by Small Shear Panels 2012 mm Above Base Section 197
Figure 4.112 Unit HS3 Development of Spiral Strain with Increasing Top Development 199
Figure 4.113 Unit HS3 Development of Spiral Strain with Increasing Lateral Load..... 199

LIST OF TABLES

Table 3.1 Properties of the Test Units 21
Table 3.2 Steel Mechanical Properties 22
Table 4.1 Predicted Capacity with Different Models 32
Table 4.2 Predicted Specimen Behavior at Different Stages 32
Table 4.3 Unit HS2 Predicted Failure Loads and Displacements 89
Table 4.4 Unit HS2 Moment-Curvature Limit States 90
Table 4.5 Unit HS3 Predicted Failure Loads and Displacement 146
Table 4.6 Unit HS3 Moment-Curvature Limit States 146

1 INTRODUCTION

Previous research in this field has shown that hollow columns may be, in some cases, economically viable when compared to usual solid members. Applications include large bridge columns and piles as well as offshore platforms. This structural type was in fact extensively used in Europe and in Japan since the early seventies. The economical convenience in the use of hollow columns is due to the cost saving afforded by reduced section area (up to 70%). Also, hollow columns are more efficient than solid ones from a structural point of view. When the weight of the vertical members is relevant in the performance of the entire structure, a significant reduction in the seismic mass may be attained by using this structural type.

From this point of view, the advantage is evident in viaducts with very tall piers, where the weight of the vertical members is no longer negligible compared to that of the superstructure. The present work shows that significant advantages appear also in short members. In fact, short hollow columns can be used when high stiffnesses are needed, since section diameter can be increased without causing construction problem related to internal cracking (generated by non uniform development of the heat of hydration).

In the past hollow columns have typically been designed with two layers of reinforcement and crossties. This aspect represents a significant inconvenience, as the time and cost needed to place that type of reinforcement was not counterbalanced by significantly improved performance. More recent studies have shown that the performance attainable with only one layer of reinforcement near the outside face is ductile, provided moderate axial load is applied and medium-low ratios of longitudinal reinforcement are used.

Zahn et al. [Zahn et al., 1990] and Whittaker et al. [Whittaker et al.,1988] investigated the ductility capacity of slender circular members without confinement on

inside face. It was found that a ductile behavior is obtained with low amounts of longitudinal reinforcement, low levels of axial load and reasonably thick wall.

In a parallel study to this one, (Hoshibuma and Priestley, 2000) Zahn and Whittaker was extended to hollow circular columns with thin walls with realistic axial load levels and reinforcement ratios. It was found that the limit to ductility was reached when the inside surface reached compression strains of about 0.005, which was followed by spalling of the inside surface, and implosion of the section.

This report presents the results of an investigation on the aspects that was remained unknown: in particular, the shear strength of simple systems with only one layer of reinforcement in the outside face. The results confirm the findings obtained for more slender members, indicating that the implosion of concrete in the inside surface governs the activation of the strength degradation mechanism. Considerations are made on the methods to be used to predict the maximum strength and deformation capacity of members characterized by a small ratio of the shear span to the section diameter. State-of-the-art shear strength models [Kowalsky et al., 2000] are used, with some modifications, and results are compared with more sophisticated sectional analysis conducted with the Modified Compression Field Theory [Bentz and Collins, 1998] [Vecchio and Collins 1986]. In both cases, comparison with experimental evidence shows good agreement in terms of ultimate strength and deformation capacity as well as load-deformation behavior.

2 DESIGN CONSIDERATIONS AND ANALYTICAL MODELS

In this section, the methods used to predict the shear strength and load deformation curves are discussed. Two commonly used models (ATC 32 and Caltrans Memo 20-4) are compared with the model from UCSD, which is modified to be applied to circular hollow sections. Results obtained with the models are shown later in the report, in the sections discussing the experimental response of the specimens. In those sections, the predicted response is compared with the actual behavior, showing good agreement. It shows that ductility capacity is dependent significantly on the neutral axis depth with respect to the wall thickness.

2.1 Shear Strength

The objective of this section is to predict the maximum shear strength of circular hollow columns and its dependence on curvature ductility. For this purpose, four different models are used: the UCSD old model, the UCSD new model, the ATC 32 model and the Caltrans Memo 20-4 model. In the following, all equations are given in S.I. units.

2.1.1 UCSD Models

The nominal shear strength, estimated based on UCSD models, is contributed from three components corresponding to concrete, transverse reinforcement and axial load contributions. The nominal shear strength is given by

$$V_n = V_c + V_s + V_p \tag{2.1}$$

(a) Concrete contribution, V_c

The V_c component considers the aggregate interlock in the concrete. It is given by

$$V_c = \text{aß?}\sqrt{f_c'}?A_g \tag{2.2}$$

In Equation (2.2), α is a factor that accounts for the aspect ratio and is given by

$$\alpha = 1 \le 3 - \frac{M}{VD} \le 1.5 \tag{2.3}$$

where M is the applied moment, V is the applied shear, and D is the external diameter of the column. β is a factor that accounts for the longitudinal reinforcement ratio and refers to the cracks width. By considering the position of the neutral axis as shown in Figure 2.1, it is given by

$$\beta = 0.5 + 20\frac{A_{st}}{\text{p}D^2/4} \le 1 \tag{2.4a}$$

$$\text{or } \text{ß} = 0.5 + 20\frac{A_{st}}{A_g} \le 1 \tag{2.4b}$$

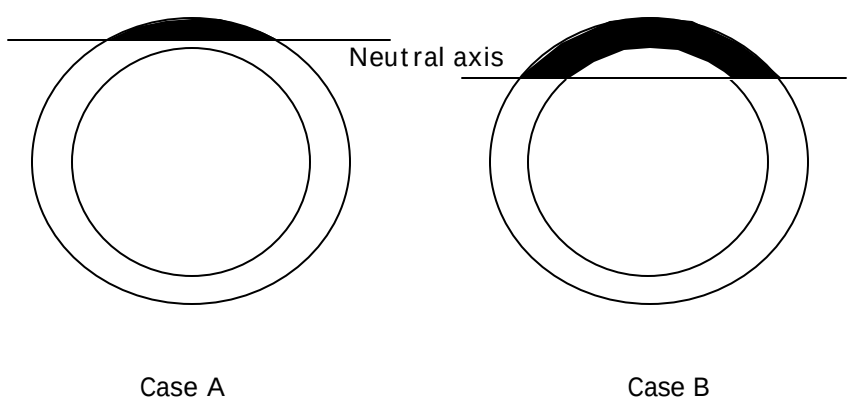

Figure 2.1 Neutral Axis Positions for Hollow Circular Columns

If the neutral axis is entirely within the wall thickness (Case A) then equation (2.4a) must be used. The Equation (2.4b) is appropriate if the neutral axis is deeper than the wall thickness (Case B). In Equations (2.4), A_{st} is the total area of longitudinal reinforcement, and A_g (= $\mathrm{p}\left(D^2 - D_i^2\right)/4$) is the gross area of the section with D and D_i the external and internal diameters of the column. Figure 2.2 shows the variation of a parameter γ, which decreases with the increasing curvature ductility. ξ is a coefficient introduced in order to express the section shear area as a percentage of the gross area. It can be estimated on the basis of the elastic beam theory as follows. The elastic energy due to shear is expressed as

$$J_T = \frac{1}{2}\iiint_V v_{xy}\,?_{xy}\,dv \tag{2.5}$$

where v_{xy} is the shear stress given by $v_{xy} = V_y Q(s')/I_Z b(s')$ and γ_{xy} is the shear strain given by $?_{xy} = v_{xy}/G$ with G the shear modulus.

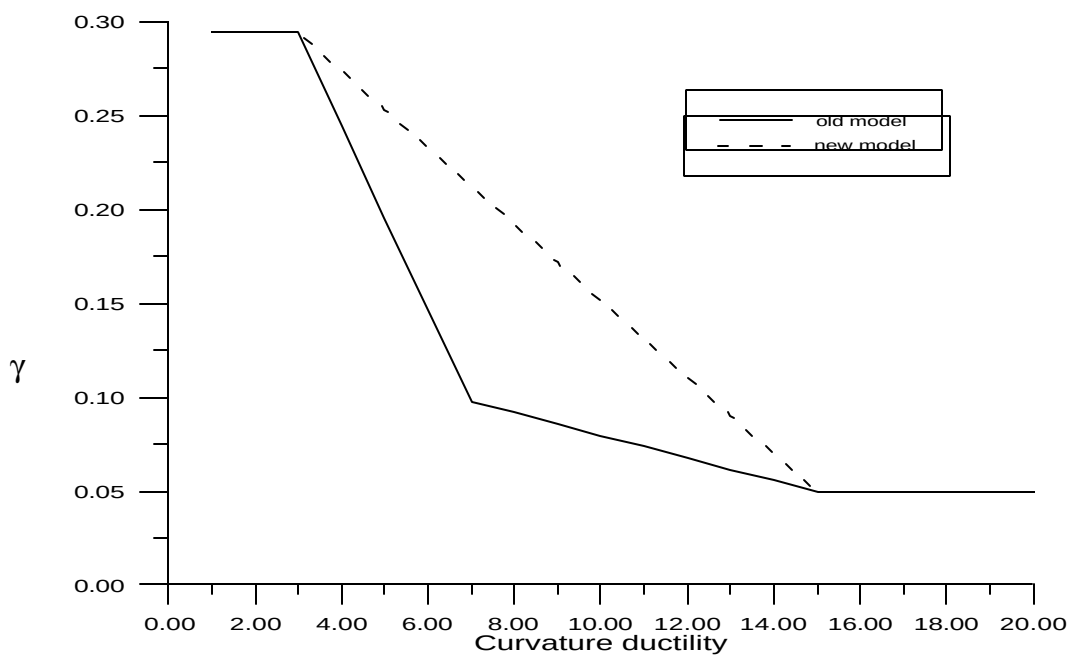

Figure 2.2 Reduction of Concrete Shear Component (8) with Curvature Ductility

Substituting v_{xy} and γ_{xy} into Equation (2.5), J_T can be written as

$$J_T = \frac{1}{2}\int_s \frac{V_y^{\ 2}}{G?A_g} ds \tag{2.6}$$

where

$$?A_g = \frac{I_z^{\ 2}}{\iint_S \frac{Q_z^{\ 2}(s')}{b^2(s')} dS} \tag{2.7}$$

In the expression of ξA_g, I_z is the moment of inertia given by $I_Z = \iint_S y^2 dS$, $Q_z(s')$ is the static moment given by $Q_z(s') = \iint_{s'} h ds'$, and $b(s')$ is the particular function that defines the width of the section, shown in Figure 2.3.

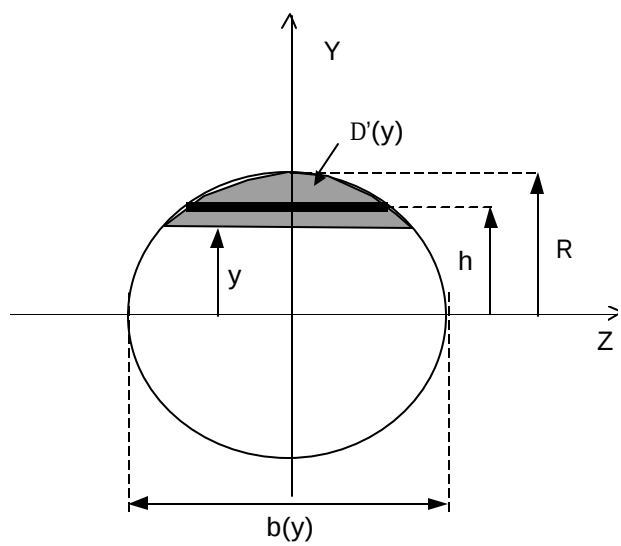

Figure 2.3 Definition of Circular Section Shear Parameters

For a circular section, I_z, $Q_z(y)$, $b(y)$ and ξA_g are expressed as

$$I_Z = \frac{1}{2}\left[\int y^2 dS + \int z^2 dS\right] = \frac{1}{2}\int_0^R r^2 dS = \frac{1}{2}\int_0^R r^2\, 2\,\mathrm{p}\, r dr = \frac{\mathrm{p}\, R^4}{4} \tag{2.8}$$

$$Q_z(y) = \int_y^R h \times 2\sqrt{R^2 - h^2}\, dh = \frac{2}{3}(R^2 - y^2)^{3/2} \tag{2.9}$$

$$b(y) = 2\sqrt{R^2 - y^2} \tag{2.10}$$

$$?A_g = \frac{\mathrm{p}^2\, R^8/16}{\int_{-R}^{R} \frac{2}{9}(R^2 - y^2)^{5/2} dy} = 0.9\,\pi R^2 = 0.9\, A_g \tag{2.11}$$

The same calculation for a rectangular column leads to ξAg = $5/6 A_g$ = 0.833 A_g. For this reason, the ASCE-ACI recommendations imply that ξ= 0.8 for both rectangular and circular solid columns. For a hollow circular column, in the expressions of I, Q, b and A_g, R^n must be replaced by (r_2^n-r_1^n) where r_2 and r_1 are the outer and inner radii. Therefore, it can easily be shown that, for a hollow circular column, ξAg is given by

$$?A_g = ?\left(0.8 A_g\right) \tag{2.12}$$

where $? = \frac{(r_2^2 + r_1^2)(r_2 - r_1)}{(r_2^3 - r_1^3)} = \frac{(1 + \mathrm{a}^2)(1 - \mathrm{a})}{(1 - \mathrm{a}^3)}$ with $\mathrm{a} = \frac{r_1}{r_2}$ (2.13)

The coefficient λ has been introduced above in order to underline the difference between hollow and solid circular sections. As shown in Figure 2.4, for r_1/r_2 >0.6, λ should be taken equal to 2/3. Therefore, in Equation (2.2), $\alpha\beta\gamma\sqrt{f_c'}$ is the shear strength of the concrete whereas $?A_g = \frac{2}{3}\left(0.8 A_g\right) = 0.533 A_g$ is the shear area for a hollow circular column.

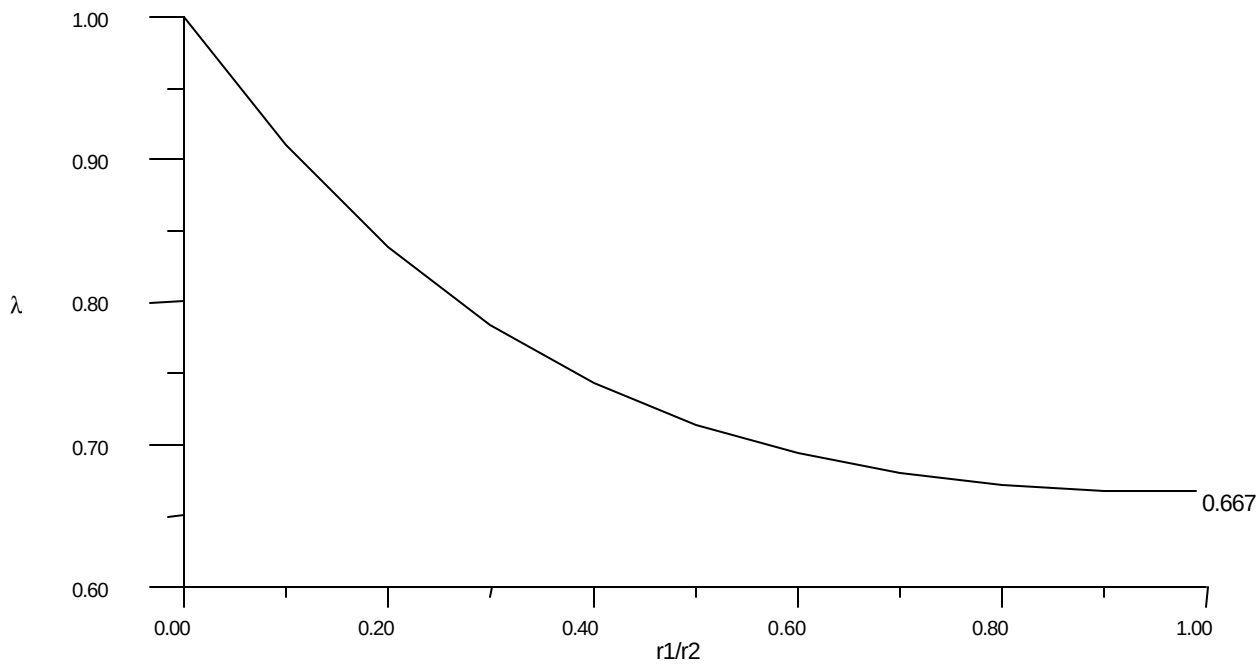

Figure 2.4 Shear Strength Reduction as Function of Radii Ratios

(b) Transverse reinforcement contribution, V_s

The V_s component is contributed from the strength of the transverse reinforcement. In our case, the transverse reinforcement is provided by a continuous spiral. The V_s component is dependent on the number of spiral layers crossed by a shear crack.

$$F_v = 2A_h f_{yh} \cos a \tag{2.14}$$

The angle α increases from 0 to $\pi/2$ as the distance x between the crack and the column axis perpendicular to the applied shear force increases from 0 to R', R' is the radius of the spiral, f_{yh} is the nominal strength of the spiral steel and A_h is the area of the spiral. The average capacity of the spirals is thus given by

$$F_{va} = \frac{1}{R}\int_{x=0}^{R} dF_v = \frac{1}{R}\int_0^R 2A_h \; f_{yh} cos a \; dx = \frac{p}{2} A_h f_{yh} \tag{2.15}$$

where $x/R = \sin a$, $da/R = \cos a \, da$

If θ is the angle of the shear crack with respect to a vertical axis, the number of spiral layers crossed by the crack is given by

$$N_{\text{spirals}} = \frac{(D - c_o - c_{ult})\cot ?}{s} \tag{2.16}$$

Where D is the external diameter of the column, c_o is the cover, c_{ult} is the neutral axis depth at ultimate and s is the spacing between the spiral layers. Therefore V_s is given by

$$V_s = V_{sa} N_{spirals} = \frac{\text{p}}{2} A_h f_{yh} \frac{D - c_o - c_{ult}}{s} cot ? \tag{2.17}$$

In the UCSD Model, θ is equal to 30°.

(c) Axial load contribution, V_p

In the UCSD Model, the shear strength enhancement resulting from axial compression is considered as an independent component of shear strength, resulting from a diagonal compression strut, as shown on Figure 2.5, given by

$$V_p = P \tan \text{a} = P \tan \frac{(D - c_{yield})}{2H} \qquad \text{for } P > 0 \tag{2.18a}$$

$$V_p = 0 \qquad \text{for } P < 0 \tag{2.18b}$$

It is shown from Figure 2.5 that P is the axial load and α is the angle between the column axis and the strut from the point of load application to the center of the flexural compression zone at the column plastic hinge critical section. c_{yield} is the neutral axis depth at the ideal flexural capacity, given by the moment–curvature analysis and corresponding to a concrete longitudinal strain in compression ε_c=0.004 or a steel strain ε_s=0.015, whichever occurs first, and H the height of the column.

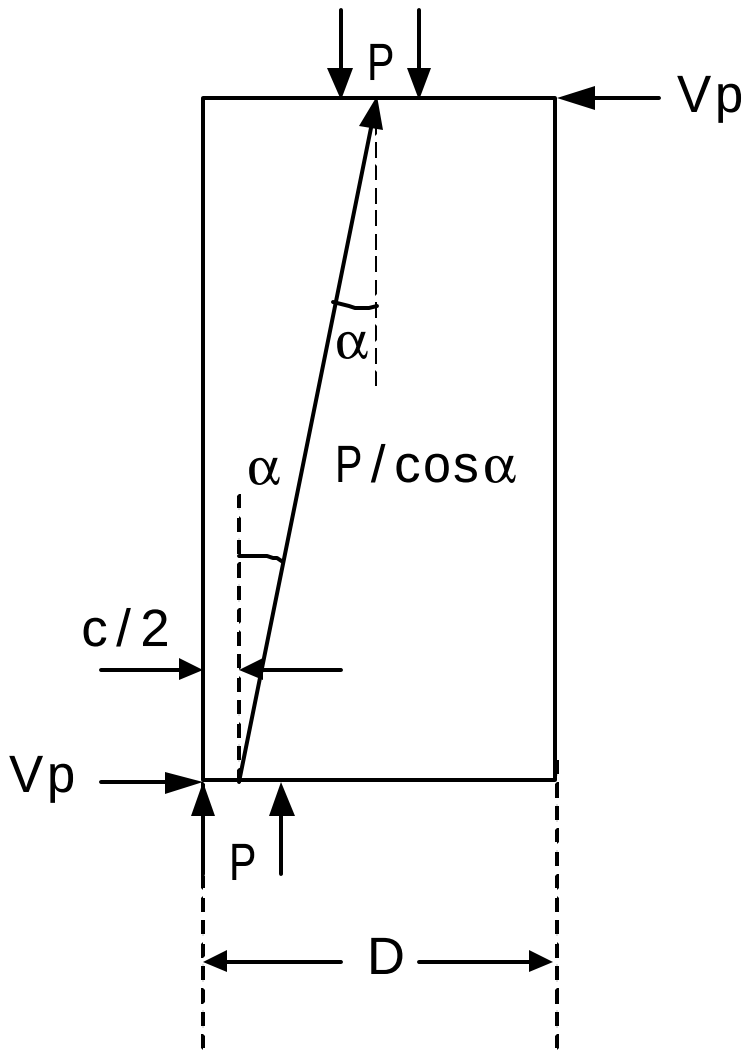

Figure 2.5 Axial Load Component of Shear Strength

It has to be noticed that three components model has provided very good results in predictions of solid columns behavior. But it might not provide such good results for hollow columns as we do not know exactly how to adapt the V_p component to this geometric particularity. Nevertheless, we will assume a full V_p contribution. Note that the preceding equations correspond to assessment as the aim of this study is to predict the behavior of the column. To transform those equations into design equations, γ and V_p have to be multiplied by a reduction coefficient of 85/100 and the angle θ has to be taken equal to 35°, which leads to a conservative margin.

2.1.2 ATC 32 Model

In the ATC 32 Model, the nominal shear strength V_n is given by

$$V_n = V_c + V_s \tag{2.19}$$

It is noted that there is no component considering the shear strength contributed from the axial load, but the contribution is incorporated in a part of the concrete component V_c.

(a) Concrete contribution, V_c

The contribution of V_c is dependent on ductility level and is defined as follows:

$$V_c = \frac{100}{85} 0.167 \left(k_1 + \frac{P}{k_2 A_g} \right) \sqrt{f_c'} ? A_g \tag{2.20}$$

where k_1 is equal to 1 for displacement ductility $\mu_? < 1$, otherwise 0.5. k_2 is 13.8 and 3.45 for P greater than zero or less than zero, respectively. The 100/85 factor has been introduced to transform design into assessment equation.

The ATC 32 model implies a step drop in assessment shear strength in the column end regions when a displacement ductility of 1.0 is reached. But this assumption might not be very precise to represent the influence of ductility on shear strength since experimental data have shown that shear strength decreases almost linearly with increasing displacement ductility. Moreover, it seems difficult to understand how a step drop can efficiently be representative of a real behavior in which no failure is supposed to occur. It is noticed that the ATC 32 model does not take into account the aspect ratio nor the longitudinal reinforcement ratio, which governs variables in the problem.

(b) Reinforcement contribution, V_s

The contribution of V_s is

$$V_s = \frac{p}{2} A_h \; f_{yh} \frac{D - c_0 - Dtran?}{s} \tag{2.21}$$

The expression is similar to the UCSD V_s expression but assumes an angle θ equal to 45° and a crack propagation into the whole core diameter, measured to the centerline of the spiral.

2.1.3 Caltrans MEMO 20-4 Model

The expression of nominal shear strength V_n is the same as that used in ATCT 32 model.

(a) Concrete contribution, V_c

The contribution of V_c is given as

$$V_c = \frac{100}{85} F_1 F_2 \sqrt{f_c'}?A_g \le \frac{100}{85} 0.33 \sqrt{f_c'}?A_g \tag{2.22}$$

In Equation (2.22), $F1$ and $F2$ are factors modifying the shear strength dependant on displacement ductility level μ_Δ and axial load level P/A_g respectively. The factor $F1$ is

$$F1 = 0.025 < 0.08?_s f_{yh} + 0.305 - 0.83\mu_? < 0.25 \tag{2.23}$$

where ρs is the volumetric transverse reinforcement ratio which, for hollow columns, is defined as follows:

$$?_s = \frac{4A_h b\, D}{(D^2 - D_i^2)s} \tag{2.24}$$

The factor $F2$ is expressed as

$$F2 = 1 + \frac{P}{13.8A_g} < 1.5 \qquad \text{for P > 0} \tag{2.25a}$$

$$F2 = 0 \qquad \text{for P < 0} \tag{2.25b}$$

The correction factor for compressive axial load is the same as the ATC 32 factor for a displacement ductility μ_Δ<1.0, but the concrete shear resisting mechanisms are taken to have no strength when the axial load on the column is tensile.

Moreover, the Memo 20-4 model does not take into account the aspect ratio nor the longitudinal reinforcement ratio but depends on the transverse reinforcement ratio. It would also appear that the curvature ductility factor, which is a more meaningful indicator of crack widths, and hence loss of aggregate interlock capacity, would be a more appropriate base than the displacement ductility factor in determining the reduction in shear strength of the concrete shear-resisting mechanism. For this reason, the MEMO 20-4 model, which is based on the displacement ductility factor, seems to be less precise than the UCSD models.

(b) Transverse reinforcement, V_s

The contribution of transverse reinforcement, V_s, is expressed in Equation (2.21).

2.2 Force-Displacement Envelope Response

The relationship of lateral force versus top displacement has been computed neglecting the deformation of the footing. It is given by

$$? = ?_{EF} + ?_{PF} + ?_S \tag{2.26}$$

where $?_{EF}, ?_{PF}$ and Δ_S are the displacements due to Elastic Flexure, Plastic Flexure and Shear.

2.2.1 Elastic Flexural Displacement

The elastic flexural displacement at the top of the column $?_{EF}$ is due to the bending of the column. During the elastic behavior, the curvature $\phi(z)$ is proportional to the moment and thus is a linear function of the height z. In fact, as shown in Figure 2.6, $\phi(z)$ decreases from ϕ to 0 when *z* increases from 0 to *H*. The displacement $?_{EF}$ can be calculated as:

$$\frac{d^2 \mathrm{d}}{d^2 z} = \mathrm{f}(z) = \mathrm{f}\left(1 - \frac{z}{H}\right) \tag{2.27}$$

$$\frac{d\mathrm{d}}{dz} = \mathrm{f}(z) = \mathrm{f}\left(z - \frac{z^2}{2H}\right)\frac{\mathrm{d}\delta}{\mathrm{dz}} \tag{2.28}$$

$$\mathrm{d} = \mathrm{f} \times \left(\frac{z^2}{2} - \frac{z^3}{6H}\right) \tag{2.29}$$

$$?_{EF} = \mathrm{d}(H) = \mathrm{f}\,\frac{H^2}{3} \tag{2.30}$$

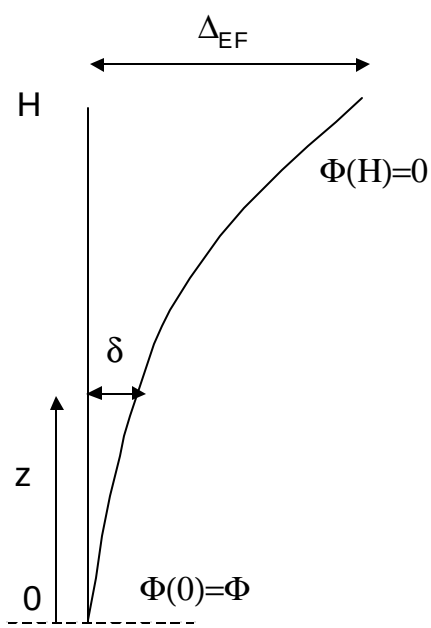

Figure 2.6 Elastic Flexural Displacement

In fact, the full length of inflexion of the column is longer than the clear height. To take into account the penetration of the longitudinal strain in the footing, H is replaced by (H + 0.022f_{yv} D_{long}). Substituting the modified column height into Equation (2.30), Δ_{EF} is thus given by

$$? _{EF} = \frac{f}{3}(H + 0.022\, f_{yv}\, D_{long})^2 \qquad \text{for } V \le V_y' \tag{2.31a}$$

$$? _{EF} = ?'_{EF} \frac{V}{V'_y} \qquad \text{for } V > V_y' \tag{2.31b}$$

In Equations (2.31), V is the lateral force, V_y' and $?'_{EF}$ are the lateral force and elastic flexural displacement at first yield given by the moment-curvature analysis and f_{yv} is the nominal strength of the longitudinal bars. Equation (2.31.b) introduces an additional elastic displacement in the plastic range resulting from the moment at first yield to the moment reached in plastic behavior.

2.2.2 Plastic Flexural Displacement

As shown in Figure 2.7, the plastic flexural displacement $? _{PF}$ is due to the rotation of the plastic hinge where the curvature $(f - f'_y)$ is assumed to be constant through the hinge where f'_y is the curvature at first yield.

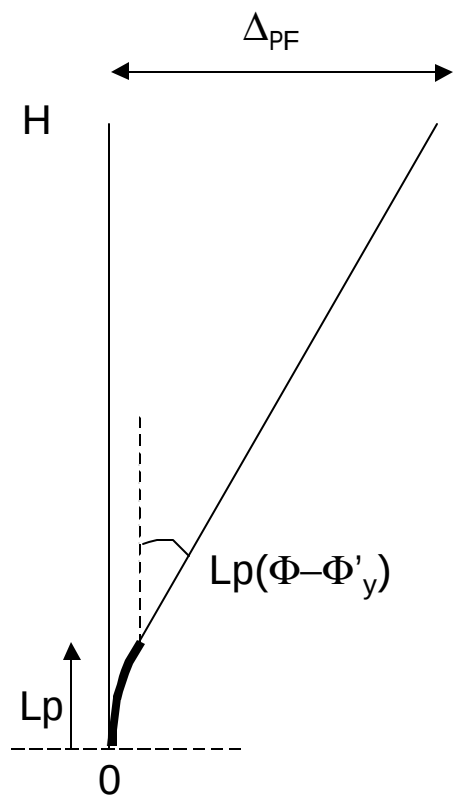

Figure 2.7 Plastic Flexural Displacement

At the top of the plastic hinge, the rotation of the column is thus equal to $L_p(\mathrm{f} - \mathrm{f}'_y)$ which corresponds to a plastic flexural displacement at the top of the column given by

$$? _{PF} = 0 \qquad \text{for } V \le V'_y \tag{2.32a}$$

$$? _{PF} = L_p(\mathrm{f} - \mathrm{f}'_y)H \qquad \text{for } V > V'_y \tag{2.32b}$$

where L_p is the plastic hinge length:

$$L_p = 0.08H + 0.022\, f_{yv} D_{long} \ge 0.044\, f_{yv} D_{long} \tag{2.33}$$

Equation (2.33) takes into account the strain penetration of the plastic hinge into the footing and relates the fact that the plastic hinge length in the column has to be at least two times the penetration length into the footing.

2.2.3 Shear Displacement

The shear displacement at the top of the column Δ_S is composed of two components: Δ_{sc} due to the concrete shear deformation, and Δ_{ss} due to transverse reinforcement deformation. Thus

$$? _S = ? _{sc} + ? _{ss} \tag{2.34}$$

For columns with low aspect ratio (H/D<2.5), it has been shown that the shear displacement can reach 30% of the total displacement whereas it can generally be neglected for columns with aspect ratio greater than 4. Therefore, the shear displacement might have a significant influence on specimens HS1 and HS2 because the aspect ratio of those specimens are about 2.5.

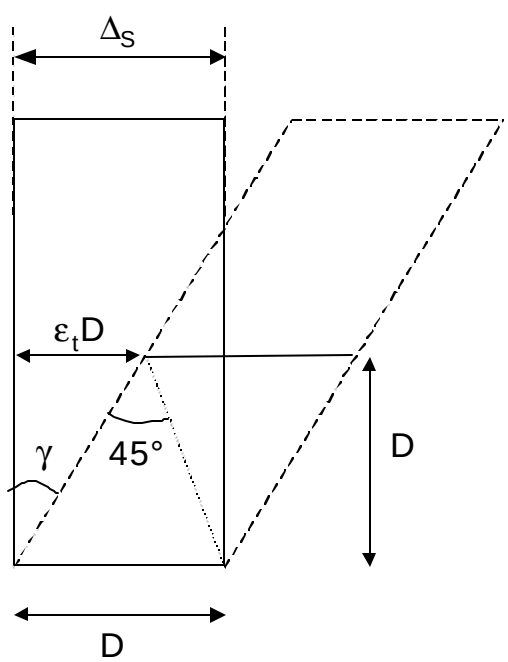

Figure 2.8 Shear Displacement

As shown in Figure 2.8, the top shear displacement can be computed on the basis of the γ deformation at the base. At the base of the column, shear cracks generally result in an extension of the flexural cracks. Therefore, the angle of the shear cracks can be assumed to be θ=45° at the base of the column. The shear distortion γ is thus given by

$$? \cong \tan ? = \frac{e_t D}{D} = \varepsilon_t \tag{2.35}$$

where ε_t is the shear strain. Therefore the shear displacement at the top of the column is given by

$$\Delta_S = \gamma H = \varepsilon_t H \tag{2.36}$$

(a) Column displacement due to concrete shear deformation, Δ_{sc}

According to Equation (2.36), the contribution of Δ_{sc} is

$$? _{sc} = e_{tc} H = \frac{2(V_v + V_P, V)_{\min}}{G ? A_g} \tag{2.37}$$

$$V_c = a ß ? \sqrt{f_c'} ? A_g \tag{2.38}$$

$$V_P = P \tan \frac{(D - c_{yield})}{2H} \tag{2.39}$$

where V is the lateral force given by the moment-curvature analysis, $G = E_c / 2(1 + ?) \approx 0.4 E_c$ with Poisson coefficient ν of 0.15. The parameter ? is calculated as $? = (2/3)0.8$. The coefficient 2 in Equation (2.37) is a simplification of the coefficient I_g/I_{cr} suggested by Priestley, et al., 1996.

(b) Column displacement due to transverse reinforcement deformation, Δ_{ss}

According to equation (2.36),

$$\Delta s = \varepsilon_{ts} H? _{ss} = e_{ts} H = \frac{s_{ss}}{E_s} H = \frac{V_s \Big/ \frac{p}{2} A_h b \frac{(D - c_o - c_{ult})}{s} \cot ?}{E_s} H \tag{2.40}$$

In Equation (2.40), E_s is the elastic modulus of the spirals and $V_s = V - (V_c + V_p) > 0$. This assumption on V_s means that at the beginning of loading history, all the shear stress is supported by concrete. As the shear demand increases, steel contribution to shear deformation is mobilized. If a shear failure is predicted, this will happen just after the spirals yielding. Therefore, the behavior of transverse steel (up to column failure) can be assumed elastic. As a consequence, transverse steel strain ε_{ts} can be computed as $e_{ts} = s_{ss} / E_{ss}$.

3 TEST SPECIMENS

When the weight of the piers contributes significantly to seismic mass, reducing the area of the pier cross-section as much as possible decreases the seismic mass considerably. However, the wall thickness has a practical lower limit governed by the potential for buckling of the concrete tube. With the objective of reducing the cross section area very substantially, it was decided to select a wall thickness equal to 10% of the section diameter. Previous work on offshore structures has shown that the wall thickness can be reduced further to 6 or 7%, however for the application on highway bridges it was decided not to reduce the wall thickness excessively in order to prevent buckling of the concrete tube during bending.

Slender hollow circular RC columns were tested in New Zealand in the 80's and it was found that a ductile behavior is obtained with relatively low levels of longitudinal reinforcement, axial load, and reasonable wall thickness. It was also found that the available flexural ductility is controlled by the position of the neutral axis with respect to the unconfined inside face of the section. If the neutral axis is forced to occur away from the inside face towards the section centroid, crushing of concrete occurs near the unconfined face, inducing rapid strength degradation. This is the case of units characterized by high longitudinal steel percentage and high axial load.

One of the main issues in this research program was to quantify the relevance of this phenomenon on the shear strength of members characterized by a reduced ratio of the shear span to the section diameter. In fact, concrete crushing near the inside face reduces substantially the flexural capacity and affects indirectly the shear strength as well.

All test units were characterized by the same amount of transverse reinforcement, while the longitudinal reinforcement and the axial load were taken as experimental variables. The main characteristics (geometry, reinforcement, axial load and concrete strength) of the test specimens are summarized in Table 3.1. The ratio of the shear span to the section diameter (*M/VD*) was selected equal to 2.5, which is a typical value for shear-

dominated tests. In Table 3.1 t is the wall thickness, $P/f_c^{'}A_n$ is the normalized axial load ratio, and A_n is the net area of the section. The longitudinal reinforcement consists of 34 bundles of two bars, while the transverse reinforcement consists of a continuous 6mm spiral with a pitch of 70mm. The concrete strength f_c' refers to the tests conducted on concrete cylindrical specimens at 28 days. For all units, nominal property of longitudinal and transverse steel is shown in Table 3.2.

The longitudinal reinforcement ratios, referred to the section net area were 1.4% for unit HS1 and 2.3% for units HS2 and HS3. The volumetric ratio of transverse reinforcement (referred to the concrete net volume is 0.35%). The section geometry with the arrangement of longitudinal and transverse reinforcement is shown in Figure 3.1. The first unit (HS1), characterized by low levels of longitudinal reinforcement and axial load was designed to fail in flexure. The second (HS2), characterized by a higher level of longitudinal reinforcement was instead designed to fail in shear. The third (HS3), with the same longitudinal reinforcement as HS2 and a higher axial load ratio was designed to induce a brittle flexural/shear failure. In the following, the results of unit HS2 will be presented in detail, while only specific information will be given on the results of HS1 and HS3. The reinforcing cage of unit HS2 is depicted in Figure 3.2.

Figure 3.3 and Figure 3.4 show the top of unit HS2 before and after concrete casting. From Figure 3.4, it can be noted that the inside formwork was removed after casting and that the inside surface was painted in white in order to identify concrete cracking.

Table 3.1 Properties of the Test Units

Specimen	*M/VD*	*D* (mm)	*t* (mm)	$P/f_c^{'}A_n$ (%)	Long. Rebars (mm)	Trans. Reinf. (mm)	f_c' (MPa)
HS1	2.5	1560	152	5	68 D13	D6 @ 70	40
HS2	2.5	1524	139	5	68 D16	D6 @ 70	40
HS3	2.5	1524	139	15	68 D16	D6 @ 70	35

Table 3.2 Steel Mechanical Properties

Type	E_s (Gpa)	f_y (Mpa)	f_u (MPa)	e_u
Long. Rebars	195	450	700	0.08
Spiral	165	635	820	0.015

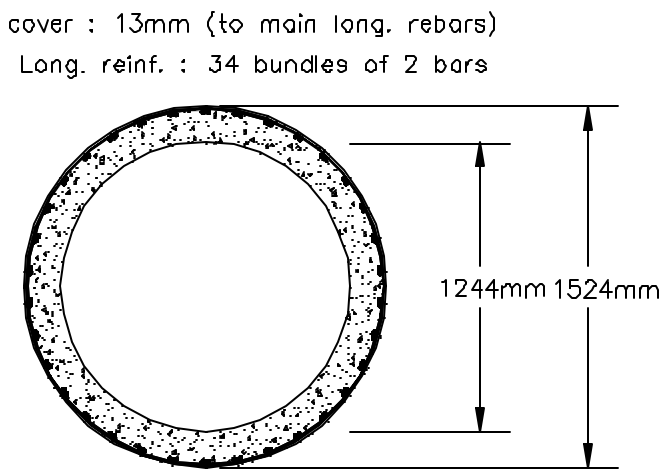

Figure 3.1 Section Geometry and Reinforcement

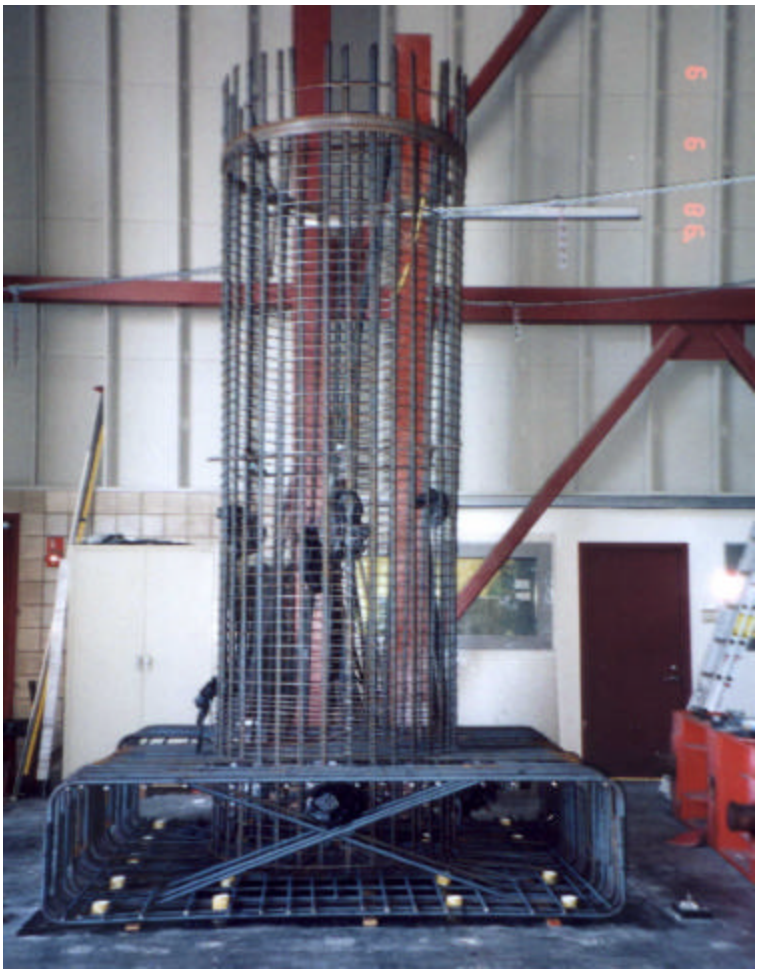

Figure 3.2 Unit HS2 – Reinforcing Cage

Figure 3.3 Unit HS2 Before Casting

Figure 3.4 Unit HS2 After Casting

3.1 Test Setup and Loading Schemes

The test setup is depicted in Figure 3.5. The test unit was loaded quasi-statically with constant axial load. Lateral displacements were applied at the top of the column with the aid of a couple of hydraulic actuators, working in parallel. The vertical force was applied with the aid of an axial load system consisting of two steel rocking beams and four vertical prestressing bars. The prestressing bars were attached at the end of the rocking beams and strongly connected to the floor.

The inside of the column was monitored during the test with the aid of a video-camera. A specific device was built in order to rotate the camera and move it up and down to guarantee a good view of ¾ of the inside surface.

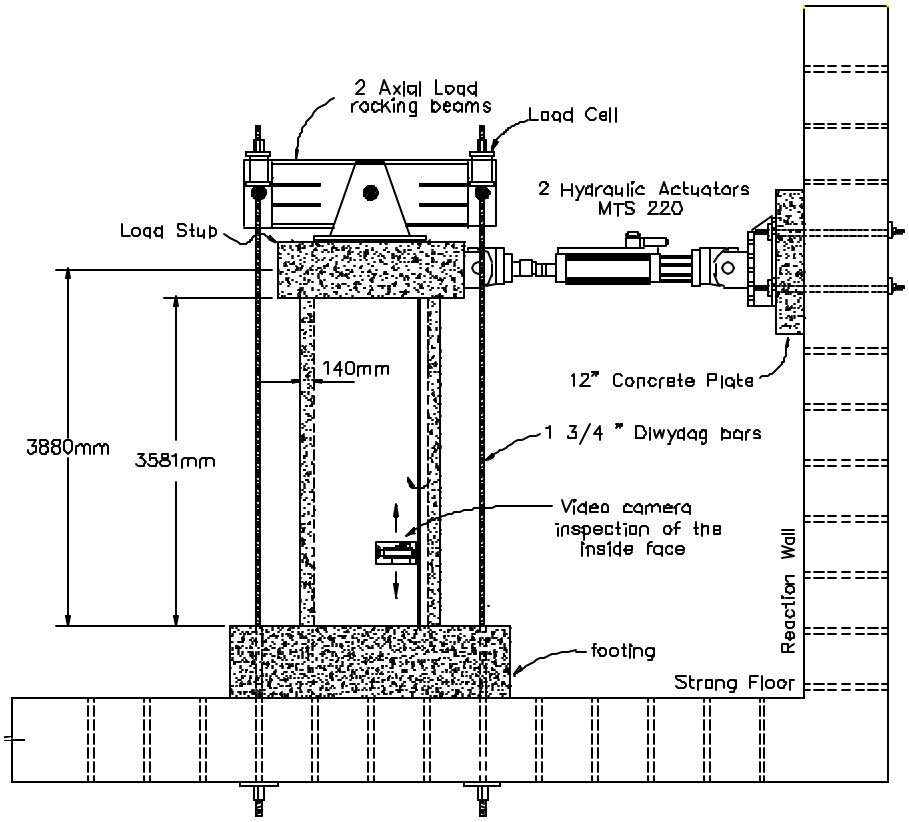

Figure 3.5 Test Setup

The specimens were anchored to the strong floor by means of 18 prestressing bars attached to the foundation footing. The bars were post-tensioned in order to prevent concrete cracking during testing. The hydraulic actuators were attached at the column top on one side and against the reaction wall on the other side. The rocking axial load system was needed in order to apply high axial forces without transmitting flexural actions on the column top. The force acting on the four vertical bars employed to apply the axial load was monitored by means of two load cells. In fact the axial load varies slightly when applying lateral forces. Lateral actions (with increasing amplitude) were applied alternatively in the push and pull directions, following the standard loading protocol represented in Figure 3.6. Elastic cycles were conducted in load control up to the theoretical first yield of longitudinal rebars (100% V_y'), while inelastic cycles were conducted for increasing levels of displacement ductility (1, 1.5, 2, 3, 4 and 6) with three repeated cycles at each ductility level.

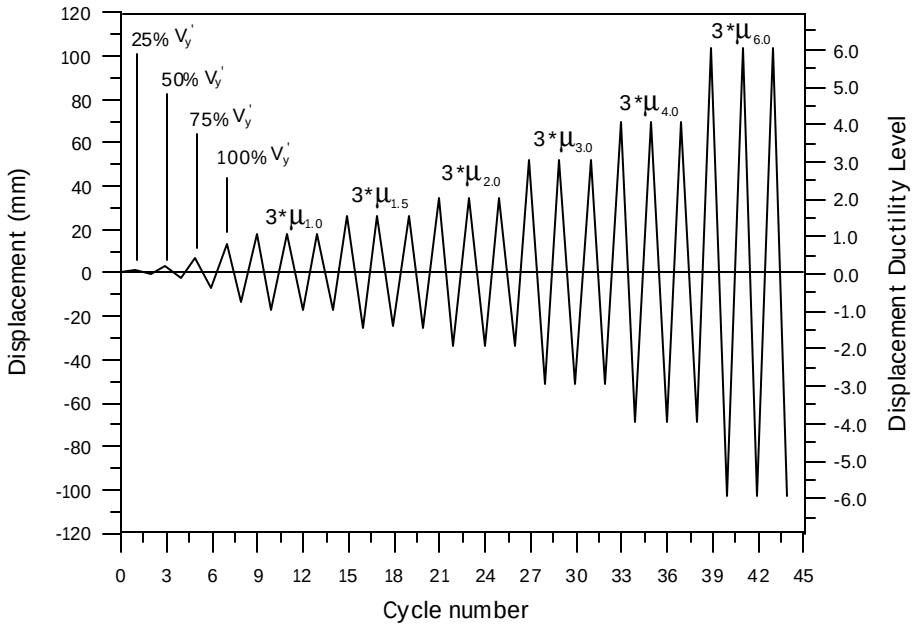

Figure 3.6 Lateral Loading Protocol

3.2 Instrumentation

A reference system is used to easily identify the location of the instruments (see Figure 3.5). Around the circular column, four vertical generators are defined as follows: the south generator is that closer to the reaction wall while that on the opposite side is denoted as north generator. The west side of the column is that visible from Figure 3.5. A vertical reference axis is used to identify the vertical location of the instruments, where the origin is placed at the column base. With this definition, a negative ordinate identifies instruments located inside the foundation footing.

Strain gauges were mounted along the main longitudinal rebars and on the continuous spiral along the four above-mentioned generators. In units HS1 and HS3 additional gauges were also mounted along intermediate generators (e.g. north-west, south-east, etc.). On the main longitudinal rebars gauges were mounted up to a height of 1500mm above the column base with a 150mm interval. On the spiral instead gauges were mounted up to the column top with an interval of 140mm near the base region and

with an interval of 210 mm in the upper part of the column. On the longitudinal rebars gauges were mounted also inside the footing to control the development of plastic deformation inside the foundation block.

Curvatures were measured along the column height by means of 8 curvature cells. The height of the curvature cells was reduced to the minimum afforded by the size of the potentiometers near the column base, while it was larger in the upper part of the column (see Figure 3.7).

The shear deformations were measured by means of two shear deformation panels mounted on the column east and west sides. Each of these panels was subdivided in three blocks (see Figure 3.8). In each of these rectangular blocks the change in length of each side of the rectangle is measured along with the change in length of one of the diagonals. Note that the change in length of the vertical sides of these blocks is measured via the curvature cells. In addition to this instrumentation, two small shear deformation panels were mounted along the east and west generators to monitor the local shear behavior within the region that is more critical for shear (see Figure 3.8). The size of these small square panels was selected in order to be sufficiently small to capture the local behavior. In fact the size could not be less than 305mm because, in order to measure the average strain behavior, it was necessary to develop at least 2 or 3 cracks within the panel size. It will be shown that in unit HS3 more local shear deformation panels were mounted in order to measure the shear deformations over the section depth. This is an important aspect that will be discussed later in more detail. The column top displacement was measured by means of a string potentiometer attached at the column top on one side and on a strong reference column on the other side. The rotation of the column top was measured by an inclinometer. The displacement of each of the two actuators was monitored during the test by means of two displacement cells.

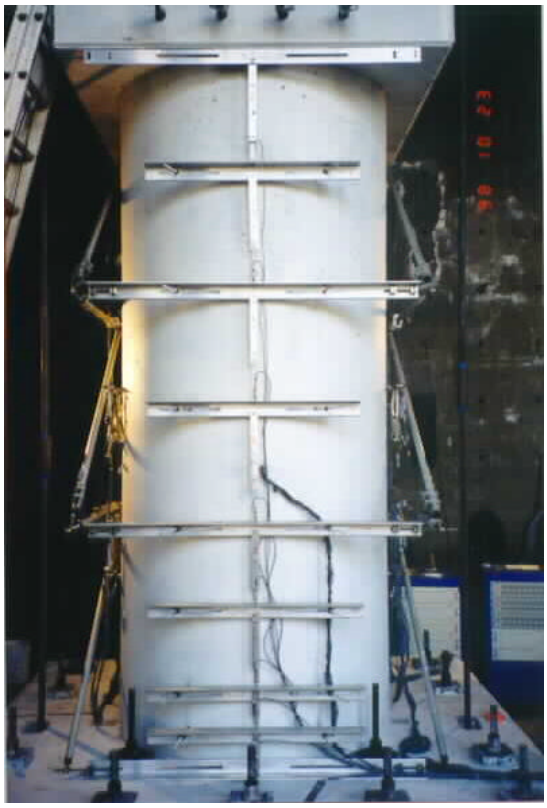

Figure 3.7 North Side of Unit HS2

Figure 3.8 West Side of Unit HS2

4 EXPERIMENTAL RESULTS

4.1 Specimen HS1

The first specimen was designed with a low flexural capacity in order to prevent a brittle shear failure. The relatively low longitudinal reinforcement ratio (1.4%) should ensure a good deformation capacity. This enables to analyze the problem of shear strength degradation in a wide range of lateral displacement ductilities. The axial load ratio was chosen to be in the lower side of the design range, always to exclude premature failure due to concrete crushing in compression.

4.1.1 Predicted Response

The response of the test unit was predicted both in terms of global force-displacement behavior and in terms local flexural and shear behavior. The main results obtained from pre-test analysis are discussed in the following two sections. The same topic will be commented later during the discussion, in order to verify the assumptions by comparing the predicted response with that observed during the test. All predictions are monotonic and are intended to be representative of the envelope behavior under cyclic loading.

4.1.1.1 Force-Displacement Predicted Response

The predicted response of the column was obtained by using the procedures described above in Section 2.2. In particular, only three of the four shear models were used, since the newer version of the UCSD shear model was not yet available at the time column HS1 was tested. Results are presented in Figure 4.1. The force displacement predicted behavior was determined based on the concept of equivalent plastic hinge length, where $L_p = 483$ mm. The ultimate point of the load-deflection curve corresponds to a strain in the longitudinal reinforcement in tension equal to 6%. As discussed above, the determination of the ultimate point along the predicted curve depends both on the compressive strain near the inside face and on the steel strain in the extreme fiber in

tension. In this case, moment-curvature analysis showed that a strain of 6% was reached in the longitudinal bars while the compressive strain near the inside face was 0.1% tensile (i.e. the compression depth is less than the wall thickness). Using the procedure described in Section 2.2 at failure we predict that at 10% of the total top displacement is due to shear.

The three shear models, considered in this analysis, indicate that a shear failure is not likely to happen. With the conservative assumption of $q = 30°$ (angle of inclination of the shear cracks), only the Caltrans MEMO 20-4 curve intersects the predicted load-displacement curve. This model would in fact predict a shear failure at ductility 4.0, while that from ATC-32 is essentially tangent to the predicted curve at ductility 6.0. Note that for all predicted shear envelopes a conservative assumption was made that the yield stress of transverse steel equals 635 MPa, while the steel does not have a well-defined yield point. A value of 700-750 MPa would probably be more appropriate to be representative of real inelastic behavior. We therefore conclude that failure should be of the flexural type, since all our assumptions were conservative in calculating shear strength. The moment curvature analysis though neglects the effects of shear on the longitudinal strains. As a consequence, failure might occur due to concrete failure in compression (rather than steel failure in tension) as an effect of the presence of shear inclined struts. One more assumption has to be made when considering the effect of axial load on shear strength. It is not yet fully understood if this effect can be properly accounted for by means of an arch mechanism and the enhancement of shear strength evaluated with the formula suggested in Section 2.1.1.

In Figure 4.1, the shear strength calculated based on the UCSD model includes the V_p component, evaluated with the same expression used for solid sections. The axial load component was found to be 221kN. If it is believed that this component cannot be developed due to the hollow shape of the section, it should drag down the UCSD shear curve by 221kN. In this case it would not still intersect the predicted force displacement envelope. In other words, if the assumption of full development of the V_p component is theoretically unconservative, it does not change the predicted type of failure. We will

discuss this aspect in more detail in Sections 4.1.1.2 and 4.1.6. The main results of predicted strengths and deformation capacities are summarized in the following Table 4.1. The flexural properties determined on the basis of moment-curvature analysis were used to drive the initial stages of testing. Cracking, first yielding and ideal (or nominal) flexural properties are summarized in Table 4.2.

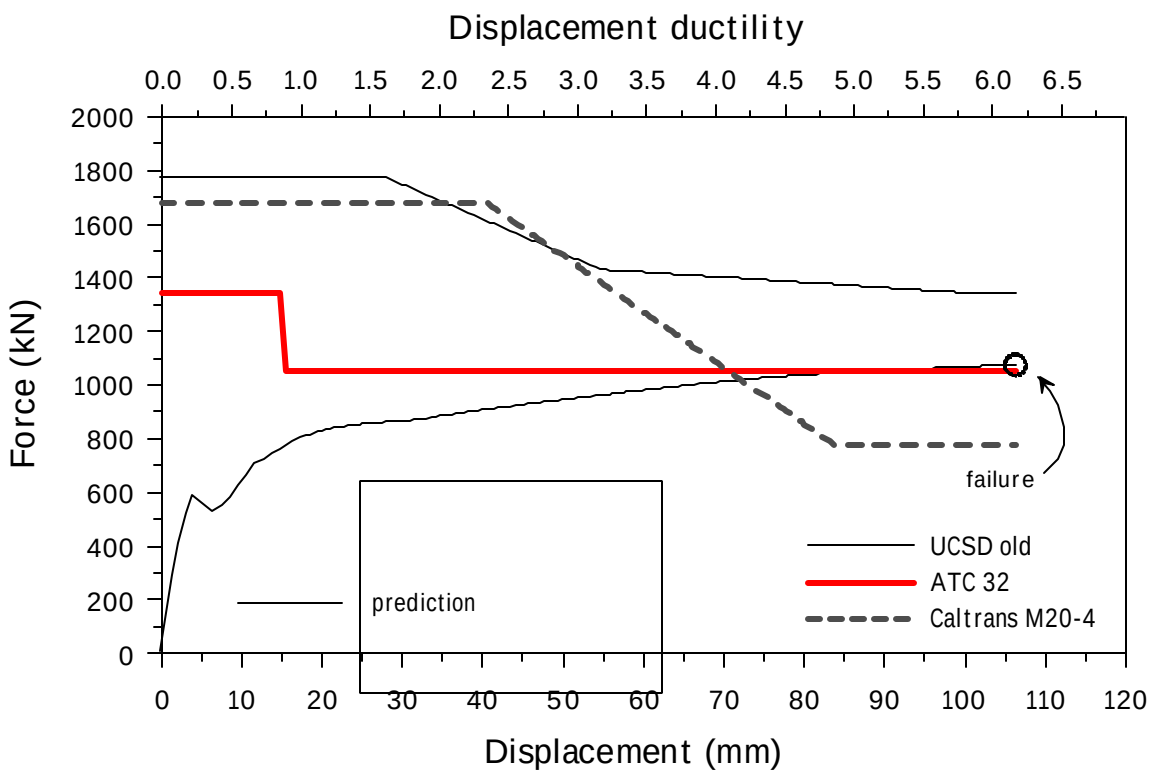

Figure 4.1 Comparison of Predicted Force-Displacement Response of Unit HS1 with Different Shear Strength Models

Table 4.1 Predicted Capacity with Different Models

Model	***V* at failure (kN)**	**D at failure (mm)**	**Type of failure**
UCSD	1340*	106	Flexural
UCSD (without V_p)	1119*	106	Flexural
ATC-32	1055	106	Flexural
Caltrans MEMO 20-4	1008	72	Shear

*predicted flexural failure is at 1069kN

Table 4.2 Predicted Specimen Behavior at Different Stages

Test stage	**Moment (kNm)**	**Curv. (1/km)**	***c* (mm)**	**e_{if} (%)**
Cracking	2010	0.46	815	-0.03
First yield	2790	2.2	384	-0.049
Nominal strength	3445	-	-	-
Ultimate strength	4150	44.5	139	0.103

The concrete strain e_{if} near the inside face and the depth c of the compression zone are also indicated in the table for each stage. Note that the wall thickness (in this unit) is 156mm. As we discussed above in Section 2.1.1, when the neutral axis depth is within the wall thickness, the behavior should be similar to that of a solid section.

These flexural properties were estimated by assuming that a constant confining pressure of 800 kPa would be acting on the concrete. This estimate was made based on elastic FE analysis and it was recognized that high circumferential stresses should appear due to the presence of a rather thin wall. Using the Mander model the confined peak concrete strength is therefore 45 MPa and the peak strain $e_{cc} = 0.003$. Cracking was estimated by assuming a tensile strength equal to $f_t = 0.75\sqrt{f_c'}$ that shows to be rather high. In fact, the force-displacement curve shows a sharp peak at cracking that seems

unrealistic. However, previous experience showed that concrete (with a nominal strength greater than 35MPa) in flexural tension has a rather high cracking point.

4.1.1.2 Shear Behavior

Given the nature of the test we would like to also predict the envelope behavior of transverse steel at various stages of testing. The strain in the transverse reinforcement has a direct influence both on shear and flexural properties. The development of shear strain in the transverse reinforcement was estimated by considering the flexural behavior of the base section and by superposing the UCSD shear model in order to determine transverse steel strains from the available shear strength. The procedure used in determining these behaviors is described in Section 2.2.2. Results are presented in Figure 4.2 in terms of the average spiral strain as a function of the applied lateral displacement and in Figure 4.3 in terms of the applied lateral force as a function of the average spiral strain. In using the UCSD shear model to determine the spiral strain, two separate analyses were conducted with and without the V_p component. It is pointed out that these curves represent the average behavior of transverse steel in the column region where significant inelastic flexural behavior occurs (i.e. less than one diameter from the base).

A significant increase in spiral strains occurs at ductility 1.5 regardless of the influence of the axial load (see Figure 4.2). Figure 4.3 shows that the inclusion of the axial load effect has a direct influence on the level of lateral force that corresponds to the strain activation in the spiral reinforcement. While this is 500kN when the V_p component is absent, it is 700kN if this latter is accounted for. The beneficial effect of axial load essentially postpones the mobilization of lateral strains. In the discussion, predictions will be compared with the readings from the strain gauges in several locations in the region affected by significant inelastic flexural behavior. Since no shear failure is predicted in these two cases (with and without the V_p component), the transverse steel never reaches the assumed yield strain (corresponding to 635MPa).

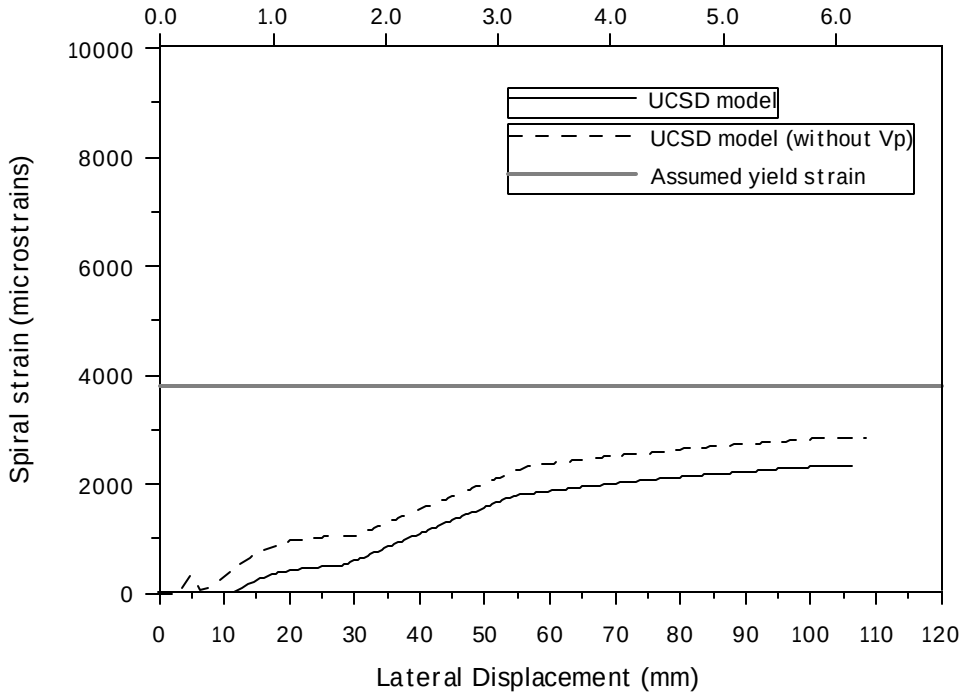

Figure 4.2 Predicted Lateral Displacment/Sprial Strain Relationship for HS1

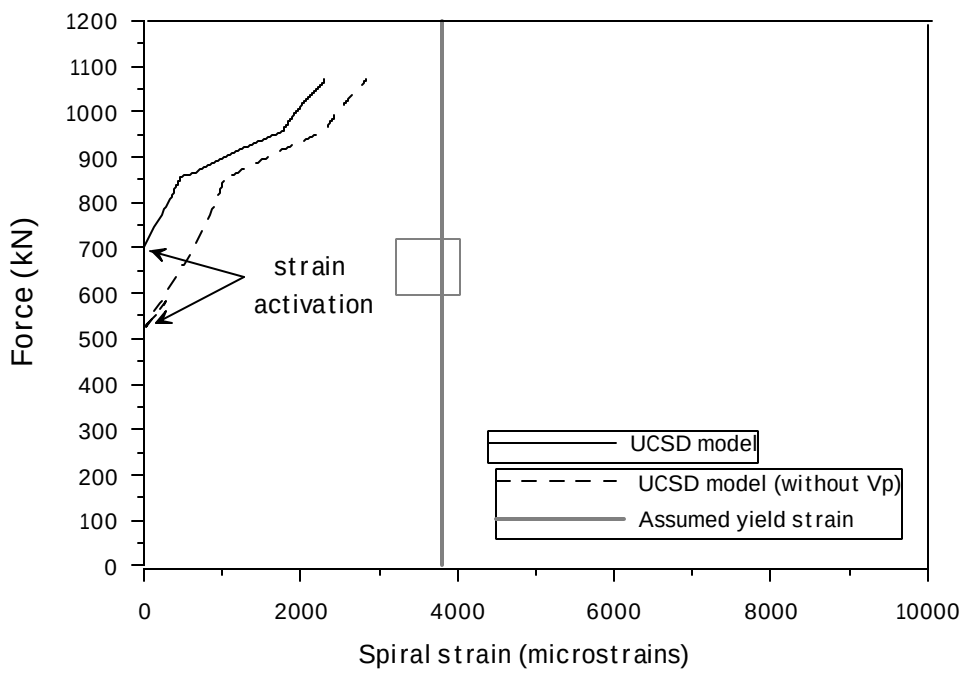

Figure 4.3 Predicted Force/Spiral Strain Relationship for HS1

4.1.2 General Observations

The test unit was subjected to the loading history described in section 3.5 and the concrete crack was marked to show the damage. During the force-control phase (elastic cycles) cracks were marked at each peak value of the applied lateral load (in both push and pull directions). During the displacement-control phase (inelastic cycles) cracks were marked at the first peak of the applied lateral displacement in the push direction and at the third peak in the pull direction for each ductility level. Surface cracks generated by actions applied in the push direction were marked with a black pen while cracks generated by actions applied in the pull direction were marked with a red pen. At the end of each crack the values of the applied load (or displacement) were also marked. The cracks that were formed in the third cycle of each ductility level were differentiated from others by adding a superscript "^{3}" to the corresponding label (e.g. cracks that were formed at the third cycle at ductility 1.0 in the pull direction were labeled μ_1^3).

The inside face of the test unit was monitored by the video camera mounted in the south side of the column (facing north). This device was able to show the presence of surface cracks in a range of approximately 180 degrees, therefore including the West, North and East generators. A reference system was drawn in the inside face of the column, indicating the distance in mm from the column base along each of the above said generators. Experience showed that the resolution of the camera was able to clearly show cracks with a width of at least 0.2mm.

4.1.2.1 Elastic Cycles

Elastic cycles were conducted in load control by monitoring the force applied in the two hydraulic actuators. The applied force was the same in the two actuators throughout the elastic cycles. The axial load was applied by using the oil jacks as described in Section 3.1. At the beginning of the test with no lateral action applied, the forces were 608 kN and 612 kN in the east and west bar, respectively. The total axial load on the column was therefore 1220 kN, and it did not induce any cracking in the test unit.

The applied axial load was monitored throughout the test and it was found that it varied slightly during the application of lateral actions. The maximum value recorded during the test was 1310kN, which is corresponding to a 7% increase in compression. The recorded minimum force was 1090kN, which is corresponding to a 11% decrease in compression.

± **175 kN cycles** (25% of theoretical first yield)

There were no cracks observed on either sides of the test unit at this stage.

± **350 kN cycles** (50% of theoretical first yield)

Flexural cracks (0.1-0.15mm in width) started to form in both push and pull direction at 250 mm away from the base of the column. Flexural cracking occurred at this load level, indicating that the concrete tensile strength is $0.45\sqrt{f_c'}$ lower than $0.75\sqrt{f_c'}$ (= 4.74 MPa) used in the analysis.

± **525 kN cycles** (75% of theoretical first yield)

More flexural cracks formed with a similar pattern in both push and pull direction at this stage. The spacing of these flexural cracks was approximately 140 mm. The column has cracks up to about 1400 mm from the base and the wall was completely cracked through its thickness because the same crack pattern was observed from the inside of the column. Shear cracks also formed as extension of the flexural cracks in the east and west faces of the test unit. These cracks (also visible from the inside) and had an average width of 0.2mm.

± **700 kN cycles** (100% of theoretical first yield)

At this load level, it was found that gauges on north and south bars at column base indicated a strain of 2100με in push and pull directions (note that the average value of yield strain for these bars was found to be 2200με from material testing). New flexural cracks formed up to a height of 2300mm from the column base, with the same spacing of existing cracks. More shear cracks formed as extensions of flexural cracks. The average width of shear cracks was 0.3 mm, while that of flexural cracks was 0.2 mm. The angle

of inclination of the shear cracks (with respect to a vertical axis) was measured in several locations along the west and east generator and it was found to be 35 degrees (see Figure 4.4). The top lateral displacement was used to define the target yield displacement (corresponding to ductility 1.0). The recorded displacement in the push and pull directions was averaged to be:

$$\Delta_y = \left(\frac{13.3 + 13.9}{2} \right) \frac{888}{700} = 17.25mm \tag{4.1}$$

where 888 kN and 700 kN were the theoretical nominal flexural strength and first yield flexural strength respectively. The behavior showed to be symmetric, indicating that no major lacks of symmetry were introduced during construction due to inevitable inaccuracies.

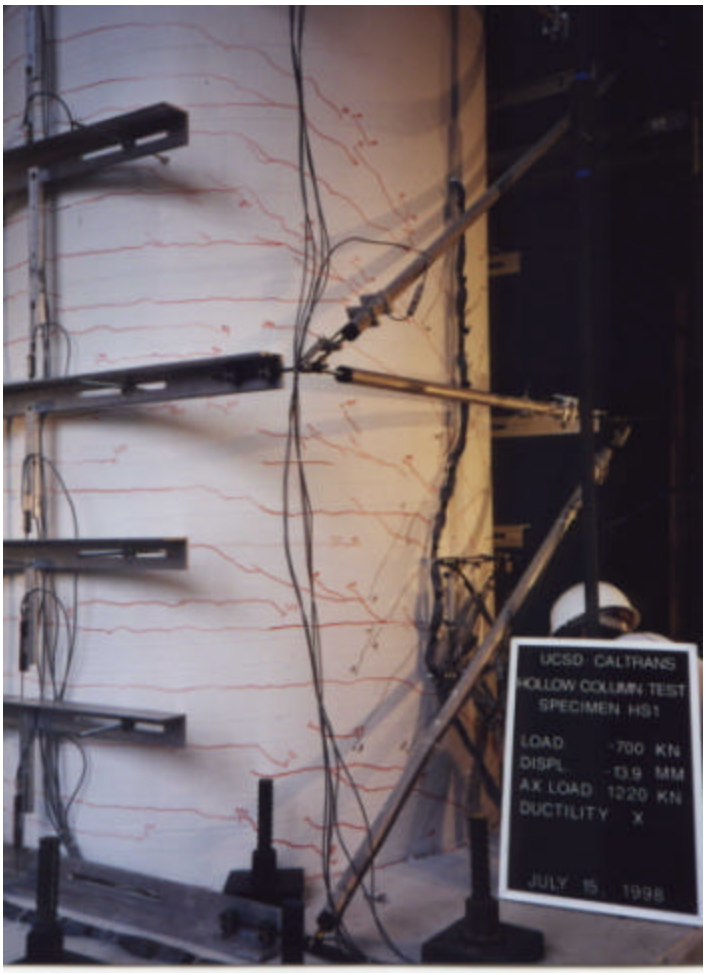

Figure 4.4 Photo at 700kN – from NW

4.1.2.2 Inelastic Cycles

Inelastic cycles were conducted in displacement control, but only one of the actuators was used in displacement control, while the other one was constrained to apply exactly the same lateral force. Note that to control both actuators by nominal identical displacements would inevitably result in large force differences between the two actuators as a consequences of inevitable, though small differences in displacement calibration.

m_D=1.0 (3 cycles, drift=0.45%)

During the cycles at ductility 1.0 the existing cracks were extended and had a considerable increase in width. At the end of the third cycle the width of shear cracks

along the west and east generators ranged 0.45-0.65 mm. New shear and flexural cracks formed in the upper part of the column, up to a height of 2700 mm from the base. The new shear cracks had the same average inclination of approximately 35 degrees (see Figure 4.5 and Figure 4.6)

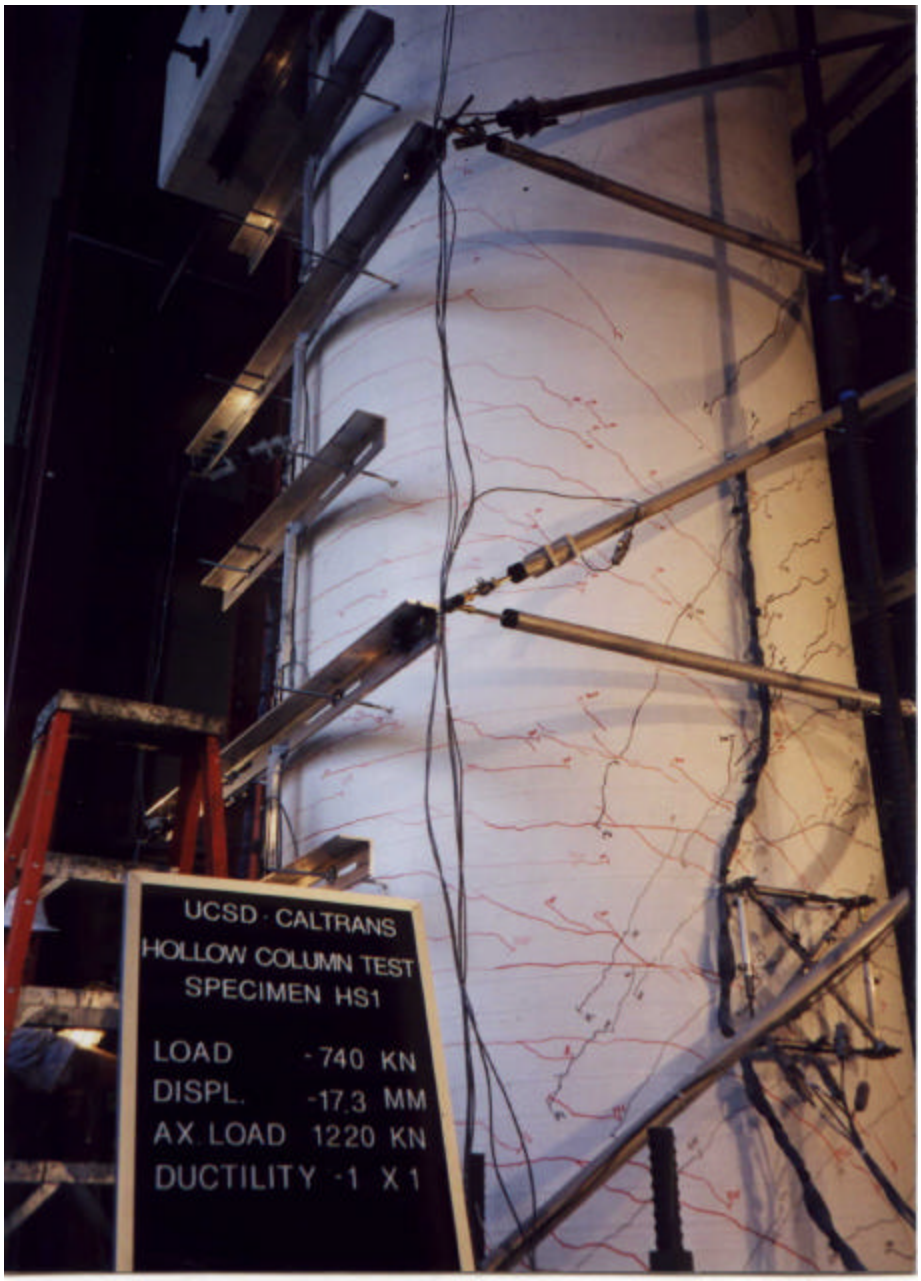

Figure 4.5 Unit HS1 Condition After 1 Cycle to $\mu_\Delta = 1$. (Side View)

Figure 4.6 Unit HS1 Condition After 1 Cycle to $\mu_\Delta = 1$. (Front View)

m_D=1.5 (3 cycles, drift=0.67%)

At this stage minor extension of the existing cracks formed, a few new cracks appeared on the column top and the existing cracks slightly increased in width. In several locations (both in the inside and in the outside face) some minor concrete flaking was observed along some of the major cracks.

m_D=2.0 (3 cycles, drift=0.9%)

Cycles at this ductility level did not induce formation of new significant cracks, but some of the existing shear cracks were extended further. The main flexural cracks at the base were considerably widened. From the inside of the column some vertical cracks were observed in the north side of the column. Moderate concrete flaking on the surface of the test unit was observed along major shear cracks.

m_D=3.0 (3 cycles, drift=1.3%)

Incipient concrete spalling in the compression region was observed in the outside face of the column base. In the inside face concrete flakes were clearly visible, even though it was not possible to detect whether or not this was a sign of incipient concrete spalling.

Shear cracks had a considerable increase in width. In some points along the west generator a width of 0.85 mm was measured. Note that these cracks were observed in a region 400 and 2200 mm away from the base. At the end of the cycles at this ductility level only minor concrete spalling was observed in both the north and south sides of the outside face of the column base (see Figure 4.7).

Figure 4.7 Unit HS1 Condition After 1 cycle to $\mu_\Delta = 3$ (Side View)

m_D=4.0 (3 cycles, drift=1.78%)

Considerable concrete spalling in the compression region was observed during the three cycles. At the end of the last cycle (both in the north and south column base region) the concrete cover had completely spalled off. Flexural cracks at column base were considerably widened (in some points more than 1mm). Signs of incipient spalling of concrete in the inside face were also evident. Moderate signs of buckling of longitudinal rebars were also observed in both the north and south sides of the test unit.

m_D=6.0 (2 cycles, drift=2.67%)

Towards the end of the first cycle in the push direction, major concrete spalling occurred together with significant buckling of longitudinal rebars. Buckling did not occur within the first two layers of spiral reinforcement from the base, but took place in a region of approximately 300 mm from the base, inducing significant expansion of 4 layers of spiral reinforcement (see Figure 4.8).

During the first reversed cycle to ductility –6.0, buckling of longitudinal rebars was observed and the rupture of one layer of spiral reinforcement occurred. The subsequent pull cycle (second cycle at ductility –6.0) caused buckling of more longitudinal rebars (6 of them were considerably deformed).

Figure 4.8 Unit HS1 Compression Zone and Bar Buckling on First Cycle to $\mu_\Delta = 6$

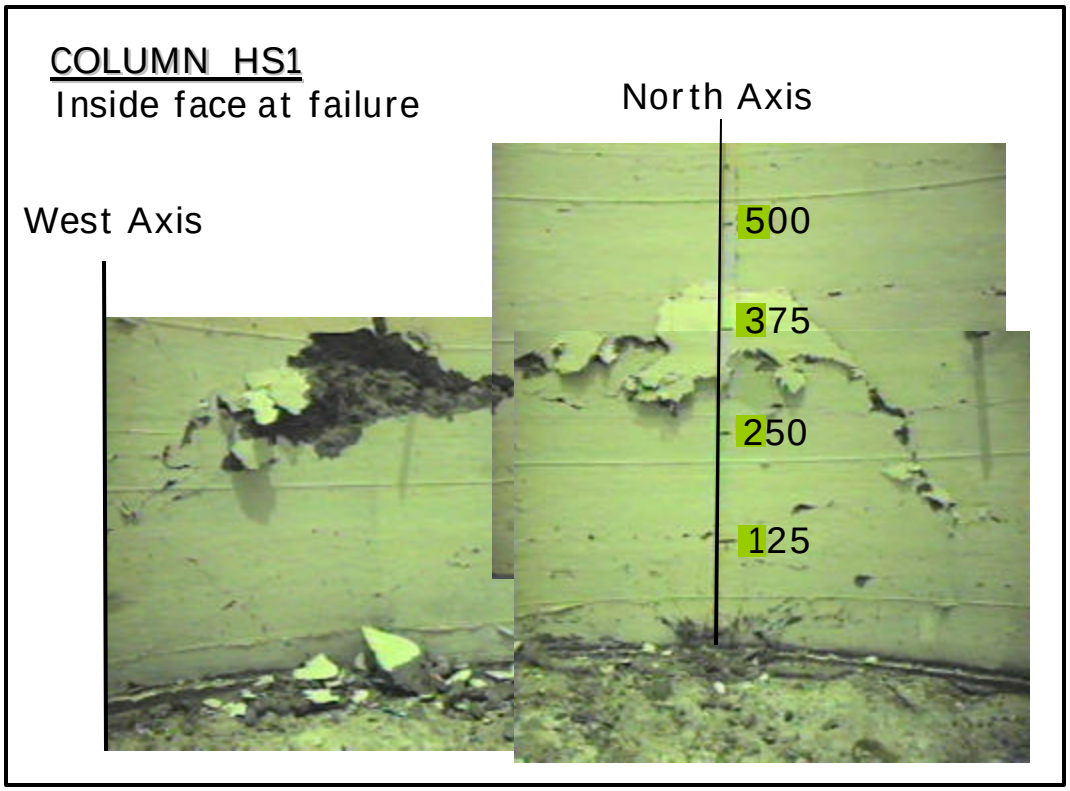

Figure 4.9 Unit HS1 – Composite Photo of Inside Face Spalling After 3 Cycles to $\mu_\Delta = 6$

Towards the third cycle in the push direction major concrete spalling was observed in the inside face in compression at about 300 mm from the base (see Figure 4.9). This induced a sudden drop of the applied lateral load by about 65% (failure). The test was brought to completion by moving back to zero lateral displacement and by removing the axial load.

4.1.3 Hysteretic Response

4.1.3.1 Force-Displacement

The force-displacement hysteresis curve shown in Figure 4.10 was obtained by plotting the total applied lateral force versus the measured displacement at the column top. The experimental displacement ductility is indicated in the top horizontal axis. In the same graph, the predicted envelope behavior and failure point are also indicated. During the inelastic phase it can be noted that repeated cycles at the same ductility level did not

induce significant strength degradation. In fact, strength degradation caused by repeated reverse cycling did not exceed 10% before failure. The sudden loss of strength associated with the concrete spalling in the inside face is clearly evident from the shape of the last cycle. The predicted envelope response matched very well with the experimental results, although the inappropriate estimate of concrete tensile strength determined a very high estimate of the cracking force. It has to be noted that the failure was predicted due to high longitudinal strains (6.0%) in the reinforcement in tension.

The overall behavior indicates a desirable ductile performance. At later stages of testing, cycles get slightly narrower near the origin due to the effect of shear deformations. This is because during the reloading phase the considerable opening of shear cracks reduces the average stiffness (loss of aggregate interlock).

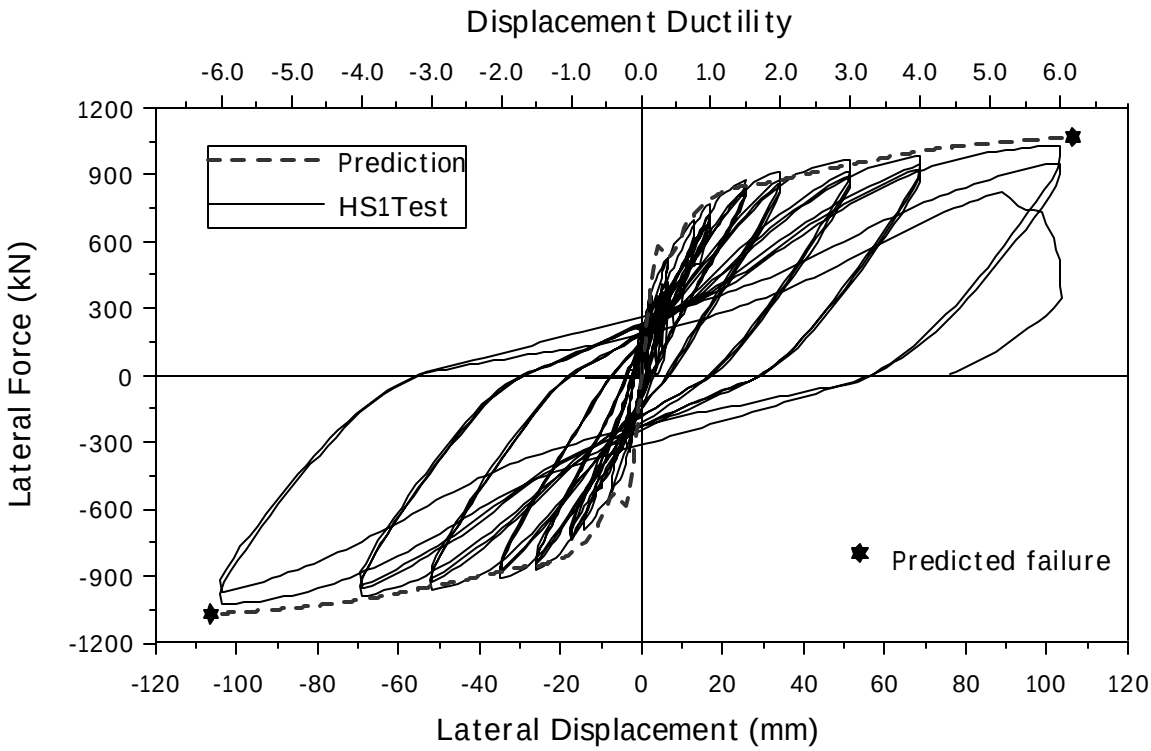

Figure 4.10 Unit HS1 Lateral Force-Displacement Response

4.1.3.2 Moment-Curvature

In this test unit, curvatures were measured along the column height in seven different sections. The base curvature (that measured from the first curvature cell near the column base) is plotted in Figure 4.11 as a function of the bending moment at the column base. It will be shown in the following, curvatures have a considerable variation with height in this region and cannot be considered constant within the cell height. However, we will assume that this was the case and that the curvature computed from the displacement transducers represents the average curvature in this portion of the column. It has to be noted though that, as discussed above, strain penetration will cause curvatures to take place also inside the foundation footing. As a result the length of the base curvature cell will be increased to account for the effect of strain penetration, according to the expression described in Section 2.2.1.

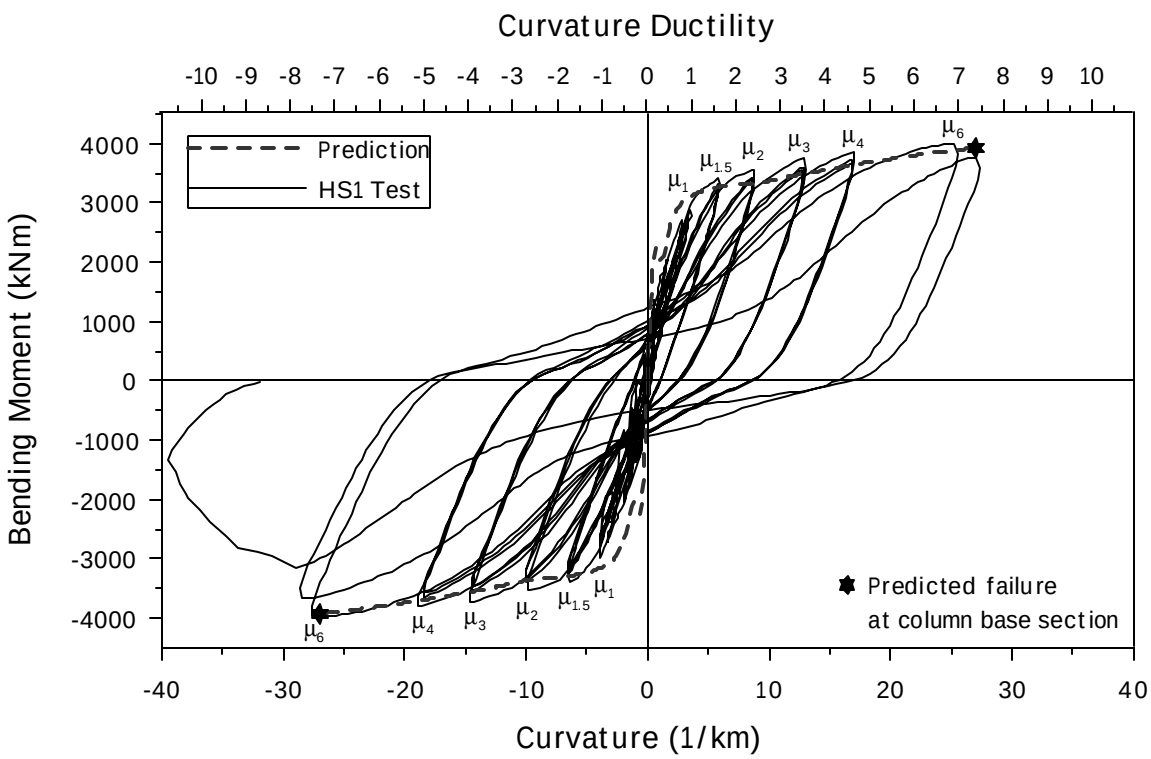

Figure 4.11 Unit HS1 Base Section Moment-Curvature Response

In Figure 4.11 the curvature and the bending moment can therefore be regarded as those at column base. In the same graph the experimental hysteretic behavior is compared with the predicted envelope response calculated with moment-curvature analysis of the base section under constant axial load.

The top horizontal axis indicates the curvature ductility scale. This was computed based on the experimental results by extrapolating the yield curvature from that recorded at first yield of longitudinal rebars (700kN cycle). The procedure, similar to that used in calculating displacement ductilities is described in Priestley et al (1996). The displacement ductilities corresponding to each stage of the test are also indicated in the graph, near the peaks with the notation μ_n, with n=1,1.5….6.

It can be noticed that significant loss of average stiffness among repeated cycles occurs only at the last load stage, when considerable concrete spalling and longitudinal rebar buckling occurred. Similar behaviors were observed from the other curvature cells within the region where inelastic curvatures occurred. In the following it will be shown that inelastic flexural actions take place within the first 600 mm from the base (i.e. the first three curvature cells show inelastic behavior).

4.1.3.3 Axial Load

The axial load varied during the test depending on the level of applied lateral displacement; the variation was in a range of 7% increase at the target peak displacement and 11% reduction during the unloading phases. This is shown in Figure 4.12 where the axial load is plotted as a function of the lateral displacement measured at the column top. In the vertical axis on the right the values of normalized axial load $\left(P/f_c^{'}A_g\right)$ are also indicated.

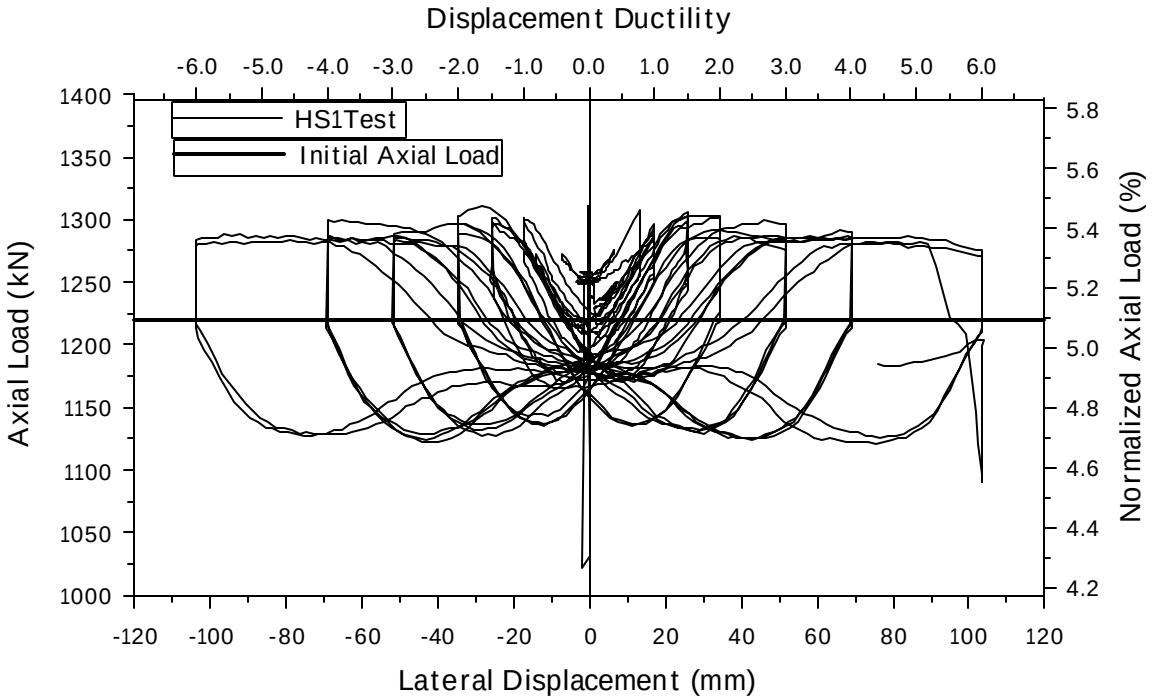

Figure 4.12 Unit HS1 – Variation of Applied Axial Load with Displacement

4.1.3.4 Shear Deformation

The global shear behavior was monitored by the shear deformation panels mounted on the east and west sides of the test unit. Each panel was subdivided in three blocks where a measure of the average shear distortion over the block height was taken. The height of each block is about ¾ of a column diameter. The bottom panel monitors the average shear behavior of the portion of the column that undergoes significant flexural damage (as we will see in the following), while the other ones essentially describes the shear behavior where the flexural behavior remains within the elastic range. Also note that the ratio of the average moment to shear is 3.3 for the bottom block, 2.12 for the middle block and 0.93 for the top block.

In the graphs, the size of each block of the shear panel is indicated along with the number of curvature cells used to derive the change in length of the vertical sides. The applied lateral force is plotted in Figure 4.13 as a function of the shear distortion computed from each panel (bottom, middle and top). In the bottom panel, it is observed that significant shear deformations occur even within the elastic phase (i.e. before

ductility 1.0) but the average stiffness is still relatively high. At later stages of testing, a considerable loss of average stiffness occurs. After ductility 3.0 (when the width of the shear cracks exceeds 0.85mm in some points) the reloading part of the hysteresis loops indicates extremely low shear stiffness. This is because the shear can no longer be carried across the cracks.

In the middle block we observe that, since the crack width was considerably less, the average shear stiffness remains roughly the same during the elastic and the inelastic phase. It is found that very small shear deformations occur before ductility 1.0. The shear measured from the top block shows an elastic behavior throughout the test.

The shear behavior was also measured by two small shear panels located along the east and west generators at 0.4 diameters above the base, and the response is shown in Figure 4.14. This instrumentation was used to measure the local shear deformation as described above in Section 3.2. In fact the readings from the big shear deformation panels represent an average over a considerable portion of the column, where damage varies considerably. As a matter of fact, the results from the small shear panels confirm the results found from the big shear panels. It is noticed that the local shear deformation was measured at the section mid-depth. It has to be pointed out that the maximum shear deformation might not occur at this location. In order to investigate this aspect in more detail, the third test unit was instrumented so as to measure the local shear deformation in several locations over the section depth.

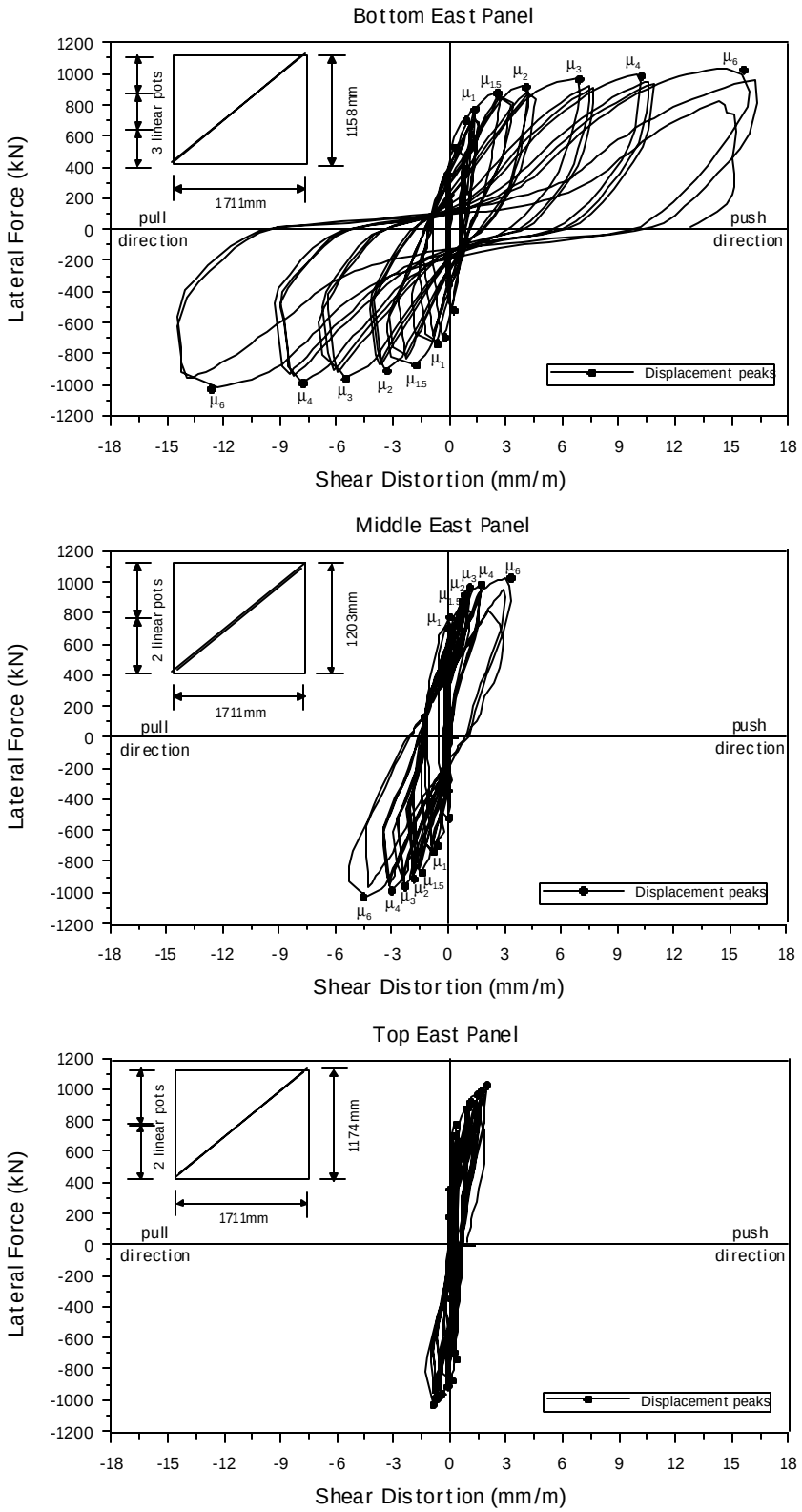

Figure 4.13 Unit HS1 – Lateral Force/Shear Distortion From Gross Column Measurements

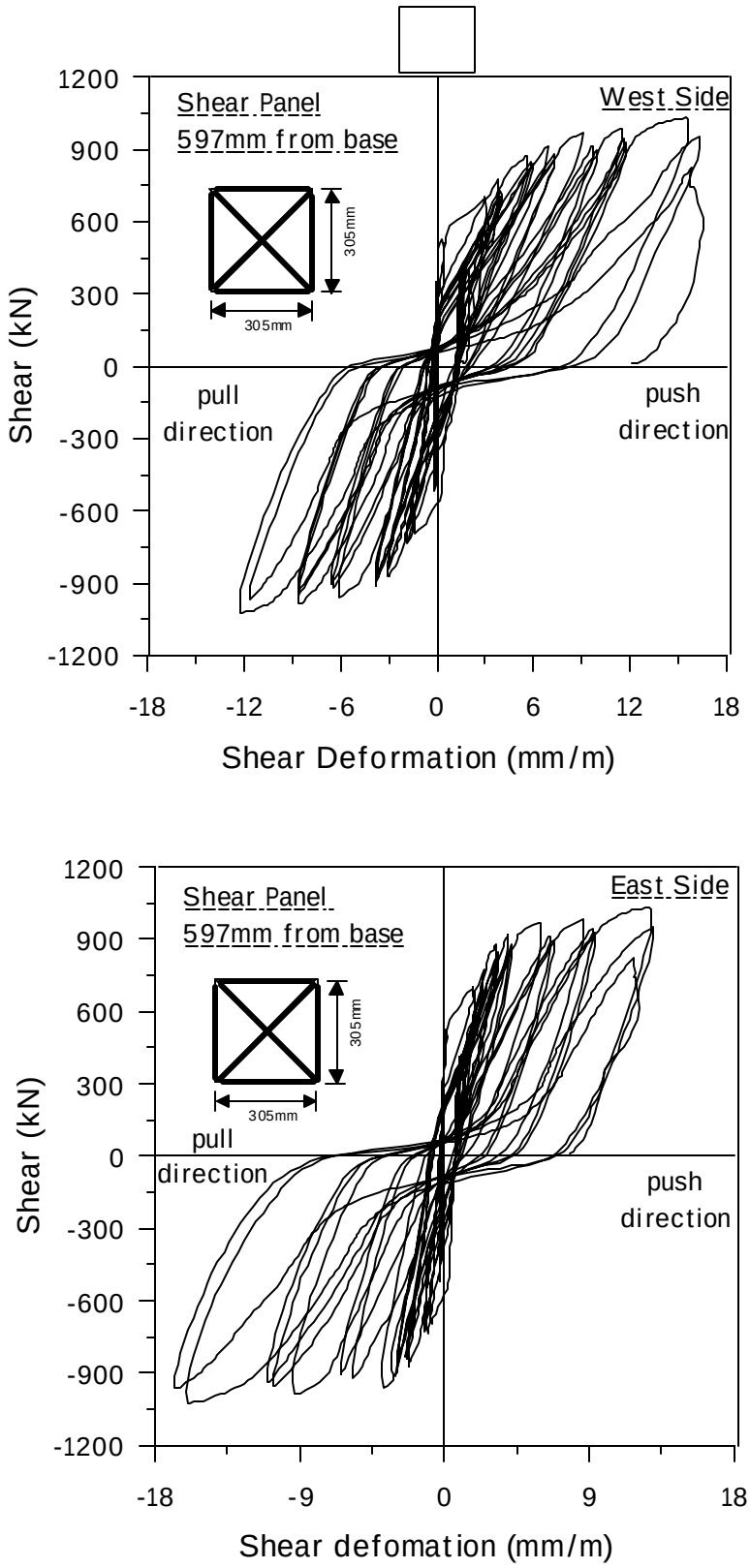

Figure 4.14 Unit HS1 – Lateral Force/Shear Strain from Small Shear Panels

4.1.4 Envelope Response

The envelope response describes the behavior of the structure at the peaks of applied load or displacement. For the load control phase all peaks will be considered, while for the inelastic phase, at each displacement ductility level, only the first peak in the push direction and the last peak in the pull direction will be considered.

4.1.4.1 Displacement Components

Shear and flexural contribution to top displacement are analyzed at each stage of the test in the following section. The flexural displacement component is computed from the readings of the curvature cells with the assumption that the curvature remains constant within the cell height. Curvatures are integrated along the column height to obtain the contribution to the top displacement.

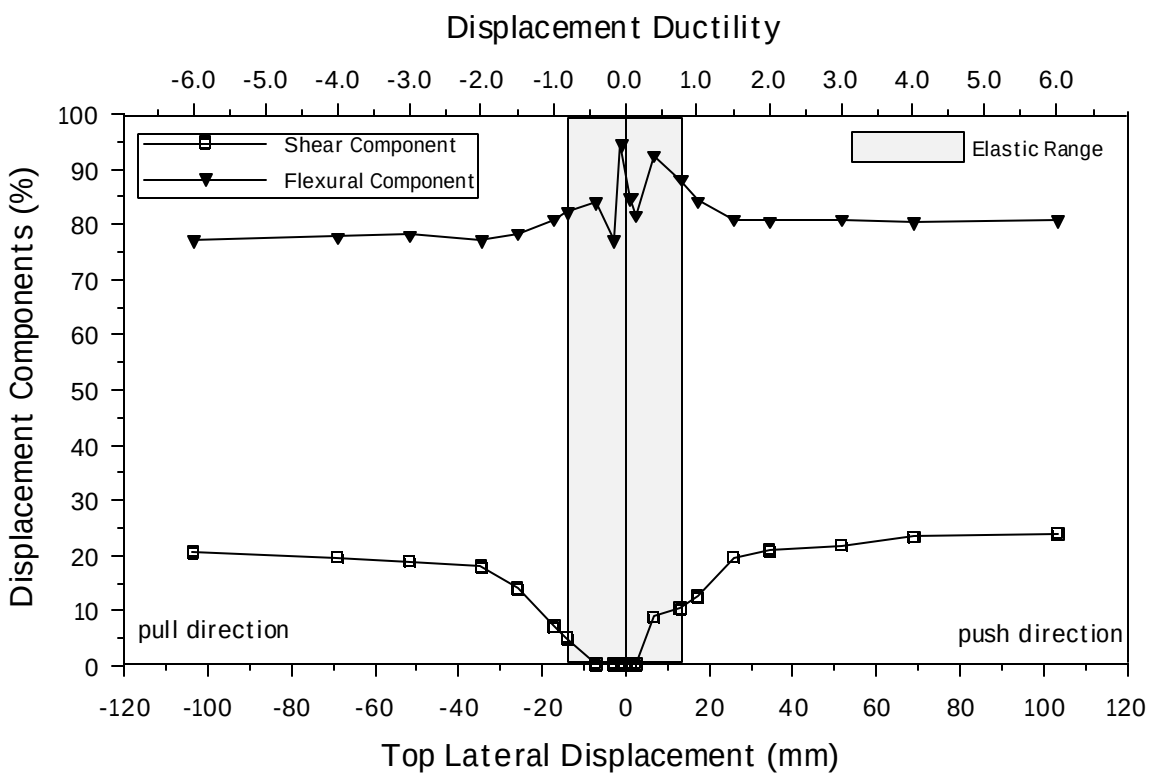

Figure 4.15 Unit HS1 Shear and Flexural Components of Total Displacement

The shear displacement component is computed from the readings of the shear deformation panels. Readings from the east and west panels are averaged in order to calculate the average shear distortion in each of the three pannels of the shear deformation panel. Shear distortions are integrated along the column height to obtain the shear contribution to the total displacement.

In Figure 4.15, shear and flexural deformation components are expressed as a percentage of the total displacement measured on the column top. It can be noted that the behavior is not symmetric in the push and pull direction. However, a similar trend is shown in both directions of loading with respect to the mutual interaction between shear and flexure. During the elastic phase and loading cycles up to displacement ductility of 2.0 in the inelastic phase, the shear deformation component increases steadily while the flexural component decreases. In the later stages of testing (from displacement ductility 2.0 to 6.0) the two contributions remain roughly the same. It is noticed that the flexural contribution to the top displacement is always greater than 75% of the total displacement.

The displacement components are plotted in Figure 4.16 as a function of the total displacement measured on the column top. The purpose of the graph is to check if the readings from curvature cells and shear deformation panels were accurate. If the shear and flexural deformation components, calculated based on the procedure described previously, are added, the summation should be theoretically equal to the total displacement measured on the column top. It is verified from the test that there are no other significant contributions to the column top displacement except for the column shear and flexural deformations (e.g. the shear deformation of the foundation footing is negligible). It can be noted in Figure 4.16 that the computed and measured top displacement envelopes match quite well, and it is concluded that the readings from the curvature cells and shear deformation panels were accurate and that the procedure adopted to calculate the top displacement is accurate enough for the test. Shown in Figure 4.17 is the applied lateral load versus various displacement components. It can be clearly observed that the significant shear deformations do not appear until after a lateral load of 600 kN.

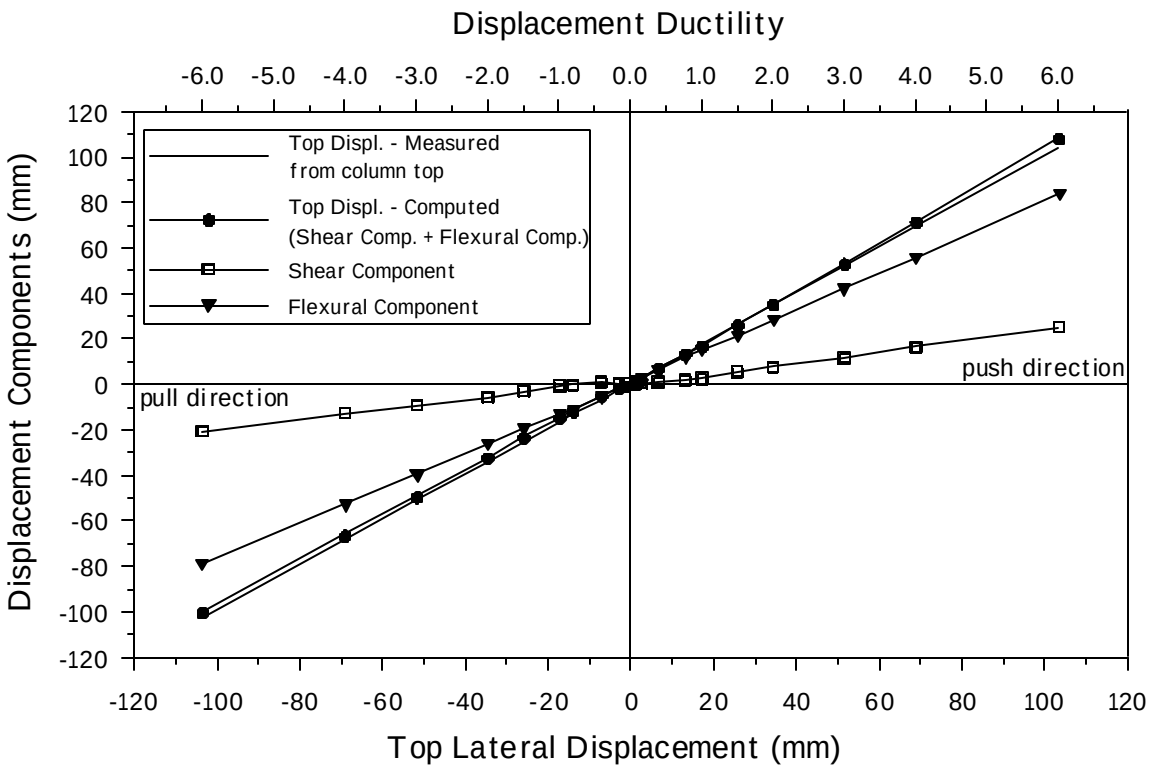

Figure 4.16 HS1 Displacement Components vs. Total Top Displacement

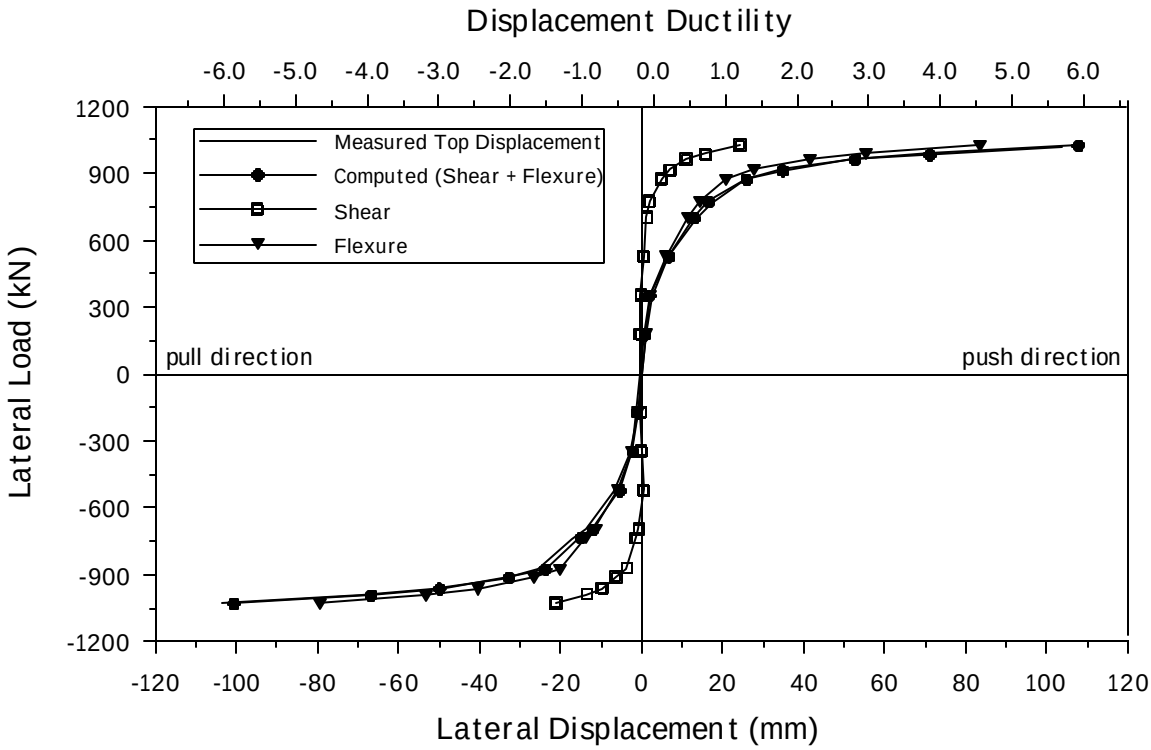

Figure 4.17 Unit HS1 Lateral Force/Displacement-Component Response

4.1.4.2 Plastic Hinge Length

The effective plastic hinge length may be calculated from the lateral force-displacement plot (Figure 4.10) on the base section moment-curvature plot (Figure 4.11) as follows.

$$\angle_p = \frac{\Delta_p}{\phi_p H} = \frac{(\Delta - \Delta_y)}{(\phi - \phi_y)H} \tag{4.2}$$

where ? and f are the maximum displacement and curvature at the considered ductility level, and Δ_y and ϕ_y are the yield displacements and curvatures. In calculating the plastic hinge length, the curvature in Figure 4.11 have been reduced by 23%, since the effective curvature cell length is increased by the strain penetration length of 127 mm ($424/+(424+127) = 0.77$). The resulting plastic hinge length calculated by $\mu_?$ = 2,3,4 and 6 gives values of 0.97 m, 1.14 m, 1.18 m, 1.18 m, which are more than twice of the calculated values of 0.44 m. Part of the reason is that the recorded displacements include significant shear deformations (approximately 25% at $\mu_?$ = 6 (see Figure 4.15)). Reducing the plastic displacements to account for the measured shear deformations would reduce the place hinge lengths to approximately 0.86 m. This is still much larger than expected for solid columns.

4.1.5 Profiles At Load (or Displacement) Peak Level

Strain or displacement profiles describe the distribution of a generic deformation parameter along a line on the structure at peak load or displacement levels. Profiles can be plotted along the column height or the section depth in order to describe the distribution of the deformation parameter for increasing lateral forces.

Profiles are presented herein for each load step in the push and pull direction during the load control phase (elastic range). During the inelastic phase for each displacement ductility level, profiles are presented for the first peak in the push direction and for the

last peak in the pull direction. The behaviors during the elastic and inelastic phases are printed in different graphs, using different scales in the horizontal axis. The load stages in the elastic phase are identified with a label indicating the load level in kN, while load stages in the inelastic phase are identified with the displacement ductility level.

4.1.5.1 Flexural and Shear Deformation Components

As it was discussed above, shear and flexural deformations vary as a function of the applied lateral force. In fact, these deformation components have significantly different distributions along the column height. Shear displacement profiles are obtained by computing the lateral displacement due to shear at the top of each of the three portions of the shear deformation panels. Flexural displacement profiles are obtained instead by plotting the lateral displacement due to flexure at the top of each of the 7 curvature cells. Shear and flexural profiles at different ductility levels are shown in Figure 4.18 and Figure 4.19. Shear profiles in the elastic response stages are somewhat erratic, but in the inelastic stages, show a characteristic profile with the shear displacement concentrating at the base of the column. Flexural profiles shown in Figure 4.19 indicate an increasing concentration of plastic rotation at the base of the column as the ductility level increases.

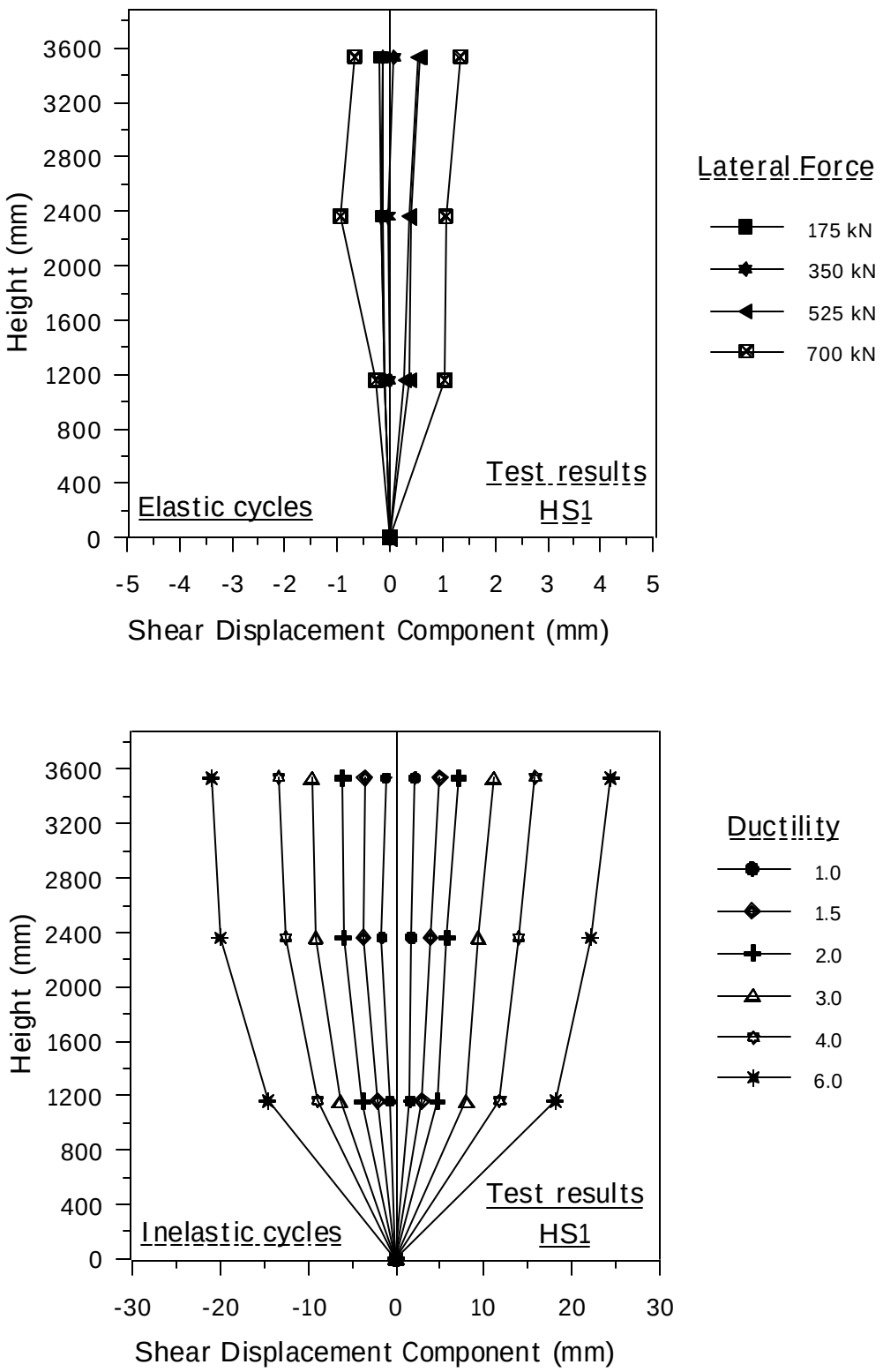

Figure 4.18 Unit HS1 Shear Displacement Profiles at Different Ductility Levels

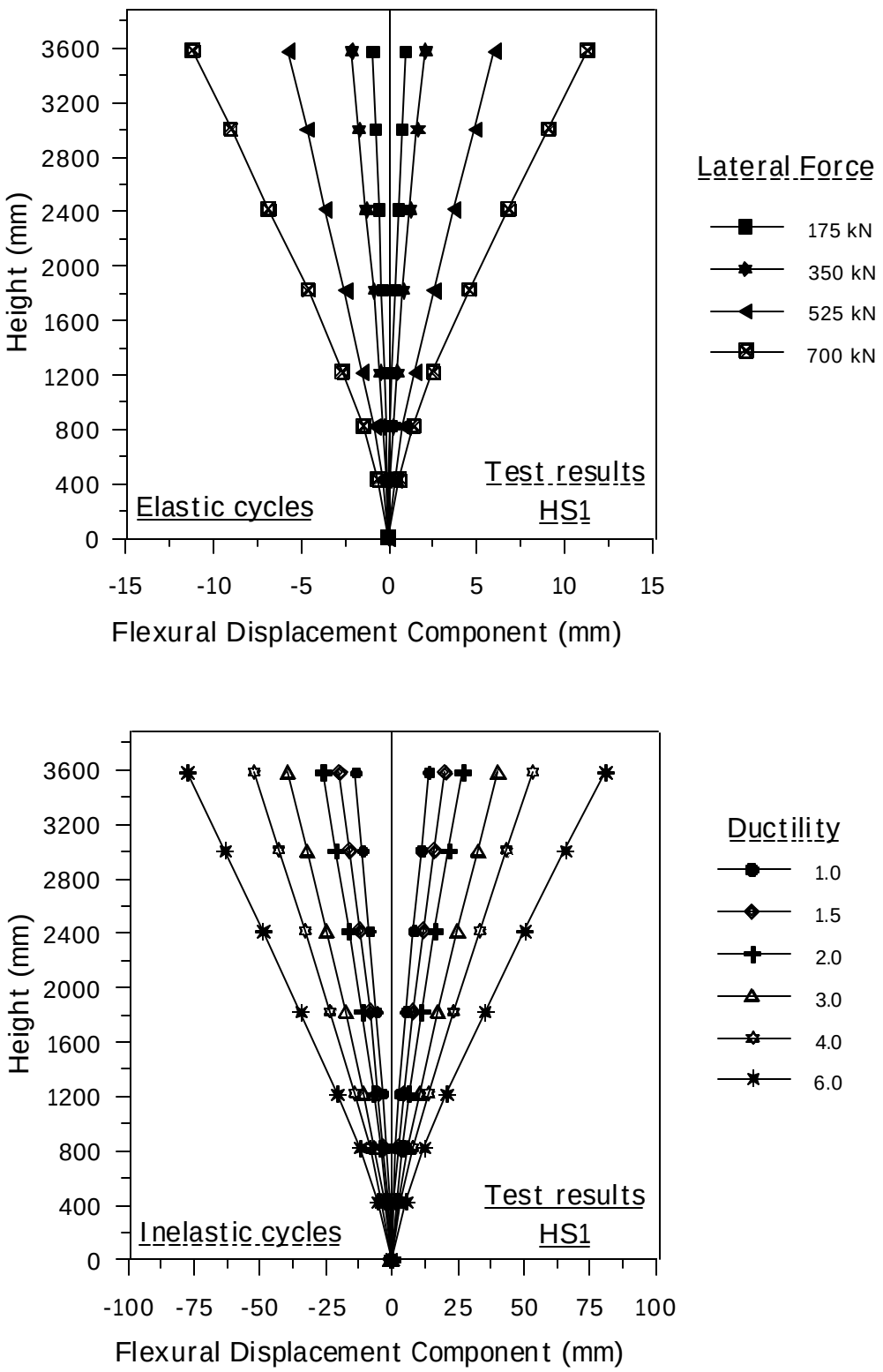

Figure 4.19 Unit HS1 Flexural Displacement Profiles at Different Ductility Levels

4.1.5.2 Curvatures

Curvature profiles are presented in Figure 4.20 and Figure 4.21. In the first case the effect of strain penetration on the base curvature is not accounted for. The curvature obtained from readings of the first curvature cell is supposed to be averaged over the cell height and is plotted at mid-height of the first curvature cell (214mm above the column base). In the second graph the effect of strain penetration is taken into account by using a revised height of the first curvature cell according to the equation described in Chapter 2. In this case, the curvature value obtained from reading of the first curvature cell is plotted at mid-height of the revised cell (111.5 mm above the column base).

In both cases the assumption of constant curvature over the cell height might be inaccurate. A better estimate of the curvature profile near the column base can only be achieved by subdividing the base curvature cell in two different cells. This will be the case of the second test unit (HS2).

Note that the yield curvature (calculated using the procedure described above in Chapter 2 from the curvature at first yield of longitudinal rebars) is equal to 2.72rad/km. During the inelastic phase it can be noticed that the region were the curvature exceeds this value (plastic hinge region) extends up to about one diameter from the base. The plastic hinge length was probably underestimated based on Equation (2.33), which gives $L_p = 480$ mm. In fact, during the test it was observed that from early stages of testing flexural cracking occurred up to 1.5 diameters from the base, causing large deformations in longitudinal reinforcing bars. As a result, large curvatures occur in the region where large inelastic deformations occur in the longitudinal bars. Also it can be noted that within the elastic range of response the curvature profiles follow (in average) a linear profile. Local variations from the linear profile might be due to the effect of local cracking within the curvature cell height.

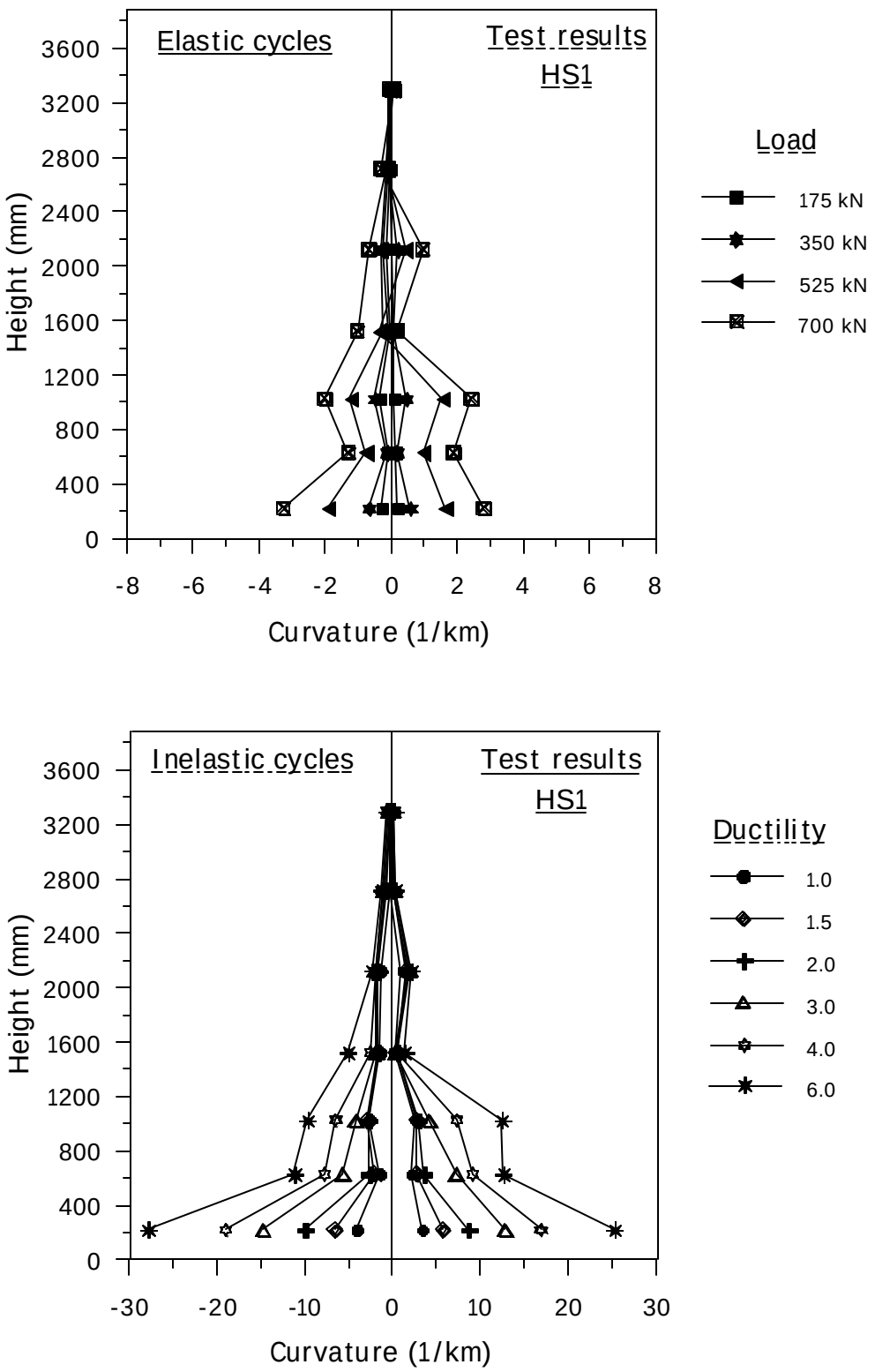

Figure 4.20 Unit HS1 Curvature Profile at Different Ductility Levels – Strain Penetration Ignored

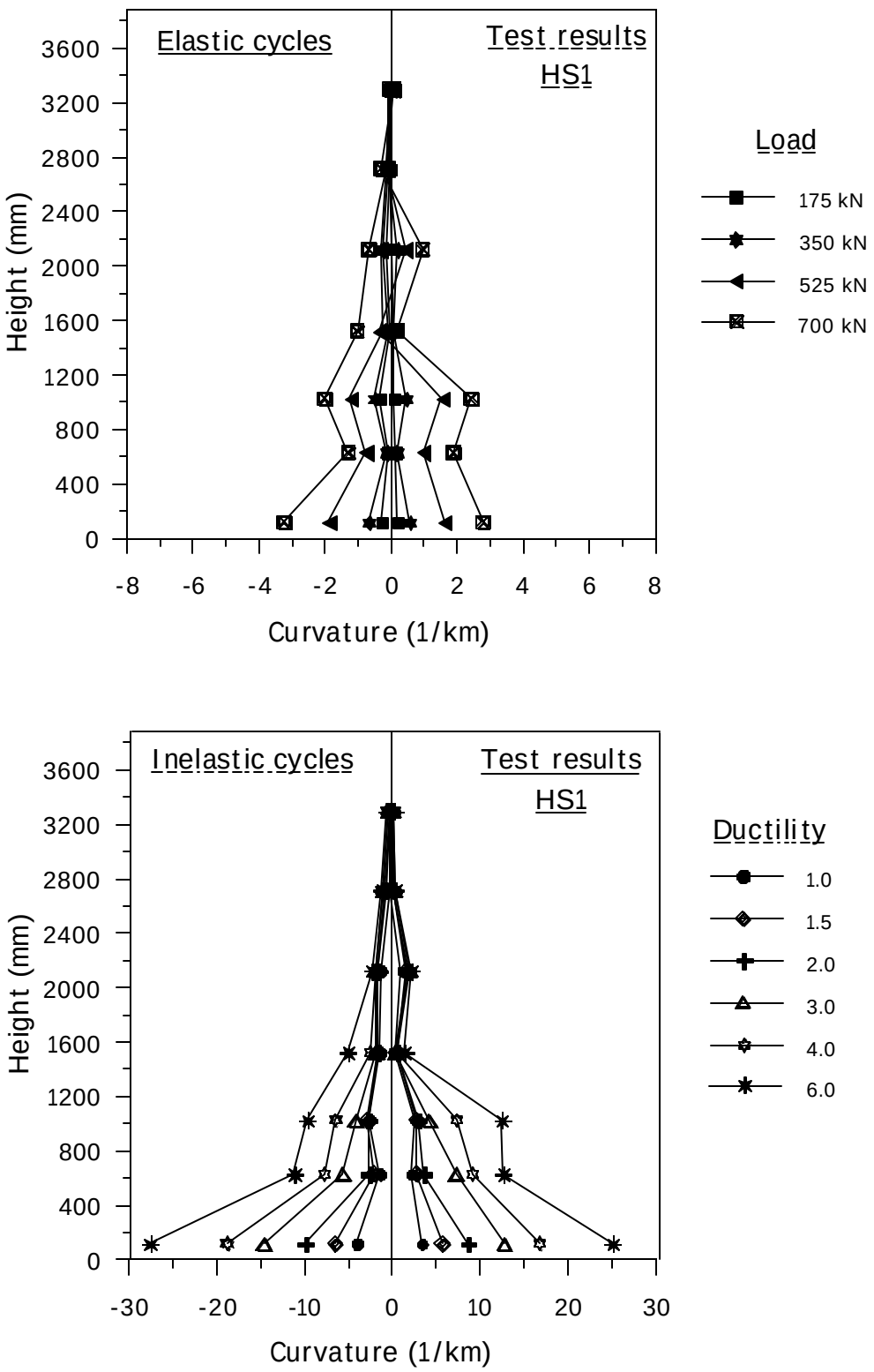

Figure 4.21 Unit HS1 Curvature Profile at Different Ductility Levels – Strain Penetration Included

4.1.5.3 Longitudinal Reinforcement Strains

Profiles of the strains recorded along the instrumented longitudinal bars are presented in Figure 4.22 and Figure 4.23 for the north and the south bar respectively. It can be noticed that, as anticipated before, large strains occur within the first diameter from the column base at later stages of testing. Since the yield strain of these bars was 2300$\mu\varepsilon$, it can be concluded that after a displacement ductility of one, the longitudinal bar strains at the sections from the column base up to 1400 mm were completely yield. It confirms the statement for describing the curvature profiles that the inelastic flexural actions occurred in a considerably large region, about one diameter in size.

Looking at the behavior below the column base (inside the foundation footing), it can be noted that significant strains occur within the first 300 mm. In particular, inelastic tensile strains occur at later stages of testing within the first 100 mm below the column base. From the result it can be concluded that the strain penetration be able to be estimated by Equation (2.33). It should be pointed out that the readings from gauges at the column base are not very reliable, especially in the inelastic phase, where local buckling of longitudinal bars might significantly affect the measurement.

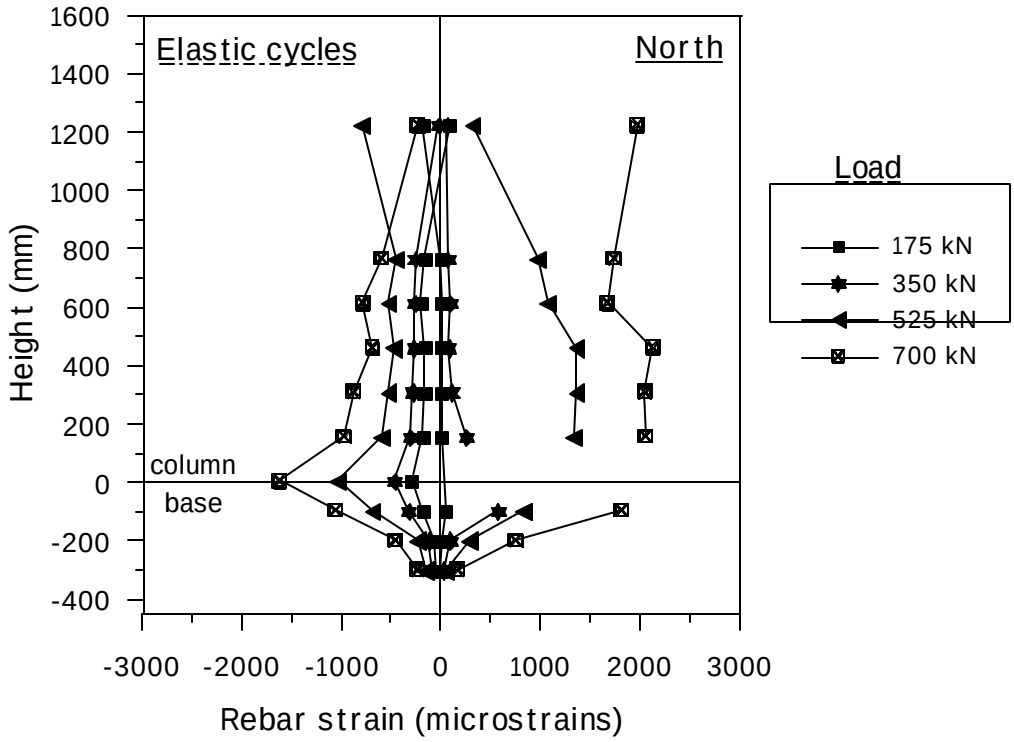

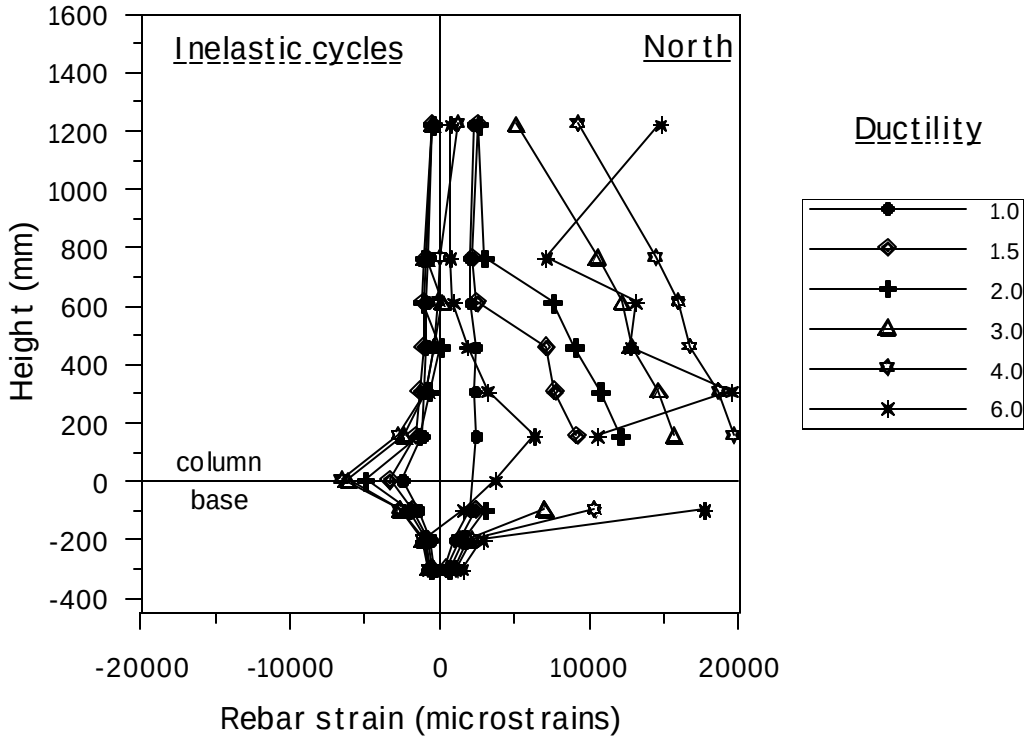

Figure 4.22 Unit HS1 Profile of Longitudinal Rebar Strain at Extreme North Tension Location (Push Loading)

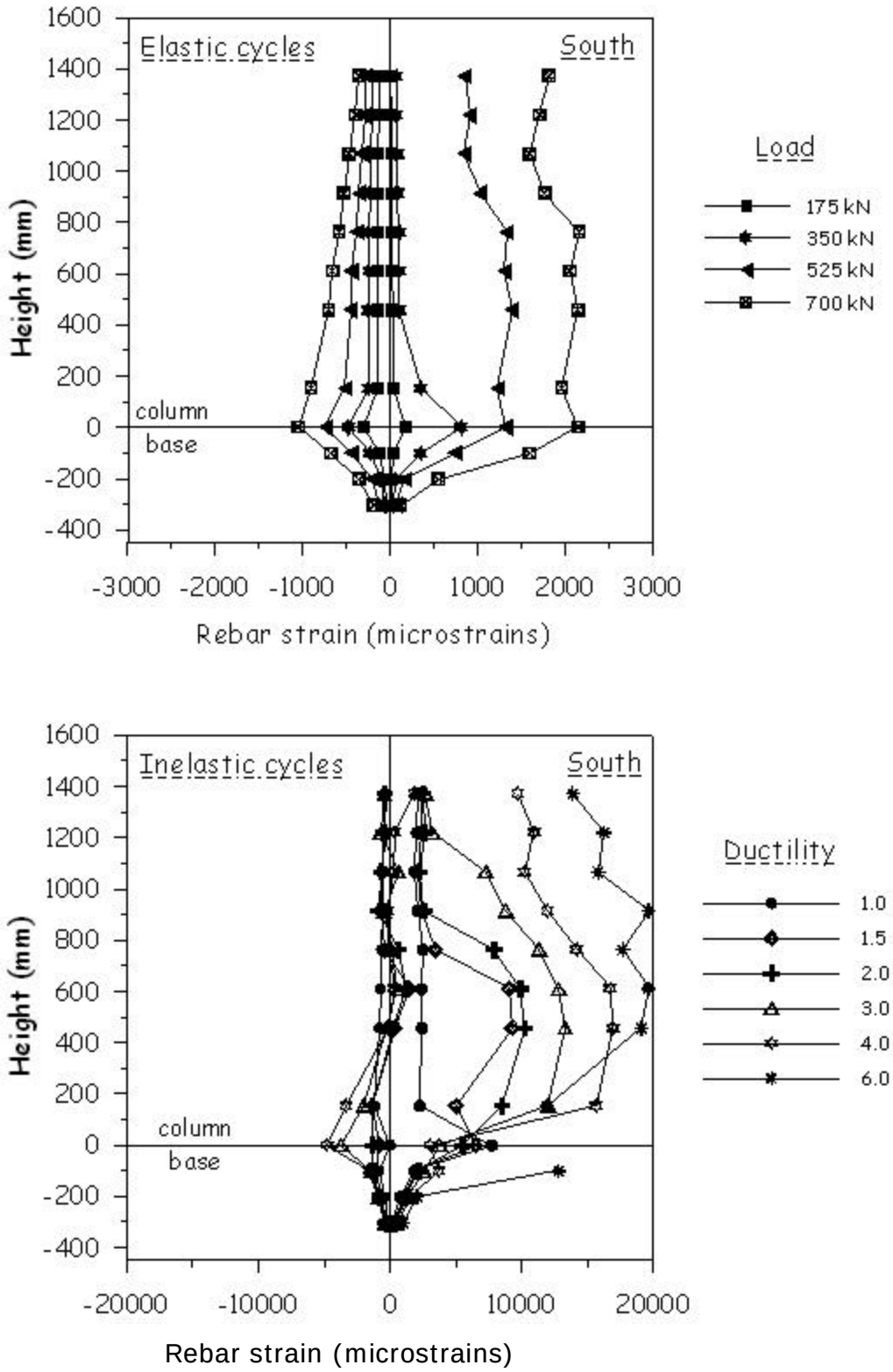

Figure 4.23 Unit HS1 Profile of Longitudinal Rebar Strain at Extreme South Tension Location (Pull Loading)

4.1.5.4 Transverse Reinforcement Strains

The strains in the transverse reinforcement were measured in several locations along the continuous spiral. Given the type of test, it appears particularly interesting to look at the strains along the west and east generators (section mid-depth), where shear strains should reach the largest values. In fact, it is observed that lateral strains (strains in the transverse reinforcement) have a non-symmetric distribution over the section depth and that the maximum value does not always occur at section mid-depth. However, the profiles of the lateral strains at the section mid-depth are good indicators of the overall distribution of shear deformations, since lateral strains are proportional to the width of the inclined shear cracks.

For simplicity, profiles from elastic and inelastic phases are plotted in the same graph. Two different graphs are presented instead for the push and pull direction since spiral strains are always positive (tensile). Spiral strain profiles are shown in Figure 4.24 and Figure 4.25 for the west and east generator respectively. A similar behavior is shown along the two generators in the push and pull directions. Relatively low strains occur within the first 400-500 mm from the column base. This is due to the influence of the confining action provided by the foundation footing. This latter provides a significant restraint to the shear deformations. In the region between 500 mm and 2000 mm above the column base, strains reach comparable values with some local peaks. Above 2000 mm from the base, spiral strains smoothly tend to zero as the location of the measuring moves further up. From the photographic documentation and the observations in Section 4.1.2, it can be noticed that the inclined cracks with considerable width (up to 0.85mm) occurred along the east and west generators exactly in that region. It confirms that the shear critical portion of the column is identified from 0.5 to 1.5 diameters above the base. This is because relatively low shear strains occur at column base due to the confining effect of the footing and extremely low shear strains occur towards the column top because of the presence of low bending forces.

Furthermore, it is found that the transverse strains are almost exactly zero up to the 525 kN load step, when significant shear cracking occurred. After that stage lateral strains started to appear in the bottom part of the column (say within the first 1600mm from the base) and subsequently extended further up (compare the 700 kN profile with those from ductility 1.0 and 1.5). It is also interesting to note that lateral strains do not exceed the yield strain of 3200 με until high ductility levels and peak strains are always less than 4000 με except at displacement ductility of 6. It would appear that the shear capacity had just been reached in HS1, and any further increase in shear capacity would only be achieved by strain hardening of the spiral bar.

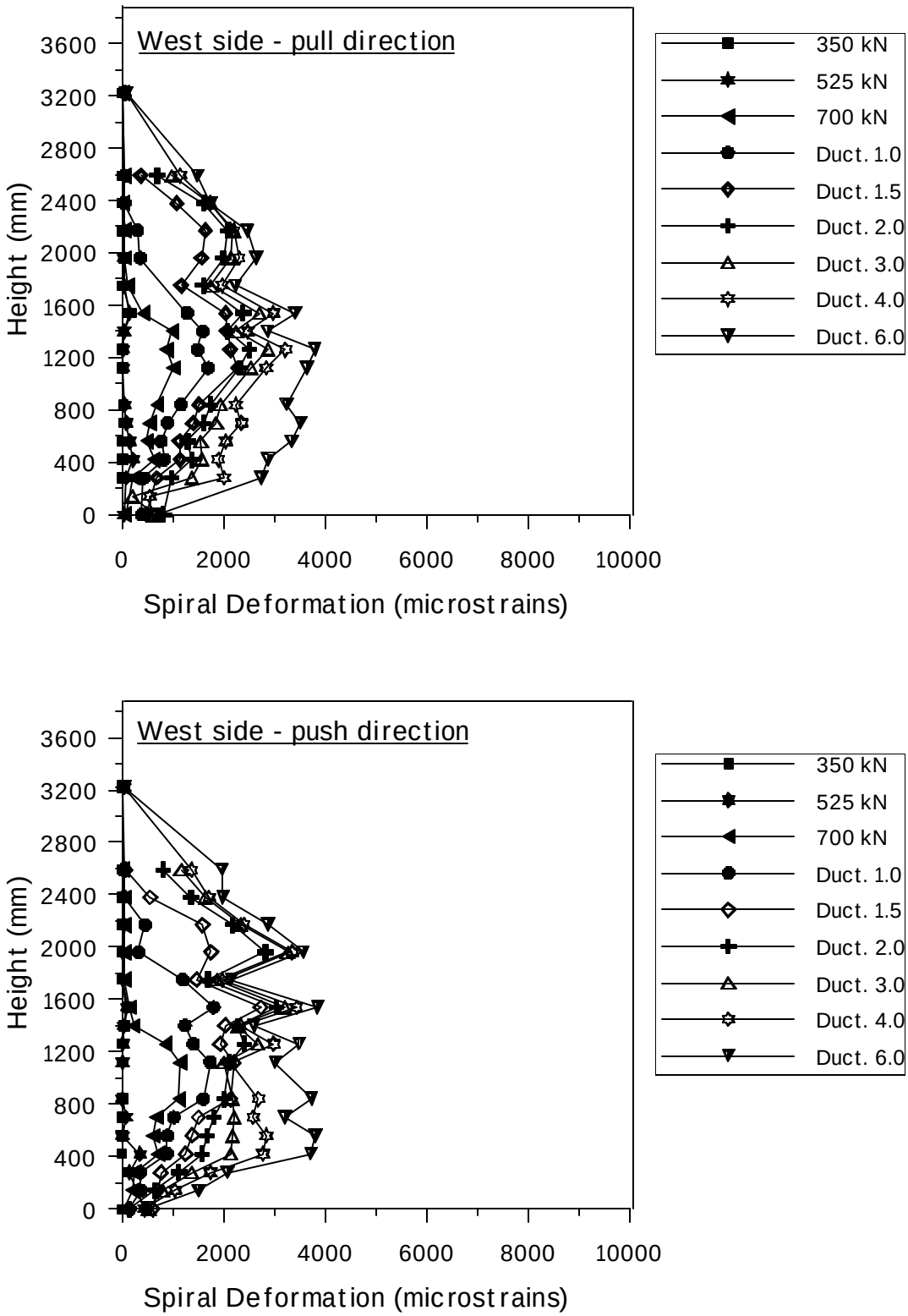

Figure 4.24 Unit HS1 Vertical Profiles of Spiral Strain on West Side

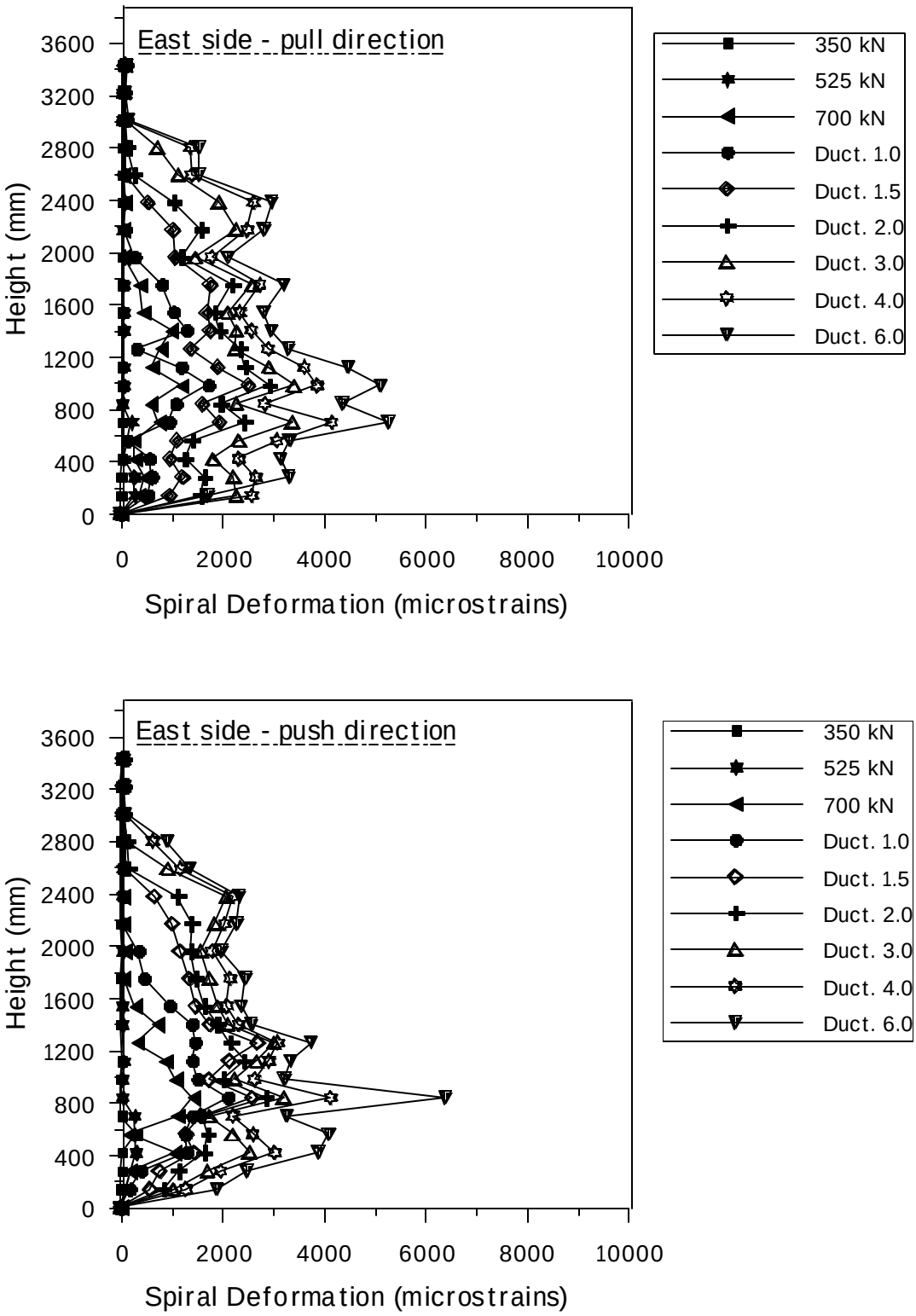

Figure 4.25 Unit HS1 Vertical Profiles of Spiral Strain on East Side

4.1.5.5 Section Longitudinal Strain Profiles

The distribution of the longitudinal strains over the section depth is analyzed in Figure 4.26 to Figure 4.31 for three different sections, one below the column base and two above the column base. The first section is located at 102mm below the column base, where it was observed that tensile strains reached and exceeded the yield point. The second section is at 152 mm above the base, where it is expected to have reasonably accurate readings up to the later stages of testing. The third one located at 609 mm above the column base is out of the predicted plastic hinge region. As it was observed instead, considerably high inelastic strains occur in this section as well.

The longitudinal strain profile is obtained by plotting, for the same section, the strain values recorded along the north and south bars located at the extreme tension and compression sides of the test unit. The average value of the east and west gauges is plotted at the mid section. The horizontal axis indicates the location of the gauges expressed as a function of the distance from the section centroidal axis.

The analysis done at these three sections is to provide a clear description of the region where inelastic flexural actions occurred. Different plots are provided for the push and pull direction, dividing into elastic and inelastic stages of the testing. In the graphs two vertical dashed lines are provided in order to indicate the location of the inside face of the column wall. An additional continuous horizontal line is provided in the graphs to indicate the level of the steel yield strain, which is at 2300 $\mu\varepsilon$.

Looking at the first section it is observed that longitudinal strains maintain a linear profile throughout the test except for the level of ductility 6. The depth of the compression zone during the inelastic phase is not the same in the push and pull directions. While it is about 450 mm in average in the push direction, this values drops down to 300-350 mm in the pull direction. The depth of the compression zone does not vary significantly from the elastic to the inelastic phases.

In the second section, located at 152 mm above the base, it is observed that the depth of the compression zone decreases rapidly during the inelastic phase. At failure the position of the neutral axis is very close to the wall inside face for both in push and pull directions. In fact, it is observed that at failure concrete spalled off at this location under the effect of significant compressive strains, which do not vary significantly across the wall thickness in that region. The fact cannot be confirmed by other measurements, because there is no other gauges in this section indicating the value of longitudinal strains. As a consequence, these conclusions should be taken with caution.

The analysis of the behavior in the section at 609 mm above the base indicates that the section has a tendency to be completely in tension as the lateral applied displacement is increased. It can be noted in the push direction that there is no strain compression zone after ductility 1.5. Again the profile of the longitudinal deformations is almost linear at each load stage. In fact, looking at the readings from curvature cells it is found that the compression is almost zero.

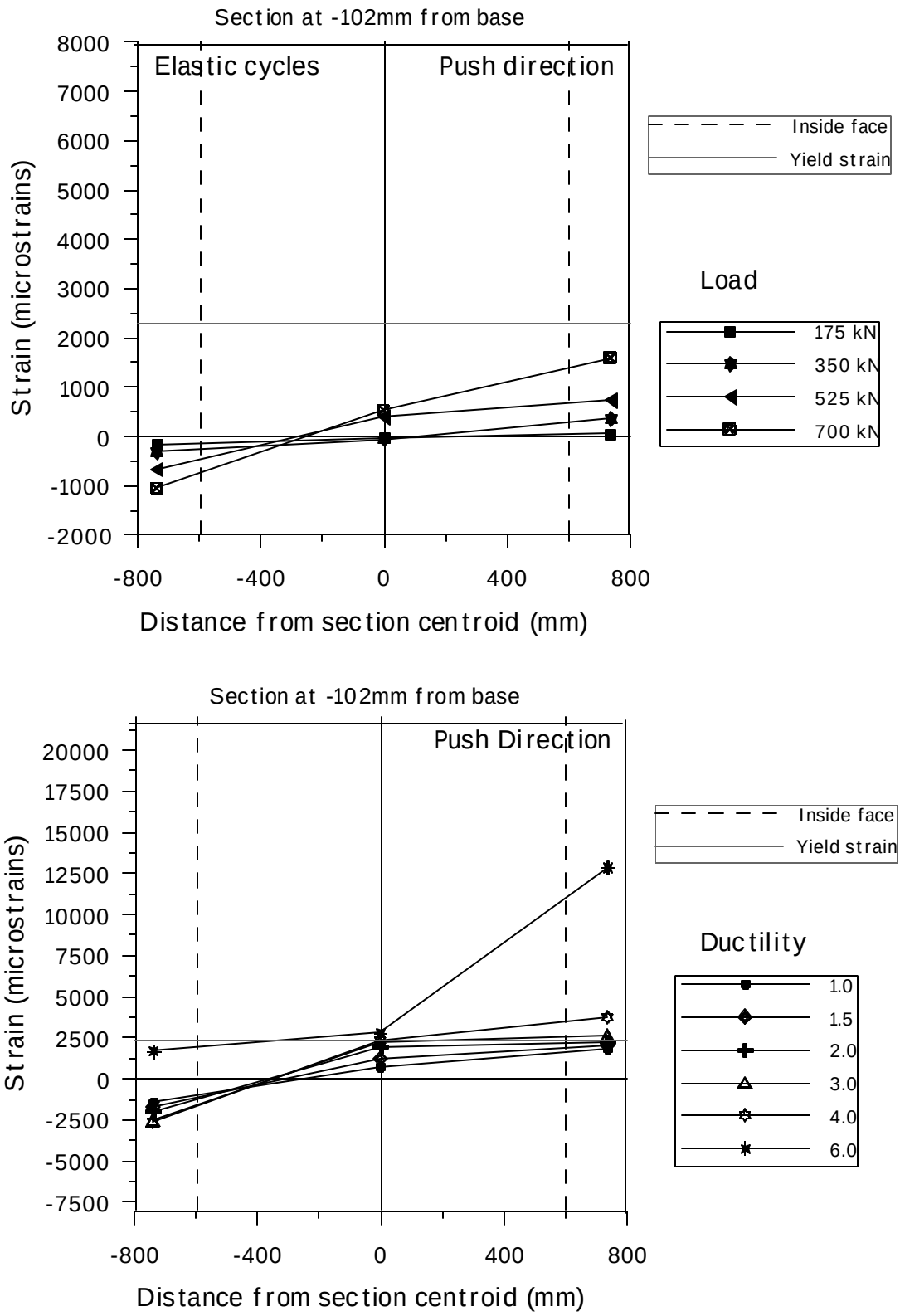

Figure 4.26 Unit HS1 Section Longitudinal Bar Strain Profiles, 102 mm Below Base Section, Push Loading

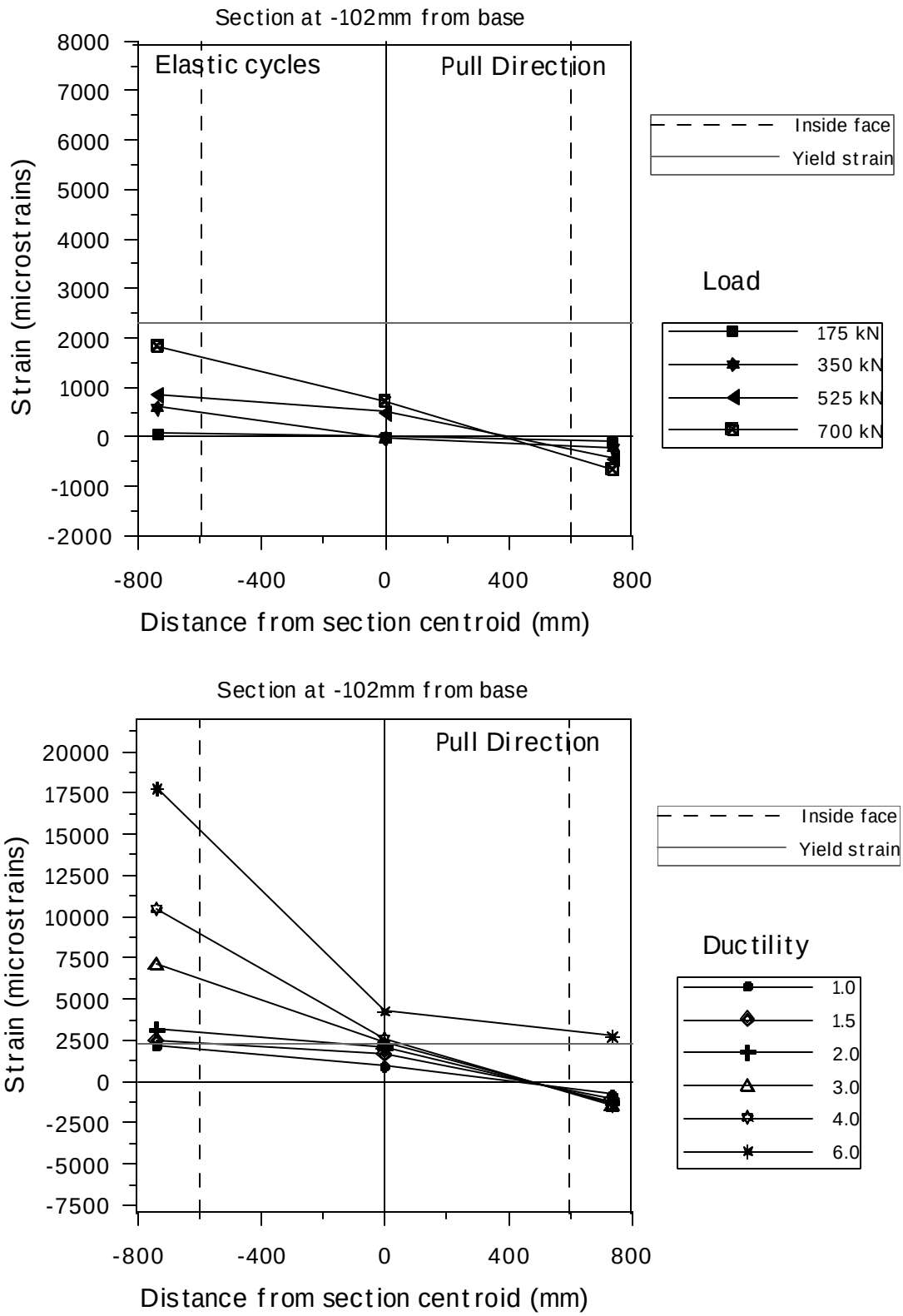

Figure 4.27 Unit HS1 Section Longitudinal Bar Strain Profiles, 102 mm Below Base Section, Pull Loading

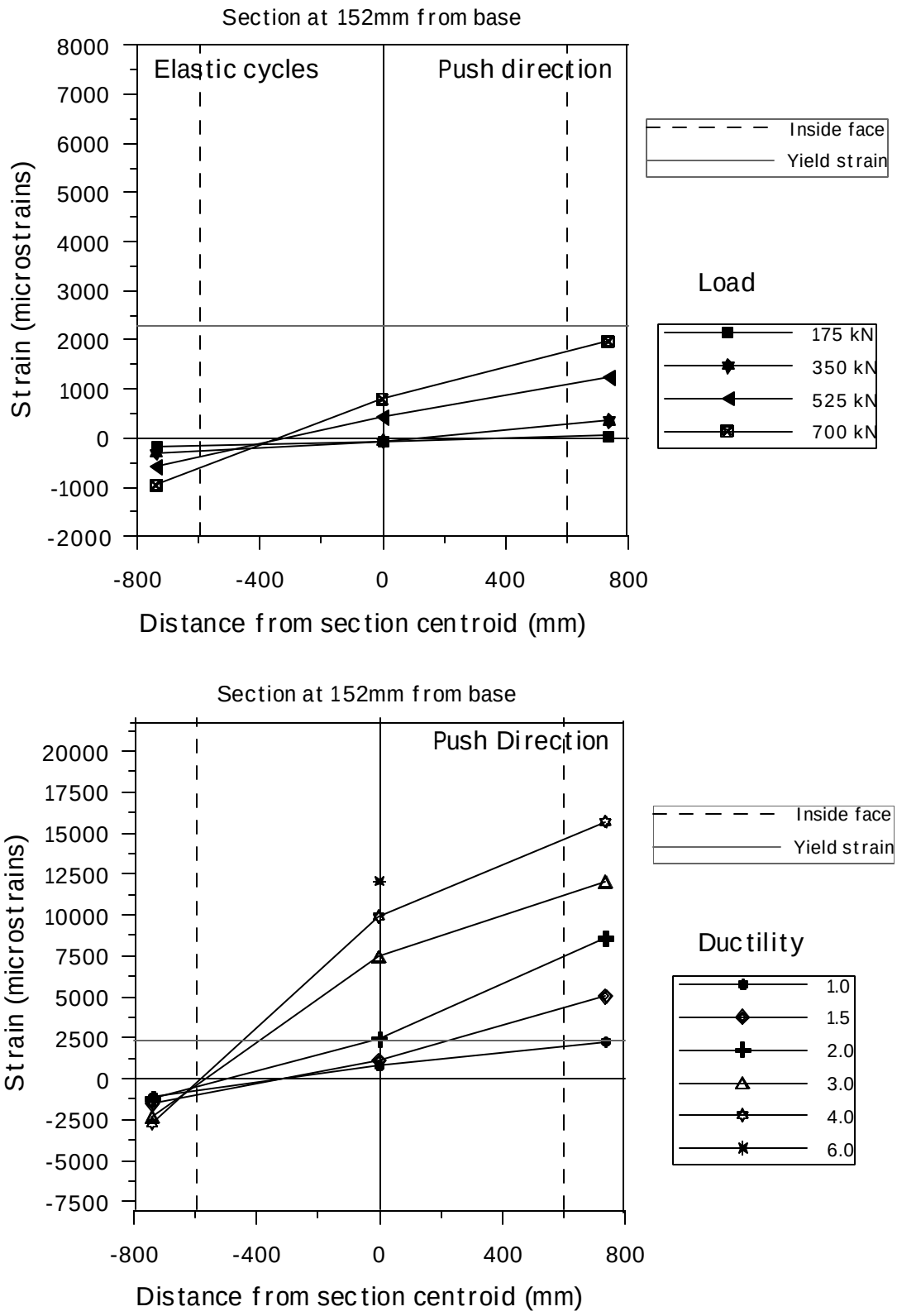

Figure 4.28 Unit HS1 Section Longitudinal Bar Strain Profiles, 156 mm Above Base Section, Push Loading

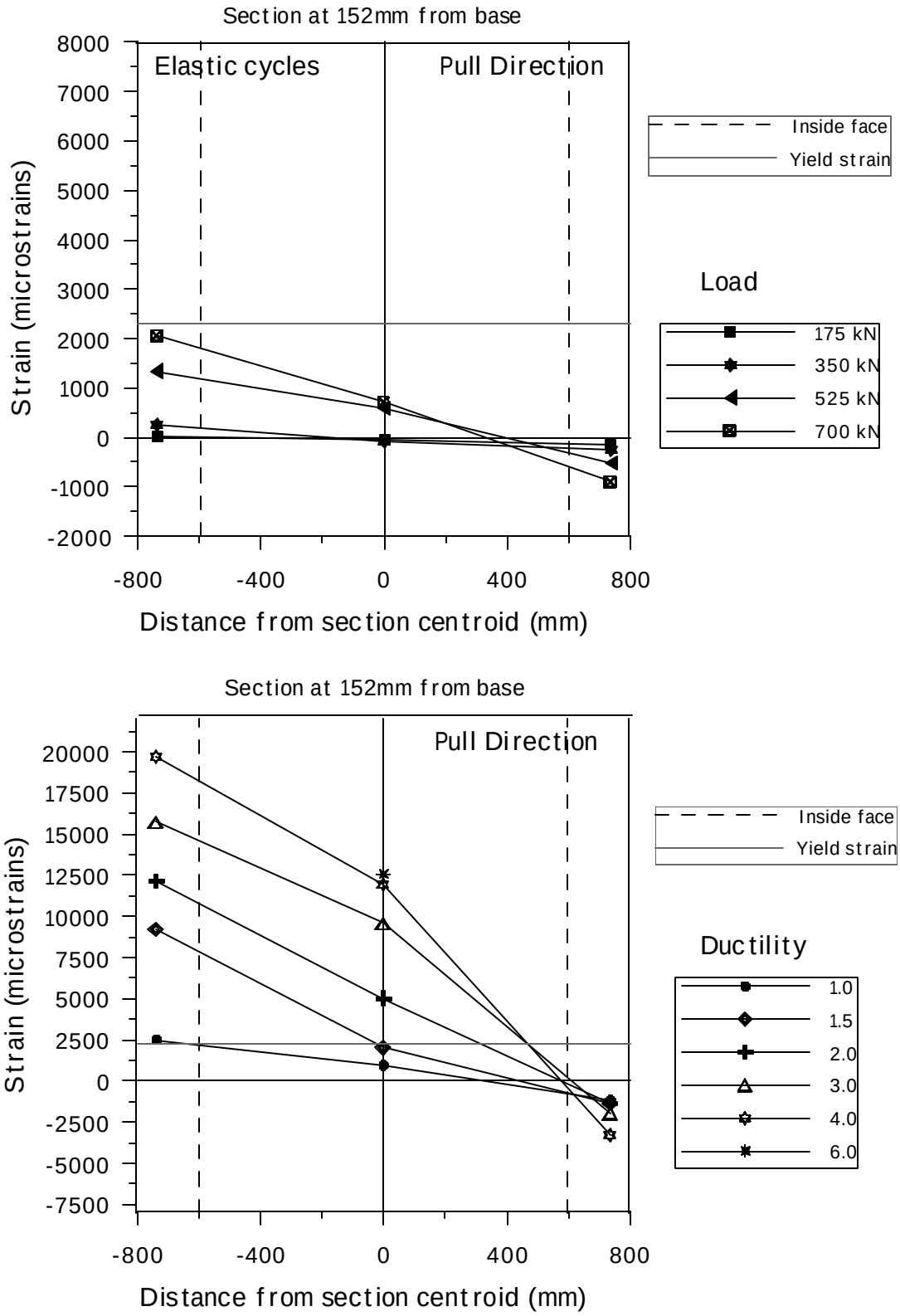

Figure 4.29 Unit HS1 Section Longitudinal Bar Strain Profiles, 156 mm Above Base Section, Pull Loading

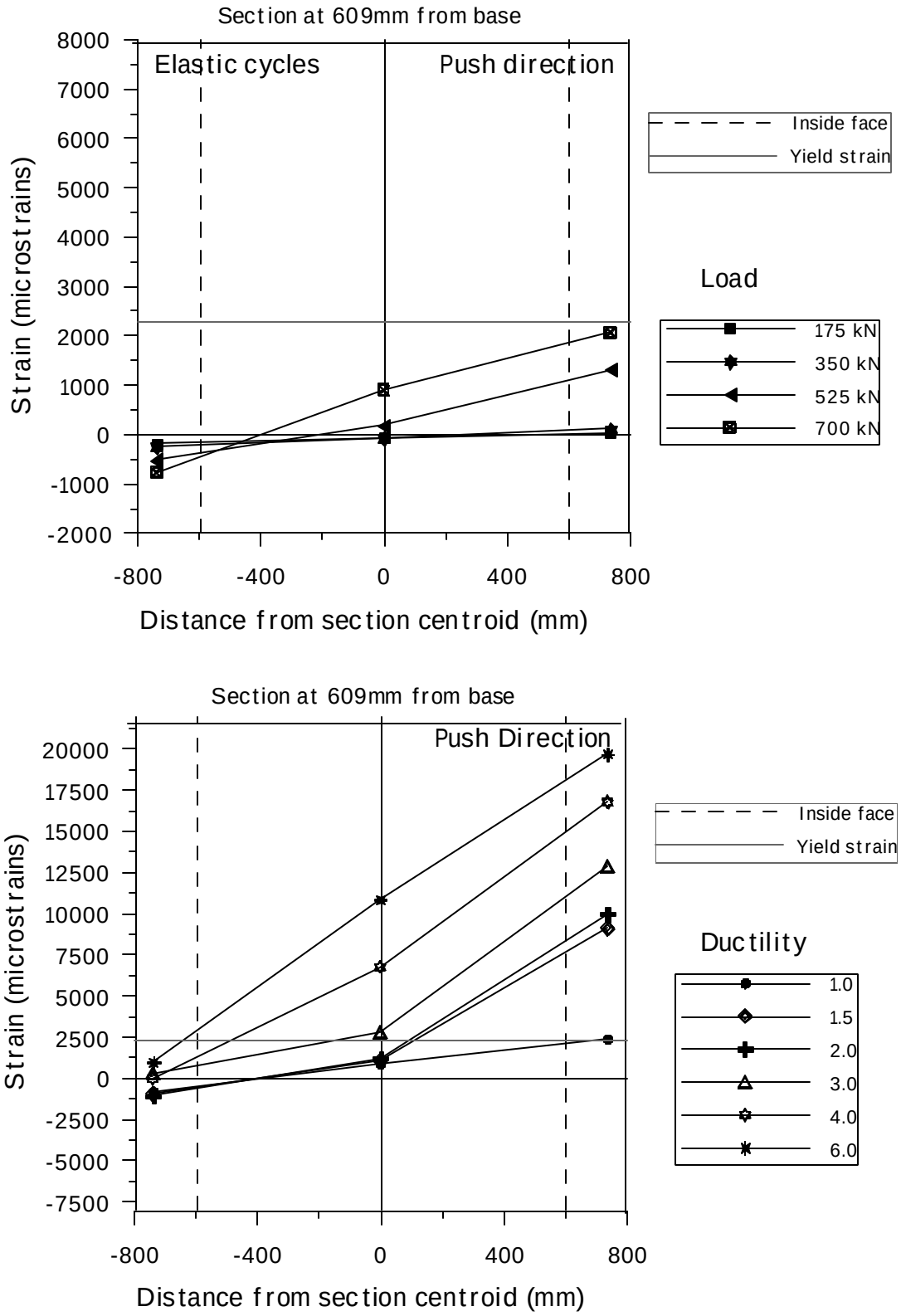

Figure 4.30 Unit HS1 Section Longitudinal Bar Strain Profiles, 609 mm Above Base Section, Push Loading

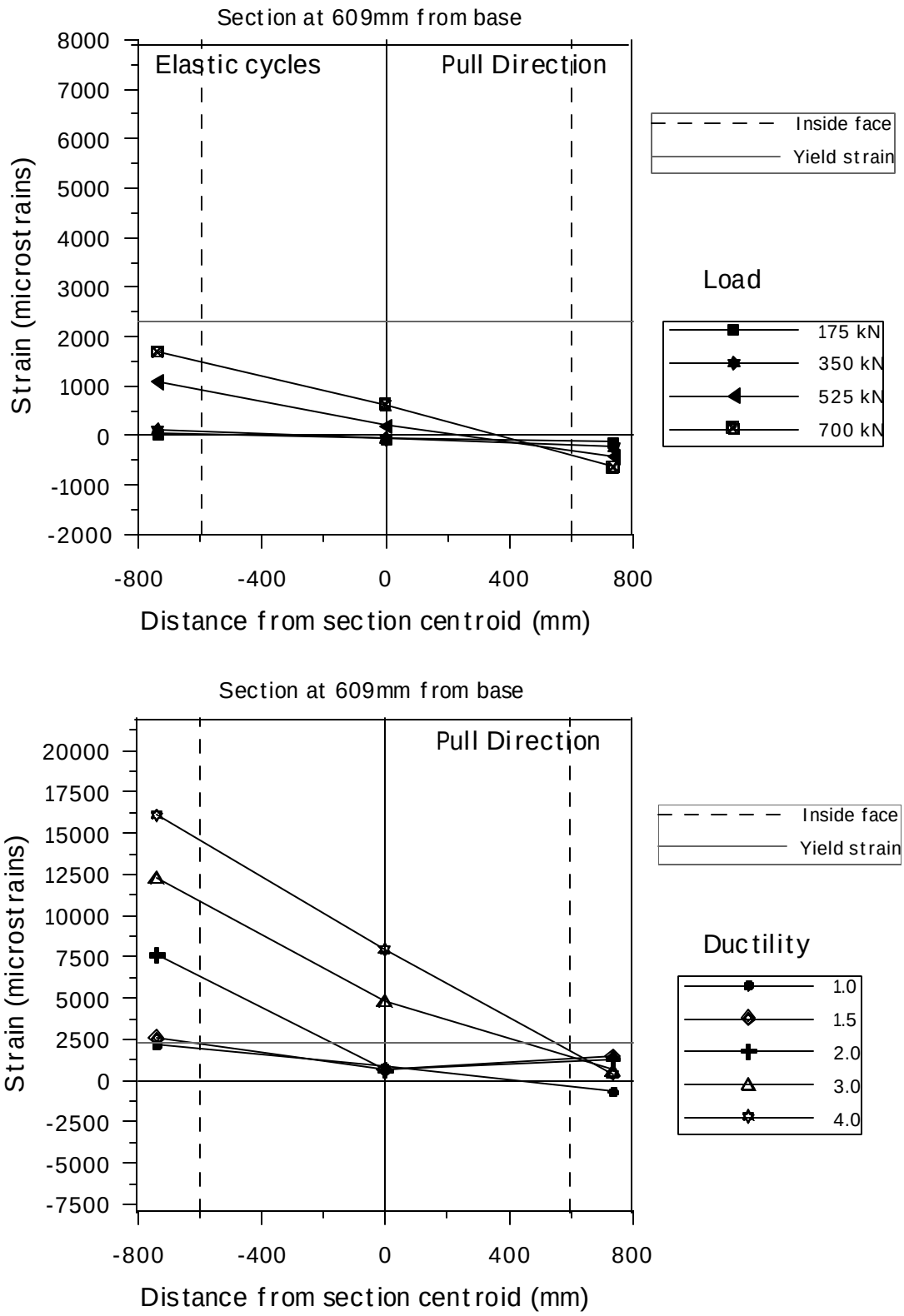

Figure 4.31 Unit HS1 Section Longitudinal Bar Strain Profiles, 609 mm Above Base Section, Pull Loading

4.1.5.6 Section Transverse Strain Profiles

Transverse strains recorded on the spiral reinforcement are plotted as a function of the distance from the section centroid, with the same format used to describe the distribution of longitudinal strains over the section depth. There are total of 7-instrumented points spaced at every 30 degrees over the section depth. Gauges with symmetric location in the east and west sides are averaged. Results are presented in Figure 4.32 to Figure 4.33 for three sections located respectively at 280, 840 and 1400 mm above the column base.

It was discussed above in Section 4.1.5.4 that the region has the largest transverse strains, and expected that the maximum strains do not necessarily occur at the section mid-depth. Figure 4.32 shows that the maximum value occurs in the tension side of the section, at approximately 400 mm from the section centroid. The behavior is symmetrically shown in the push and pull directions. Also note that in the extreme compression side there is a local increase in transverse strain at high ductility levels (from displacement ductility 2.0 to 6.0) due to the effect of longitudinal rebar buckling. Figure 4.33, however, shows that the distribution over the section depth is a little more uniform, but the peak is still located at 400 mm away from the section centroid, towards the tensile side of the section.

In the two sections analyzed so far it is noted that within the elastic range of response (before displacement ductility 1.0), the maximum value is not reached towards the tensile side of the section (as it clearly is during the inelastic phase) but it occurs exactly at the section mid-depth. This is due to the behavior in shear. Within the elastic behavior shear stresses reach the maximum at the section mid-depth because of the section shape. Shear strains will therefore have a maximum at section mid-depth as well. During the inelastic phase instead, the section is significantly damaged and larger shear strains tend to occur where the section is more damaged (i.e. the tensile side). Figure 4.34 shows the strain profiles at 1400 mm above the column base, and it is observed that the peak value is always reached at the section mid-depth. As discussed about the longitudinal strain profiles in Section 4.1.5.5, this is no inelastic flexural deformations

occurred above this section. It is therefore reasonable to conclude that the flexural damage strongly governs the distribution of shear deformations and therefore of strains in the transverse reinforcement. This conclusion will be confirmed in the third test unit (HS3), where a measure of the shear deformation distribution over the section depth is taken with the aid of additional small shear panels. It will be confirmed that the flexural damage tends to shift the maximum values of shear and transverse strains towards the tensile part of the section.

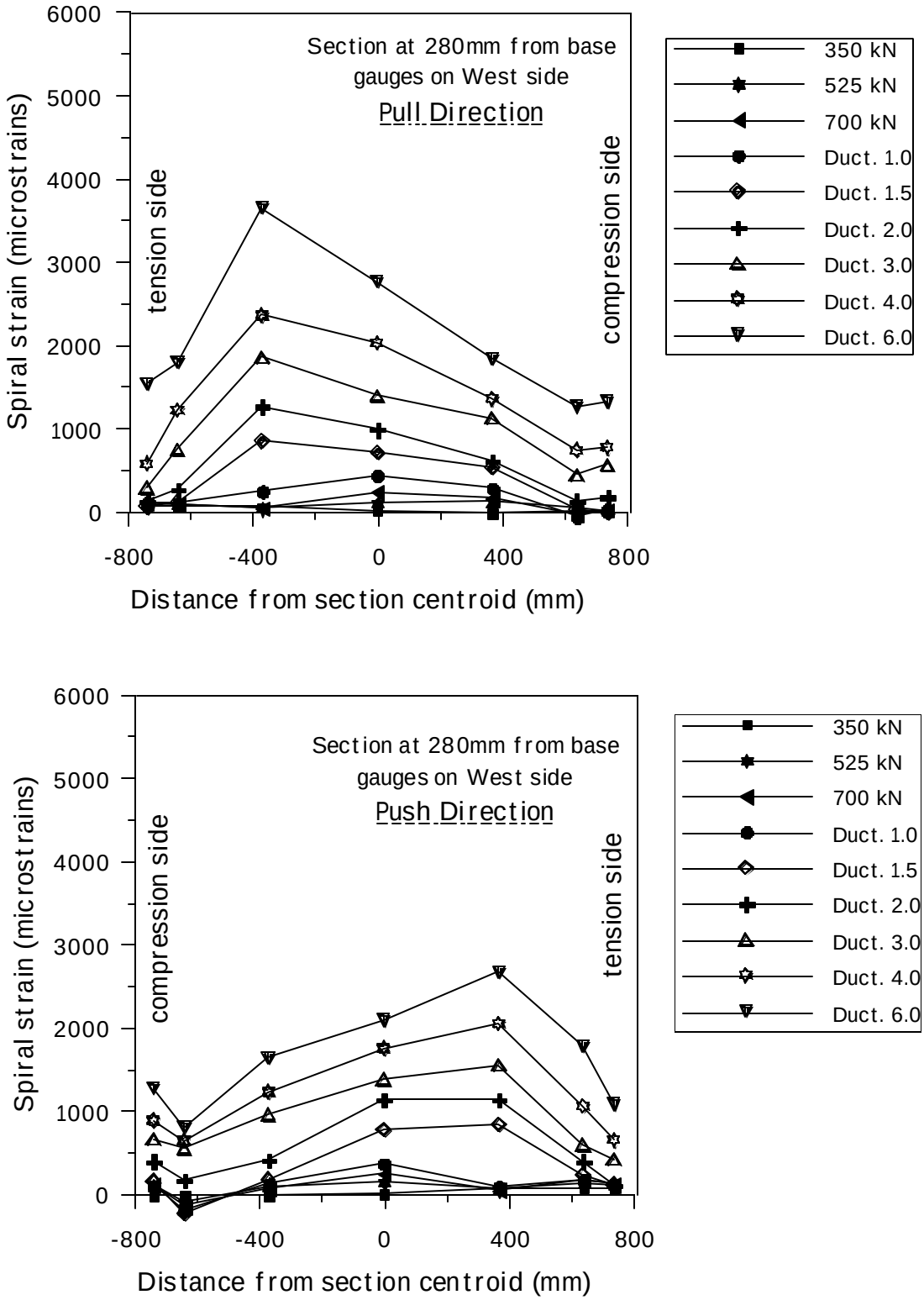

Figure 4.32 Unit HS1 Section Transverse Bar Strain Profiles 280 mm Above Base Section

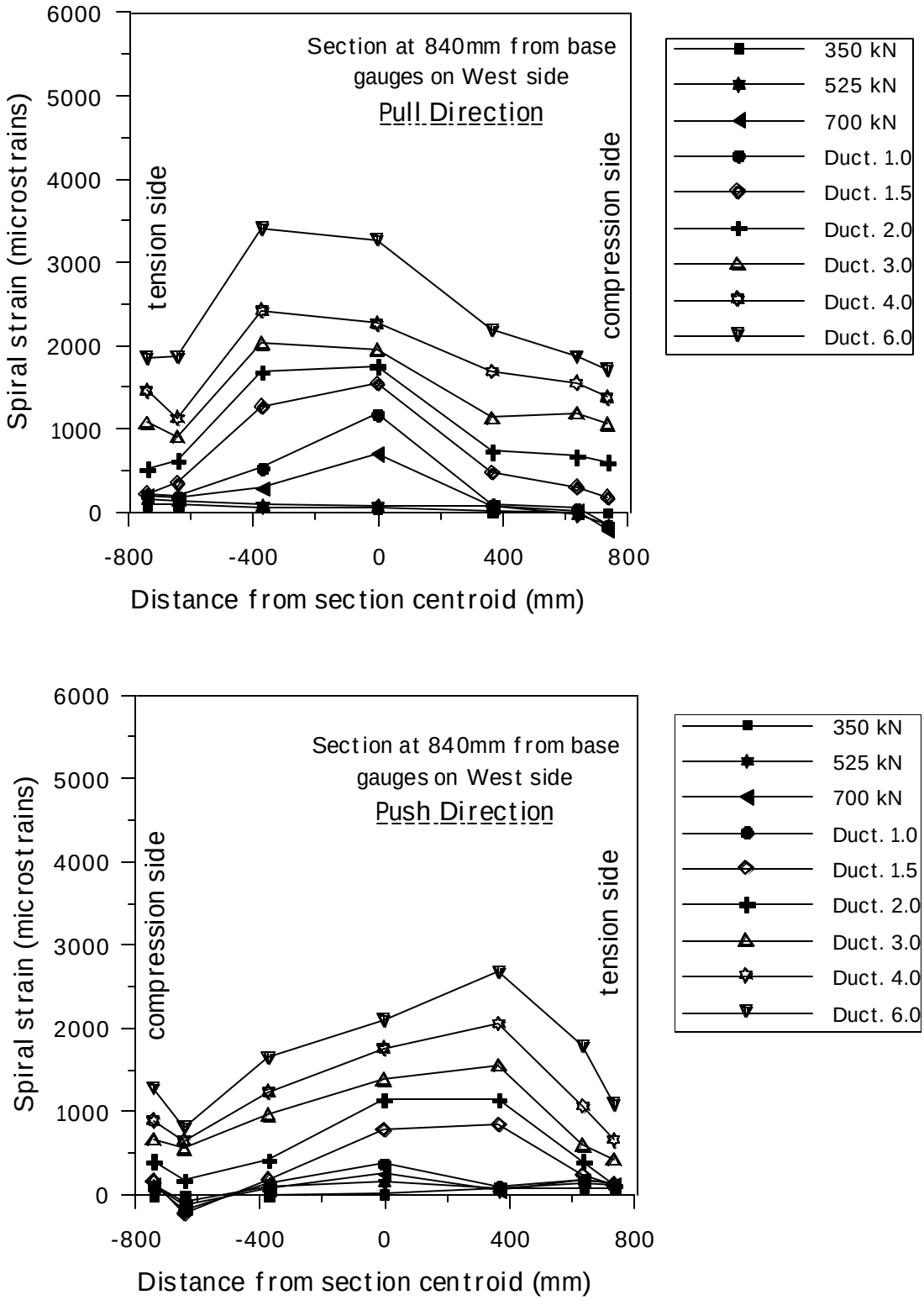

Figure 4.33 Unit HS1 Section Transverse Bar Strain Profiles 840 mm Above Base Section

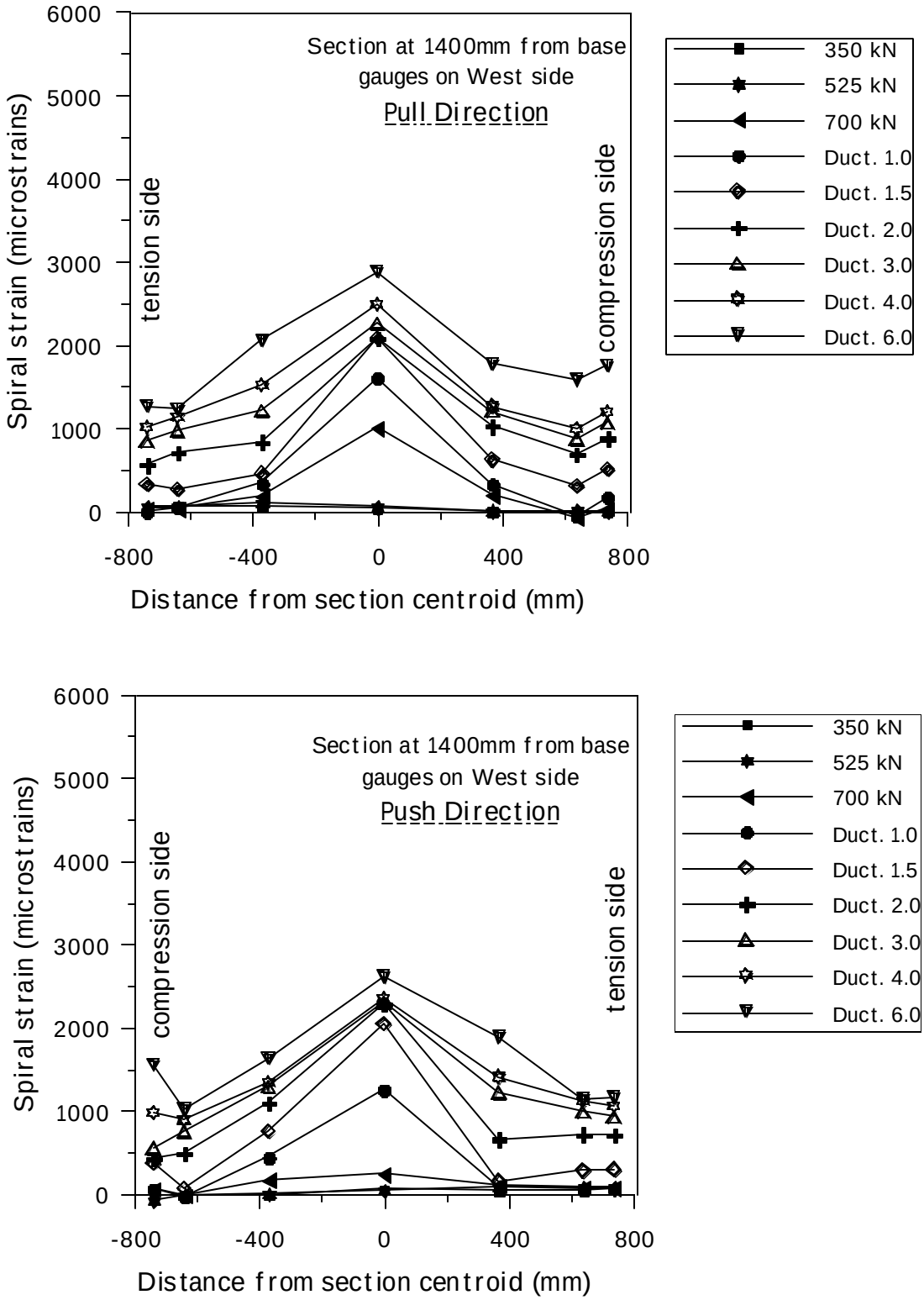

Figure 4.34 Unit HS1 Section Transverse Bar Strain Profiles 1400 mm Above Base Section

4.1.6 Discussion

The experimental evidence has been presented in the previous section. Unit HS1 performed satisfactorily, showing a desirable ductile performance. As predicted the failure has been of the flexural type. Nonetheless, shear deformations were large and found to be 25% of the total top displacement at failure. The combination of a low longitudinal reinforcement ratio (1.4%) and of a light axial load ratio (5%) generated a relatively low flexural capacity compared to the shear strength.

A key element in the analysis of the performance of the test unit is the behavior of concrete near the inside (unconfined) face. Flexural failure happened when significant spalling of concrete near the inside face occurred. At that stage a layer of probably 35-40mm of concrete was lost from the column wall (about 25% of the total wall thickness). Maximum recorded tensile strains in the longitudinal reinforcing bars were close to 2%.

In the flexural predictions it is assumed that a confining pressure of 800 kPa was mobilized from the beginning of the test. In fact, from the test results it is noted that the strain activation in any transverse steel did not occur before the 525 kN. This assumption would not change the behavior near failure because at that stage the strain in the transverse reinforcement was very close to that assumed. But, the estimate of 800 kPa is probably too high. If a lower value of the confining pressure is assumed, we would predict a lower concrete peak strain that would justify the observed concrete spalling at failure.

Another key element in flexure behavior at later stages of testing is the buckling of longitudinal rebars. There has been a lot of discussion on the requirement to be adopted for circular columns in order to avoid different buckling modes. It has been shown that in order to avoid buckling of longitudinal rebars between two adjacent layers of transverse reinforcement, the spacing (s) of hoops or spirals should be less than $6d_{bl}$, where d_{bl} is the diameter of the longitudinal bars.

This requirement was met since the 70 mm spacing used in the test unit was less than 6 bar diameters. The buckling mode that involves several layers (the type that happened during the test) does not usually appear when the M/VD ratio is less than 4.0. In our case though, in spite of a mere 2.5 value for that ratio, significant buckling occurred involving 4 to 5 different layers. It is believed that the recommendations given [Priestley et al, 1996] for flexural columns in plastic hinges should be extended to columns with lower shear span ratios. This was originally believed to be too onerous, but it will be confirmed by the second test unit, not even a spacing of 35 mm would be sufficient to avoid this buckling mode. Since the ratio of the spiral diameter to the longitudinal bar diameter was rather small (2.0) it is believed that the only way to provide effective restraint to buckling is to use high strength transverse reinforcement in the plastic hinge region. This is because the spacing of transverse steel cannot be further reduced in order to avoid reinforcement congestion.

As described in Section 4.1.1, particular attention was devoted to monitoring the behavior of the transverse steel within the first diameter above the column base. The reason is to possibly refine the ability to predict the strength of the transverse steel that contributes to shear resistance during the test. In Figure 4.35 and Figure 4.36 the strains recorded in three different locations (350, 838 and 1397 mm above the column base) along the west generator are plotted against the applied lateral displacement and force respectively.

As observing from Figure 4.35, the development of strains in the transverse steel has, in average, the trend that we had predicted with the two extreme assumptions of fully including and completely neglecting the effect of axial load. It is found for the same displacement level that larger strains occur in the section at 838 mm above the base than that in the section at 350 mm above the base. This is because of the restraint to shear deformations provided by the presence of the foundation footing. It is also noted that the behavior in the plastic hinge region is well captured by gauges at 350 mm above the base when the effect of axial load is accounted for.

Figure 4.36 shows that the strain activation in all three gauge locations occurrs at roughly the same level of lateral force, 600kN. This value is exactly between two extreme predictions. It can be concluded that a more accurate prediction of the shear behavior can be obtained by considering a somewhat reduced V_p component. For the time being, there is no enough information to recommend a correcting factor for that component, but it appears that 50% of V_p would probably lead to a more reasonable prediction. This consideration is supported by the fact that the arch mechanism developed due to the effect of axial load acts along curved struts. The efficiency of this mechanism in enhancing shear strength is therefore less significant than in the case of a solid core.

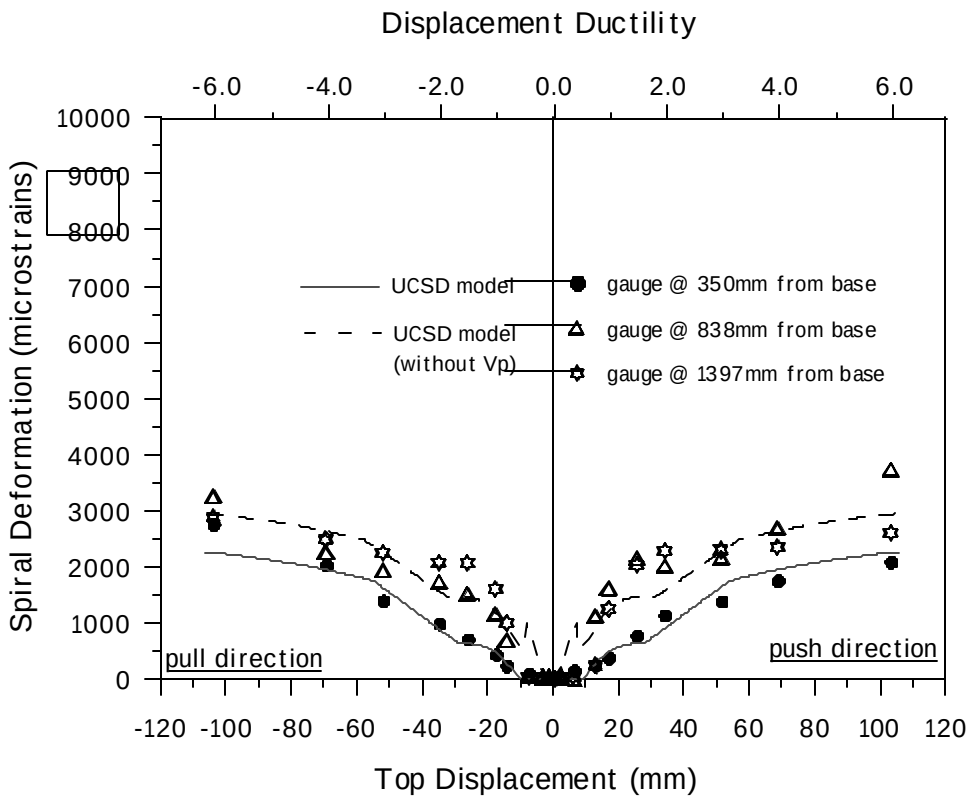

Figure 4.35 Unit HS1 Development of Spiral Strain with Increasing Top Displacement

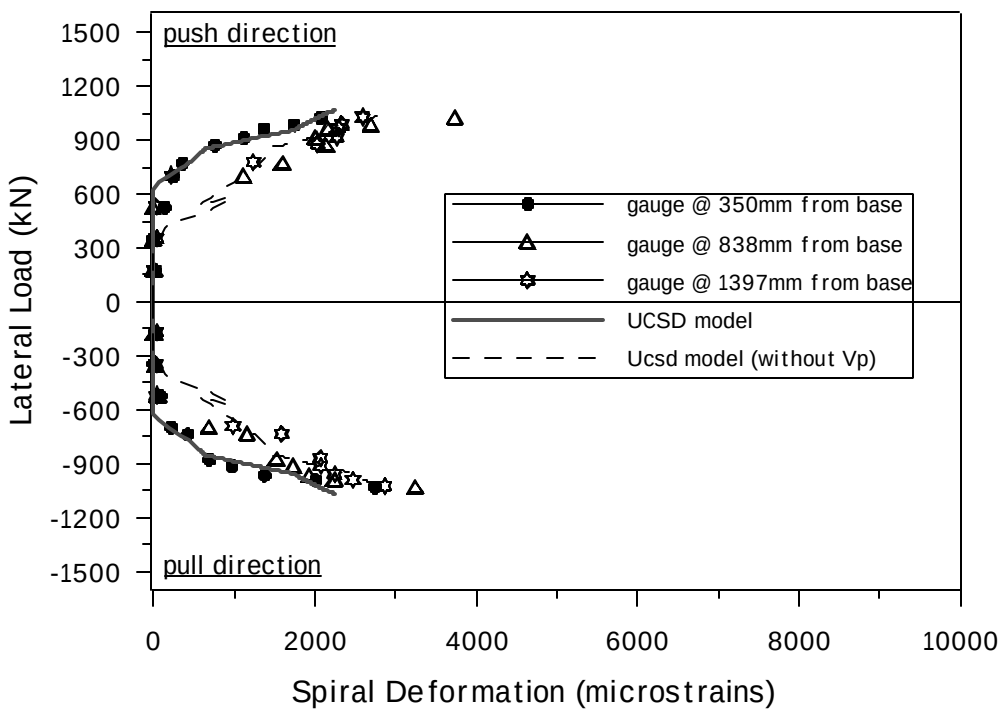

Figure 4.36 Unit HS1 Development of Spiral Strain with Increasing Lateral Load

4.2 Specimen HS2

This unit was designed to induce a shear failure. In fact, HS2 is characterized by the same geometry, the same amount of transverse reinforcement, and the same axial load ratio (5%) as unit HS1. The only difference is the amount of longitudinal reinforcement (2.3% instead of 1.4%). This difference essentially increases only the flexural capacity, while the shear strength remains almost the same. As a consequence, the column is significantly weaker in shear.

For a bridge pier with this ratio (2.5) of shear span to section diameter, a 2.3% longitudinal reinforcement represents probably upper limit for usual design practice. Shear will considerably govern the behavior of this unit, inducing large deformations in the transverse reinforcement.

4.2.1 Predicted Response

The response of the test unit was predicted both in terms of global force-displacement behavior and in terms of local flexural and shear behavior. The main results obtained from pre-test analysis are discussed in the following two sections. The same topic will be commented later during the discussion in order to verify our assumptions by comparing the predicted response with that observed during the test.

All predictions are monotonic and are intended to be representative of the envelope behavior under cyclic actions. Due to the brittle expected response, more refinement was required for the analysis of this test unit,. Particular attention has been devoted to the prediction of the behavior in shear. Analysis was conducted with simple shear strength models and with the Modified Compression Field Theory (denoted as MCFT throughout).

4.2.1.1 Force –Displacement Predicted Response

The predicted response of the column was obtained by using the procedures described in Section 2.2. A newer version of the UCSD shear model was also used for the shear strength prediction and more detailed analyses were conducted with the Modified Compression Field Theory. The force displacement relationships shown in Figure 4.37. were determined with two different methods:

(1) using the concept of equivalent plastic hinge length, where $L_p = 531$ mm

(2) using a pushover analysis conducted by subdividing the column in 5 portions and by computing shear and flexural deformations in each of these portions with the MCFT.

In the first case shear deformations are superposed to the flexural deformation calculated in the plastic hinge region, while in the second case, shear and flexure deformation are determined simultaneously along the member length. The second method also adopts more refinement in integrating curvatures along the column height. In spite of these two differences, the predicted force-displacement curves are very similar except for the estimate of the ultimate point. Refer to Section 2.2.3 for details.

In the graph, the predicted envelope behavior is terminated (for convenience) at a displacement of 120 mm, where the flexural analysis indicates that the strain in the tension reinforcement is 5.3% and that concrete in compression near the inside face is 0.375%. The ultimate point of the MCFT curve instead is located at a displacement of 68mm, where this model predicts a shear failure due to concrete crushing in diagonal compression.

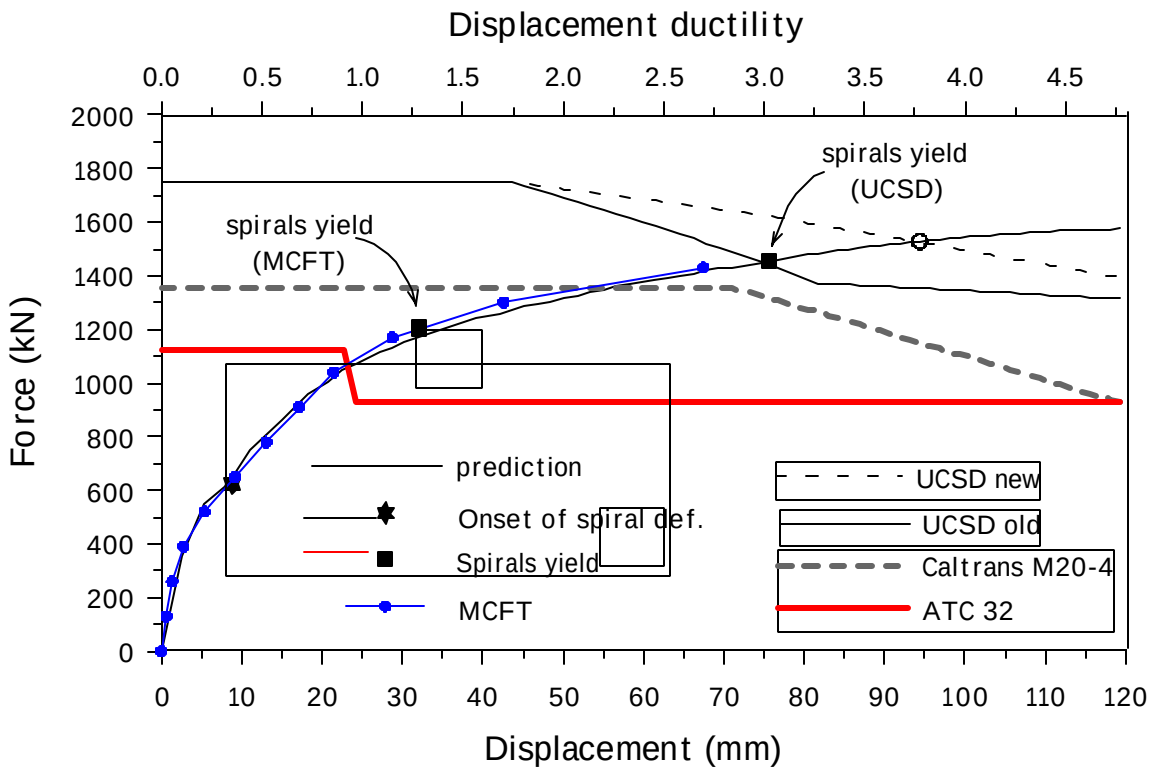

Figure 4.37 Unit HS2 Refined Force-Displacement Response Predictions

All the considered shear strength models predict a shear failure before the ultimate flexural capacity is reached. The same conservative assumptions used for HS1 in calculating the shear strength is also applied in this case. An angle of $q = 30°$ for the inclination of shear cracks was assumed and a yield stress of 635MPa was considered for the transverse reinforcement. Note that the predicted type of failure would not change if less conservative values are assumed for the angle q and for the yield stress of transverse steel. All models considered in this analysis would still predict a shear failure.

A large scatter in the expected failure point is observed among the considered models. While the model from ATC-32 predicts a shear failure within the elastic phase (at displacement ductility 0.8), the Caltrans MEMO 20-4 model indicates that the shear failure will occur at ductility 2.0. The UCSD models (older and newer version) predict a shear failure between ductility 3.0 and 3.75. Note that in this case the V_p component is 203 kN, which is a little less than what it was in HS1 due to the different position of the neutral axis. If this component is neglected, the predicted failure would be between

ductility 2.3 and 2.8. As discussed in Section 4.1.1.1, the shear strength curve with V_p=0 can be obtained by shifting down the curve of Figure 4.37 by 203 kN, because the axial load component is independent on the level of applied displacement. A better understanding of the predicted behavior is obtained by analyzing the development of strains in the transverse reinforcement. Two characteristic points are indicated along the predicted force-displacement curves in Figure 4.37. The first point corresponds to the strain activation in the transverse reinforcement (onset of spiral deformation). The second point indicates that the steel starts to yield. Note that the predicted strain activation points based on UCSD and MCFT models coincide, while there is a substantial difference in the estimate of the yield point. The behavior of the transverse steel is particularly important in this unit because it strongly influences the mechanism that induces the column failure. The behavior will be analyzed in more detail in Section 4.2.1.2. The main results of predicted strengths and deformation capacities are summarized in Table 4.3. The flexural properties determined based on the moment-curvature analysis at the base section are summarized in Table 4.4.

Table 4.3 Unit HS2 Predicted Failure Loads and Displacements

Model	**V at failure (kN)**	**D at failure (mm)**	**Type of failure**
UCSD-1*	1440	76	Shear
UCSD-1 (without V_p)	1380	64	Shear
UCSD-2*	1525	94	Shear
UCSD-2 (without V_p)	1410	73	Shear
ATC-32	1000	22	Shear
Caltrans MEMO 20-4	1350	57	Shear

***UCSD-1=**UCSD traditional model, **UCSD-2**=UCSD newer model

Table 4.4 Unit HS2 Moment-Curvature Limit States

Test stage	Moment (kNm)	Curv. (1/km)	C (mm)	e_{if} (%)
Cracking	1670	0.431	795	-0.03
First yield	3570	2.37	417	-0.06
Nominal strength	5100	-	-	-
Ultimate strength	6130	48.7	235	-0.47

The flexural analysis indicates that the test unit has a considerably higher compression depth due to the higher amount of the longitudinal reinforcement. At theoretical flexural failure the compressive depth is 235 mm compared to 139 mm of wall thickness. In fact this condition should never occur, because it is expected that a shear failure would occur before the ultimate flexural capacity is reached. However, keep in mind that high compressive strains near the inside face might anticipate the concrete spalling. As we observed from the first test unit, this phenomenon was underestimated from the moment-curvature analysis, but it was determinant for the overall behavior and for the column failure. At the expected failure point according to the UCSD traditional shear model, concrete compressive strain near the inside face should be close to 0.2%.

Concrete properties were determined based on the Mander model, assuming a confining pressure of 800kPa. This value seemed to be a little high for the previous test unit, but it would probably be more accurate here, where larger strains are expected to occur in the transverse steel since early stages of testing. Cracking was estimated by assuming a concrete tensile strength equal to $0.5\sqrt{f_c^{'}}(\mathrm{MP_a})$.

4.2.1.2 Shear Behavior

The shear behavior of this unit is particularly relevant in predicting the global response. The degradation of the shear strength cause inelastic strains to occur in the transverse reinforcement and consequently shear deformations will be more significant than in the previous unit. It is therefore interesting in this case to analyze the development of strains in the transverse reinforcement as a function of the applied load or displacement. Note that by using the procedures described in Section 2.2.2 to derive the lateral strains from the available shear strength, an equivalent bilinear stress-strain relationship for the transverse steel needs to be assumed. With this assumption it will be possible to evaluate the average transverse steel strains for stress values greater than the assumed yield stress. Referring to the steel properties found in Section Table 3.2, the parameters E_s, E_{sh}, and f_y are the elastic modulus (165 GPa), strain-hardening modulus (8.6 GPa), and the assumed yield stress (635 MPa).

Based on the bilinear approximation for the transverse steel behavior, lateral strains can be calculated by using the UCSD traditional model, up to the ultimate flexural point. Given the nature of the three-component model, it is obtained that the shear failure point corresponds to yielding of transverse steel. However, it is interesting to see what happens to lateral strains when the shear strength is less than the flexural capacity. Strains will obviously increase rapidly after the yield point is reached. It is interesting to know how much additional force or displacement is needed to rupture the transverse steel. From material testing it is observed that the rupture strain can be as low as 1%.

Predictions were conducted (as for HS1) by using the UCSD traditional model with and without the V_p component. The development of lateral strains is analyzed again both as a function of the applied lateral displacement and as a function of the lateral load. Figure 4.38 shows that yielding of transverse steel occurs between ductility 2.5 and 3.0, while rupture should occur instead between ductility 3.0 and 4.0 (the lowest value corresponding to the absence of the V_p component). Figure 4.39 shows that once the yield stress is reached, it takes almost zero additional lateral force to rupture the

transverse steel. This is because of the low strain hardening properties of this particular type of steel.

The strain activation in the transverse reinforcement should occur between 550 kN and 750kN, depending on the effect of the axial load component V_p. We appreciate that the option of fully including or totally neglecting the V_p component has a significant influence on the strain activation load, while it has less influence on the load at which rupture of transverse steel will occur.

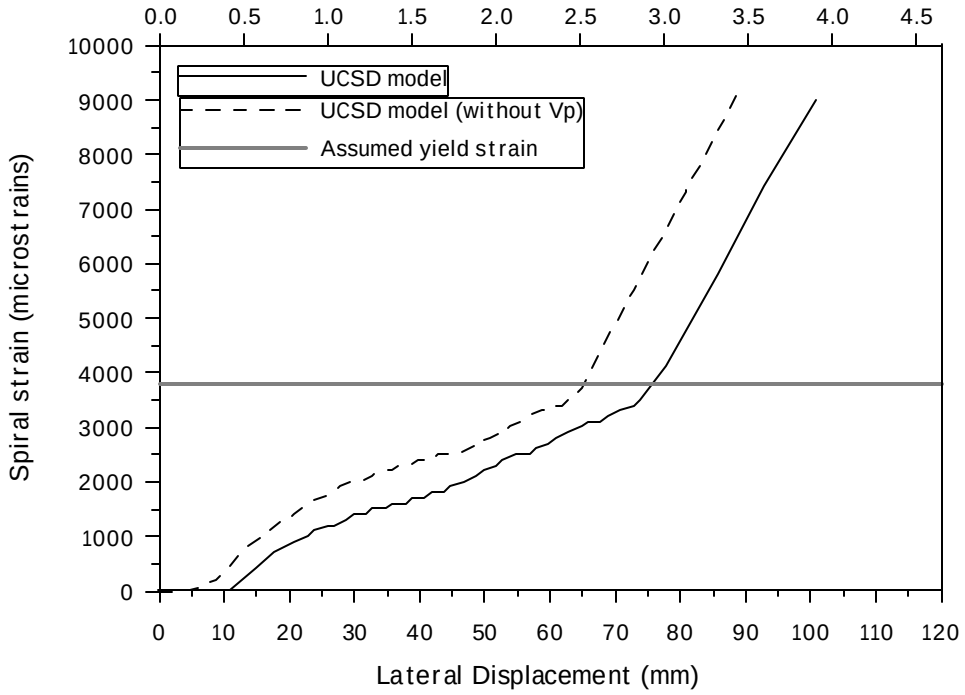

Figure 4.38 Unit HS2 Predicted Displacement/Spiral Strain Relationship

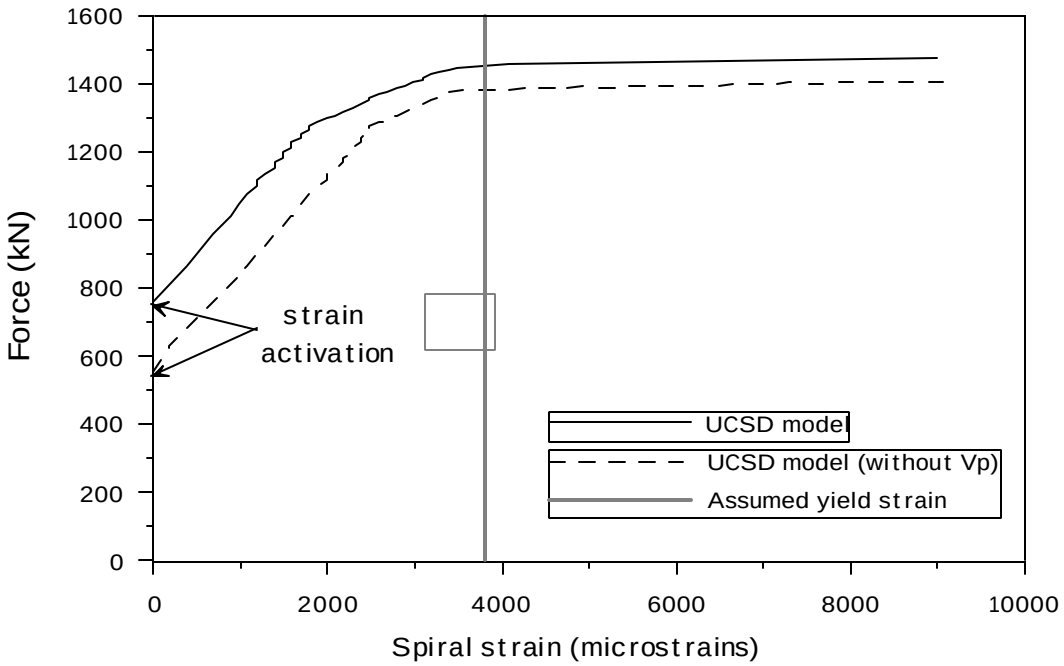

Figure 4.39 Unit HS2 Predicted Force/Spiral Strain Relationship

4.2.2 General Observations

The test was conducted with the same procedures used for unit HS1. The damage was monitored according to the methods described in Section 4.1.1. The behavior of the column in the inside face was monitored by using the same system used for testing HS1.

4.2.2.1 Elastic Cycles

Elastic cycles were conducted in load control by monitoring the force applied in the two hydraulic actuators. The applied force was exactly the same in the two actuators throughout the elastic cycles.

The axial load was applied by acting on the oil jacks as described in Section 3.5. The target load was reached by reading the force value indicated from each of two load cells. At the beginning of the test, when no lateral action was applied, the values of these forces were 616 kN in the east bar and 602 kN in the west bar. The total axial load on the column was therefore 1218 kN. The application of the axial load did not induce any cracking in the test unit. The value of the applied axial load was monitored throughout the test and it was found that it varied slightly during the application of lateral actions. The maximum value recorded during the test was 1276 kN (corresponding to an increase of 5% in axial compression) while the minimum recorded value was 1160 kN (corresponding to a decrease of 3% in axial compression). Details of this aspect will be given in Section 4.2.3.3.

± **225kN cycles** (25% of theoretical first yield)

At this stage no cracks were visible on either sides of the test unit, as predicted by the analysis.

± **450kN cycles** (50% of theoretical first yield)

Flexural cracking occurred with a spacing of approximately 150-160 mm up to 550 mm above the column base. No cracks were visible in the inside face of the column. Concrete cracking was expected at 430 kN, exactly when it occurred. This confirms that the estimate made for the concrete tensile strength was accurate $\left(f_t = 0.5\sqrt{f_c^{'}}\right)$.

± **675kN cycles** (75% of theoretical first yield)

More flexural cracking appeared above the existing flexural cracks. The width of these cracks was estimated to be 0.1mm in average. Strains in the longitudinal reinforcement were ranging 1300-1400 με. Some flexural cracks near the column base were also visible from the inside of the column. Shear cracking occurred up to 2100 mm above the base. These cracks shown in Figure 4.40 had almost the same inclination in this region (about 50 degrees from a vertical axis along the east and west generators).

± **900kN cycles** (theoretical first yield)

At this stage more flexural cracking was observed in the upper part of the column and more shear cracks formed. The average width of shear cracks along the east and west generators was 0.25 mm. The angle of inclination of diagonal cracks reached a minimum of 35 degrees in the upper part of the column. The test unit was cracked up to two diameters above the base. A similar crack pattern was observed from the inside of the column, indicating that the wall was completely cracked. The tensile strain in the longitudinal reinforcement at column base was 0.22% in average.

The top lateral displacement reached at this load stage was used to define the target yield displacement (corresponding to ductility 1.0). The average recorded displacement in the push and pull direction was taken and the displacement at ductility 1.0 was defined as:

$$D_y = \left(\frac{17.16 + 16.81}{2}\right)\left(\frac{1315}{900}\right) = 25.78mm \qquad (4.3)$$

where 1315 kN and 900 kN were the theoretical nominal flexural strength and first yield flexural strength respectively. The behavior showed to be remarkably symmetric, indicating that no major lacks of symmetry were introduced during construction due to inevitable inaccuracies.

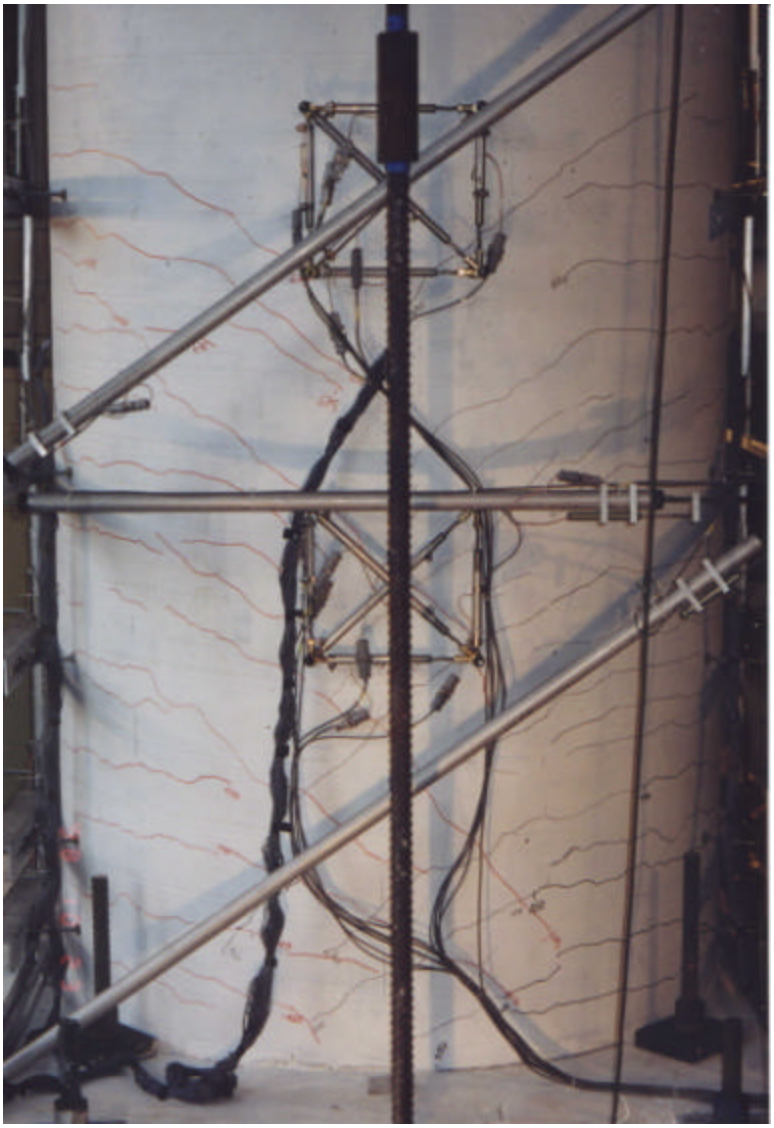

Figure 4.40 Unit HS2 Crack Pattern at 75% of First Yield (Side View)

4.2.2.2 Inelastic Cycles

Inelastic cycles were conducted in displacement control, but only one of the actuators was used in displacement control, while the other one was constrained to apply exactly the same lateral force.

m_D=1.0 (3 cycles, drift=0.66%)

During the cycles at ductility 1.0 new shear cracks formed in the upper part of the column and existing ones increased in width up to 0.55-0.65 mm (Figure 4.41). Transverse steel reached an average strain of 0.25% in the first cycle and 0.32% at the end of the third cycle (note that material testing revealed an average yield strain of 0.38%). As expected, transverse steel remained within the elastic range at this stage. In the inside face some flakes were visible along major shear cracks.

m_D=1.5 (3 cycles, drift=1.0%)

Longitudinal bars at the column base reached a strain of 1% in tension and 0.2% in compression. Moderate signs of incipient concrete spalling were visible on the outside compression region. Flexural cracks increased in with up to 0.7 mm. No signs of incipient spalling were visible from the inside. Shear cracks increased in width up to 0.7 mm. Several flakes were observed in the inside face along several shear cracks. Spiral reinforcement reached a peak strain of 4000 $\mu\varepsilon$, indicating that the estimate of the yield point made with the UCSD models was a little unconservative.

m_D=2.0 (3 cycles, drift=1.33%)

Concrete spalling occurred in the outside face (Figure 4.42) but no significant rebar buckling was observed. Strength degradation among the three cycles was limited to less than 10%. Strain in the transverse reinforcement reached a peak of 5300 $\mu\varepsilon$. At the column base, longitudinal strains in the vertical bars reached 1.4% in tension and 0.53% in compression, indicating a compression depth of at least 400mm.

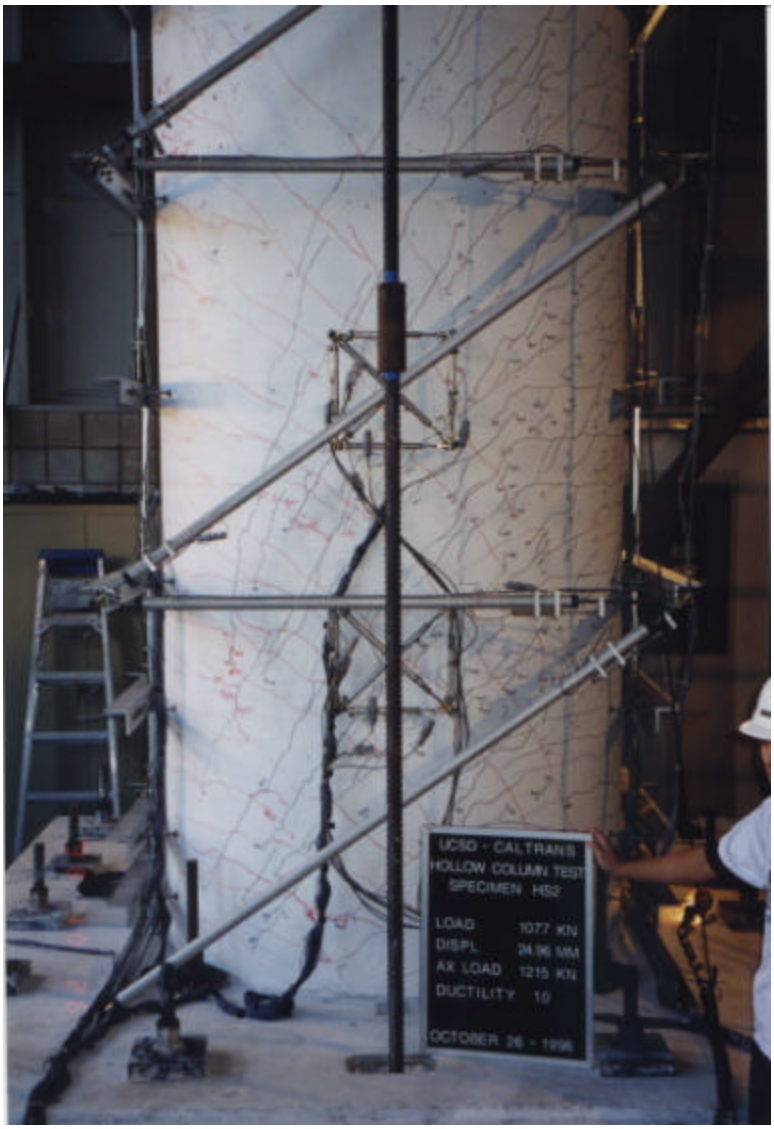

Figure 4.41 Unit HS2 Crack Pattern at Ductility 1 (Side View)

m_D=3.0 (2 cycles, drift=2.0%)

While approaching the target displacement at ductility 3.0 major spalling of concrete in compression occurred in the inside face) at a height of approximately 400 mm from base (Figure 4.42). This caused a sudden drop in the applied lateral force of about 25%. Shear cracks reached an average width of 0.9mm inducing a deformation in the transverse steel of 0.7%. More spalling was also visible from the outside.

The subsequent cycle at ductility 3.0 caused longitudinal rebar buckling in the base region, where a reduced spacing of transverse reinforcement (35mm) had been adopted to prevent it. It has to be noted that rupture of transverse steel in the compression region (see Figure 4.44) did not occur exactly in the North and South direction, but in a location about 30 degrees away from it (symmetrically on both sides). This was probably due to the presence of large and steep inclined compressive concrete struts for shear. The same compressive struts are clearly visible from the inside shown in Figure 4.43.

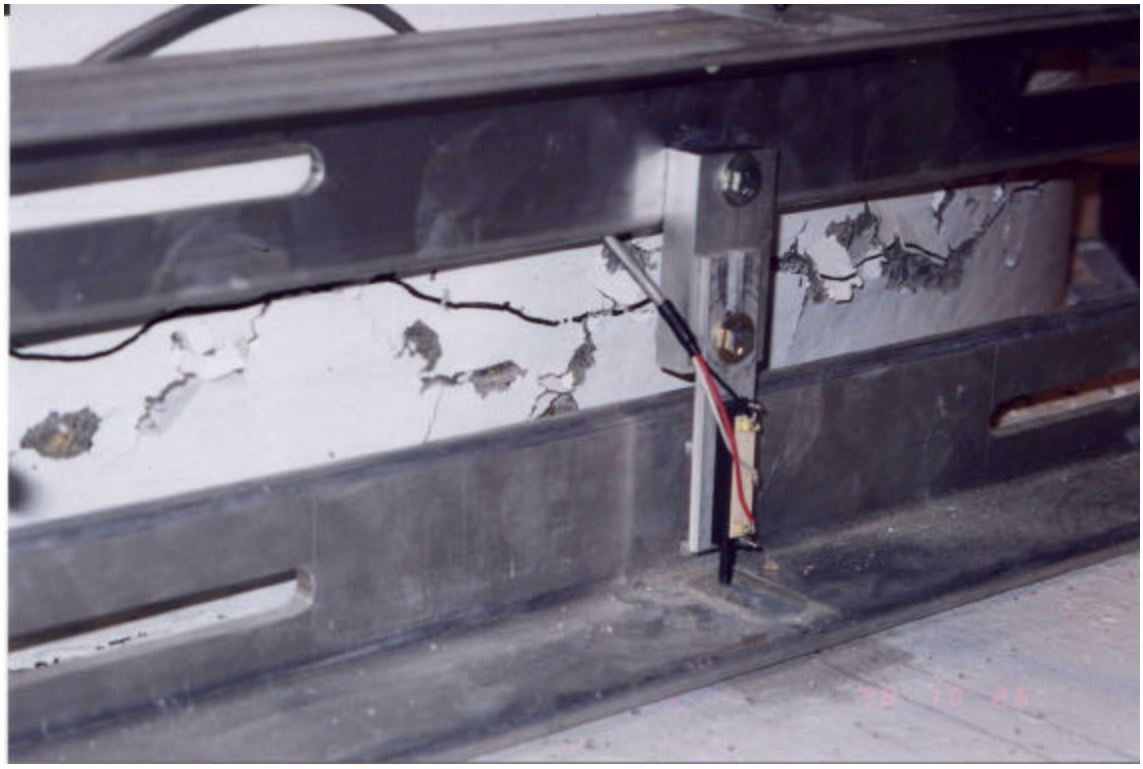

Figure 4.42 Unit HS2 Concrete Spalling on Compression Zone, Outside Surface at μ_Δ = 2.0

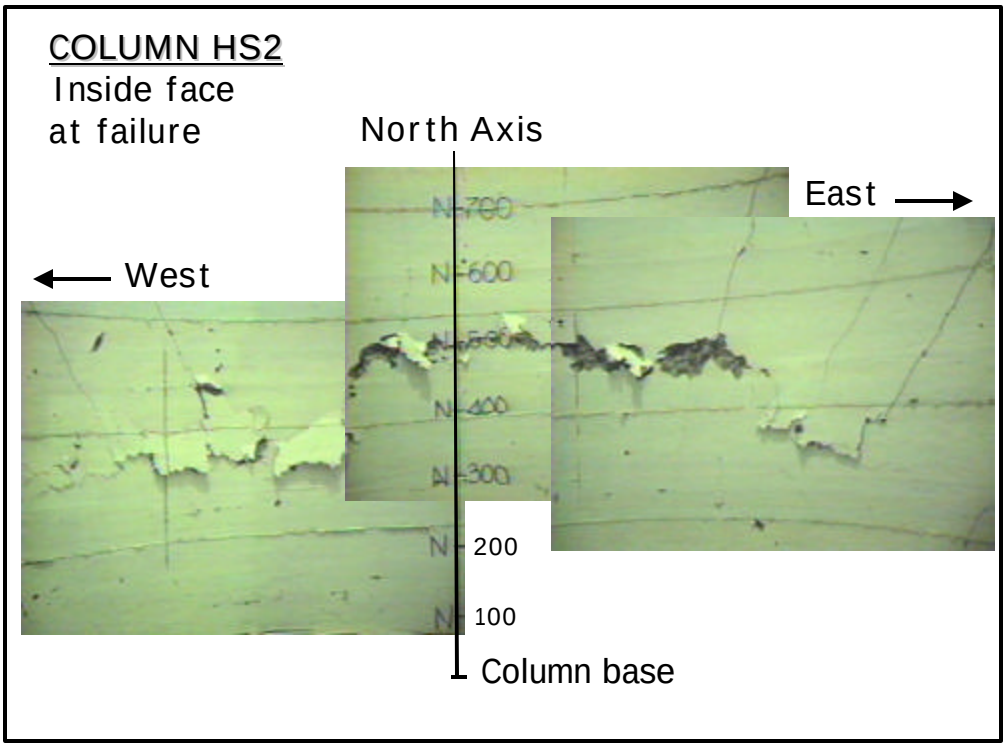

Figure 4.43 Unit HS2 Spalling of Inside Surface of Compression Zone at $\mu_? = 3.0$, First Cycle

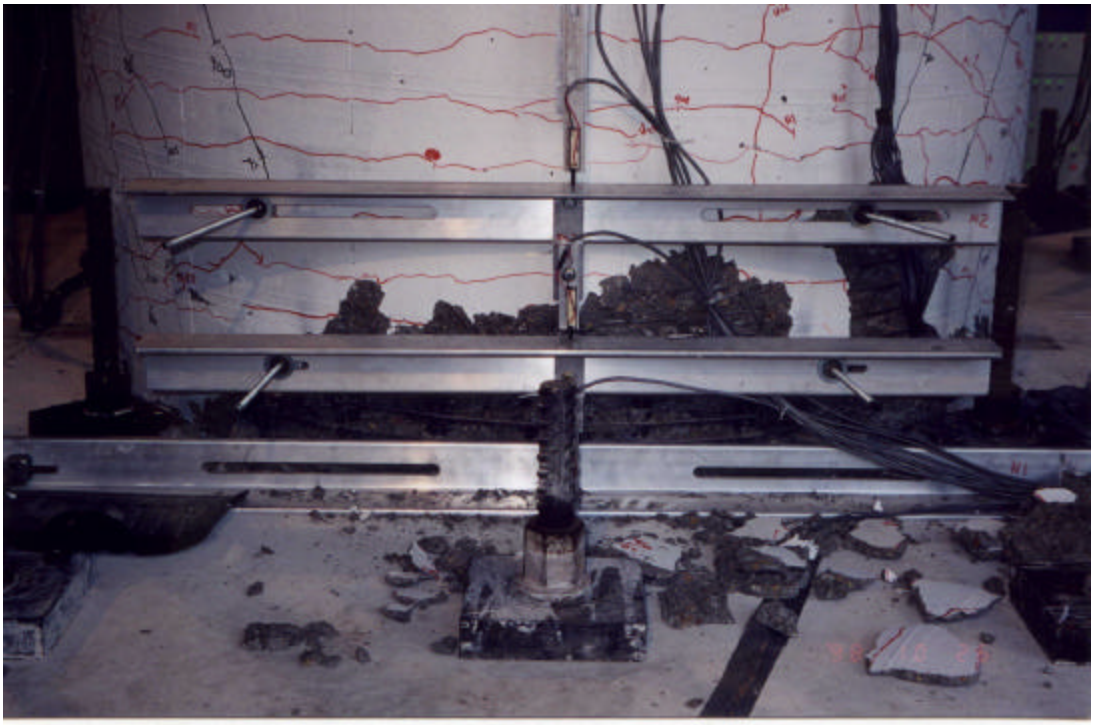

Figure 4.44 Unit HS2 Spalling and Crusing of Compression Zone, and Rebar Buckling, at $\mu_? = 3.0$, Second Cycle

m_D=3.5 (1 cycle in the pull direction, drift=2.33%)

Since a substantial loss in strength was already obtained in the push direction after two cycles at ductility 3.0, it was decided to proceed towards ductility 4.0 in the pull direction. A major shear failure occurred at ductility 3.5 with a large shear crack inclined at 35-40 degrees forming in the east side of the column from the base to a height of approximately 1000 mm (see Figure 4.45). Transverse steel fractured all along the crack and a considerable sliding (about 15 mm) of the two faces of the crack was observed. Longitudinal bars were also significantly deformed along the crack. Considerable buckling of longitudinal bars was observed, involving 5-7 layers of transverse steel (see Figure 4.46). Rupture of transverse steel was observed in two layers. The test was brought to completion by moving back to zero displacement and by removing the axial load.

Figure 4.45 Unit HS2 Shear Failure, with Spiral Fracture, at $\mu_?$ = 3.5

Figure 4.46 Unit HS2 Buckling of Longitudinal Bars and Fracture of Spirals in Compression Zone at $\mu_? = 3.5$

4.2.3 Hysteretic Response

4.2.3.1 Force-Displacement

The force-displacement hysteresis curve was obtained by plotting the total applied lateral force as a function of the lateral displacement measured at the column top. This curve is shown in Figure 4.47. The scale of the experimental displacement ductility is indicated in the top horizontal axis. The predicted envelope behavior and failure points are also indicated in the same graph. The different failure points refer to the UCSD shear models and to the Modified Compression Field Theory. During the inelastic phase it can be noted that repeated cycles at the same ductility level did not induce significant strength degradation before ductility 3.0. In fact, before ductility 3.0, strength degradation caused by repeated reverse cycling did not exceed 10%.

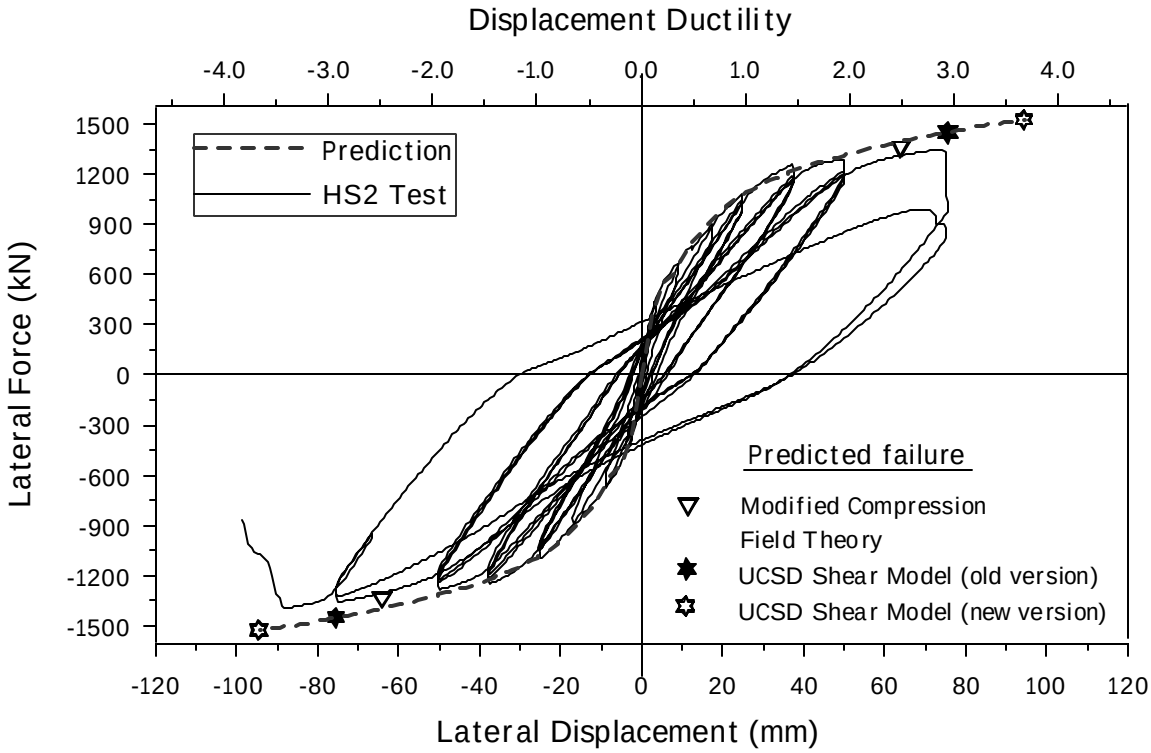

Figure 4.47 Unit HS2 Compression of Theoretical and Experimental Force-Displacement Response

As is often the case with shear failures, the behavior was not symmetric. Concrete spalling in the inside face occurred only in the push direction and a corresponding loss in strength of 25% was observed. In the pull direction instead, significant strength degradation was not reached until failure in shear at ductility 3.5.

The behavior at failure matched well the predicted one. According to the UCSD traditional shear model, the rupture of the transverse steel between ductility 3.0 and 4.0 was expected. This is in fact what happened during the test. The aspect will be analyzed in more detail during the discussion.

4.2.3.2 Moment-Curvature

Curvatures were measured along the column height by means of eight curvature cells (one additional curvature cell was mounted at column base). This modification was made after unit HS1 was tested, when it was recognized that for an accurate measurement of

the base curvature it was more convenient to decrease as much as possible the height of the first two curvature cells. The reading from the first curvature cell should therefore represent with more accuracy the behavior of the column base.

The base curvature is plotted in Figure 4.48 as a function of the base moment. In computing the base curvature the effect of strain penetration was taken into account. Note that in this case the revised cell height differs substantially from the original value. This aspect will be described in more detail in the following Section 4.2.5.2. In Figure 4.48 the experimental moment-curvature response is compared with the predicted one. The ultimate points corresponding to the shear failures predicted by the UCSD models are also indicated in the graph. The top horizontal axis indicates the curvature ductilities as identified from the experimental results. For each peak during the inelastic phase, the displacement ductility is also indicated near the peak with a label.

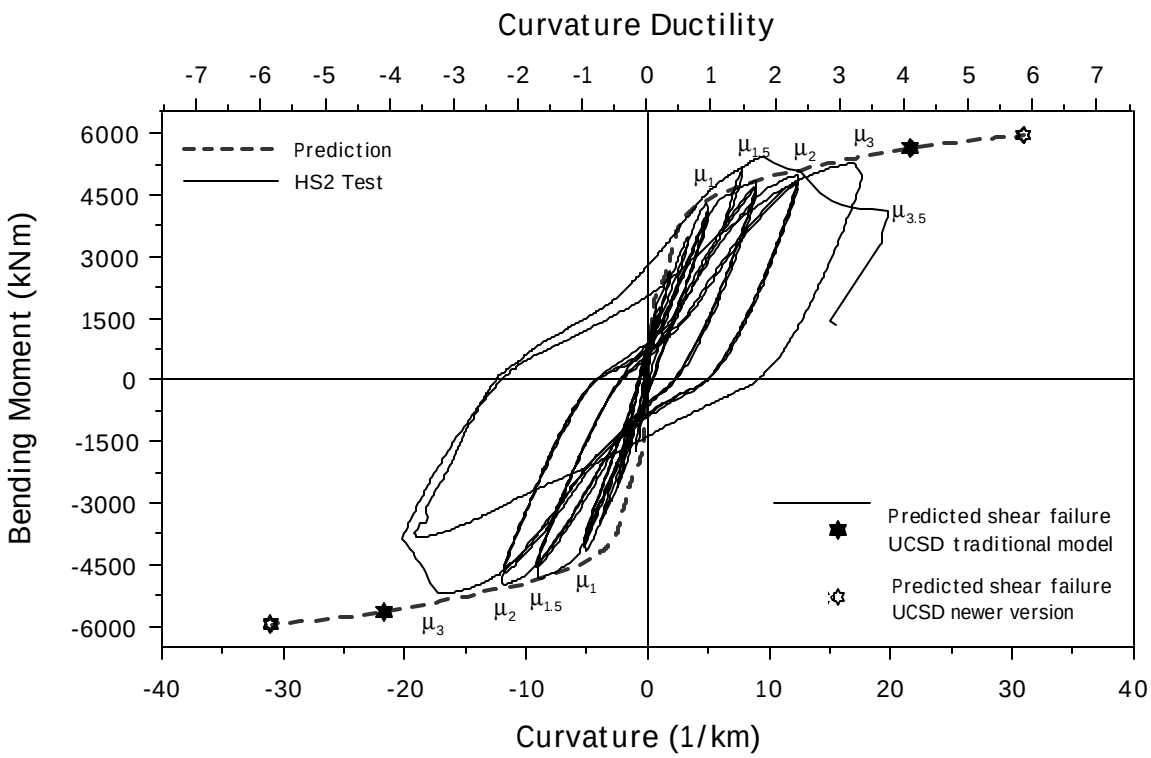

Figure 4.48 Unit HS2 Base Moment/Curvature Experimental Response

From the graph of Figure 4.48 it is evident the effect of shear cracks on the shape of the cycles after ductility 1.5. A low stiffness near the origin is due to the presence of a considerable width of the shear cracks. During the reloading phase, shear cannot be transferred across the cracks and consequently the average stiffness is very low.

4.2.3.3 Axial-Load

Figure 4.49 shows the variation of the axial load during the test as a function of the applied lateral displacement. The normalized axial load $\left(P/f_c^{'}A_g\right)$ is indicated on the vertical axis on the right side of the graph. In comparison to the previous test unit, it is observed that there is a less significant oscillation in axial force for the same level of the applied lateral displacement. This fact is probably due to the higher axial stiffness resulting from a higher level of longitudinal reinforcement.

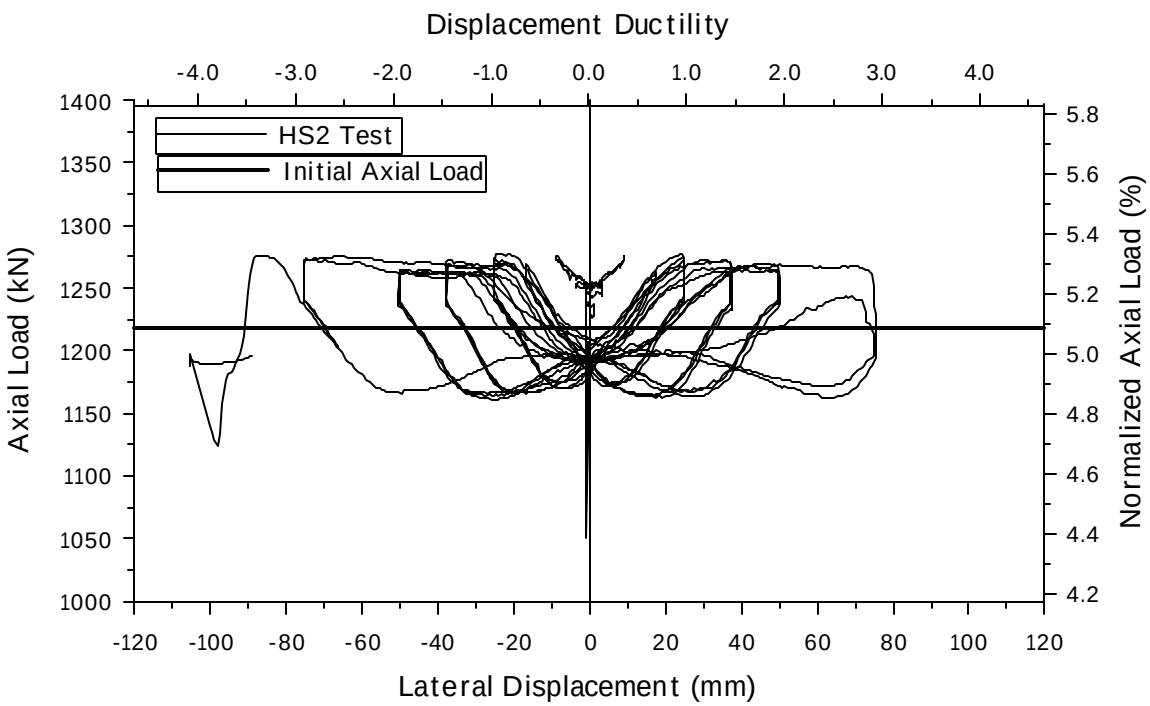

Figure 4.49 Unit HS2 Lateral Displacement/Axial Load Relationship

4.2.3.4 Shear Deformation

The shear behavior was monitored by the shear deformation panels mounted on the east and west sides of the column. Each shear deformation panel was divided into three blocks and the results from each of the three blocks are plotted in Figure 4.50. In the graphs, the peak values are identified with a black dot and the corresponding displacement ductility level is indicated with a label. Note that the average moment to shear ratio is 3.3 in the bottom panel, 2.12 in the middle panel and 0.93 in the top panel. Refer to the considerations given in Section 3.2 for the meaning of the measured deformations in reading the results from the graphs. Also note that in the bottom panel the change in length of the vertical sides was measured by means of 4 displacement transducers instead of 3.

In general it is observed that large shear deformations occur only in the base region just as the test unit HS1. Note that the amount of the shear deformation is about the same as it was in unit HS1 for the same level of applied lateral displacement. Due to the different flexural properties, the displacement ductility is quite different, but the amount of shear deformation corresponding to a given drift ratio is about the same in the two test units. It is therefore concluded that for the same level of flexural damage this unit undergoes larger shear deformations than unit HS1.

It is observed that the considerable opening of shear cracks at later stages of testing (up to 0.85mm) caused a remarkable loss of shear stiffness in the reloading phases. This is paticularly evident in the bottom region. It is also evident the lack of symmetry in the behavior. While the shear deformation at ductility 3.0 in the first peak in the push direction was 9mm/m, in the first peak in the pull direction was 12mm/m.

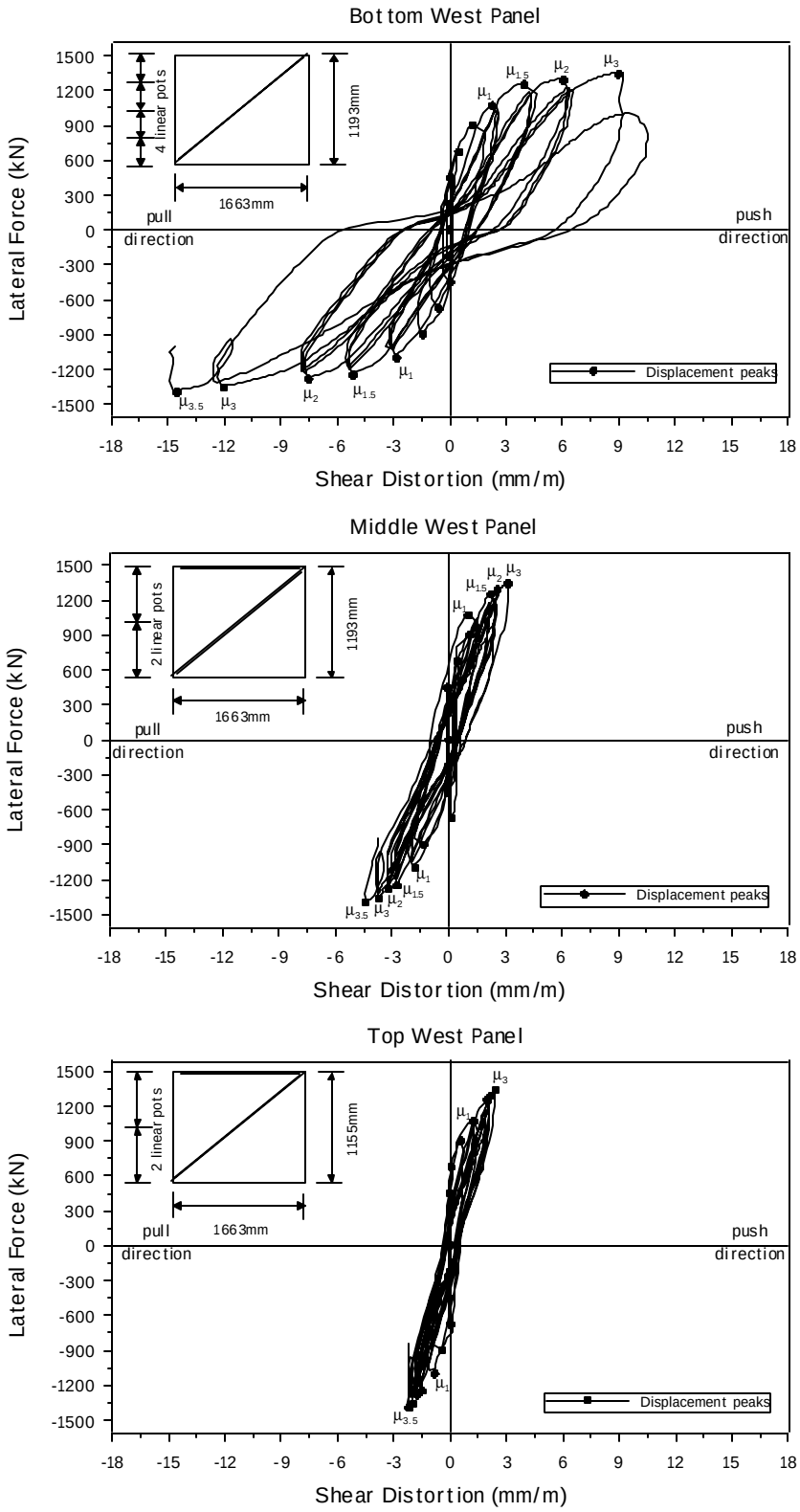

Figure 4.50 Unit HS2 Lateral Force/Shear Distortion from Gross Column Measurements

The shear behavior was also monitored locally by means of four small shear deformation panels, mounted along the east and west generators. Two panels were mounted on each side of the column in two strategic locations, considered to be good points where to monitor the shear deformations. It is observed from the previous unit (HS1) that the shear behavior in region within the first 500mm above the column base was significantly altered by the confining effect provided by the foundation footing. It is noted that the shear critical region (as identified from the crack pattern and from the readings on the gauges mounted on the spiral along the east and west generators) happened to be within 0.5 and 1.5 diameters above the column base. It was therefore decided to analyze the shear behavior of this region in more detail, by subdividing it in two parts and by mounting a small deformation panel at mid-height of each of these two portions. This feature should help in analyzing the way the shear behavior changes in the shear critical region as the moment to shear ratio varies.

For practical reasons the panels were mounted only approximately at the locations indicated above. The bottom panel was located at 1016 mm above the base (where the moment to shear ratio is 2.86 m) and the top panel was mounted at 1778 mm (where the moment to shear ratio was 2.1 m). Analysis of these two sections under the mentioned moment to shear ratios was conducted with the Modified Compression Field Theory using the program Response 2000. It was found that a shear failure was expected to occur near the bottom panel. Shear force-shear strain curves obtained from the readings of the instruments are compared in Figure 4.51 and Figure 4.52 with the predictions obtained using the Modified Compression Field Theory (denoted as MCFT).

The ultimate shear deformation was underestimated in the bottom portion, but the envelope behavior was well captured. The analysis indicated that failure would have occurred in the region near the bottom panel due to concrete crushing in diagonal compression. It is believed that this expected failure mode coincided with the first substantial loss of the strength observed at ductility 3.0 when concrete spalled in the inside face. The sharp sloping of the inclined compressive struts brought the concrete crushing further down towards 600 mm above the base.

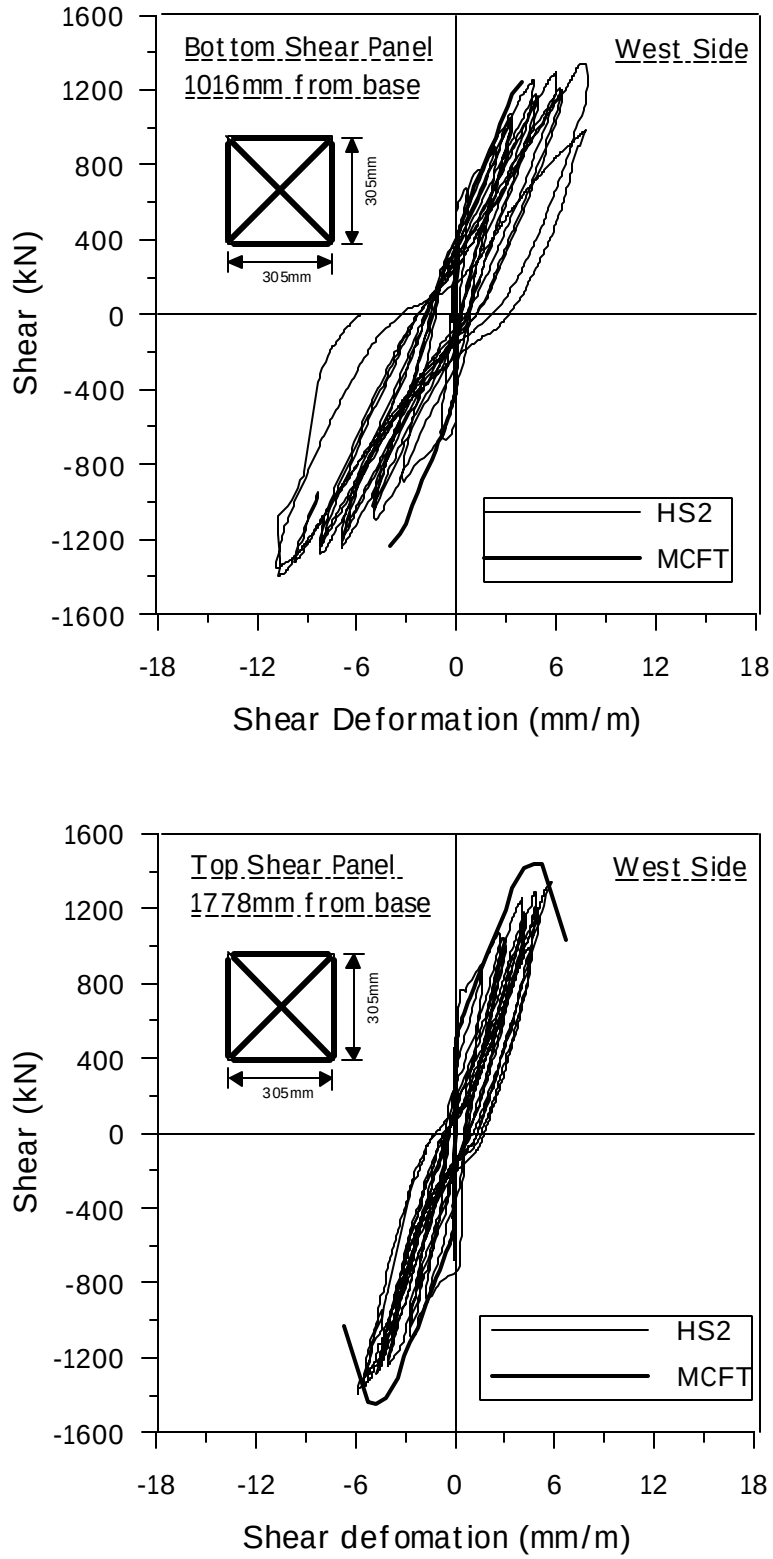

Figure 4.51 HS2 Lateral Force/Shear Strain from Small Shear Panels (West Side of Column)

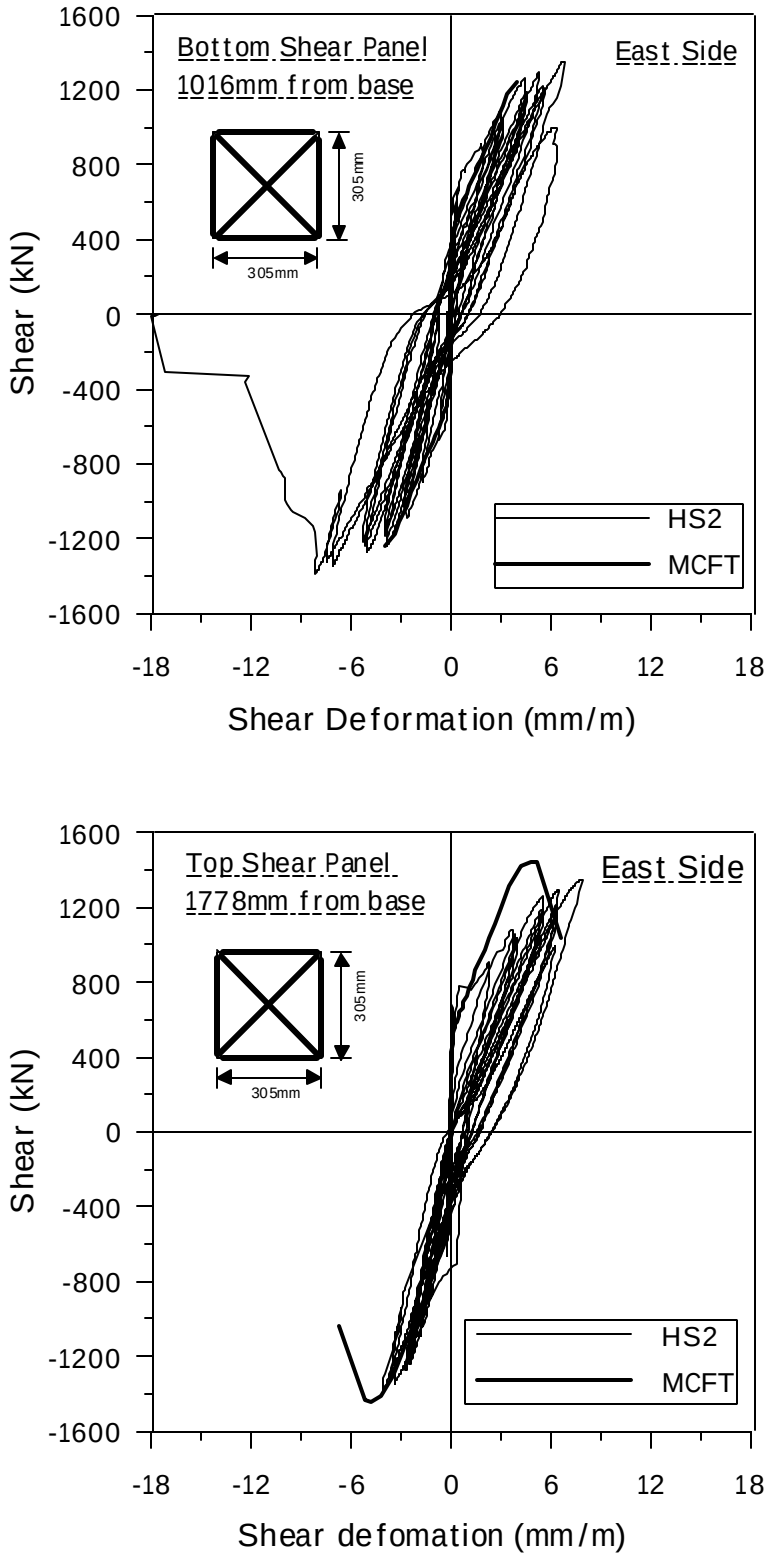

Figure 4.52 Unit HS2 Lateral Force/Shear Strain from Small Shear Panels (East Side of Column)

4.2.4 Envelope Response

The envelope response describes the behavior of the structure at the peaks of applied load or displacement. For the load control phase all peaks will be considered, while for the inelastic phase, at each displacement ductility level, only the first peak in the push direction and the last peak in the pull direction will be considered.

4.2.4.1 Displacement Components

Shear and flexural contributions to top displacement are analyzed in the following, at each stage of the test. The flexural displacement component is computed from the readings of the curvature cells with the assumption that the curvature remains constant within the cell height. Curvatures are integrated along the column height to obtain the contribution to the top displacement.

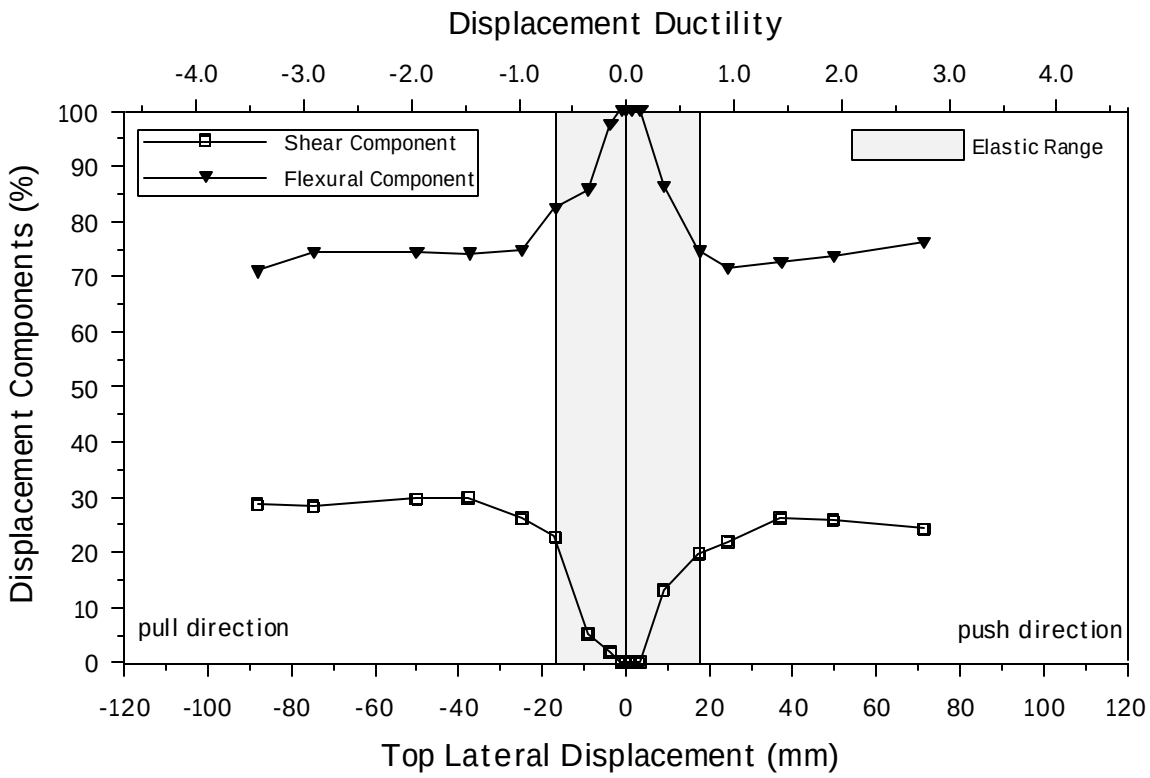

Figure 4.53 Unit HS2 Shear and Flexural Components of Total Displacement

The shear displacement component is computed from readings of the shear deformation panels. Readings from the east and west panels are averaged to calculate the average shear distortion in each of the three portions of the shear deformation panel. Shear distortions are integrated along the column height to obtain the shear contribution to the total displacement.

In Figure 4.53, shear and flexural deformation components are expressed as a percentage of the total displacement measured on the column top. It can be noted that the behavior is not symmetric in the push and pull direction. However, a similar trend is shown in both directions of loading with respect to the mutual interaction between shear and flexure.

During the elastic phase and up to displacement ductility 1.0 in the inelastic phase, the shear deformation component grows steadily while the flexural component decreases. The two contributions remain roughly the same in the later stages of testing from displacement ductility 1.5 to 3.5. Note that the shear contribution to the top displacement accounted for about 30% of the total displacement (10% more than in column HS1).

In Figure 4.54 the displacement components are plotted as a function of the total displacement measured on the column top. The main purpose of this graph is to check if the readings from curvature cells and shear deformation panels were accurate. If the shear and flexural deformation components, calculated based on the procedure described above, are added, this summation should be exactly the same as the total displacement measured on the column top. It is true in this simple case in which there are no other significant contributions to the column top displacement except for the column shear and flexural deformation (e.g. the shear deformation of the foundation footing is negligible). As it was observed in the previous unit this check was successful, because the computed displacement matches quite well that measured on the column top. In Figure 4.55 the shear and flexural components to the top displacement are plotted as a function of the applied lateral load. No significant shear deformations appear before the 900 kN cycle.

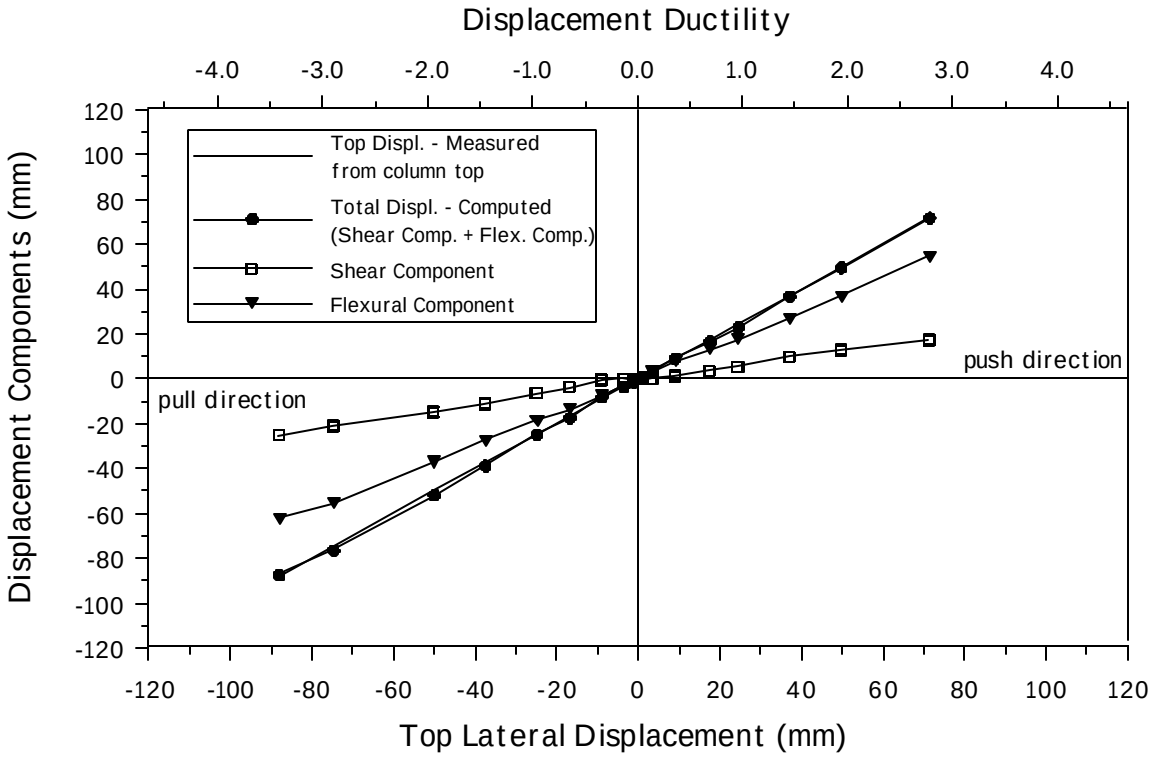

Figure 4.54 Unit HS2 Displacement Components vs Total Top Displacement

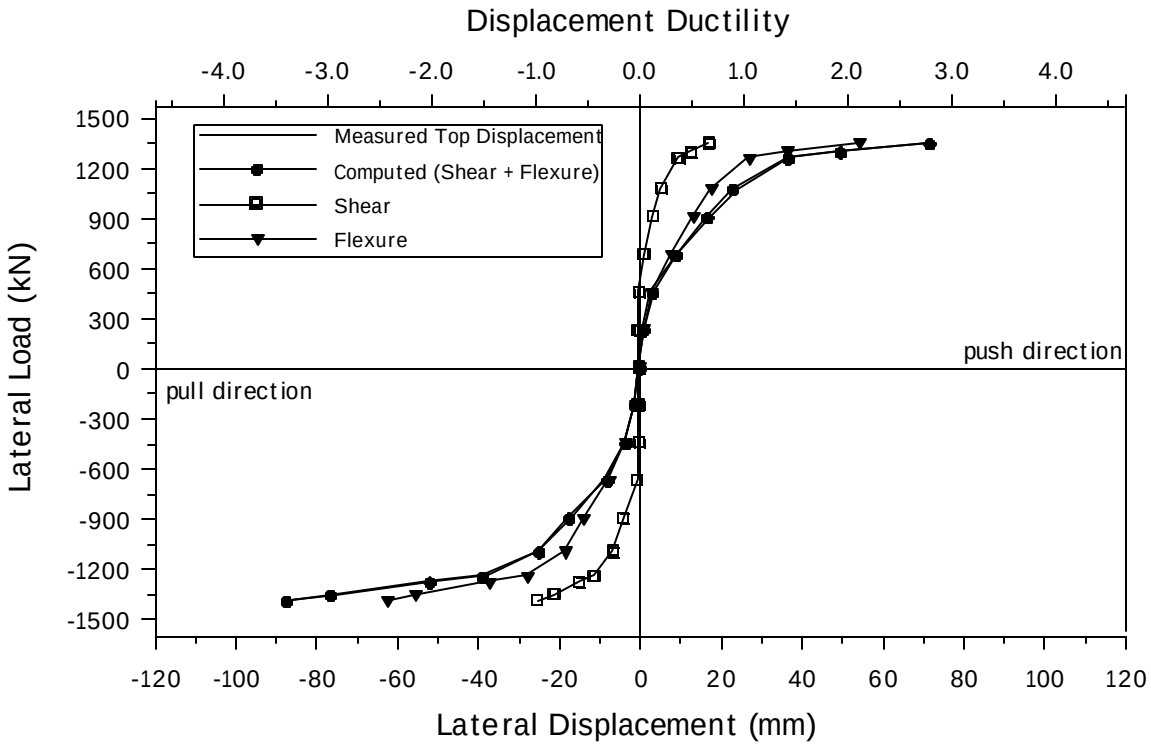

Figure 4.55 Unit HS2 Lateral Force/Displacement-Component Response

4.2.4.2 Plastic Hinge Length

Plastic hinge lengths at $\mu_\Delta = 2$ and $\mu_\Delta = 3$ were calculated from the displacements and curvatures of Figure 4.47 and Figure 4.48, respectively, using the procedure outlined in Section 4.1.4.2. The resulting values for plastic hinge length are 0.77 m and 0.91 m respectively, again larger than values expected for solid columns.

4.2.5 Profiles at Peak Load (or Displacement) Levels

Strain or displacement profiles describe the distribution of a generic deformation parameter along a line on the structure at peak load or displacement levels. Profiles can be plotted along the column height or over the section depth in order to describe the distribution of the deformation parameter for increasing lateral forces.

Profiles are presented herein for each load step in the push and pull direction during the load control phase (elastic range). During the inelastic phase instead, profiles are presented for the first peak in the push direction and for the last in the pull direction, at each displacement ductility level. The behaviors during the elastic and the inelastic phases are printed in different graphs, adopting different scales in the horizontal axis. The load stages in the elastic phase are identified with a label indicating the load level in kN, while load stages in the inelastic phase are identified with the displacement ductility level.

4.2.5.1 Flexural and Shear Deformation Components

As it was discussed above, shear and flexural deformations vary as a function of the applied lateral force. In fact, these deformation components have significantly different distributions along the column height. Shear displacement profiles are obtained by computing the lateral displacement due to shear at the top of each of the three portions of the shear deformation panels. Flexural displacement profiles are obtained by plotting the

lateral displacement due to flexure at the top of each of the 8 curvature cells. Comparing the results presented in Figure 4.56 with those of unit HS1, it is observed that larger shear deformations appear within the elastic range of response. Flexural deformations are very similar to those of unit HS1. This clearly indicates that unit HS2 was relatively weaker in shear than unit HS1, as expected as a consequence of higher flexural strength but equal shear reinforcement.

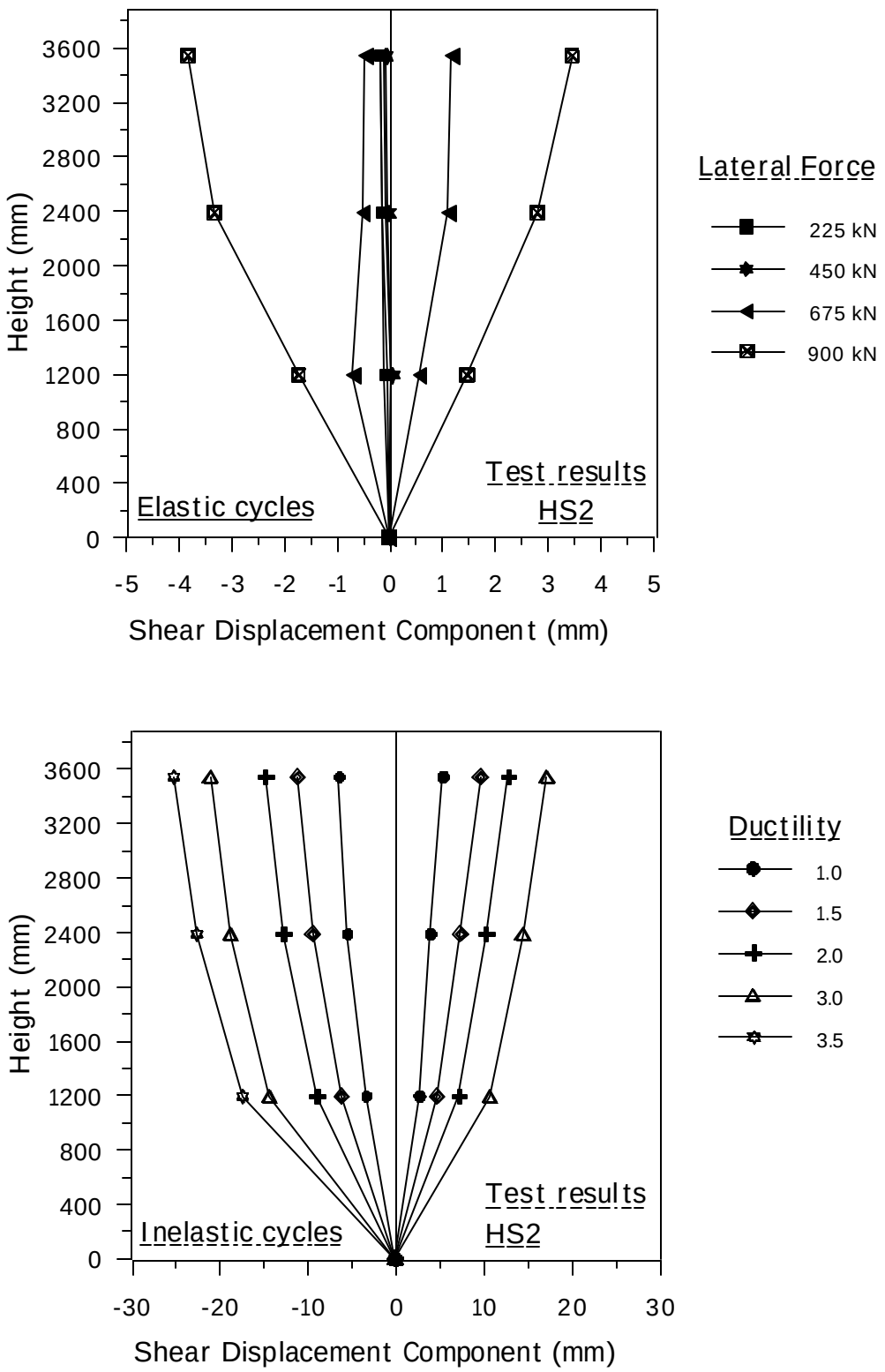

Figure 4.56 Unit HS2 Shear Displacement Profiles at Different Ductilities

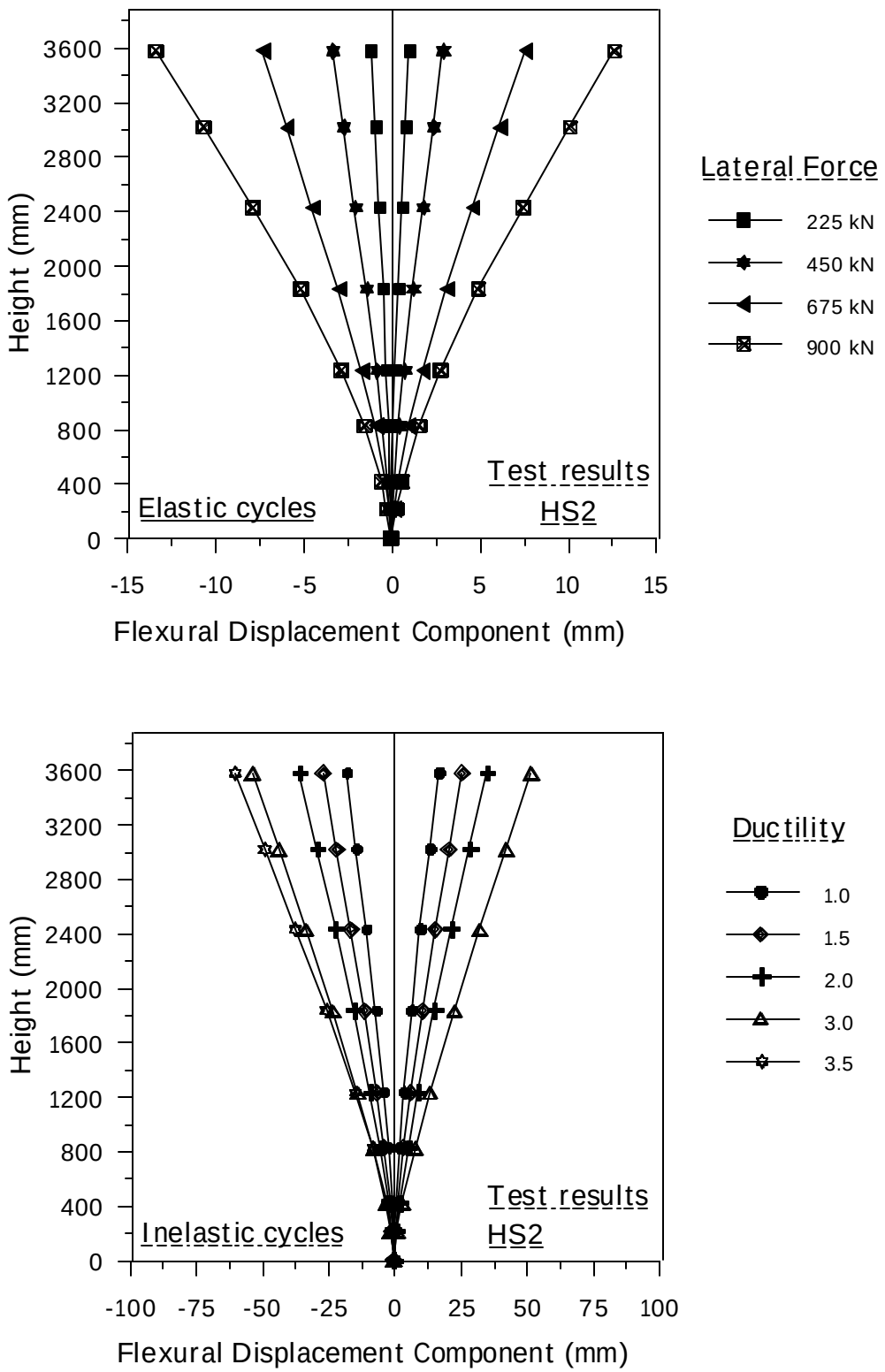

Figure 4.57 Unit HS2 Flexural Displacement Profiles at Different Ductilities

4.2.5.2 Curvatures

Curvature profiles are presented here in Figure 4.58 and Figure 4.59. In the first case the effect of strain penetration is not accounted for. The curvature obtained from the readings of the first curvature cell is supposed to be the averaged value over the cell height and is therefore plotted at mid-height of the first curvature cell (108 mm above the column base). In Figure 4.59 the effect of strain penetration is taken into account by considering a revised height of the first curvature cell according to the equation described in Chapter 2. In this case the curvature value obtained from the reading of the first curvature cell is supposed to occur at mid-height of the revised cell height (18.7 mm above the column base). It can be seen that the influence of strain penetration on the value of the base curvature is considerable. In this case the strain penetration, is rather high (158 mm) when compared to the height of the base curvature cell (215 mm).

Note that the experimental yield curvature, calculated using the procedure described in Chapter 2 from the curvature at the first yield of longitudinal rebars, is equal to 3.0 rad/km. During the inelastic phase it can be noted that the region where the curvature exceeds that measured in the plastic hinge region is probably contained within the first 600 mm above the base. The behavior is also not symmetric in the push and pull directions. The estimated plastic hinge length was 531 mm (obtained using the equation presented in Section 2.2.2). It appears that inelastic flexural actions occurred only in the base region, while the rest of the column remained within the elastic range of response. This fact is quite evident from the curvature profiles during the elastic phase. These latter do not show in average a linear profile, which was observed for unit HS1. High values of curvatures occur only at column base.

This localization of flexural inelastic response might be confirmed by looking at the profiles of strains in the longitudinal reinforcement. However, it should be cautions in drawing these conclusions, since strains in the longitudinal reinforcement are also affected by shear along the column height. High strains in the upper part of the column might be due to shear rather than flexure.

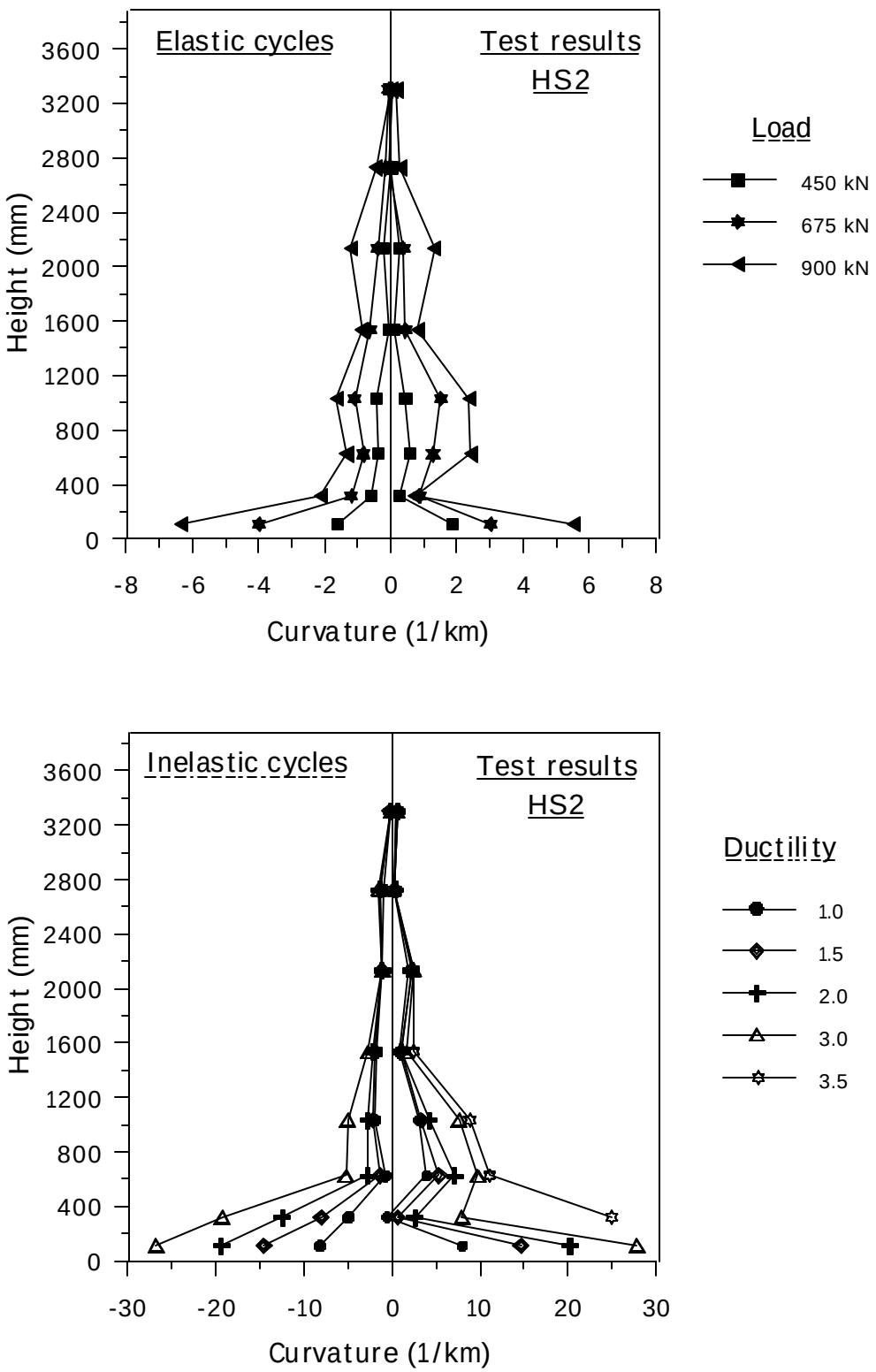

Figure 4.58 Unit HS2 Curvature Profiles at Different Ductilities – Strain Penetration Ignored

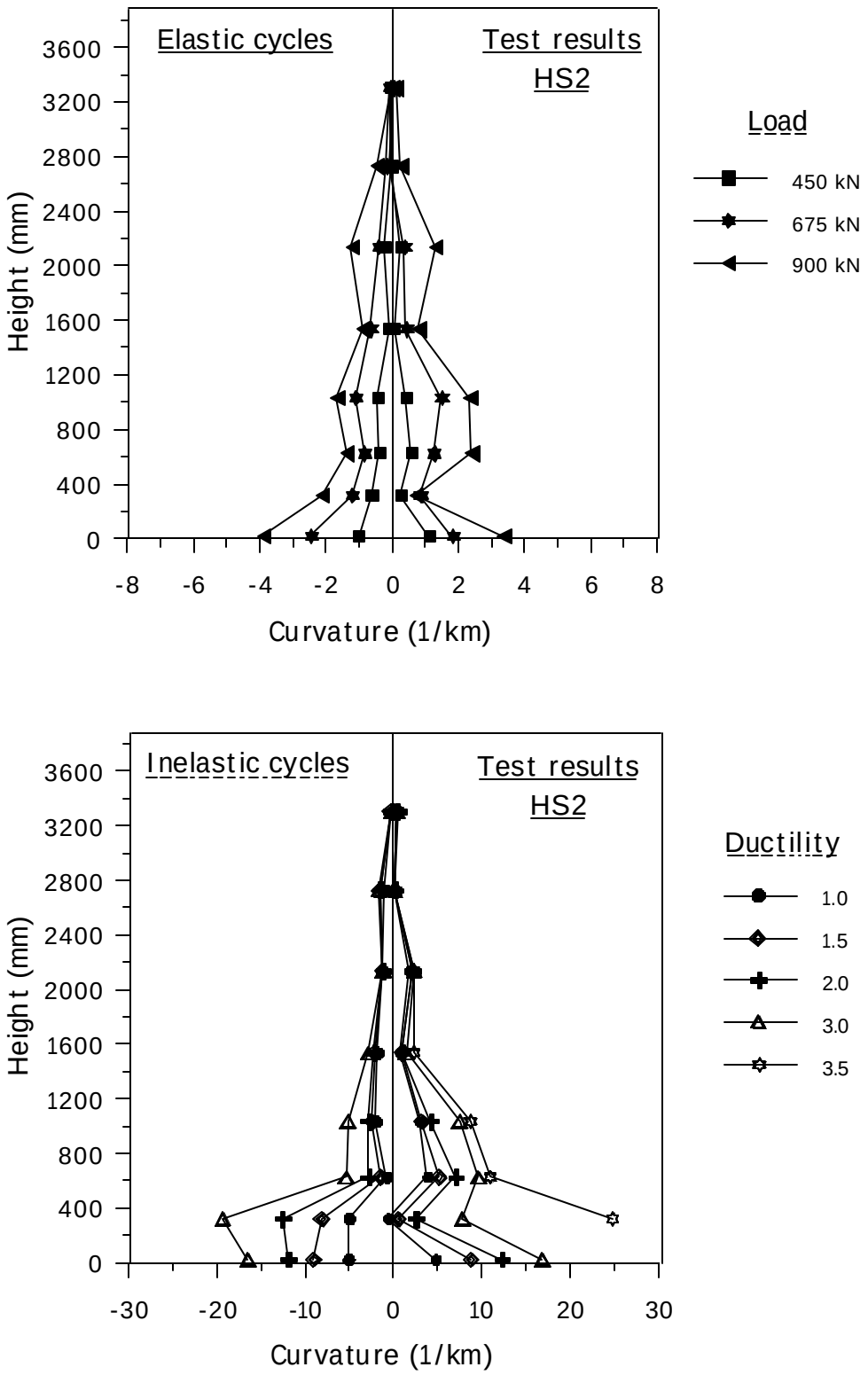

Figure 4.59 Unit HS2 Curvature Profiles at Different Ductilities – Strain Penetration Included

4.2.5.3 Longitudinal Reinforcement Strains

In Figure 4.60 and Figure 4.61 the profiles of the strains along the longitudinal bars located near the north and south generators are presented. It can be noted that strains have a uniform profile during the elastic phase. Peak strains reach almost the same value in the first diameter above the column base. The strain penetration effect is more significant than in the unit HS1 due to the larger size of the longitudinal bars. In fact, it can be seen that during the inelastic cycles, longitudinal bars are yielded up to about 200 mm below the column base. Due to the effect of the shear in the upper part of the column, it is not clearly to see the localization of inelastic deformations at the column base in the longitudinal reinforcement.

The behavior of longitudinal bars in compression is probably affected by the fact that the amount of transverse reinforcement was doubled at the column base to prevent buckling. It is observed that the maximum strains in compression do not occur at the column base but at a height of approximately 180mm above the base. Note that during the test it was observed that buckling occurred within several layers of bars and it occurred between 100 and 300 mm above the column base.

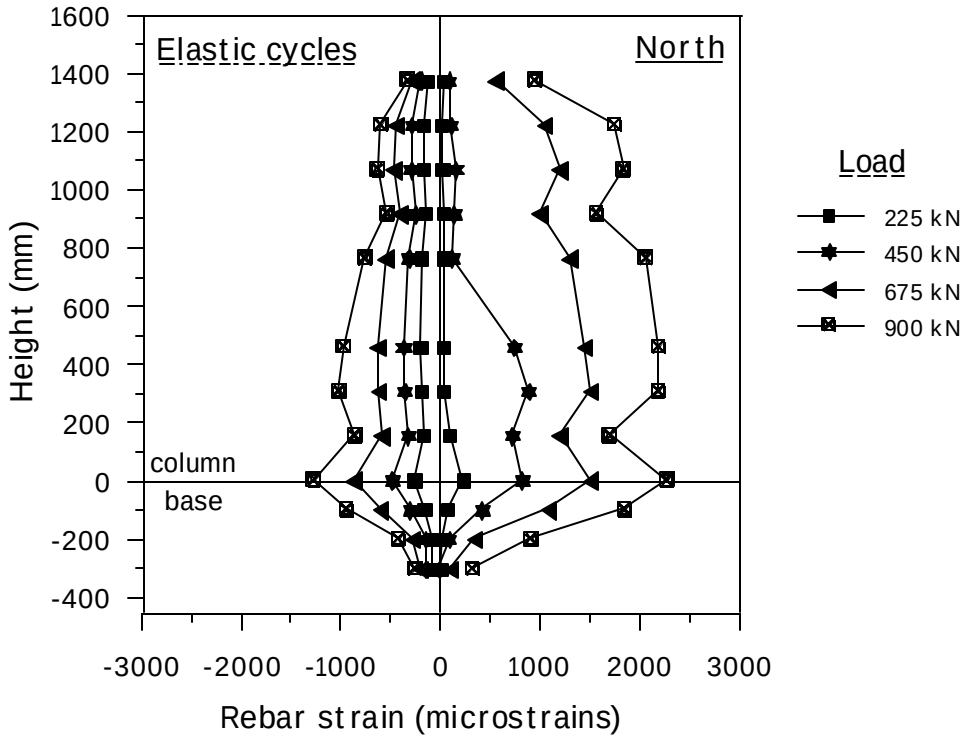

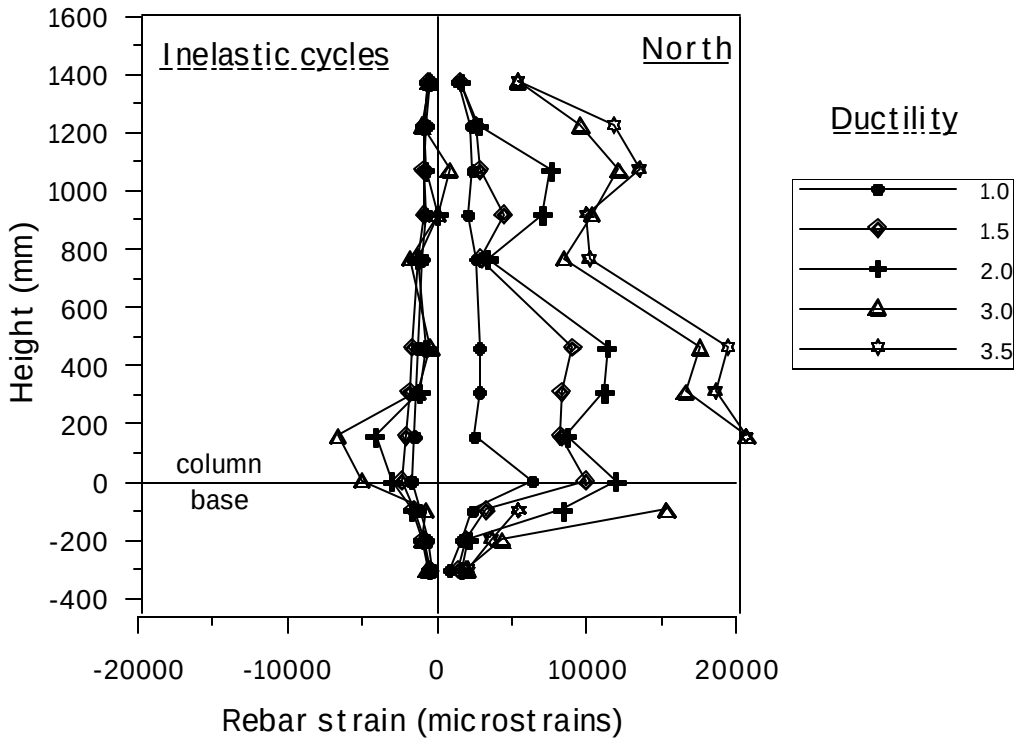

Figure 4.60 Unit HS2 Profiles of Longitudinal Rebar Strain at Extreme North Tension Location (Push Loading)

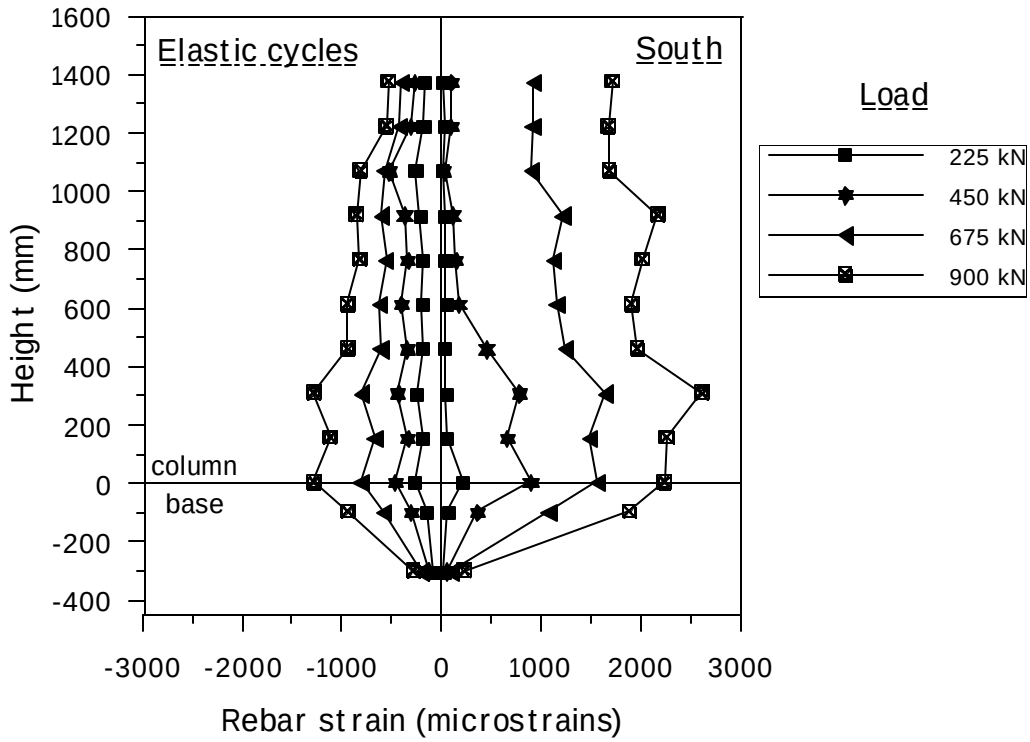

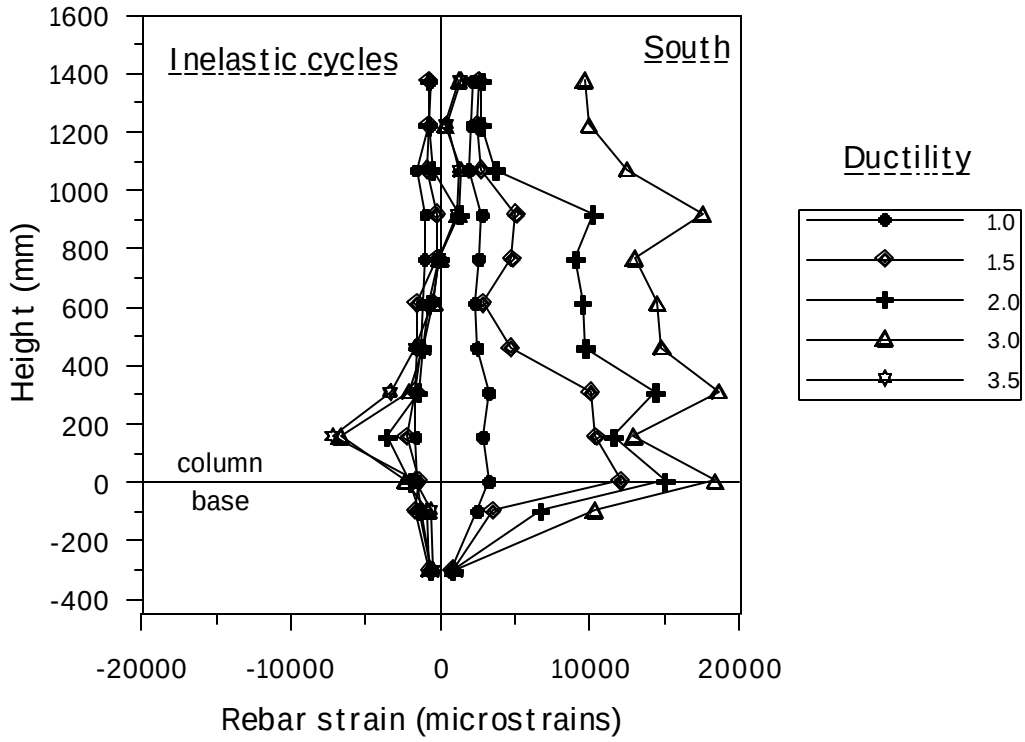

Figure 4.61 Unit HS2 Profiles of Longitudinal Rebar Strain at Extreme South Tension Location (Pull Loading)

4.2.5.4 Transverse Reinforcement Strains

Profiles of the strains recorded in the transverse reinforcement along the west and east generators are plotted in Figure 4.62 and Figure 4.63, respectively. Elastic and inelastic phases are plotted in the same graphs, while push and pull directions are differentiated in separate graphs.

It is observed that both in the push and pull directions high strains occur along the east and west generator, with maximum recorded values reaching 0.6-0.8%. Note that material testing indicated a rupture strain of 1-1.5% in average. The maximum strains were found in spirals located between 0.5 and 1.5 diameters above the column base. The bottom region (up to 400 mm above the base), as observed in the previous test, is affected by the presence of the footing which restraints the deformation in the transverse reinforcement. The profiles indicate that at later stages of testing, transverse steel is yielded uniformly in the shear critical region.

Significant strains appeared at the 675 kN cycle in the bottom part of the column (within one diameter above the base), where the damage was more consistent. Subsequently, deformation in the spiral extended up to about 2400 mm above the base (compare the 675 kN profile with that at 900 kN and that at ductility 1.0).

Figure 4.63 shows that the shear failure started at about 900 mm above the base, where the spiral strain was close to 1%. Once the shear failure mechanism started, transverse reinforcement ruptured in several layers below 900 mm from the base.

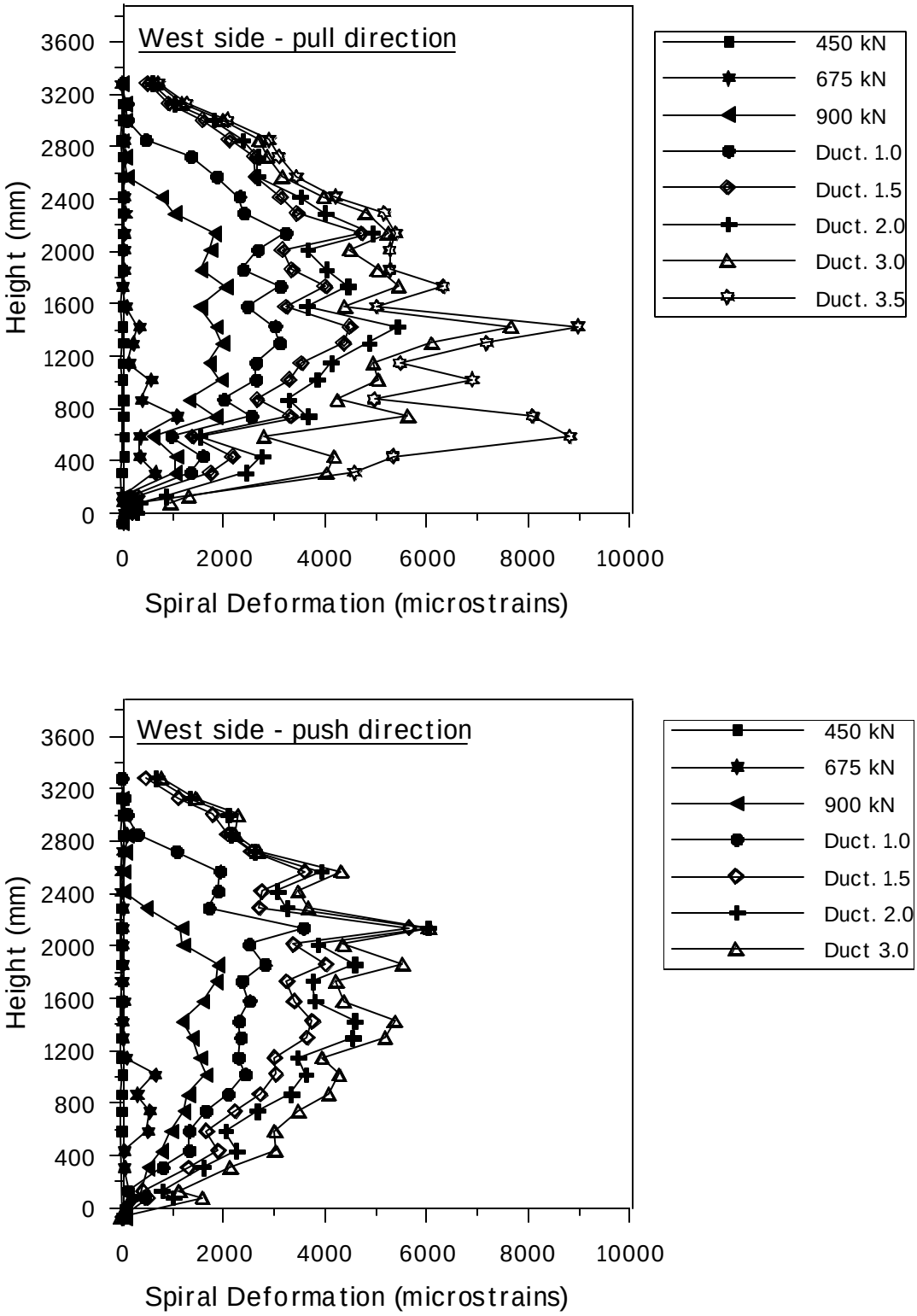

Figure 4.62 Unit HS2 Vertical Profiles of Spiral Strain on West Side

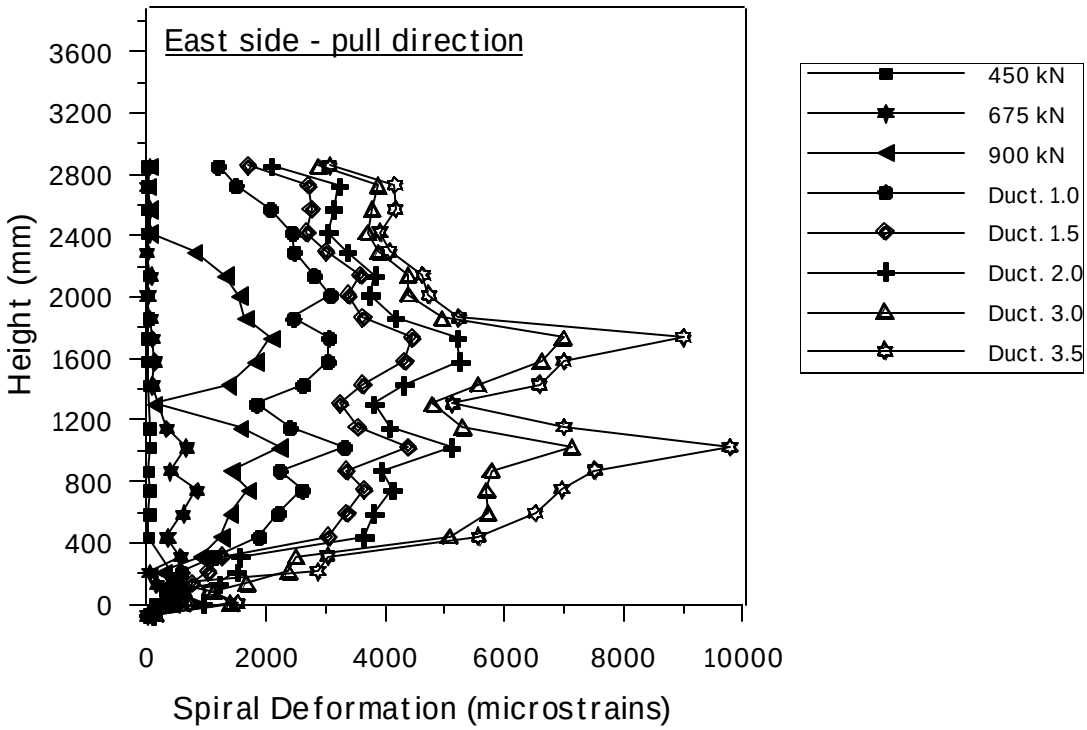

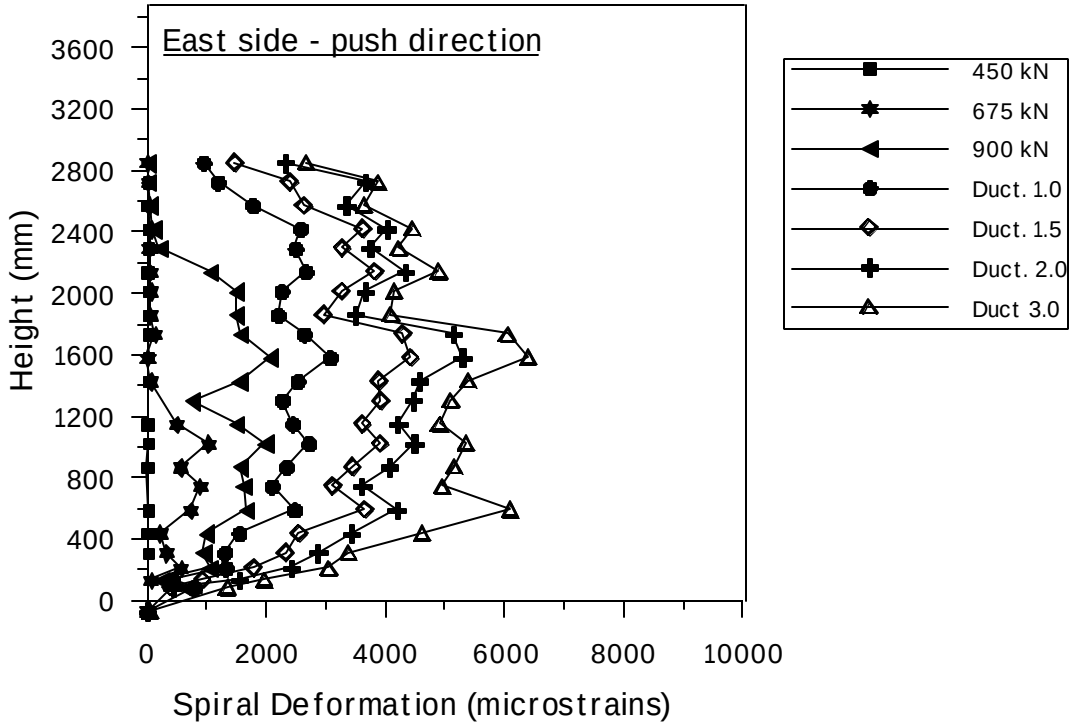

Figure 4.63 Unit HS2 Vertical Profiles of Spiral Strain on West Side

4.2.5.5 Section Longitudinal Strain Profiles

The distribution of the longitudinal strains over the section depth is analyzed in Figure 4.64 to Figure 4.69 for three different sections: one below the column base and two above the column base. The first section is at 102 mm below the column base, where it was observed that the longitudinal strains in tension exceeded the yield point. The second section is at 152 mm above the base, where it is expected to have reasonably accurate readings up to the later stages of testing. The third one, located at 609 mm above the column base, should be out of the predicted plastic hinge region. As observing from the test, considerably high inelastic strains occur in this section as well.

The longitudinal strain profile is obtained by plotting strain values recorded along the north and south bars located at the extreme tension and compression sides of the unit and the average value of the east and west gauges at the mid section. The horizontal axis indicates the location of the gauges expressed as a function of the distance from the section centroidal axis. The analysis of these three sections is to provide a clear description of the region where inelastic flexural actions occurred. Different plots are provided for the push and pull direction, dividing into elastic and inelastic stages of testing. In the graphs two vertical dashed lines are provided in order to indicate the location of the inside face of the column wall. An additional continuous horizontal line is provided in the graphs to indicate the steel yield strain. As explained before, this type of steel has a well defined yield point at 2300 $\mu\varepsilon$.

In the first section below the column base, it can be noted that the average depth of the compression zone is slightly less than what is observed in the same section in unit HS1. This is probably due to the higher value of the strain penetration caused by the increased size of the longitudinal bars. This section in this test unit is more affected by inelastic actions than the same section in the unit HS1. The neutral axis shifts rapidly towards the compression side during the inelastic phase.

In the second section, which is located 152 mm above the base, the depth of the compression zone does not vary substantially during the inelastic phases. On the contrary, it was observed in unit HS1 that the low longitudinal reinforcement ratio induced a rapid shift of the neutral axis and consequently a substantial reduction in the compression depth. It is also evident the lack of symmetry of the behavior in the push and pull directions. The important fact is that the neutral axis never intersects the column wall, which was the case in the unit HS1.

It is also quite surprising to note that very high compressive strains (up to -0.6%) are recorded in this section. These values should be treated with caution, since at later stages of testing significant buckling occurred in this region. From the behavior in the pull direction it can also be noted that the profile is not exactly linear as it appeared to be for unit HS1. Higher tensile values occur at section mid-depth.

In the section at 609 mm above the base it is observed that the compression zone is still about 180-200 mm in average during the inelastic phase, while in the unit HS1 it was clear that the compression depth was less than the column wall thickness. As it was pointed out above, this is an essential factor that governs the structural response of this type of members.

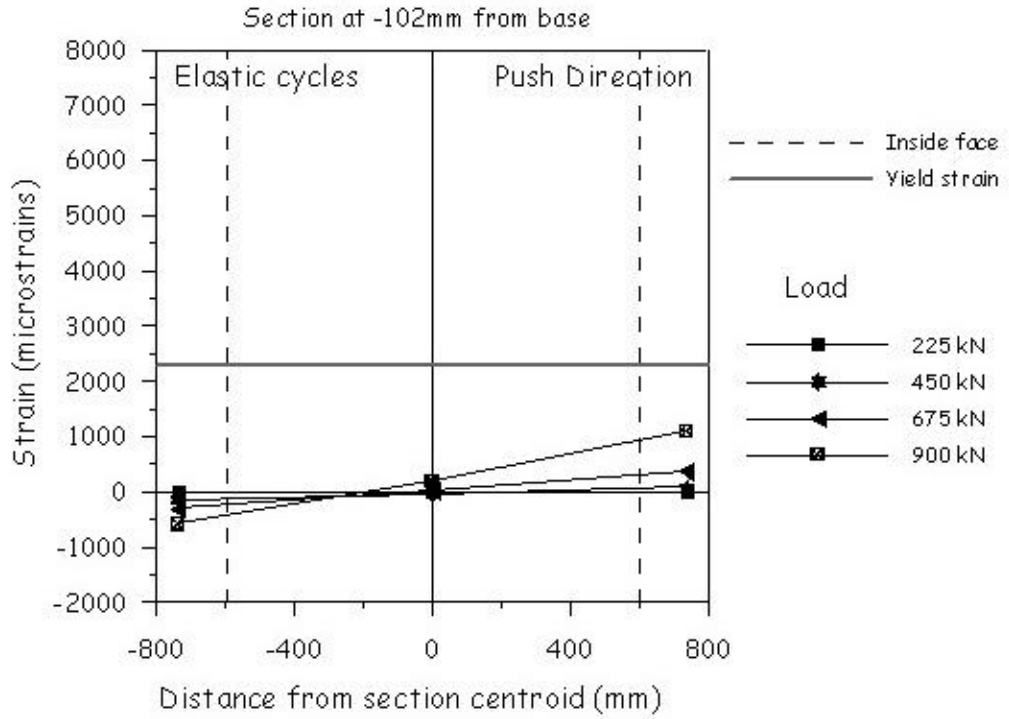

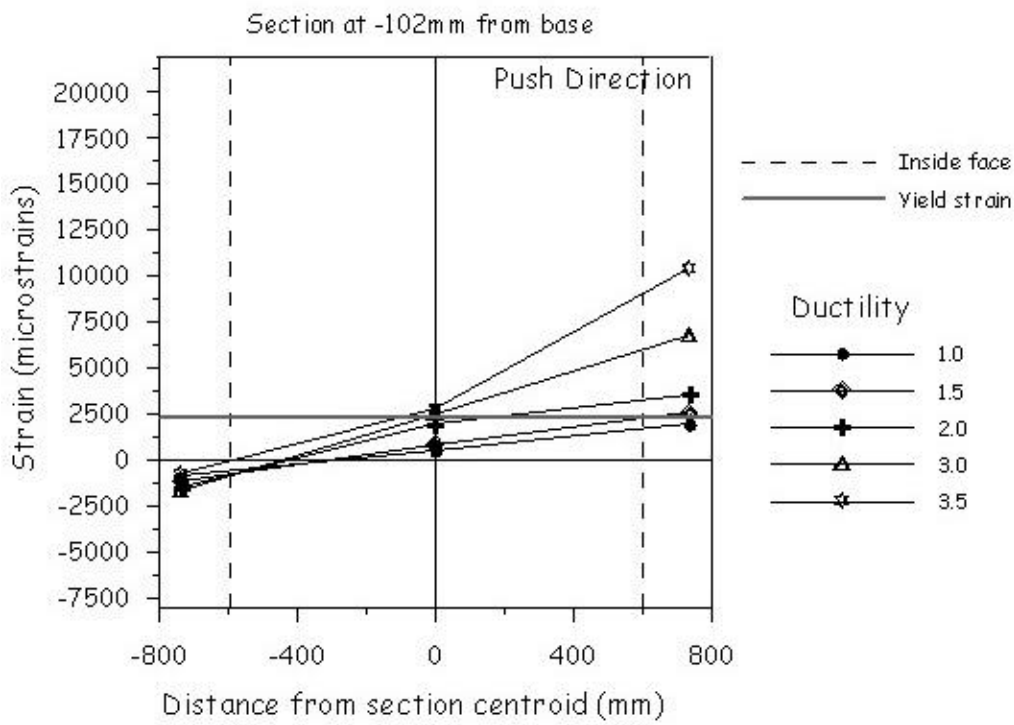

Figure 4.64 Unit HS2 Section Longitudinal Bar Strain Profiles 102 mm Below Base Section, Push Loading

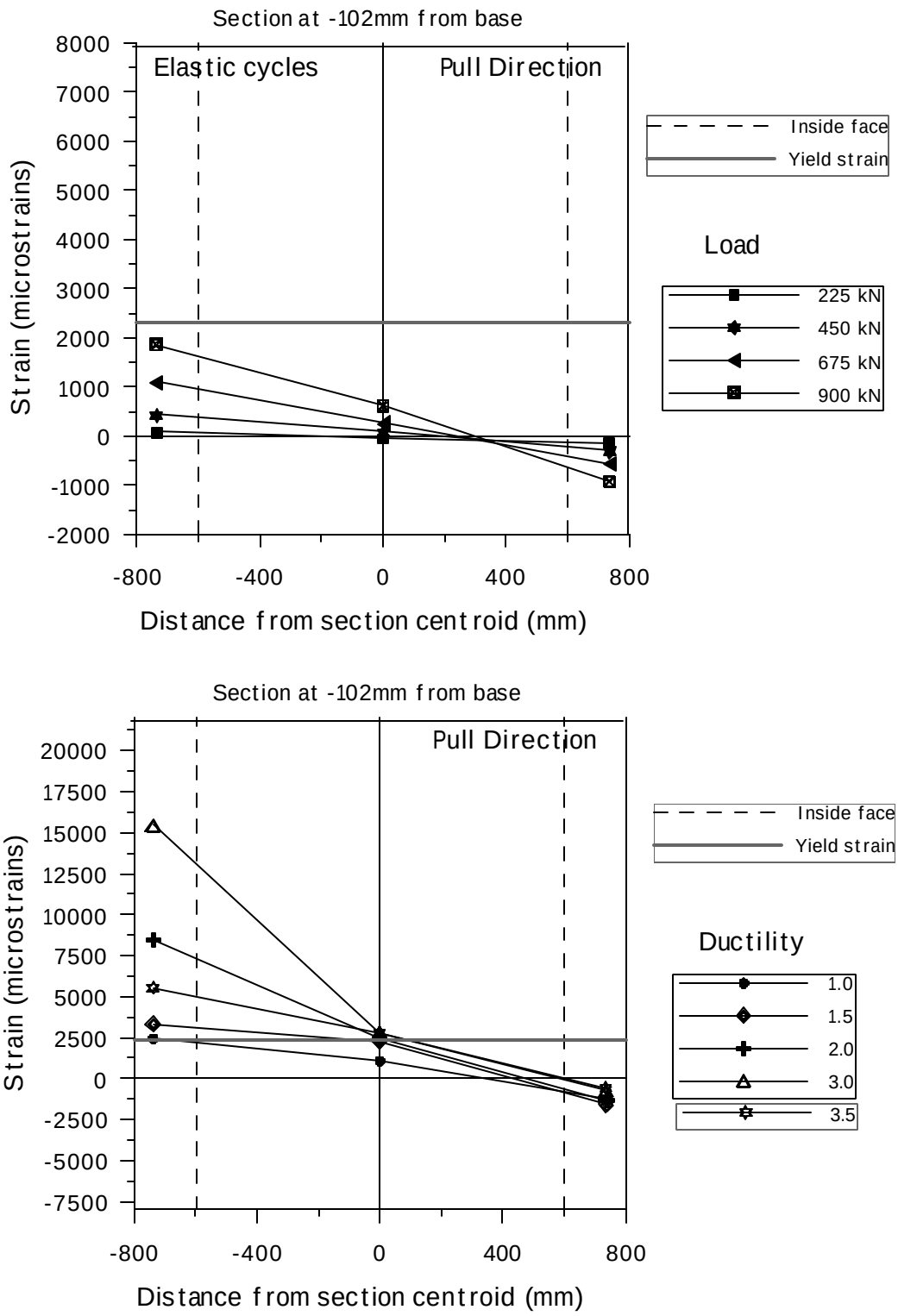

Figure 4.65 Unit HS2 Section Longitudinal Bar Strain Profiles 102 mm Below Base Section, Pull Loading

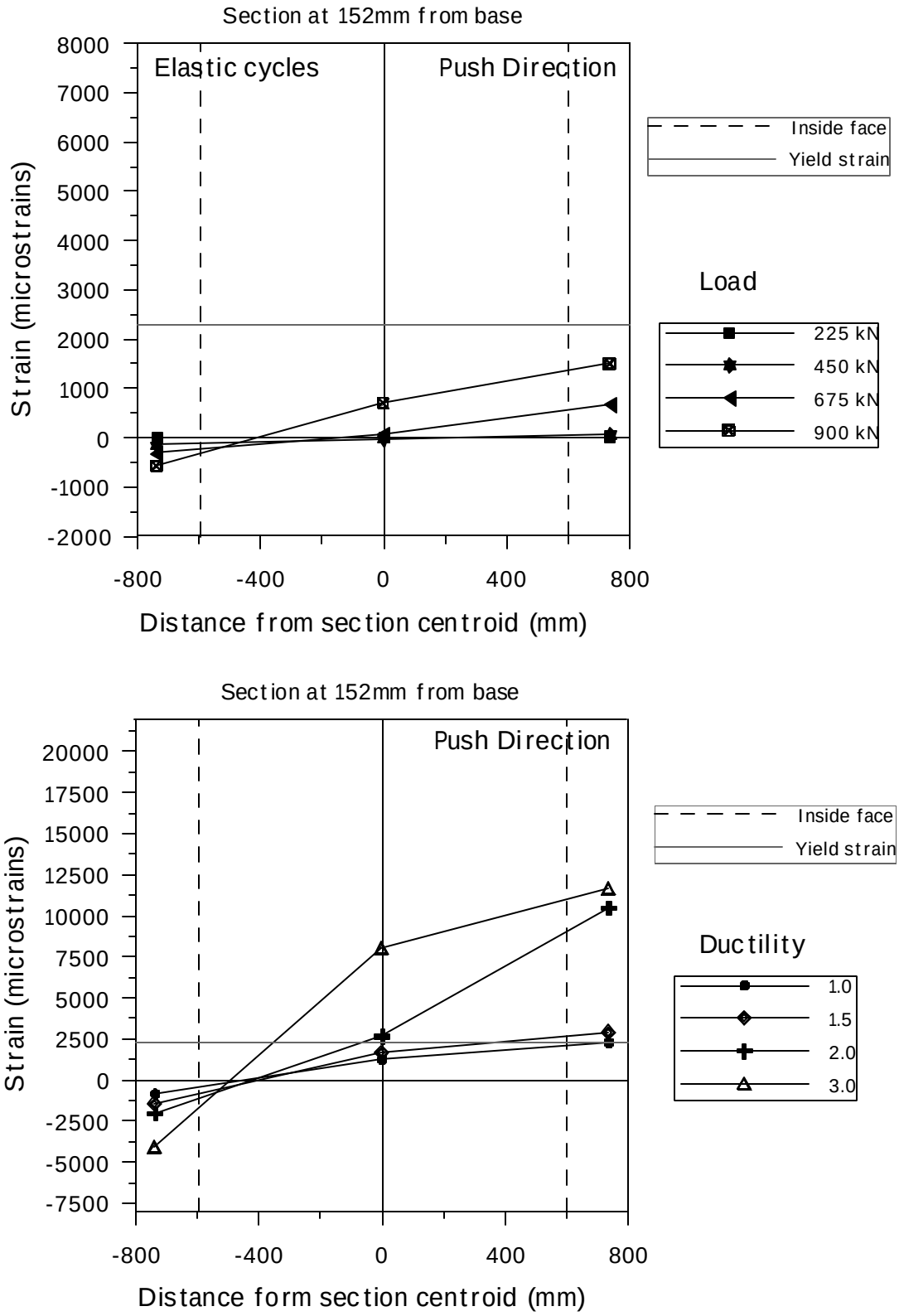

Figure 4.66 Unit HS2 Section Longitudinal Bar Strain Profiles 152 mm Above Base Section, Push Loading

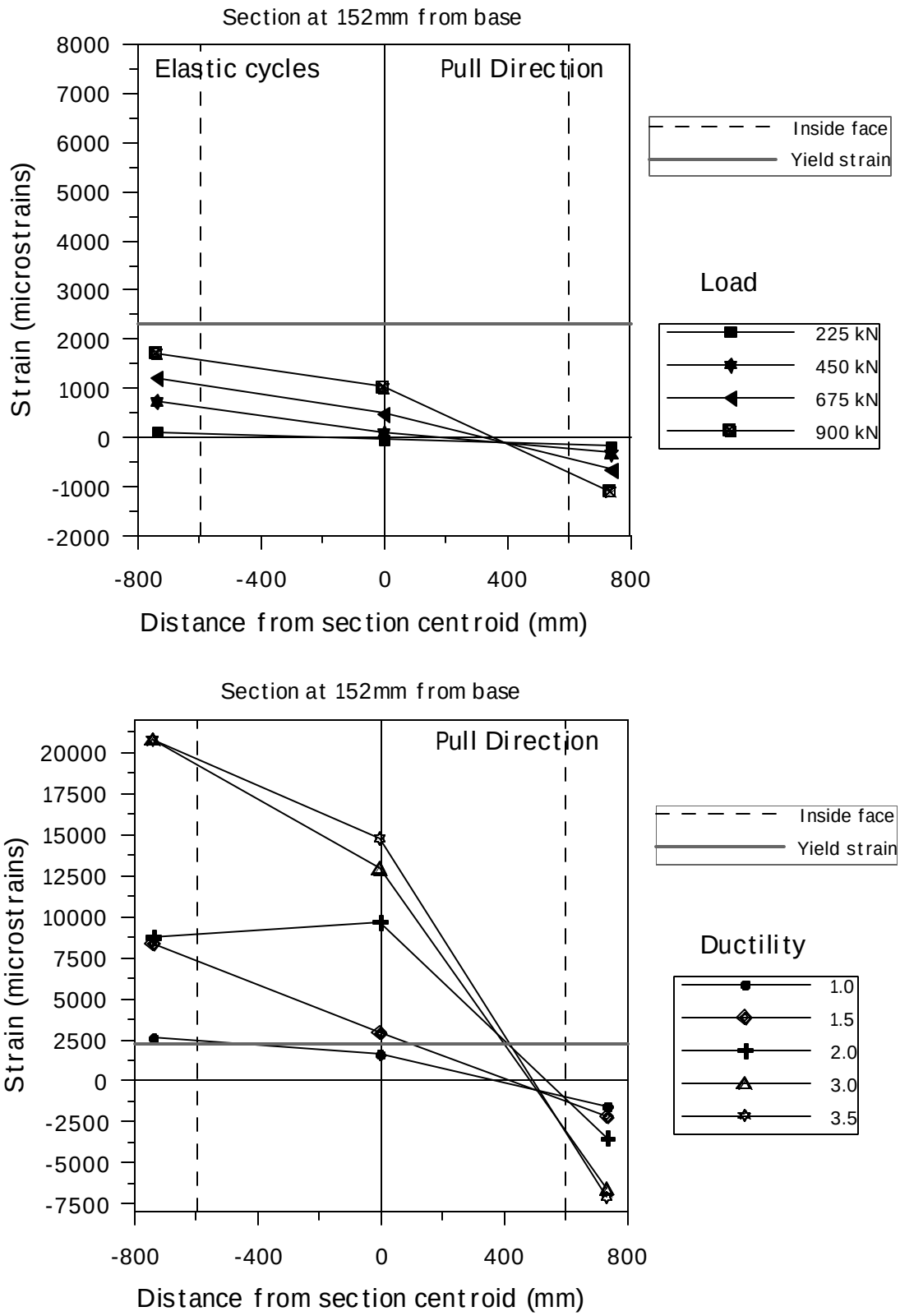

Figure 4.67 Unit HS2 Section Longitudinal Bar Strain Profiles 102 mm Below Base Section, Pull Loading

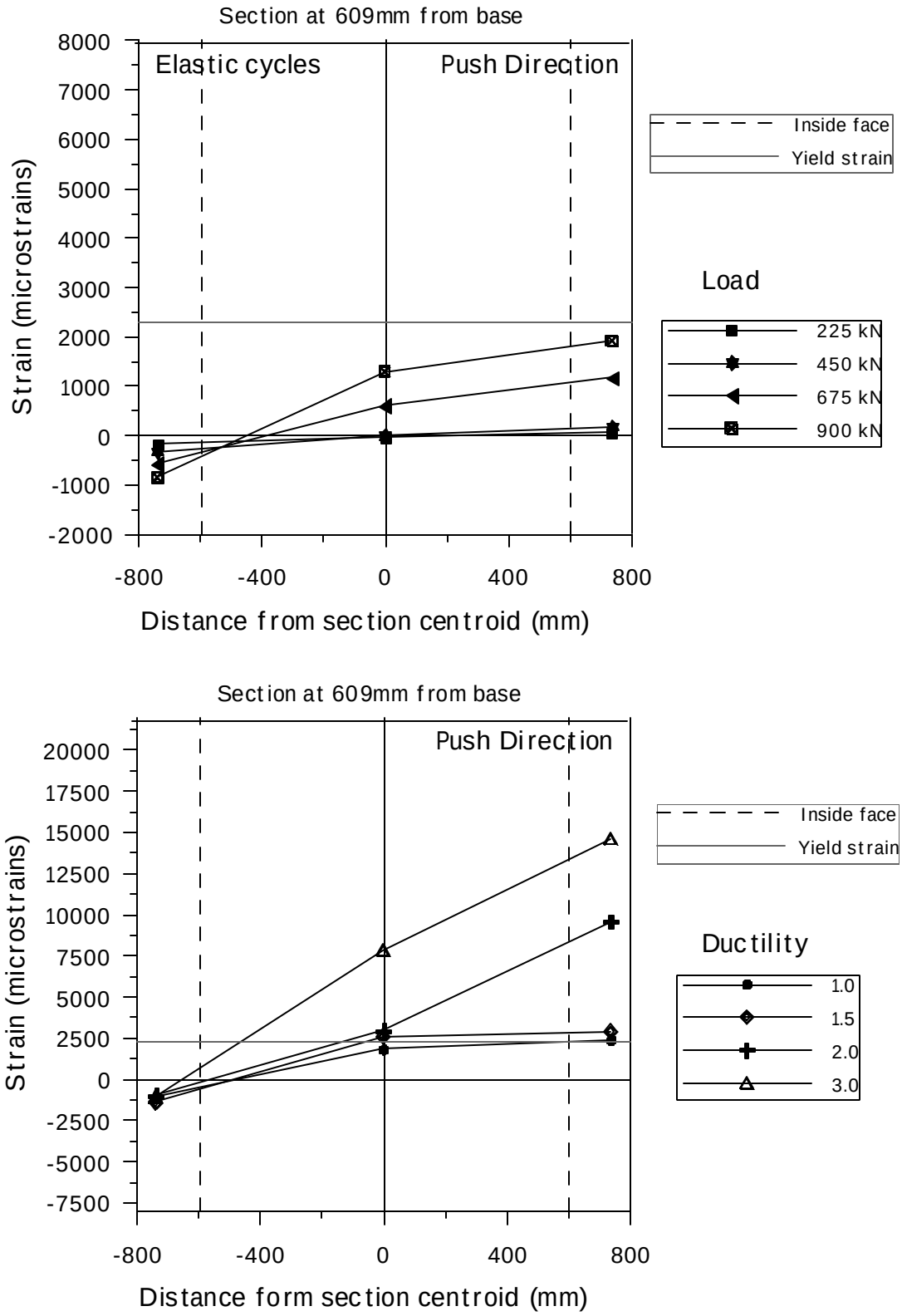

Figure 4.68 Unit HS2 Section Longitudinal Bar Strain Profiles 609 mm Above Base Section, Push Loading

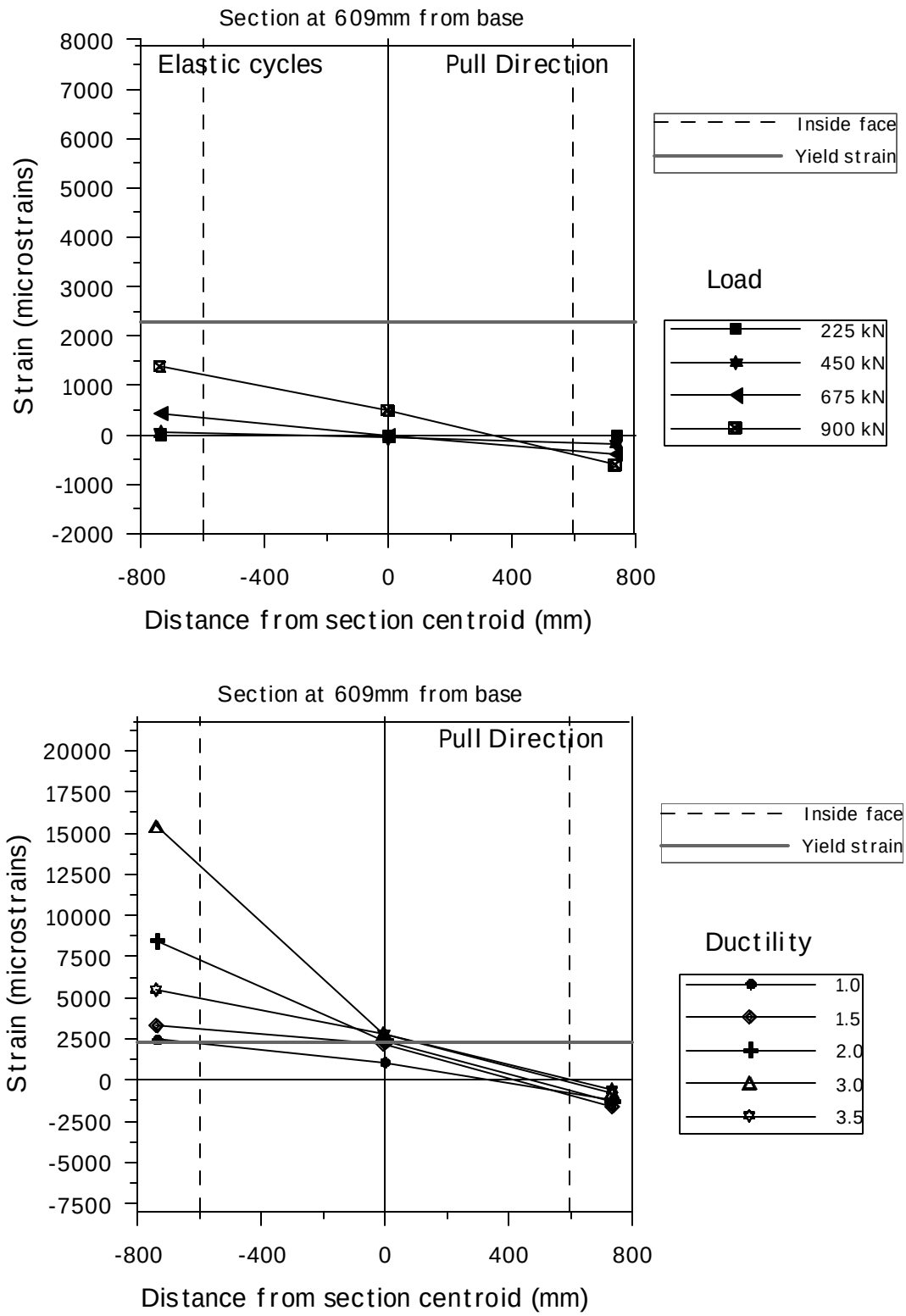

Figure 4.69 Unit HS2 Section Longitudinal Bar Strain Profiles 609 mm Above Base Section, Pull Loading

4.2.5.6 Section Transverse Strain Profiles

Transverse strains recorded on the spiral reinforcement are plotted as a function of the distance from the section centroid, with the same format used to describe the distribution of longitudinal strains over the section depth. There are total of three instrumented points over the section depth (along east, west, north and south generators). Gauges with symmetric locations in the east and west sides are averaged. As a consequence it will not be possible to analyze properly the distribution of lateral strains. As we observed in the previous unit in fact, maximum strains tend to occur towards the tensile part of the section instead that at column mid-depth, especially near the column base. The strain values recorded at the section mid-depth and at the extreme tensile and compressive sides of the section are presented. Results are shown in Figure 4.70, Figure 4.71 and Figure 4.72 for three sections located respectively at 350, 876 and 1397 mm above the column base.

Looking at the bottom section (350 mm above the base), note that if the same behavior observed in the unit HS1 occurs in this unit, it was expected to have a maximum value close to the tension side that is about 10-15% higher than that recorded at section mid-depth.

While the unit HS1 was observed to have similar values of the maximum strains in the three sections, the unit HS2 shows that the maximum value increases more rapidly with column height. Note that in the top section (1397 mm above the base) the maximum values at section mid-depth at ductility 3.0 and 3.5 exceed 0.8% and are not plotted in the graph. The graphs have the same scale on the vertical axes as it was used for the description of column HS1 to help in conducting comparisons.

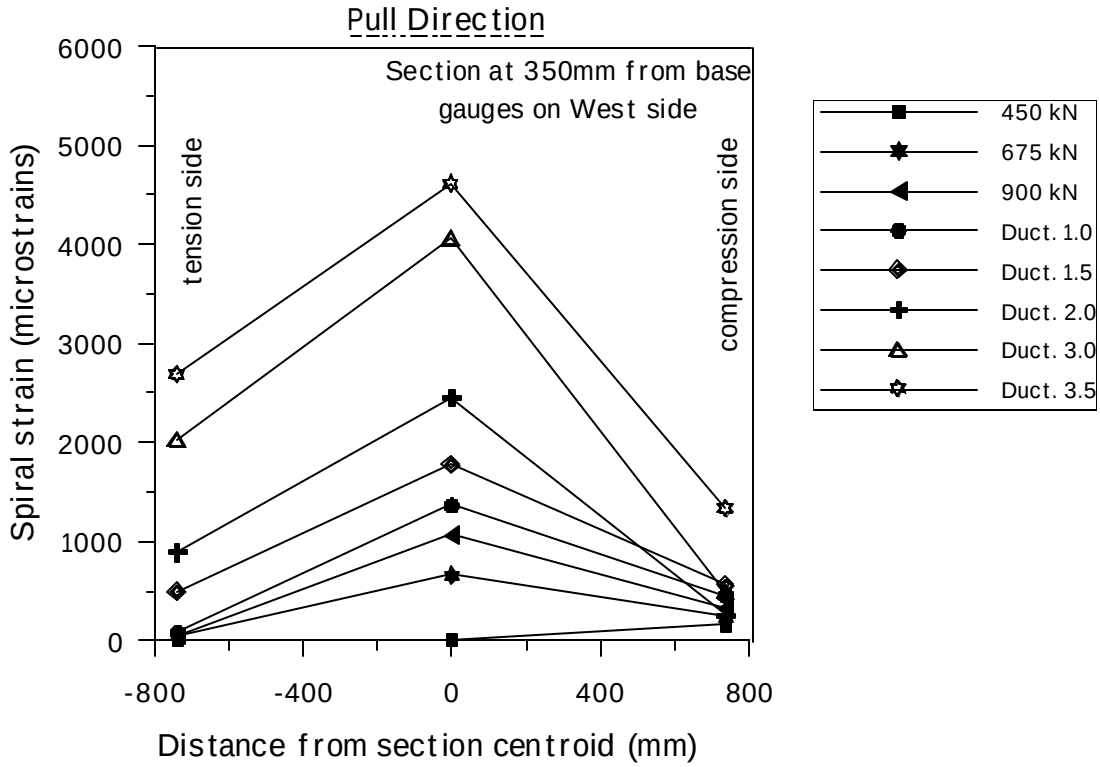

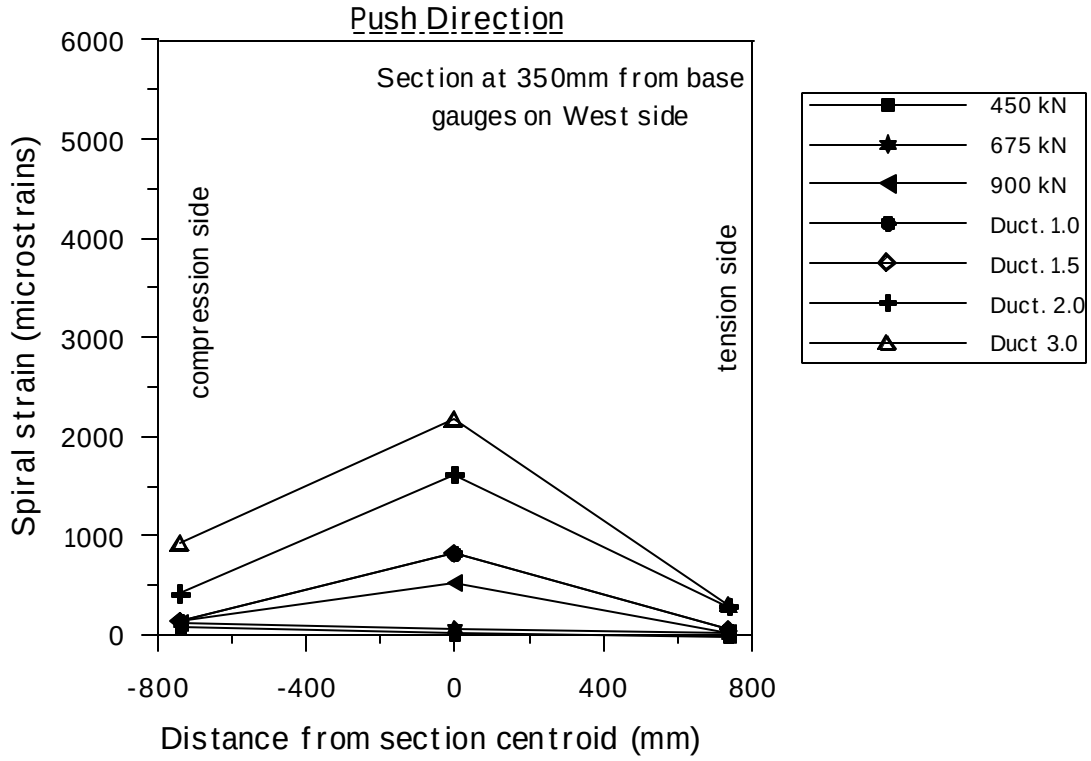

Figure 4.70 Unit HS2 Section Transverse Bar Strain Profiles 350 mm Above Base Section

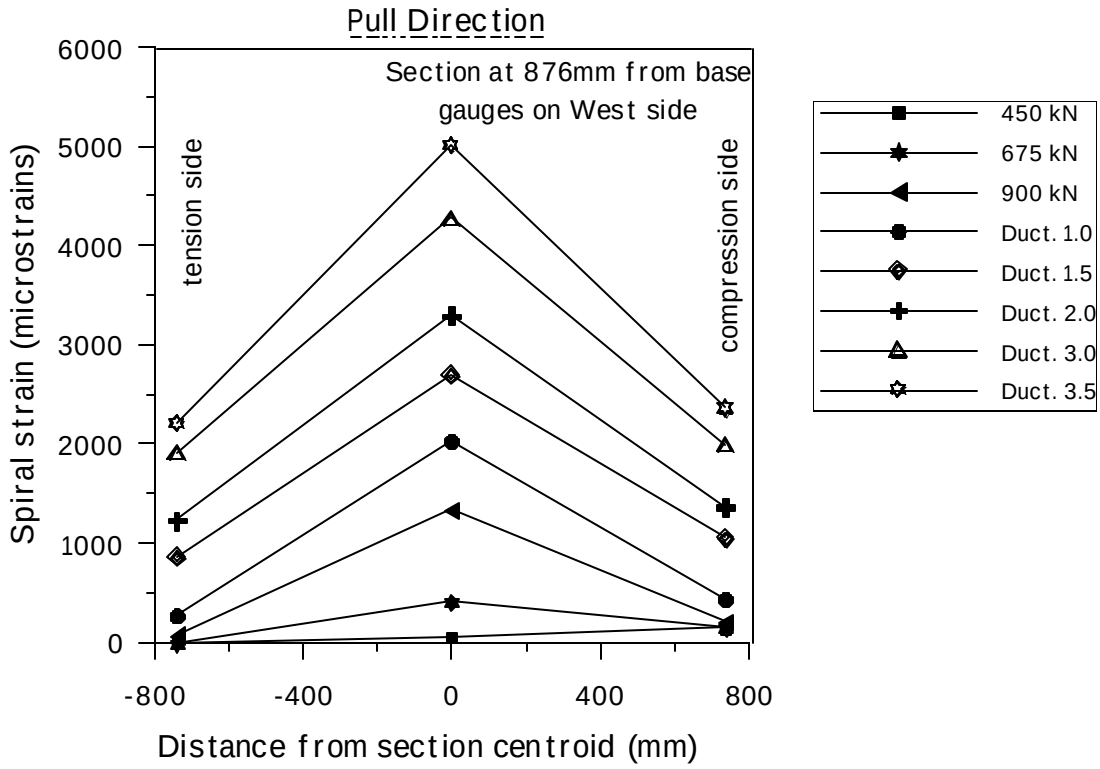

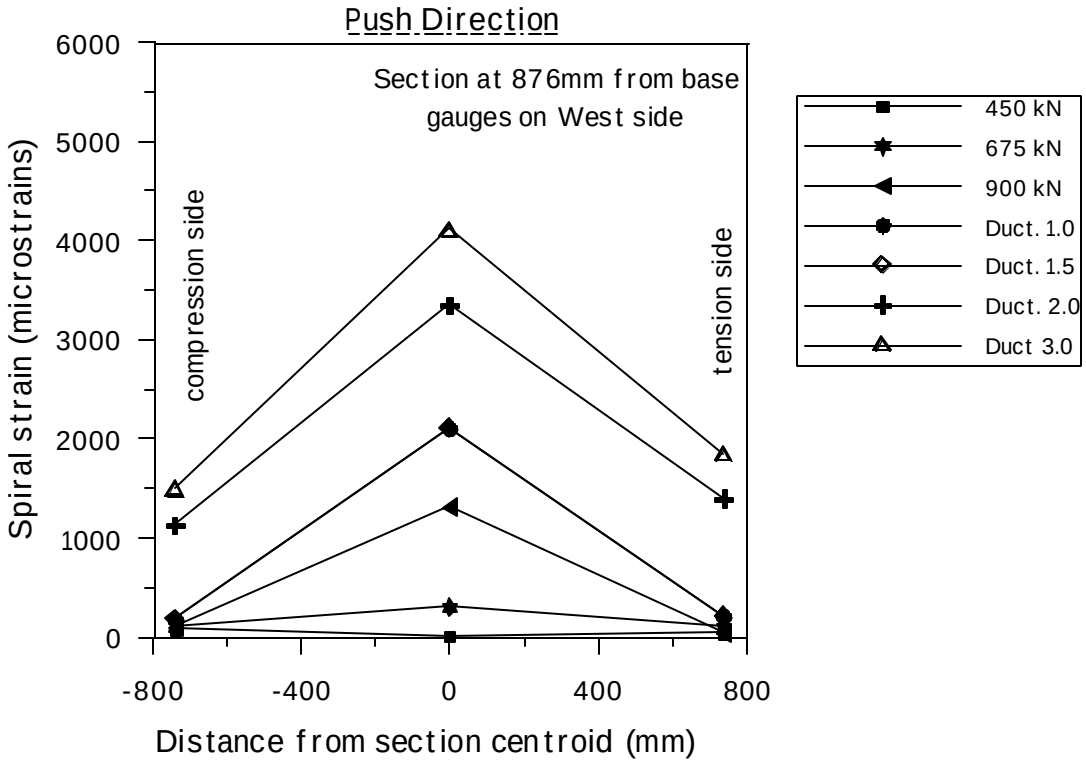

Figure 4.71 Unit HS2 Section Transverse Bar Strain Profiles 876 mm Above Base Section

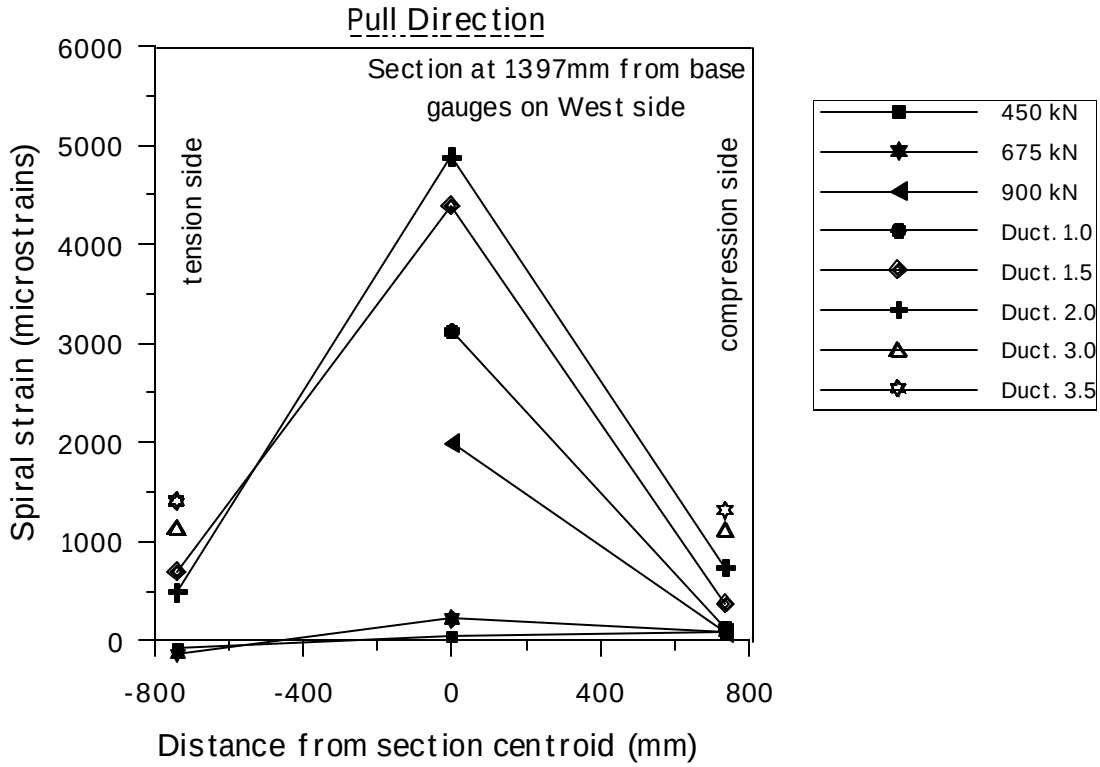

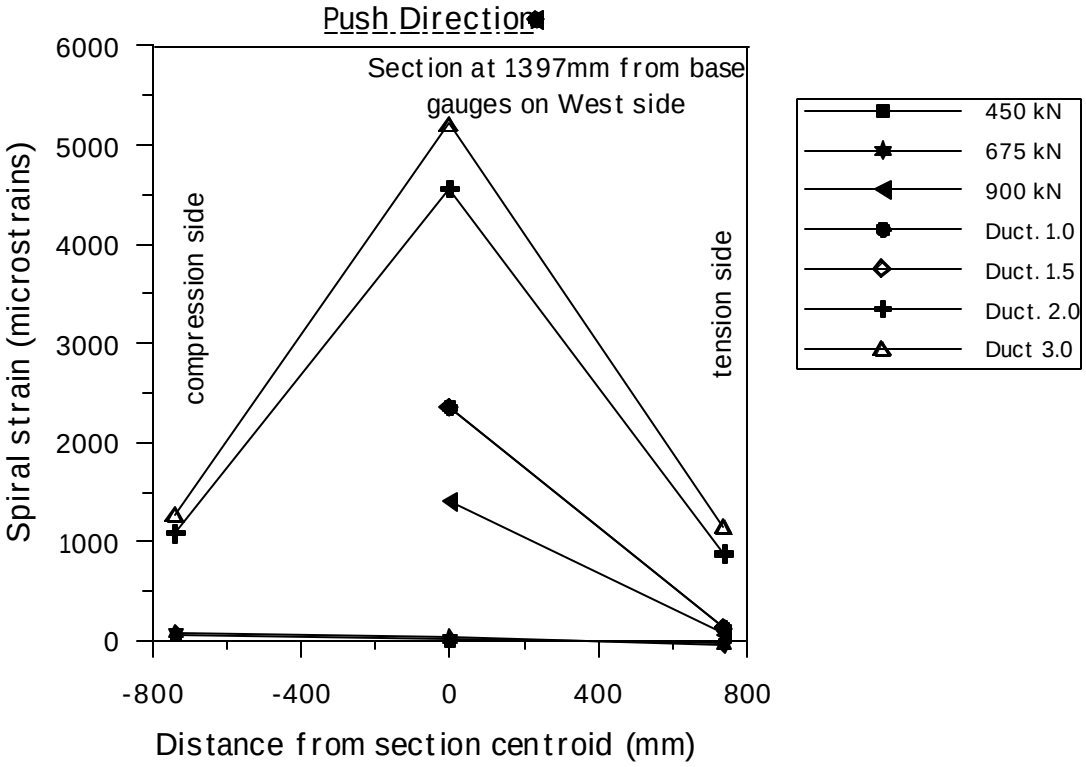

Figure 4.72 Unit HS2 Section Transverse Bar Strain Profiles 1397 mm Above Base Section

4.2.6 Discussion

This test unit revealed a deformation capacity similar to that of the unit HS1 (the maximum lateral drift of 2.33% was attained instead of 2.66% of HS1). The experimental evidence showed that the prediction of a shear failure was quite accurate. According to the UCSD shear models, a "classical" shear failure was observed at ductility 3.5. Note that this value is between two predicted values by the older and the newer versions of the UCSD shear models. In this case a good agreement was obtained by fully considering the effect of axial load on shear strength. If the V_p component is neglected, it is predicted that a shear failure occurs between ductility 2.5 and 2.8. From this preliminary comparison between the two test units it is therefore concluded that it is not necessarily the case to assume that the arch mechanism does not develop in hollow members. This one test would in fact confirm the opposite. More information is needed to come to a more reliable conclusion. The results of the third unit will be used to refine our estimates of the shear strength with respect to the role played by the axial load component.

Before reaching the shear failure in the pull direction at ductility 3.5, a substantial loss of strength due to spalling of concrete in the inside face was observed at ductility 3.0 in the push direction. While in the unit HS1 this phenomenon was observed at approximately 300 mm above the base, in this case the spalling occurred at 500 mm above the base. Also, it was quite evident from the photo presented in Section 4.2.2.2 that high compression stresses were caused by shear along the line where spalling occurred. Inclined compression struts were very clearly terminating with a steep inclination on the line where spalling occurred. It is therefore believed that while in the unit HS1 spalling was substantially caused by flexural actions, in unit HS2 the same effect was due to the high compression caused by shear. This phenomenon clearly represents a weakness of the system, but as it appears from this test that it does not dramatically affect the deformation capacity. A loss of strength occurs when a part of the compressed concrete is lost, but this does not necessarily cause the member to failure. It

is noted that these preliminary observations were made based on the results of units tested under a low level of axial load. It will be observed from the results of the unit HS3 that this weakness becomes more evident when a high axial load is being applied.

In regard to the problem of longitudinal rebars buckling, it is confirmed that doubling the amount of shear reinforcement in the base region is not sufficient to completely restraint against this undesirable effect. Buckling was less significant than that observed in the unit HS1 at failure, but still some layers of transverse reinforcement fractured near the column base. It is suggested that an effective restraint to longitudinal rebar buckling can only be obtained by using high strength transverse reinforcement instead of usual grade 60 steel.

In Figure 4.73 and Figure 4.74 the development of lateral strains as a function of the applied lateral displacement (or lateral load is analyzed). Similarly to what commented in unit HS1, the option of completely including the axial load effect on shear strength brings to a good estimate of the behavior near the column base (compare the predicted behavior with the readings from the gauge at 305mm above the base). If the axial load component is neglected, a closer prediction in the upper parts of the column is obtained. As discussed above, it is more evident in this unit than in the previous one that for a given lateral displacement level, lateral strains increase rapidly as a function of the distance from the base.

Figure 4.74 shows that the predicted behaviors agree quite well with the experimental evidence also in the inelastic range of response of the transverse steel (strains greater than 3800$\mu\varepsilon$). This fact supports that the USCD shear strength model can successfully be employed in estimating not only strength but also shear deformation capacity with reasonable accuracy.

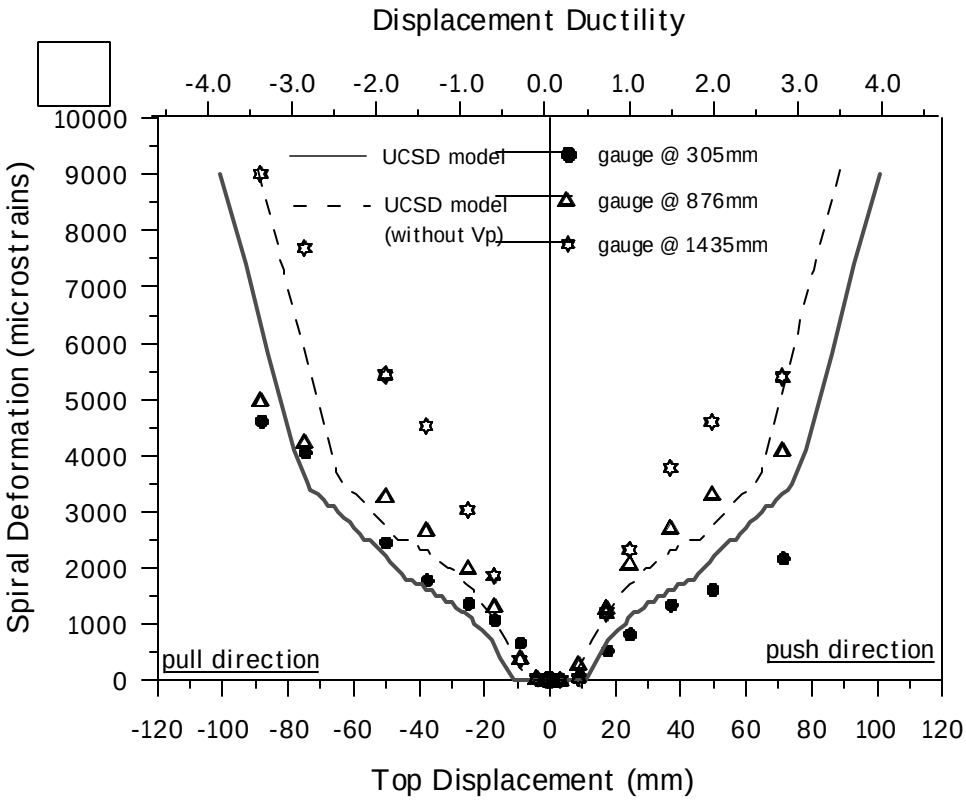

Figure 4.73 Unit HS2 Development of Spiral Strain with Increasing Top Development

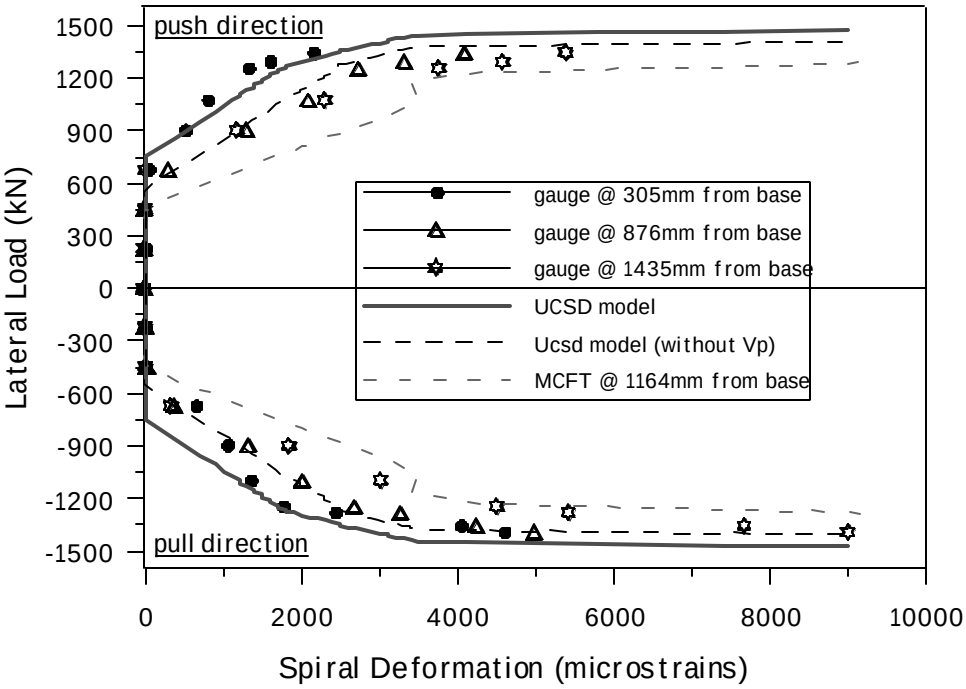

Figure 4.74 Unit HS2 Development of Spiral Strain with Increasing Lateral Load

4.3 Specimen HS3

The unit HS3 was designed with the main objective of investigating the effect of axial load on strength and deformation capacity of the hollow column system. This test specimen had the same geometry and reinforcement as the unit HS2, but the axial load was three times higher ($P/f_c^{'}A_g = 15\%$ instead of 5%). Such an increase in axial load with all other experimental variables being the same increases both shear and flexural strength and decreases the deformation capacity. An axial load ratio of 15% is a little more than what is usually recommended in design as the maximum axial load under static conditions. In these circumstances, the behavior tends to be governed by the ability of confined concrete to resist high compressive stresses. In fact, it is quite complex to determine weather or not a shear failure is likely to occur. The results of this unit will be used to confirm some of the findings obtained from the analysis of the response of the two previous units and to investigate in more detail some of the aspects that were still unclear.

4.3.1 Predicted Response

The response of the test unit was predicted both in terms of global force-displacement behavior and in terms local flexural and shear behavior. The main results obtained from pre-test analysis are discussed in the following two sections. The same topic will be commented later during the discussion in order to verify our assumptions by comparing the predicted response with that observed during the test.

All predictions are monotonic and are intended to be representative of the envelope behavior. In the case of this test unit, the assumed behavior of the confined concrete drives the results of these analyses, especially in regard to the problem of concrete spalling near the inside face. For the time being, we will retain the assumption, suggested by experience, that a maximum compressive strain of 0.5% can be resisted by compressed unconfined concrete before significant spalling occurs.

4.3.1.1 Force –displacement Predicted Response

The predicted response of column HS3 was obtained by using the procedures described in Section 2.2. The newer and older versions of the UCSD shear model were used in the shear prediction and more detailed analyses were conducted with the Modified Compression Field Theory and with the finite element program FIBER. Results are presented in Figure 4.75. The force displacement predicted response was determined with three different methods:

(1) according to the concept of equivalent plastic hinge length, where $L_p = 531$ mm
(2) using a pushover analysis with the MCFT, according to the procedure described in Section 2.2.3.
(3) using a pushover analysis with the finite element program FIBER.

Predicted force-displacement envelopes look very similar except for the ultimate point. Note that while the first method accounts for the effect of shear deformations by means of a shear displacement component computed based on the UCSD traditional model, the other two methods incorporate the shear-flexure interaction in the definition of the model. The predicted curves are very similar, but failure points are very different. Three of the four considered shear strength models predict a shear failure before the ultimate flexural capacity is reached.

As for previous units with all models, the same conservatism in calculating the shear strength was used. An angle $q = 30°$ for the inclination of shear cracks was assumed and a yield stress of 635 MPa was considered for the transverse reinforcement. In this case, the predicted type of failure according to the UCSD models would change if less conservative values are assumed for the angle q and for the yield stress of transverse steel. Analysis conducted with the Modified Compression Field Theory and the beam model implemented in the program FIBER, indicate that shear failure will occur between ductility 0.75 and 1.25.

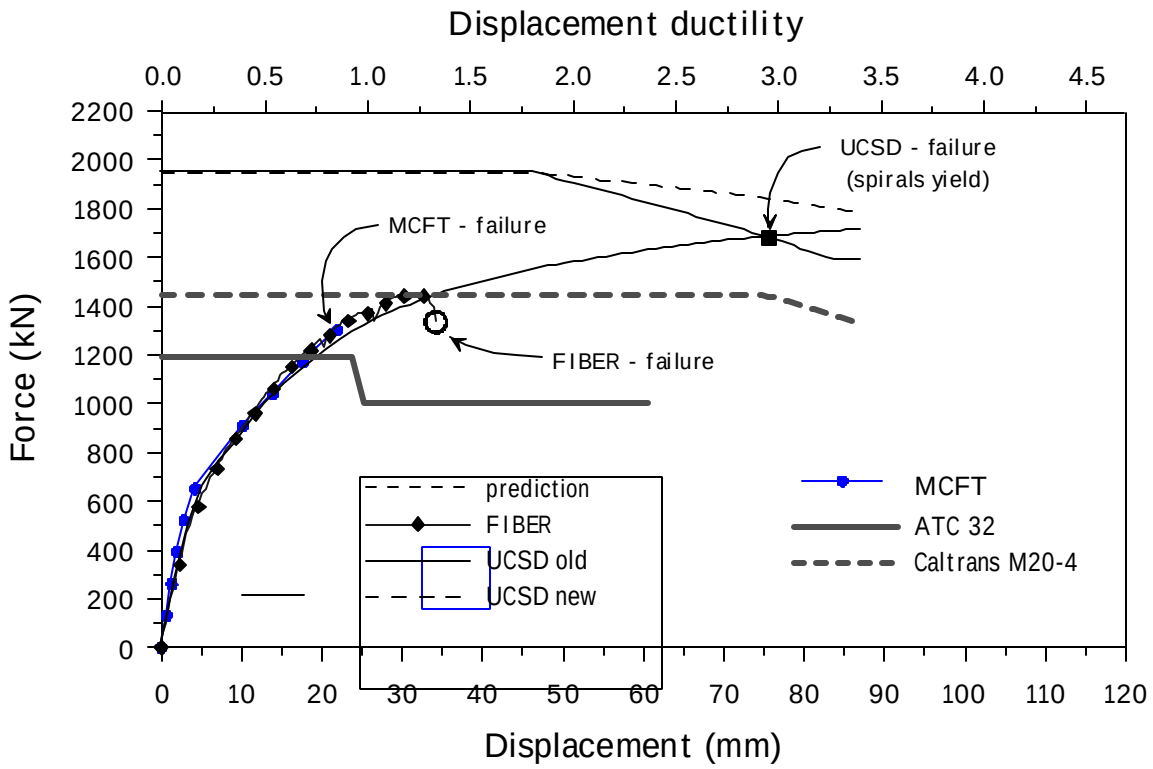

Figure 4.75 Unit HS3 Refined Force-Displacement Response Predictions

It was commented above when discussing the predictions of previous units, a shear failure might occur prematurely without rupture of the transverse steel. It is also possible to obtain a shear failure before the transverse steel yields. Plane stress analysis with the MCFT shows that, under this relatively high axial load, the principal compressive stress exceeds the available concrete strength while the transverse steel is still within the elastic range. In the shear critical region, the combination of high axial load and shear force determines (at 300 mm below the extreme compressive side of the section) high principal compressive stresses associated with high principal tensile strains. In this condition the concrete can no longer resist with its full strength and it will probably spall off. With the shear models adopted in these analyses it is not able to predict a shear failure caused by the lack of concrete capacity to resist high compression. As commented before, the

considered shear models imply that a shear failure occurs if the transverse reinforcement yields.

It can be noted from Figure 4.75 that the models from ATC-32 and Caltrans MEMO 20-4 do not seem to properly take into account the axial load effect. In these models, the influence of axial load is accounted for in the concrete component, but the predicted enhancement of shear strength due to axial load is definitely underestimated. The UCSD models appropriately indicate that the positive effect of the axial load on the shear strength will substantially postpone yielding of transverse steel. Note that in the UCSD models the axial load component is equal to 498 kN, about ¼ of the total maximum strength. In these circumstances, the transverse steel will not reach the target 635 MPa before ductility 3.0. More comments will be made on this issue during the discussion, but at this stage it is concluded that, comparing these results with those from more sophisticated analysis, the axial load effect seems to be properly taken into account by fully including the V_p component. This will be confirmed by the analysis of the stirrup strains calculated from the available shear strength.

Note that the predicted curve based on the concept of equivalent plastic hinge length indicates that a strain of –0.5% will not be reached near the column inside face before a displacement of 87 mm is reached. When a pushover analysis incorporating the shear deformation mechanism is carried out, the same value of concrete compressive strain is found for a lateral displacement of 35 mm. The main results of predicted strengths and deformation capacities are summarized in the following Table 4.5.

The flexural properties determined based on the moment-curvature analysis are summarized in Table 4.6. The flexural analysis indicates a higher compression depth compared to the previous units due to the higher level of axial load. At ideal flexural failure the compressive depth is 322 mm compared to 139 mm of the wall thickness. As it was mentioned, the neutral axis position will in fact be shifted towards the section centroid, even more than what calculated with flexural analyses, due to the effect of shear. Concrete properties were determined based on the Mander model, assuming a

confining pressure of 800kPa. Cracking was estimated by assuming a concrete tensile strength equal to $0.5\sqrt{f_c^{'}}(\mathrm{MP_a})$.

Table 4.5 Unit HS3 Predicted Failure Loads and Displacement

Model	**V at failure (kN)**	**D at failure (mm)**	**Type of failure**
UCSD-1*	1680	76	Shear
UCSD-1 (without V_p)	1454	41	Shear
UCSD-2*	1710	87	Flexure
UCSD-2 (without V_p)	1454	41	Shear
ATC-32	1200	21	Shear
Caltrans Memo 20-4	1440	35	Shear

***UCSD-1**=UCSD traditional model, **UCSD-2**=UCSD newer model

Table 4.6 Unit HS3 Moment-Curvature Limit States

Test stage	**Moment (kNm)**	**Curv. (1/km)**	**C (mm)**	e_{if} **(%)**
Cracking	2550	0.69	876	-0.056
First yield	4730	2.8	503	-0.103
Nominal strength	6140	-	-	-
Ultimate strength	6640	27.4	322	-0.5

4.3.1.2 Shear Behavior

The behavior of this unit should not be strongly influenced by the development of strains in the transverse reinforcement, because the ultimate capacity should be reached when concrete exceeds its compressive strength. Nonetheless, it is interesting to conduct the same analyses that were conducted for HS1 and HS2 in order to further discuss the problem related to the axial load effect.

The analyses were conducted by using the traditional version of the UCSD shear model and by deducting the transverse steel strain from the available shear strength. Two separate analyses with and without the V_p component were conducted. Figure 4.76 and Figure 4.77 show that yielding of transverse steel should not occur before ductility 1.7 (when the axial load component is neglected). At that stage, plane stress analysis with the MCFT indicated that the column should already fail due to excessive concrete compressive stress.

Since the axial load is much higher in this specimen than in the previous test units, the strain activation load is particularly sensitive to the V_p component. While the strain activation load is 500 kN when the axial load effect is neglected, it is almost twice as much when the axial load effect is fully taken into account. It is found from Figure 4.77 that if the axial load effect is accounted for, the strains in the transverse reinforcement should be exactly zero up to the loading cycle at 75% of ideal flexural strength.

Comparing the predicted response of column HS2 with that of column HS3 it is observed that roughly the same displacement capacity is expected. According to the shear strength models both columns should fail at the same lateral drift due to yielding of transverse steel. As we anticipated before, it appears that an increase in axial load increases both shear and flexural strength in similar proportion. However, since the two columns have different strengths, the type of failure and the displacement capacity could instead be very different. Rough estimates of the average shear stress as $V/b_w D$ (where b_w=280 mm and D=1300 mm) are:

(1) For V=1440kN v = 3.95MPa (for unit HS2)

(2) For V=1680kN v = 4.61MPa (for unit HS3)

Since the unit HS2 failed at that level of shear stress, it seems that the unit will not be possible for the concrete to resist such a high shear stress. If the assumption that the column will fail at the same level of average shear stress as in the unit HS2, a displacement at failure for the unit is equal to 40 mm. Note that while the concrete strength of the unit HS2 and HS3 was 40 MPa and 35 MPa, respectively, and therefore the limitation on the maximum shear stress that the concrete can resist is even more severe.

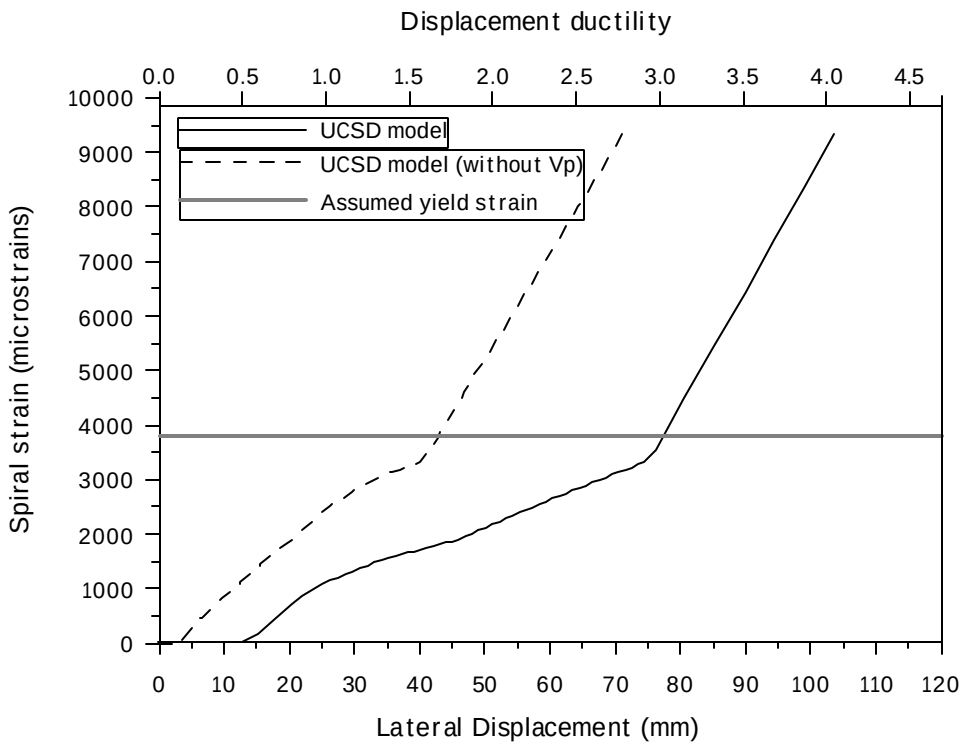

Figure 4.76 Unit HS3 Predicted Displacement/Spiral Strain Relationship

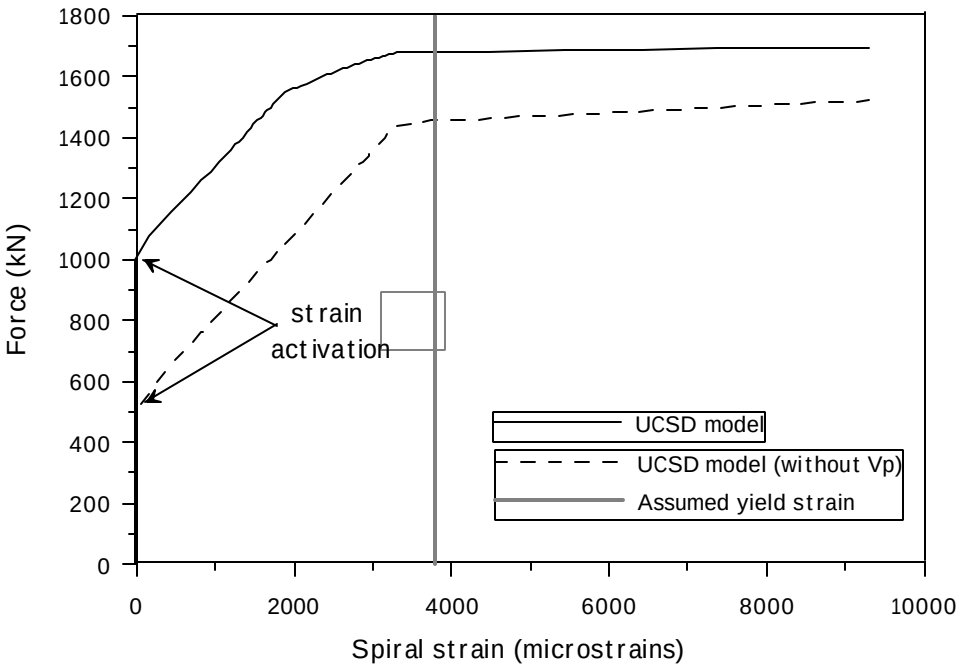

Figure 4.77 Unit HS3 Predicted Displacement/Spiral Strain Relationship

4.3.2 General Observations

The test was conducted with the same procedures used for previous units. The damage development was monitored according to the methods described in Section 4.1.2. The behavior of the column in the inside face was monitored by using the same system used for testing the previous units. The reference system along the North, East and West generators was labeled in mm.

4.3.2.1 Elastic Cycles

Elastic cycles were conducted in load control by monitoring the force applied in the two hydraulic actuators. The applied force was exactly the same in the two actuators throughout the elastic cycles. For this unit, a different axial load device was adopted, as described in Section 3.1. Two of the four vertical bars were instrumented with load cells. The total axial load acting on the column is equal to the sum of the forces acting on the four bars.

The axial load was applied by acting on the oil jacks as described in Section 3.1. The target load was reached by reading the force value indicated from the load cells. At the beginning of the test, when no lateral action was applied, the axial load on the column was 3196 kN. The application of the axial load did not induce any cracking in the test unit. The value of the applied axial load was monitored throughout the test and it was found that it varied slightly during the application of lateral actions. The maximum variation in axial force was ±8% the initial value. Details of this aspect will be given in Section 4.3.3.3.

± **300kN cycles** (25% of theoretical first yield)

At this stage no cracks were visible on either sides of the test unit, as predicted by the analysis.

± **600kN cycles** (50% of theoretical first yield)

Minor flexural cracking was observed at column base in the push direction and at 210mm above the base in the pull direction.

± **900N cycles** (75% of theoretical first yield)

More flexural cracking appeared above the existing flexural cracks. Cracks were visible up to 1600mm above the base with a spacing of 130mm. The same flexural cracks were also visible from the inside of the column, indicating that the column wall was entirely cracked. Strains in the longitudinal reinforcement were ranging 1200-1300 με. In the first diameter above the column base shear cracks were also visible (see Figure 4.78 and had an average inclination of 40 degrees from the vertical axis. These shear cracks formed as extensions of existing flexural cracks. As expected, at this stage all gauges on the transverse reinforcement indicated zero strain.

± **1200kN cycles** (theoretical first yield)

More flexural cracking was observed in the upper part of the column (up to about 3200 mm above the base) and more shear cracks formed. The width of shear cracks along the east and west generators reached 0.4 mm. The angle of inclination of diagonal cracks reached a minimum of 30 degrees in the upper part of the column (see Figure 4.79).

The strain in the longitudinal reinforcement at the column base was 0.21% in average while that in the transverse reinforcement along the east and west generators reached a maximum of 0.25%. The top lateral displacement reached at this load stage was used to define the target yield displacement (corresponding to ductility 1.0). The average recorded displacement in the push and pull directions was taken and the displacement at ductility 1.0 was defined as:

$$D_y = \left(\frac{19.36 + 19.5}{2}\right)\frac{1582}{1200} = 25.61mm \qquad (4.4)$$

The behavior showed to be remarkably symmetric, indicating that no major lacks of symmetry were introduced during construction due to inevitable inaccuracies.

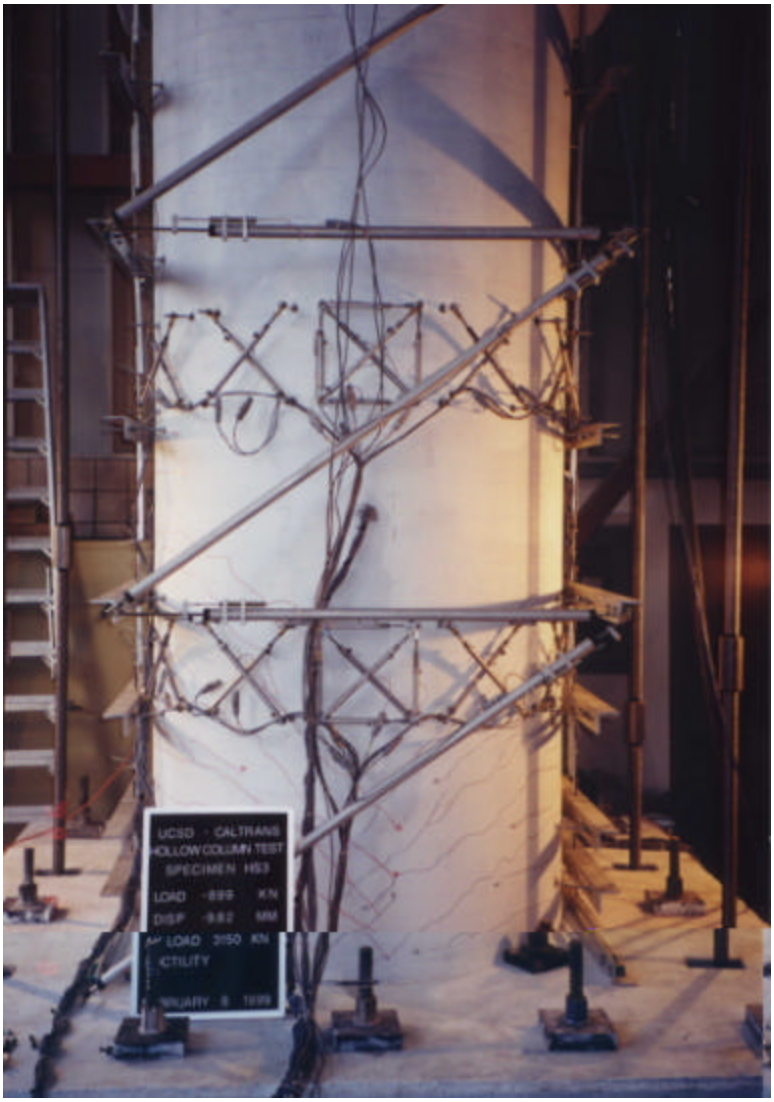

Figure 4.78 Unit HS3 Crack Pattern at 75% of First Yield (Side View)

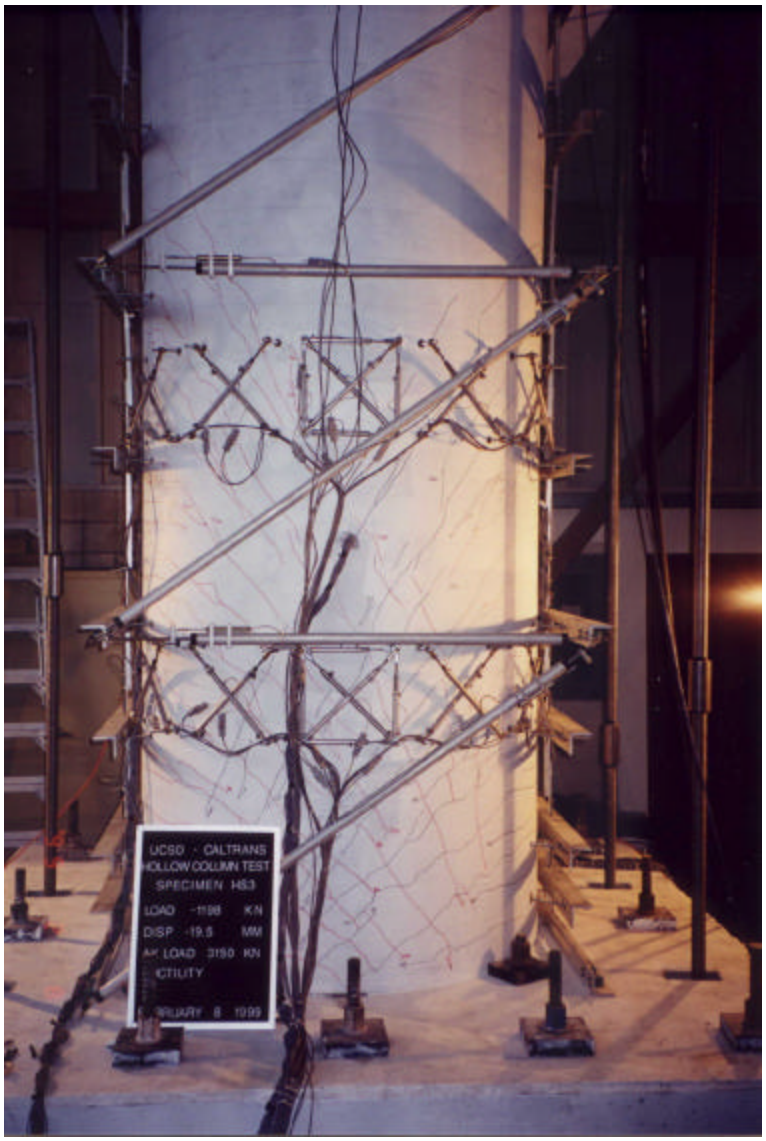

Figure 4.79 Unit HS3 Crack Pattern at First Yield (Side View)

4.3.2.2 Inelastic Cycles

Inelastic cycles were conducted in displacement control, but only one of the actuators was used in displacement control, while the other one was constrained to apply exactly the same lateral force.

m_D=1.0 (3 cycles, drift=0.66%)

More shear and flexural cracks formed. The maximum width of shear cracks was 0.55 mm, while that of flexural cracks was 0.2-0.3 mm. The maximum width of shear cracks was observed at 1.5 diameters above the base, where the strain in the transverse steel was found to be 3400 $\mu\varepsilon$. Repeated cycles at ductility 1.0 induced additional widening of shear cracks, while spacing, width and distribution of flexural cracks remained unchanged. At this stage, no signs of incipient spalling of concrete in the compression area were observed (see Figure 4.80).

m_D=1.5 (3 cycles, drift=1.0%)

Cycles at ductility 1.5 produced moderate concrete spalling in the compression zone (both in push and pull directions). Shear cracks increased in number and in width (0.8-0.85 mm) in the first cycle. In subsequent cycles the same cracks were found to have a width of 1.1mm and the strains in the transverse steel in the critical region reached a maximum of 6000 $\mu\varepsilon$. Note that this was a peak value, while the average along the shear critical region was less than 4000 $\mu\varepsilon$. Longitudinal bars reached the maximum tensile strain of 1%. In the inside of the column, some vertical cracks were observed in locations corresponding to those of longitudinal bars.

m_D=2.0 (1 cycle, drift=1.33%)

While reaching the target displacement at ductility 2.0, significant concrete spalling occurred in the inside face and subsequently in the outside face, causing the column failure (loss of strength of about 50%). Longitudinal rebars buckled and induced rupture of 3 to 4 layers of transverse reinforcement as shown in Figure 4.81. The concrete

spalling in the inside face occurred at approximately 400mm from the base. A similar behavior was found in the pull direction at ductility 2.0, with a drop in strength of 60%. A similar pattern of concrete spalling and rebar buckling was observed. At this point, the axial load was removed and the test was terminated.

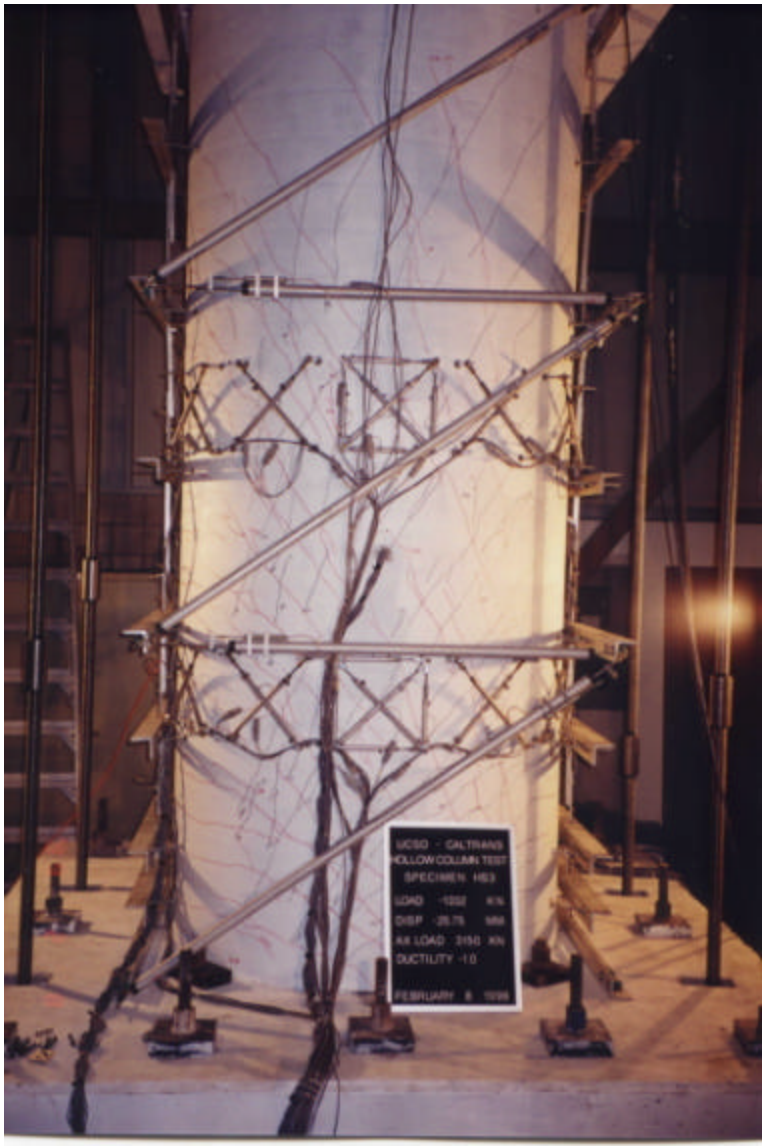

Figure 4.80 Unit HS3 Crack Pattern at Ductility 1 (Side View)

Figure 4.81 Unit HS3 Spiral Bar Fracture at Ductility 2

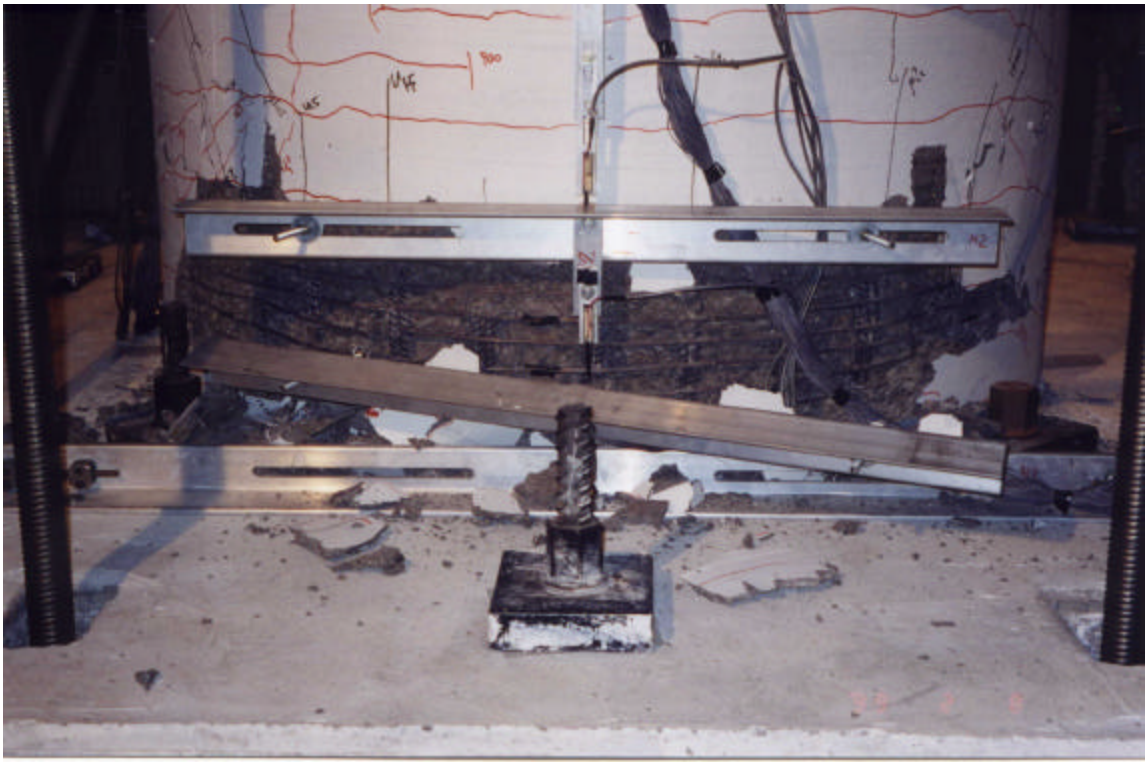

Figure 4.82 Unit HS3 Failure of Compression Zone at Ductility 2

4.3.3 Hysteretic Response

4.3.3.1 Force-Displacement

The force-displacement hysteresis curve was obtained by plotting the total applied lateral force as a function of the lateral displacement measured at the column top. This curve is shown in Figure 4.83. The experimental displacement ductilities is indicated in the top horizontal axis the scale. The predicted envelope behavior and failure points are also indicated in the same graph. The different failure points refer to the UCSD traditional model, the Modified Compression Field Theory, and the finite element analysis conducted with the program FIBER. During the inelastic phase it can be noted that the

repeated cycles at ductility 1.5 in the push direction induced a strength reduction of approximately 15%,due to the moderate concrete spalling.

The behavior predicted with FE analysis was quite accurate in Figure 4.83. The first strength degradation was observed at ductility 1.5, when the analysis indicated high principal compressive stresses. The failure point predicted with MCFT appears to be too conservative. Note that the UCSD model predicts failure with yielding of transverse steel in the shear critical region at ductility 3.0. This would have probably been the case if it was possible for the concrete to resist high compressions. Before the ultimate shear capacity given by the transverse steel was reached, concrete failed in compression.

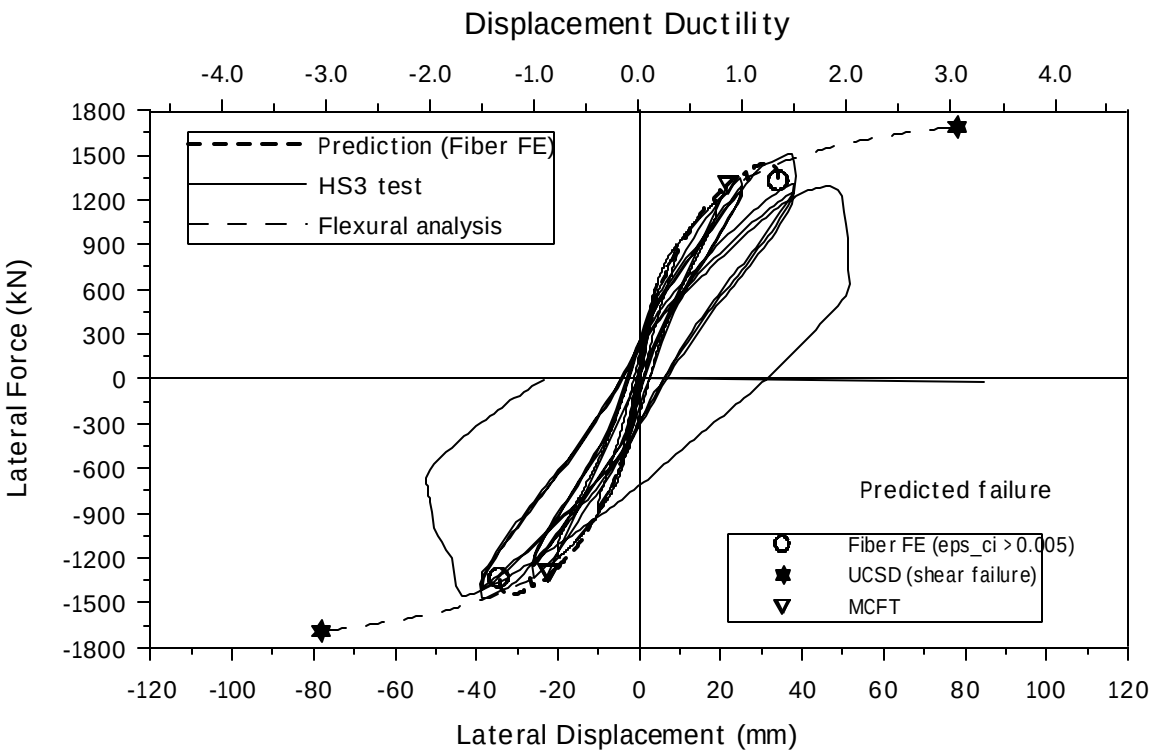

Figure 4.83 Unit HS3 Comparison of Theoretical and Experimental Force-Displacement Response

4.3.3.2 Moment-Curvature

Before presenting the results obtained from the reading of the curvature cells, it has to be pointed out that these instruments did not function properly during the test. Most of these transducers showed a noise in the signal and some showed a behavior that appears to be incorrect. Results should therefore be taken with caution.

In Figure 4.84 the experimental moment-curvature response is compared with the predicted one. Note that the experimental curve includes effects of strain penetration is taken into account. On the predicted curve, the ultimate point corresponding to the shear failures calculated by the UCSD traditional model is also indicated. The top horizontal axis indicates the curvature ductilities as identified from the experimental results. For each peak during the inelastic phase the displacement ductility is also indicated near the peak with a label.

The base cell indicated a non-symmetric behavior in the push and pull direction (as it can bee seen from Figure 4.84. The last experimental point in the curve refers to the first push at ductility 2.0, when the base curvature cell broke. The predicted elastic stiffness differed substantially from the experimental one.

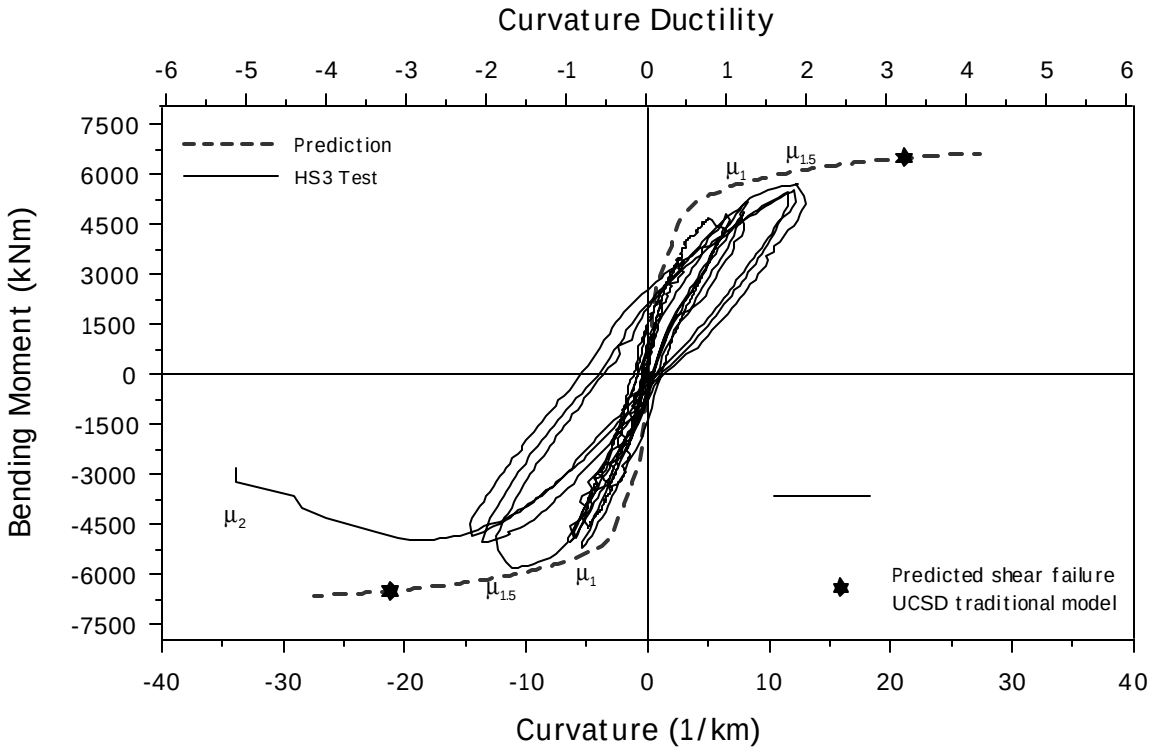

Figure 4.84 Unit HS3 Base Moment-Curvature Experimental Response

4.3.3.3 Axial-Load

Figure 4.85 shows the variation in axial load during the test as a function of the applied lateral displacement. The normalized axial load $\left(P/f_c^{'}A_g\right)$ is indicated on the vertical axis on the right side of the graph. In comparison to previous tests it is observed that a more significant oscillation in axial force for the same level of applied lateral displacement. However, a variation of 8% from the initial value has a negligible influence on the member behavior.

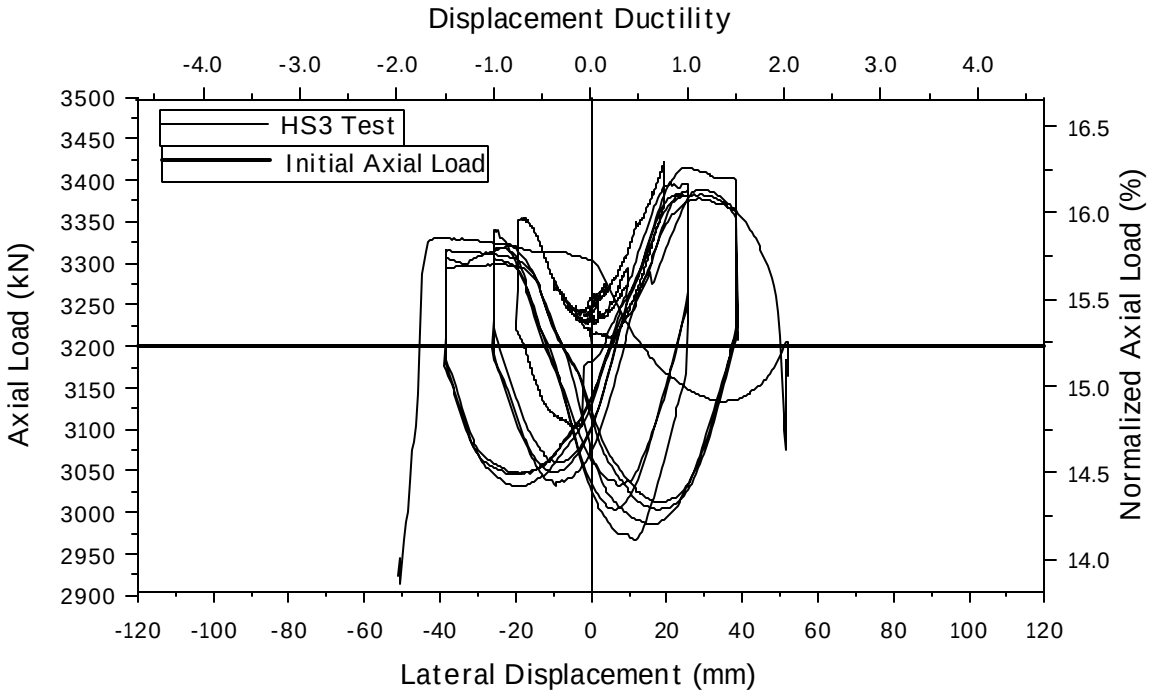

Figure 4.85 Unit HS3 Lateral Displacement/Axial Load Relationship

4.3.3.4 Shear Deformation

The shear behavior was monitored by the shear deformation panels mounted on the east and west sides of the column. As for previous units, each shear deformation panel was divided in three blocks and the results from each of the three blocks are plotted in Figure 4.86. Note that, since the curvature cells did not function properly, readings from the shear panels might be affected by the fact that the change in length of the vertical sides of the panels is not measured accurately. The average ratio of the moment to shear was 3.3 in the bottom panel, 2.12 in the middle panel and 0.93 in the top panel. Refer to the considerations given in Section 3.2 for the meaning of the measured deformations in reading the results from the graphs.

In general the large shear deformation occur in the base region. It appears that the main difference with previous test units is that reasonably large shear deformations also occur in the middle portion of the column, with a non-symmertic pattern in the push and pull direction. This phenomenon has been examined by comparing the results from the

small shear panels, which are not affected by the malfunctioning of the curvature cells. The average shear stiffness does not decrease substantially during the later stages of testing (as it was observed in previous units), since the generalized yielding of transverse steel did not occur over a considerable portion of the column.

The shear behavior was also monitored locally by means of the small shear deformation panels. Refer to Section 3.2 for the location of these instruments. For the moment, the instruments mounted along the east and west generators will be used in order to gain a better insight of the global shear behavior and to check the observations made on the results of the large shear deformation panels. The bottom panel was located at 987mm above the base (where the average moment to shear ratio is 2.8m) and the top panel was mounted at 2012mm (where the moment to shear ratio was 1.9m). Analysis of these two sections under the above said moment to shear ratios was conducted with the Modified Compression Field Theory using the program Response 2000. It was found from Figure 4.87 and Figure 4.88 that the local shear behavior was well captured by this model. In the region near the bottom panel, crushing of concrete in diagonal compression was expected to happen at a shear deformation of 5 mm/m, exactly when it occurred. In the upper portion instead, a maximum shear deformation of 3 mm/m was expected without concrete crushing. The maximum value of 6 mm/m occurring near the bottom panel, essentially confirms the results obtained from the big shear panels.

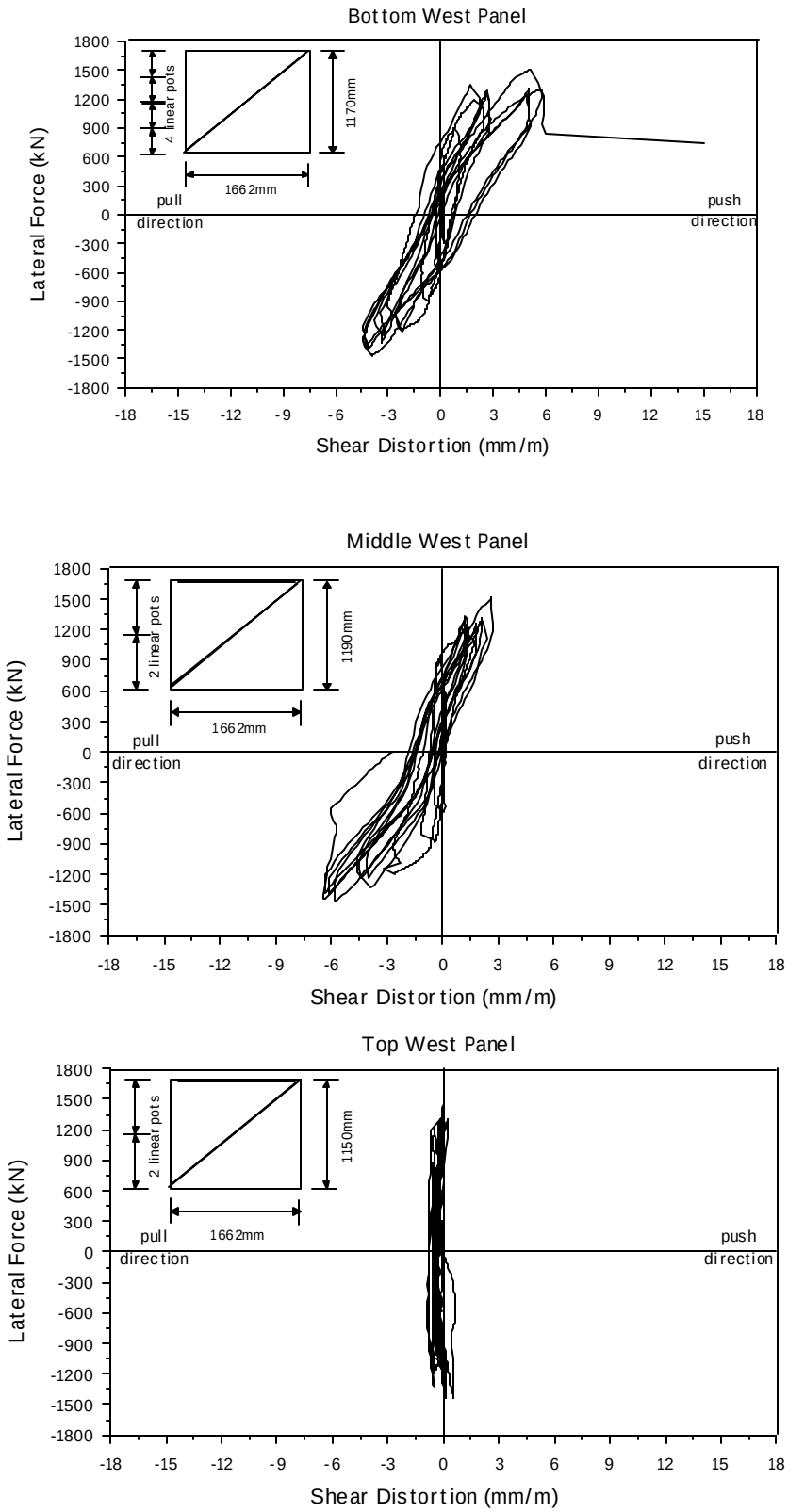

Figure 4.86 Unit HS3 Lateral Force/Shear Distortion from Gross Column Measurements

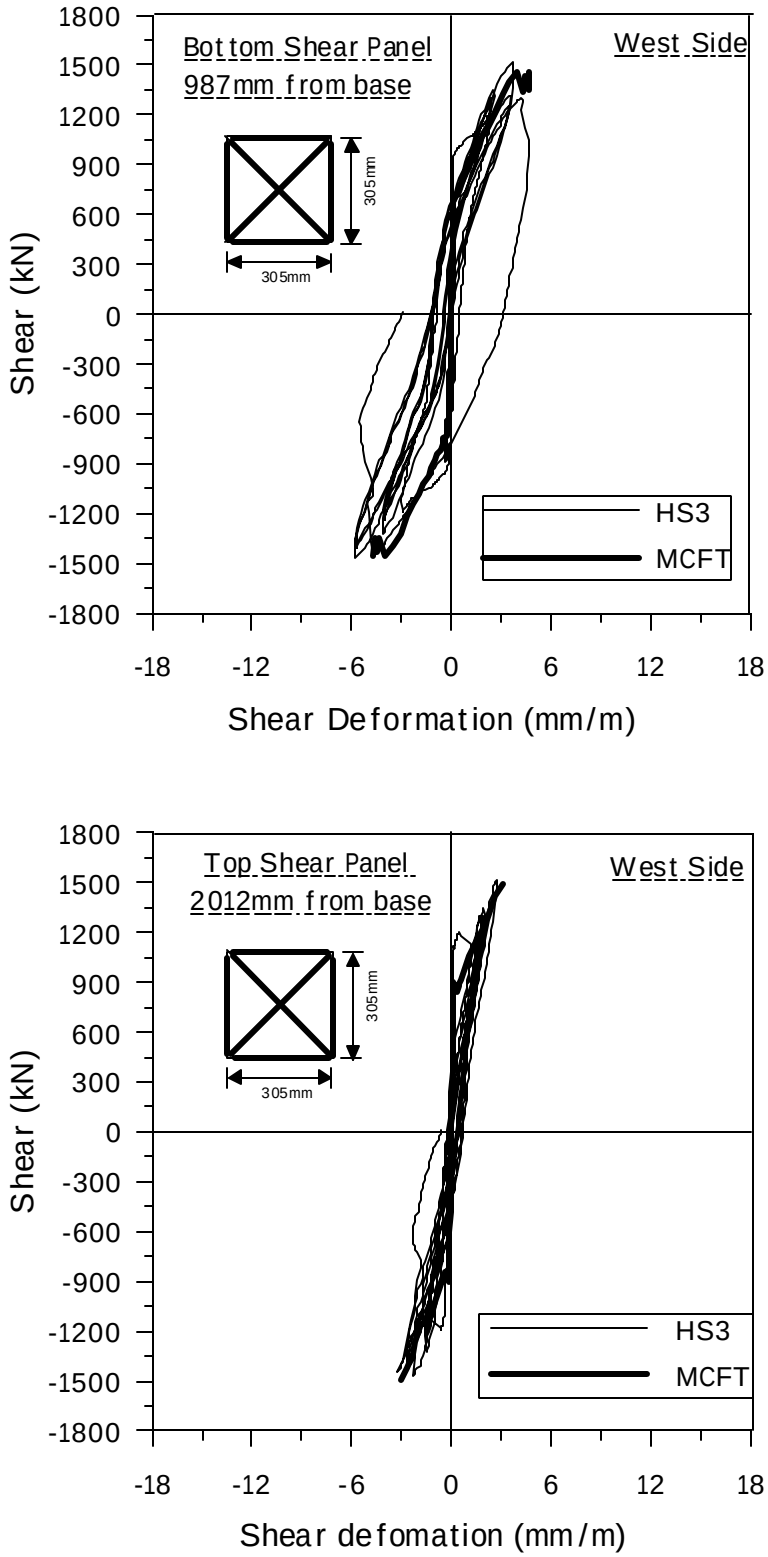

Figure 4.87 Unit HS3 Lateral Force/Shear Strain Forces Small Shear Panels (West Side of Column)

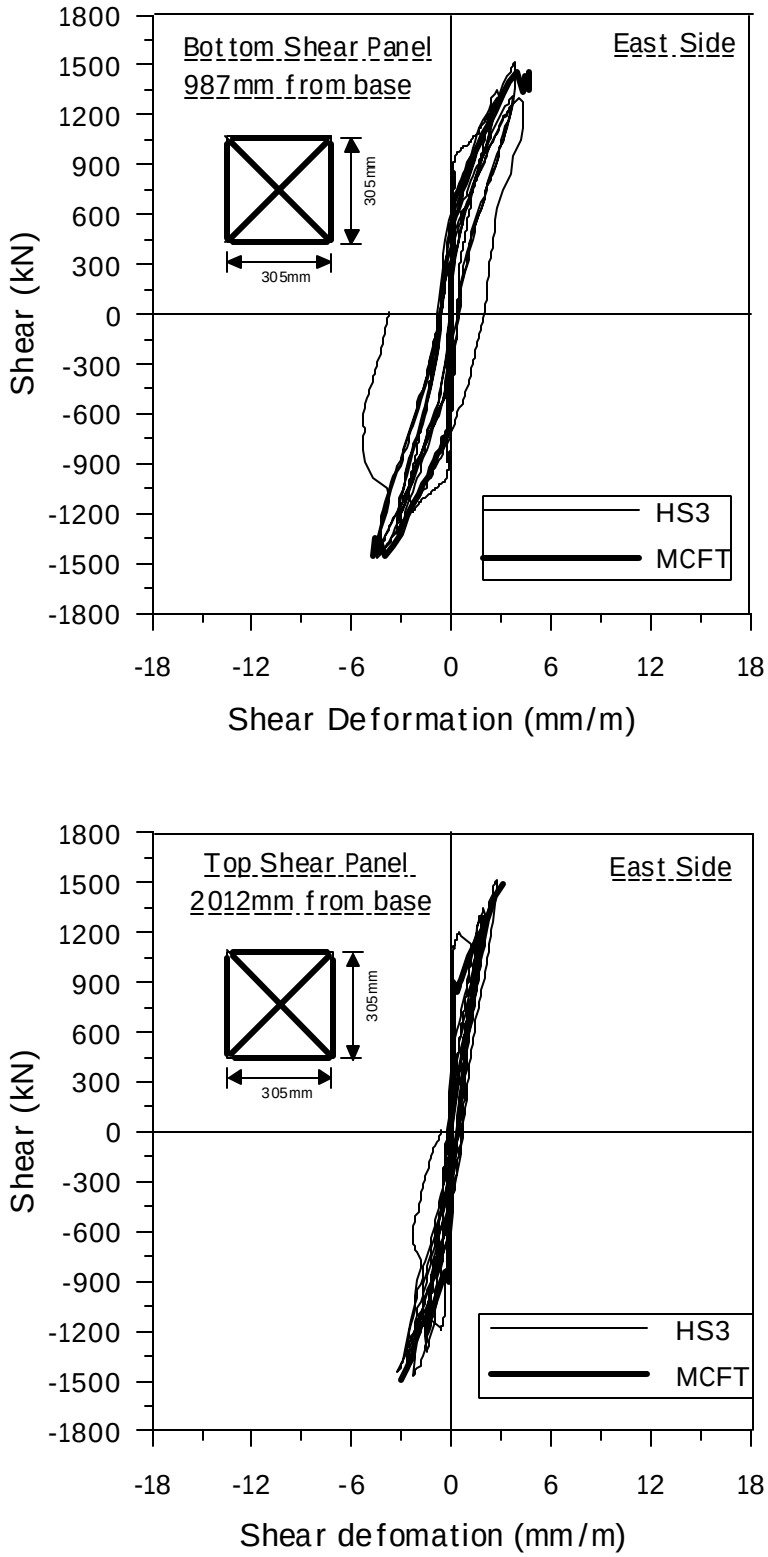

Figure 4.88 Unit HS3 Lateral Force/Shear Strain Forces Small Shear Panels (East Side of Column)

4.3.4 Envelope Response

The envelope response describes the behavior of the structure at the peaks of applied load or displacement. For the load control phase all peaks will be considered, while for the inelastic phase, at each displacement ductility level, only the first peak in the push direction and the last peak in the pull direction will be considered.

4.3.4.1 Displacement Components

Shear and flexural contribution to top displacement are analyzed in this section at each stage of the test. As commented above, measurements from the curvature cells are affected by malfunctioning of some instruments. Since shear deformations were found to be approximately accurate (a double check was conducted with the readings from the small shear panels), it was decided to evaluate the shear component from the shear deformation panels and to back-calculate the flexural component as the difference from the total lateral displacement.

Thus the shear displacement component is computed from the readings of the shear deformation panels. Readings from the east and west panels are averaged to calculate the average shear distortion in each of the three portions of the shear deformation panel. Shear distortions are integrated along the column height to obtain the shear contribution to the total lateral displacement at the column top. The procedure adopted here is only approximate and has the purpose of indicating the order of magnitude of the deformation components and their sensitivity to the applied lateral load or displacement.

In Figure 4.89, shear and flexural deformation components are expressed as a percentage of the total displacement measured on the column top. It can be noted that the behavior is not symmetric in the push and pull direction. However, a similar trend is shown in both directions of loading with respect to the mutual interaction between shear and flexure.

As observed in previous units, the shear component grows rapidly during the elastic phase, reaching a maximum of about 40% of the total displacement at ductility 1.0 in the pull direction. The value corresponding to the last peak at displacement ductility of 2.0 in the pull direction is not reported, since the bracket that supported the first curvature cell collapsed.

In Figure 4.90 the displacement components are plotted as a function of the total displacement measured on the column top. Obviously, in this graph the sum of the computed shear and flexural components is not reported because it is exactly equal to the total measured displacement. The value corresponding to the last peak at displacement ductility of 2.0 in the pull direction is not reported, since the bracket that supported the first curvature cell collapsed during the test.

In Figure 4.91 the shear and flexural components to the top displacement are plotted as a function of the applied lateral load. It is observed that significant shear deformations appear only at the 1200 kN cycle.

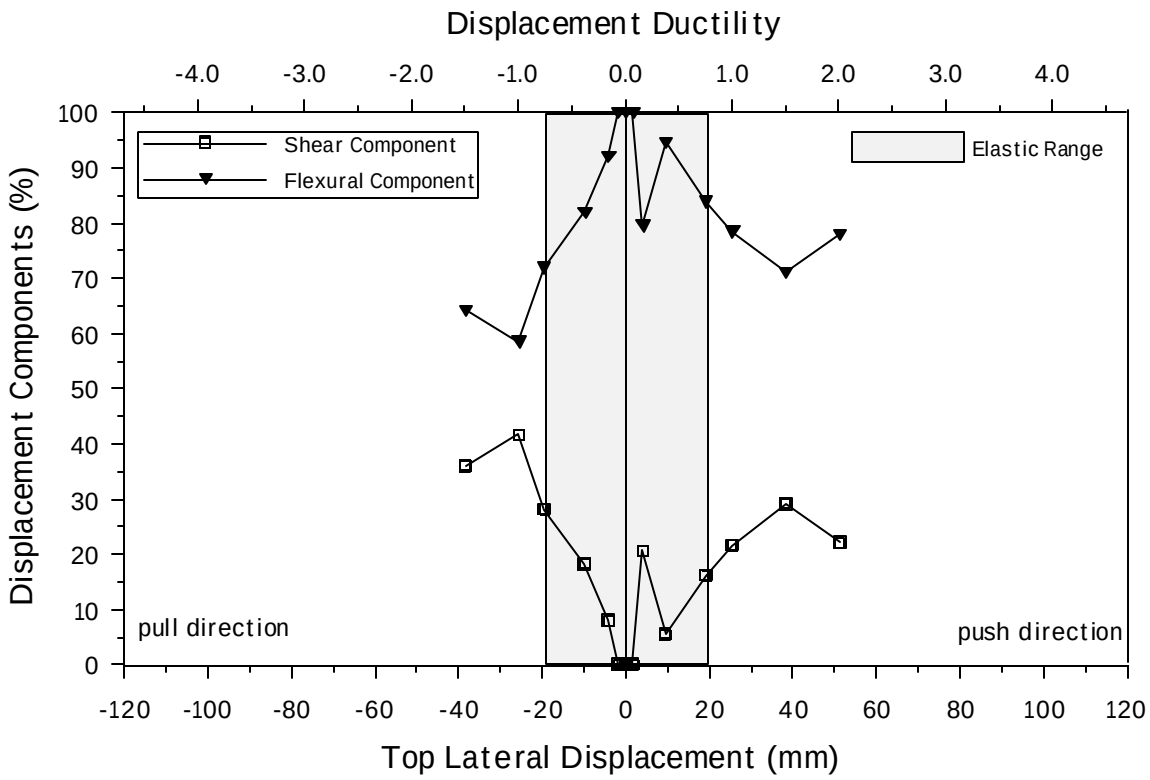

Figure 4.89 Unit HS3 Shear and Flexural Components of Total Displacement

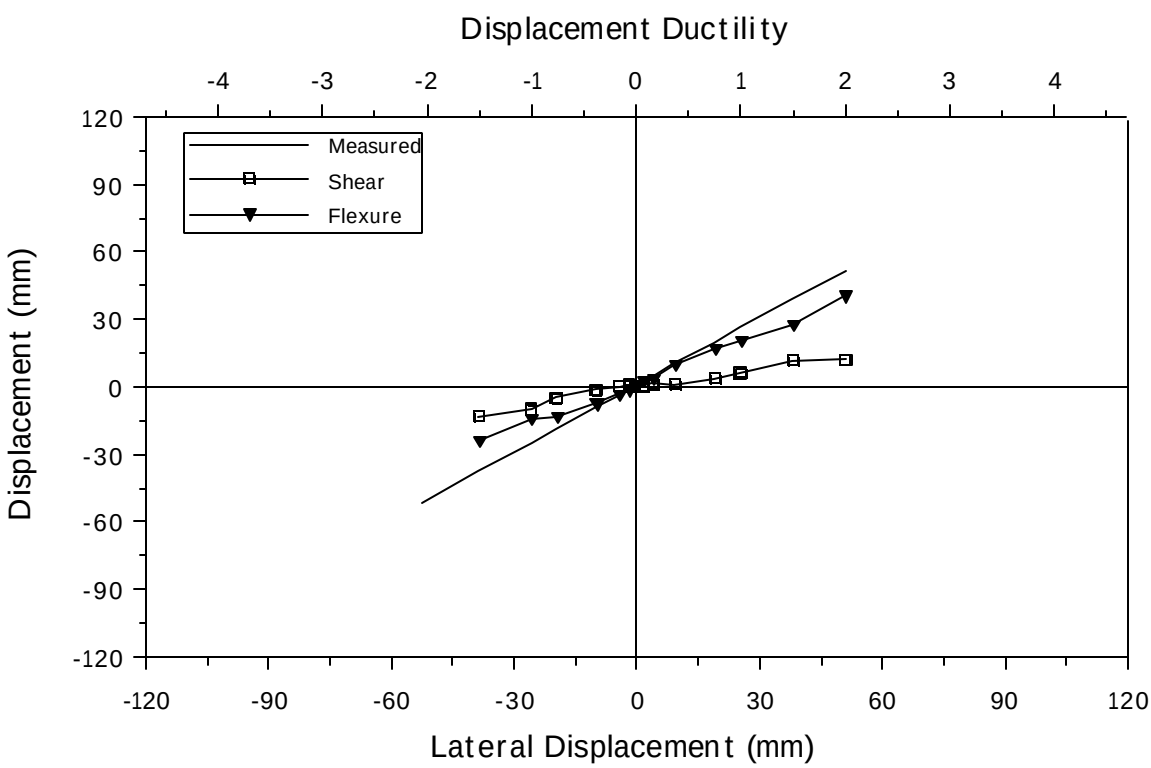

Figure 4.90 Unit HS3 Displacement Components vs Total Top Displacement

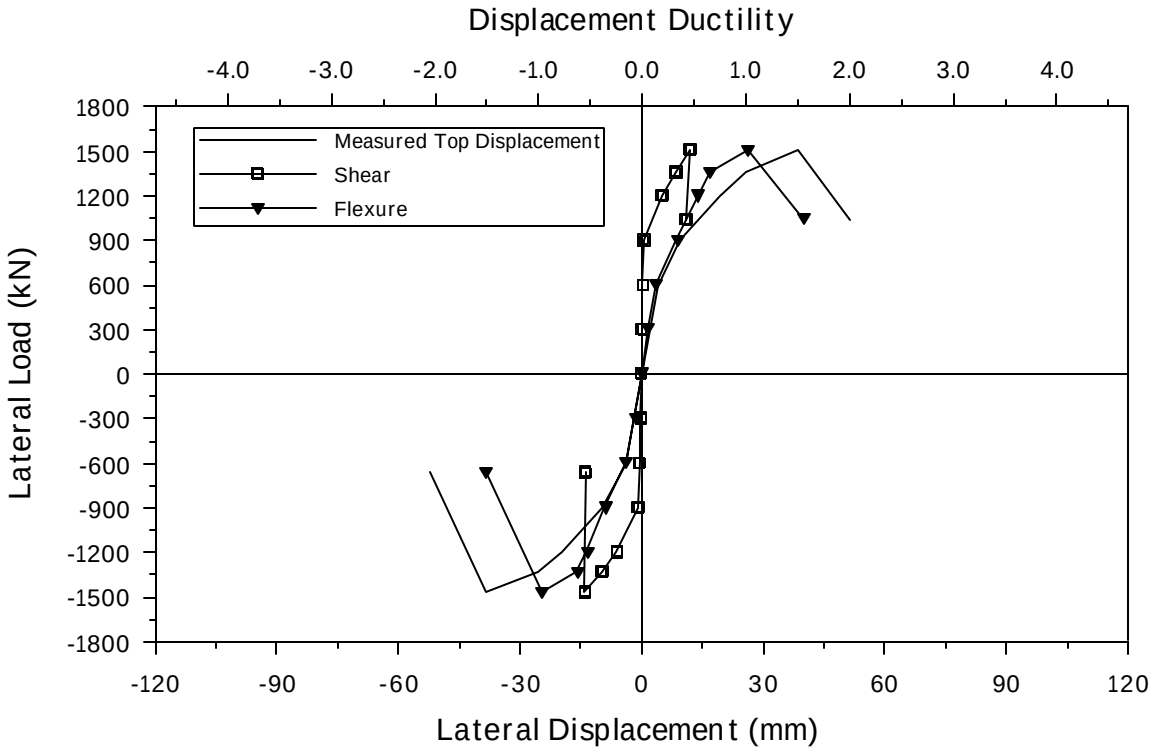

Figure 4.91 Unit HS3 Lateral Force/Displacement-Component Response

4.3.4.2 Plastic Hinge Length

Because of the low ductility achieved by Unit HS3, no meaningful measurements of plastic hinge length were possible.

4.3.5 Profiles at Peak Load (or Displacement) Levels

Strain or displacement profiles describe the distribution of a generic deformation parameter along a line on the structure at peak load or displacement levels. Profiles can be plotted along the column height or over the section depth in order to describe the distribution of a deformation parameter for increasing lateral forces.

Profiles are presented herein for each load step in the push and pull direction during the load control phase (elastic range). During the inelastic phase instead, profiles are

presented for the first peak in the push direction and for the last in the pull direction, at each displacement ductility level. The behaviors during the elastic and the inelastic phases are printed in different graphs, adopting different scales in the horizontal axis. The load stages in the elastic phase are identified with a label indicating the load level in kN, while load stages in the inelastic phase are identified with the displacement ductility level.

4.3.5.1 Flexural and Shear Deformation Components

As it was discussed above, shear and flexural deformations vary along the structure as a function of the applied lateral force. In fact, these deformation components have significantly different distributions along the column height. Shear displacement profiles are obtained by computing the lateral displacement due to shear at the top of each of the three portions of the shear deformation panels. Flexural displacement profiles are obtained instead by plotting the lateral displacement due to flexure at the top of each of the 8 curvature cells.

The malfunctioning of some curvature cells strongly affects the evaluation of the flexural components. It is observed from Figure 4.93 that large flexural deformations seem to occur during the elastic range of response (compare this graph with those of column HS1 and HS2, note that the horizontal axis has a different scale). Also, the behavior appears to be definitely non-symmetric both in the elastic and inelastic stages of testing.

Comparing the results presented in Figure 4.92 with those from unit HS1 and HS2, shear deformations seem to be of the same order of magnitude for the same level of applied lateral displacement. The profiles look also similar in shape. Clearly, shear deformations in the middle portion of the column are comparatively higher in this unit than in the previous ones.

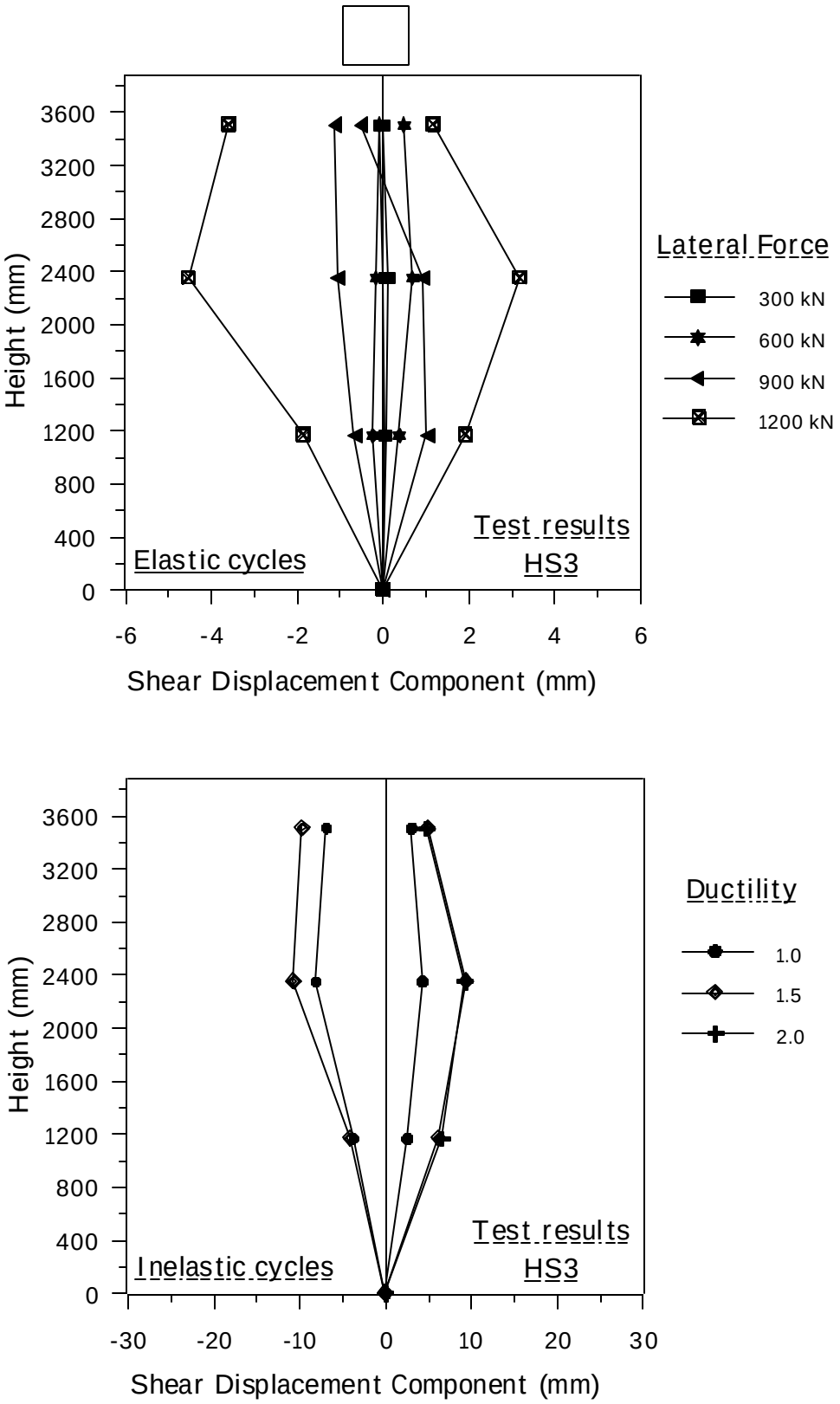

Figure 4.92 Unit HS3 Shear Displacement Profiles at Different Ductilities

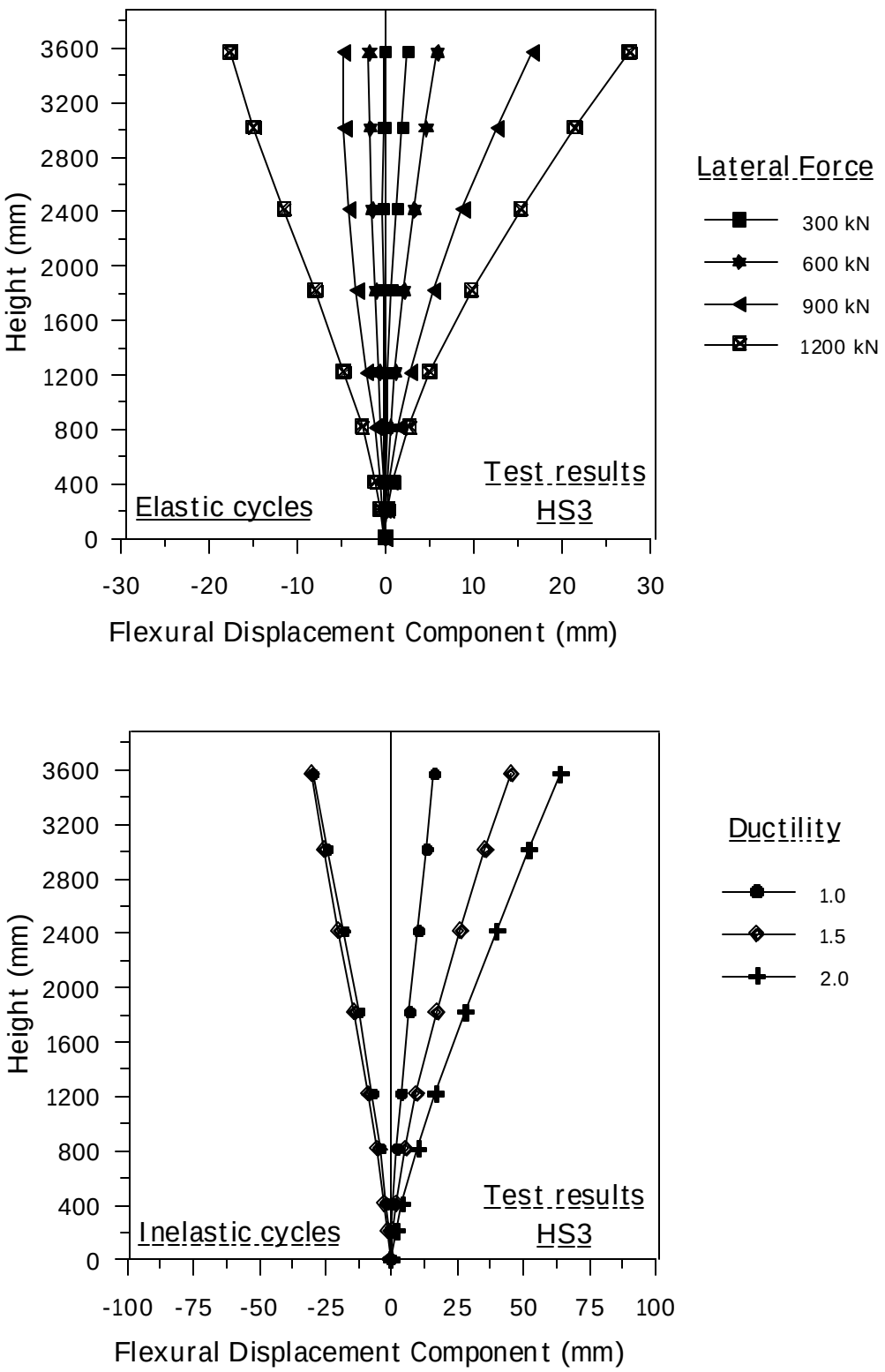

Figure 4.93 Unit HS3 Flexural Displacement Profiles at Different Ductilities

4.3.5.2 Curvatures

Curvature profiles are presented here in Figure 4.94 and Figure 4.95. In the first case the effect of strain penetration is not accounted for. The curvature obtained from readings of the first curvature cell is supposed to be the averaged value over the cell height and is therefore plotted at mid-height of the first curvature cell (108 mm from the column base). In the second graph the effect of strain penetration is taken into account by considering a revised height of the first curvature cell according to the equation described in Chapter 2. In this case the curvature value obtained from the reading of the first curvature cell is supposed to occur at mid-height of the revised cell height (18.7 mm above the column base). It can be seen that the influence of strain penetration on the value of the base curvature is considerable. In fact, in this case the strain penetration, is rather high (158 mm) when compared to the height of the base curvature cell (215 mm).

Note that the yield curvature, calculated by using the procedure described in Chapter 2 from the curvature at first yield of longitudinal rebars, is equal to 3.0 rad/km. During the inelastic phase it can be noted that the region where the curvature exceeds this value in the plastic hinge region is contained within the first 600 mm above the base. The behavior is also not symmetric in the push and pull directions. The profiles in the push direction indicate negative values in the upper part of the column during the elastic stage of testing. Even if these readings are not very accurate, it can be noted that there is a localization of flexural inelastic response in the base region. This will be confirmed by reading the strain profiles along the longitudinal reinforcing bars.

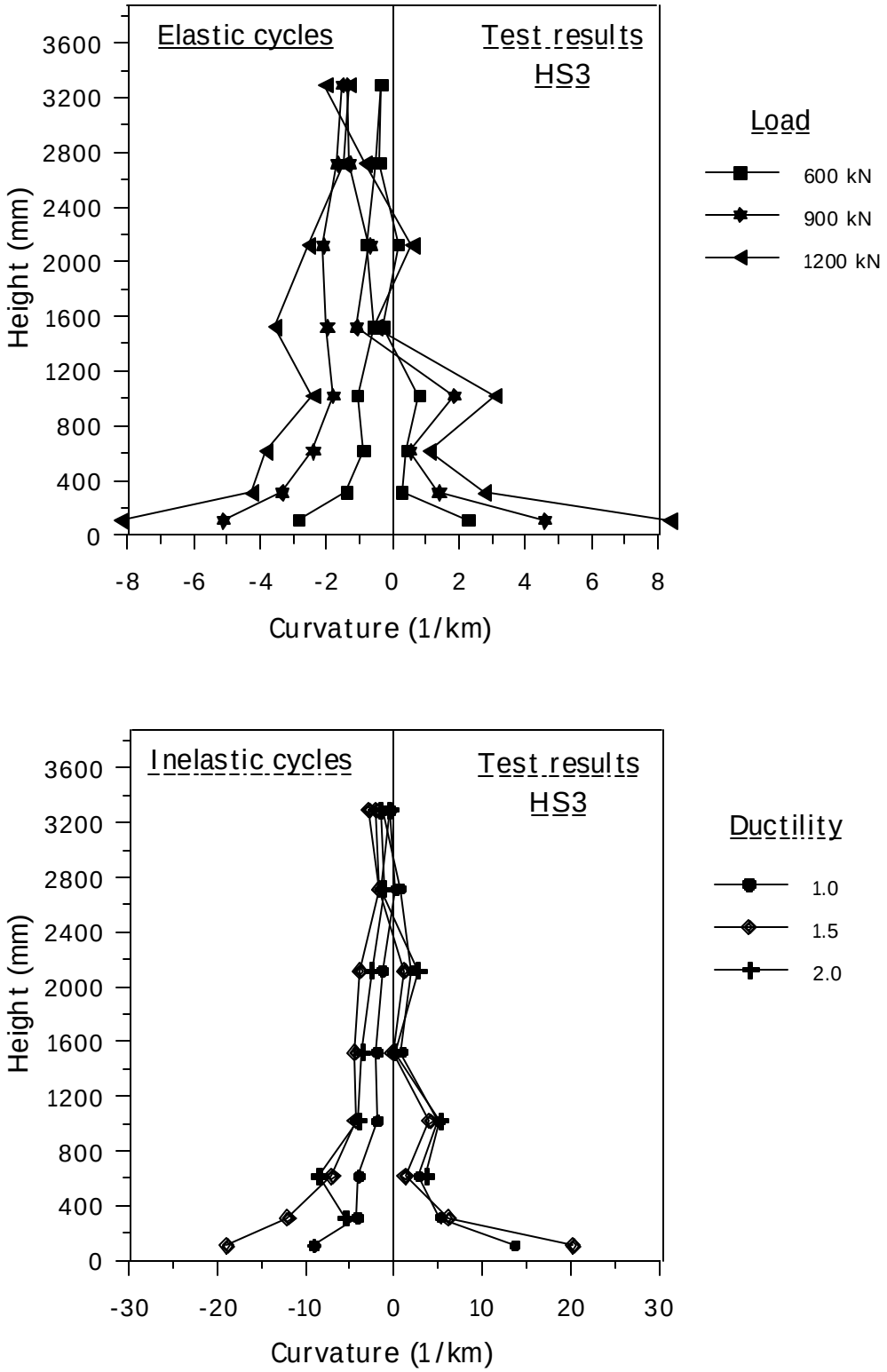

Figure 4.94 Unit HS3 Curvature Profiles at Different Ductilities – Strain Penetration Ignored

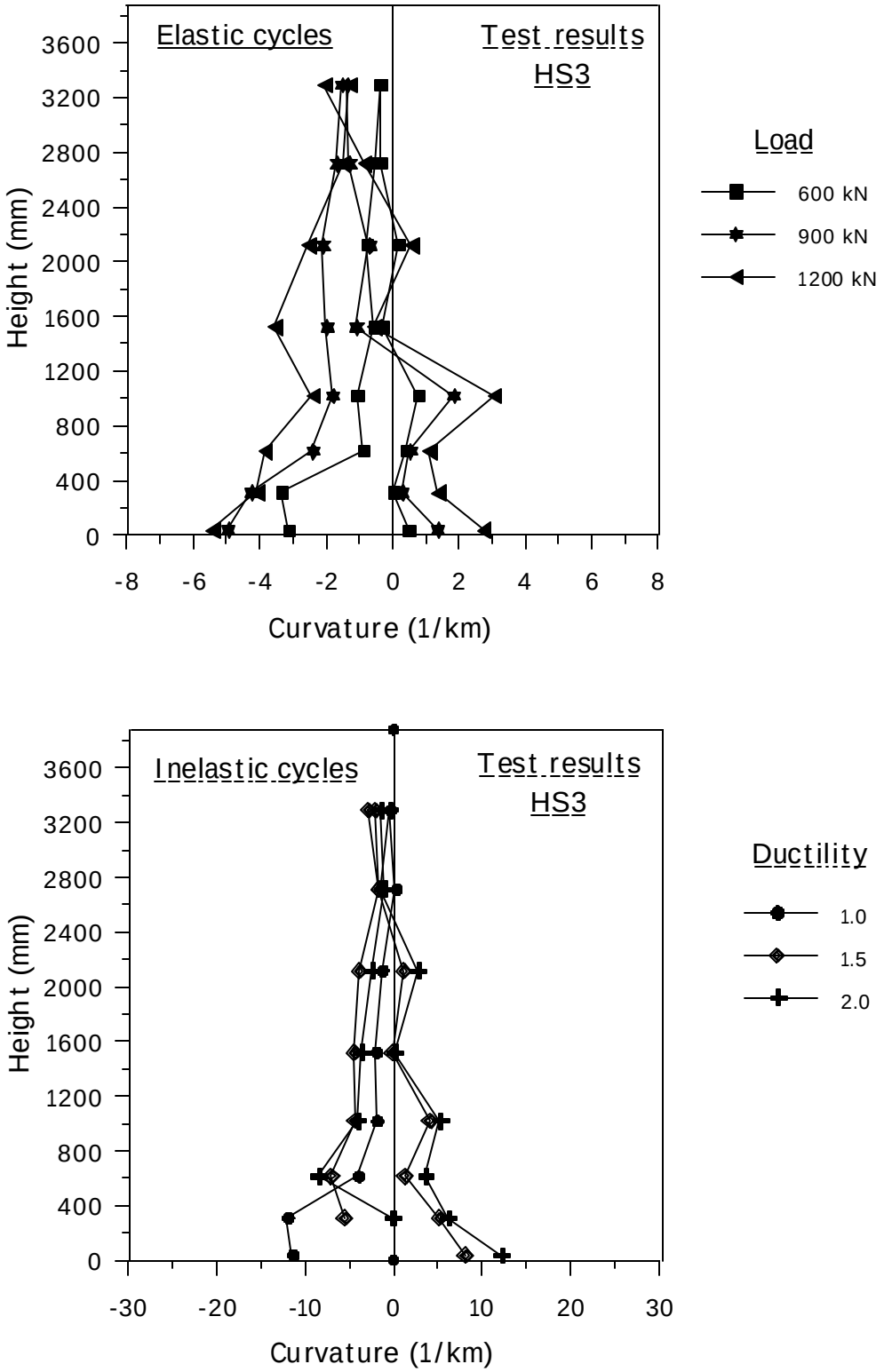

Figure 4.95 Unit HS3 Curvature Profiles at Different Ductilities – Strain Penetration Included

4.3.5.3 Longitudinal Reinforcement Strains

From Figure 4.96 and Figure 4.97 it can be noted that strains in the longitudinal bars have a uniform profile during the elastic phase. It is also evident that the strain penetration effect has less significant effect than in the unit HS2, even if the size of the longitudinal bars is the same. In fact, it can be seen that in the inelastic cycles, the longitudinal strains do not exceed the yield point at 100 mm below the column base (see south bar). This was instead the case in unit HS1.

While the profiles appear to be uniform during the elastic stages as observed in previous units, during the inelastic stages inelastic deformations are localized within the first 600 mm above the column base.

The behavior of longitudinal bars in compression indicates very high strain values (close to -1%) at 300 mm above the column base (both on the north and south bar). As observing from the photographic documentation, buckling occurred involving several layers of transverse reinforcement.

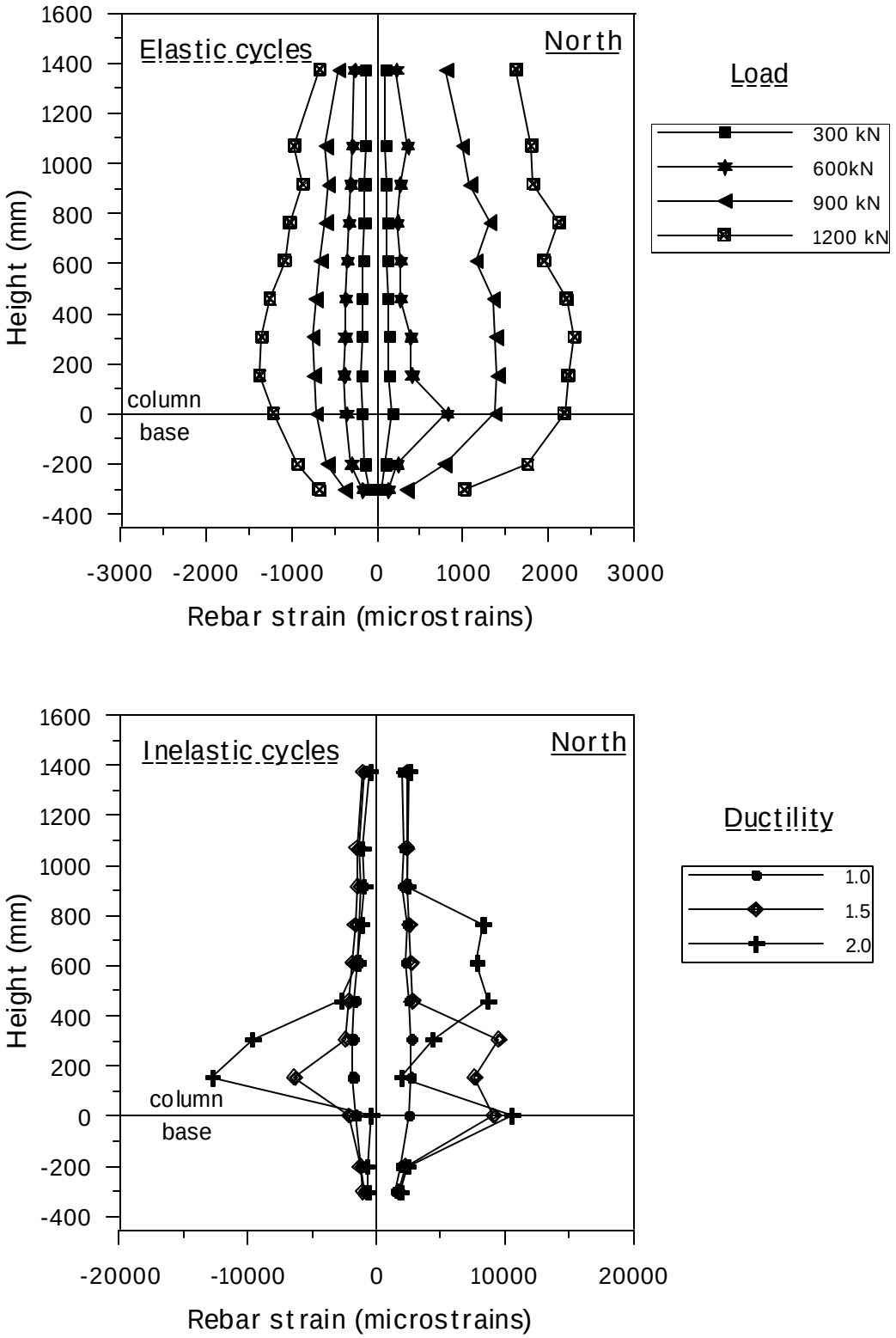

Figure 4.96 Unit HS3 Profiles of Longitudinal Rebar Strain at Extreme North Tension Location (Push Loading)

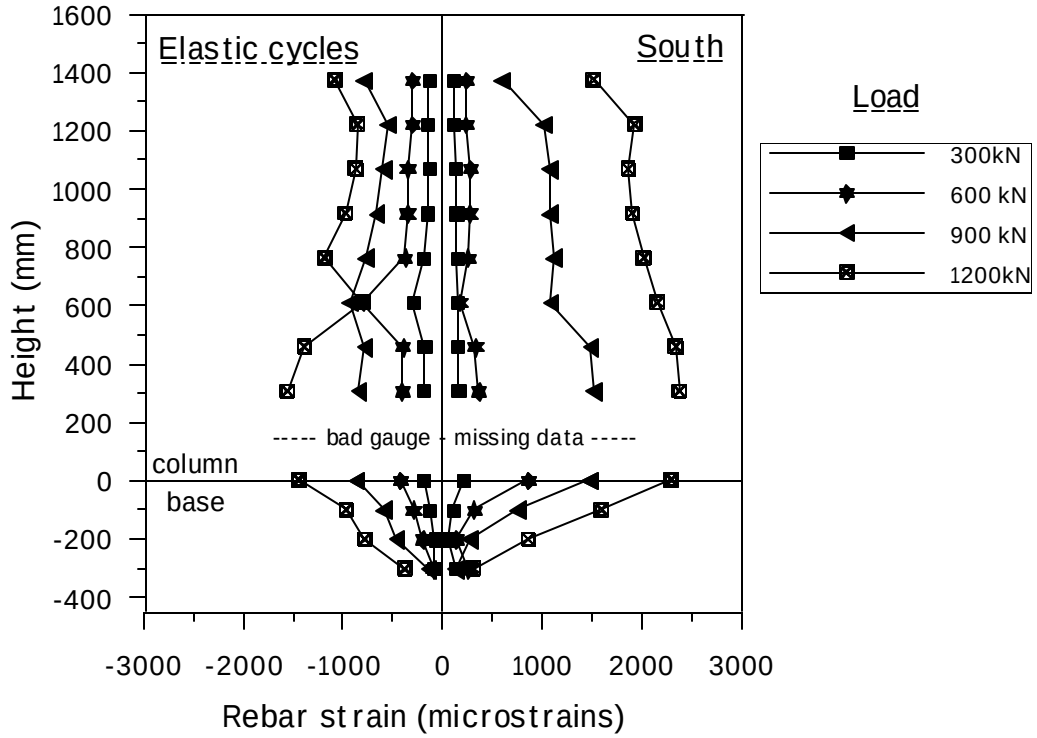

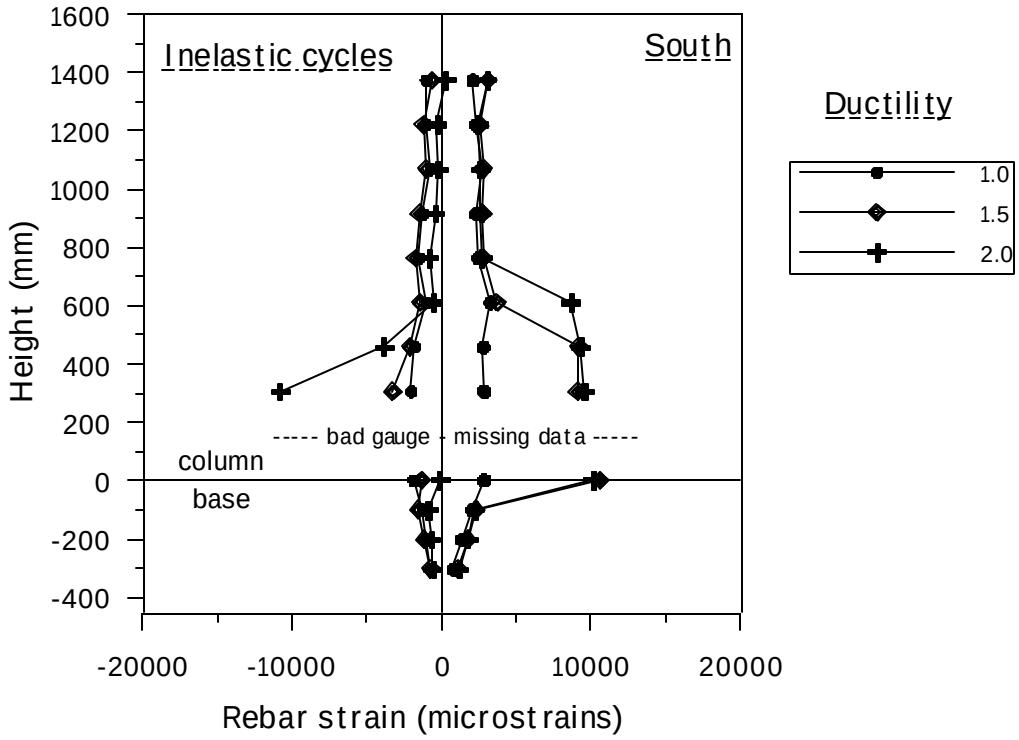

Figure 4.97 Unit HS3 Profiles of Longitudinal Rebar Strain at Extreme South Tension Location (Pull Loading)

4.3.5.4 Transverse Reinforcement Strains

Profiles of the strains recorded in the transverse reinforcement along the west and east generators are plotted in Figure 4.98 and Figure 4.99, respectively. Elastic and inelastic phases are plotted in the same graphs, while push and pull directions are differentiated in separate graphs.

It is observed that both in the push and pull directions strains exceed 4000 $\mu\varepsilon$ only in the ductility 2.0 cycles. High strains occur only in one or two locations, while the rest of the critical region maintains a lower average strain. The material testing indicated a rupture strain of 1-1.5% in average. The maximum strains occurred between 0.5 and 1.5 diameters above the column base. The restraint operated by the footing in bottom region (up to 400 mm above the base) has the same effect observed in previous tests, with low strains occurring at column base. Significant strains appeared at the 900 kN cycle in the bottom part of the shear critical region, where the damage was more consistent. Subsequently, deformation in the spiral extended up to about 2700 mm above the base. The behavior along the east and west generators appears to be quite different with larger strains occurring along the east generator.

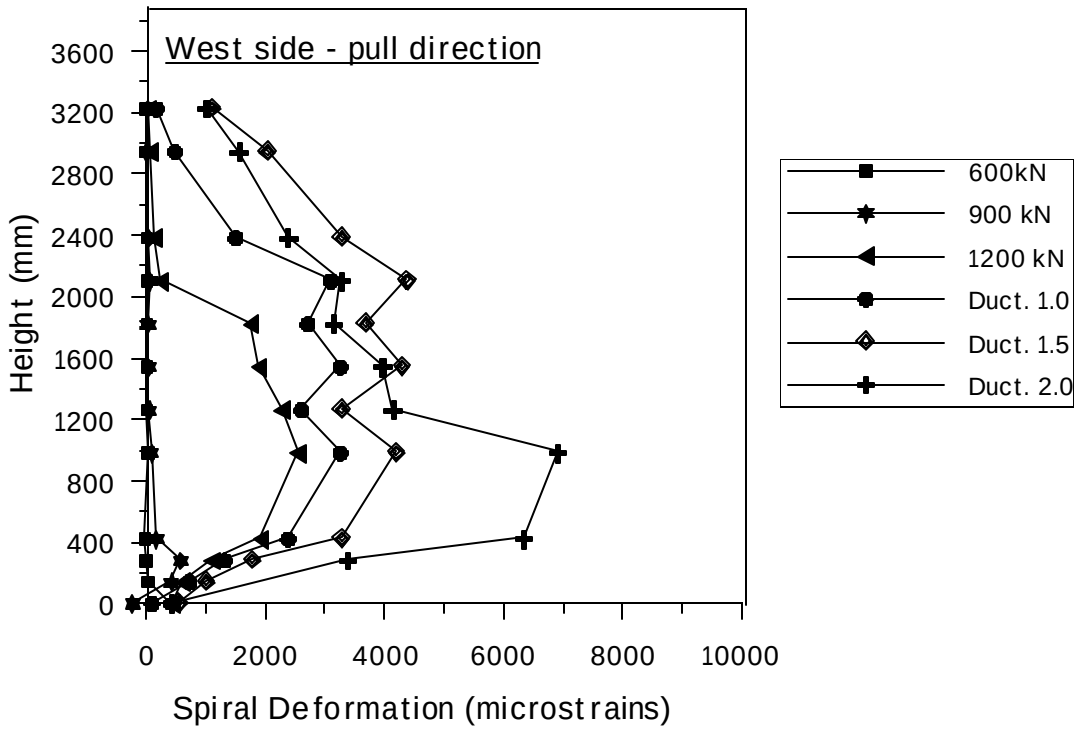

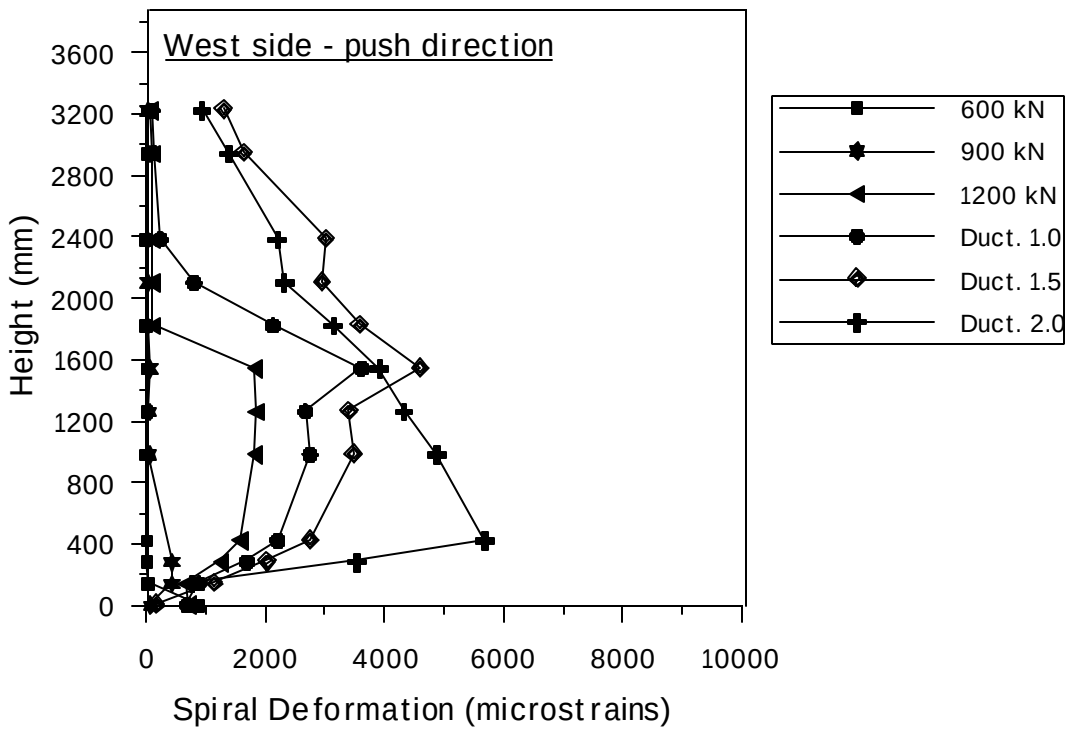

Figure 4.98 Unit HS3 Vertical Profiles of Spiral Strain on West Side

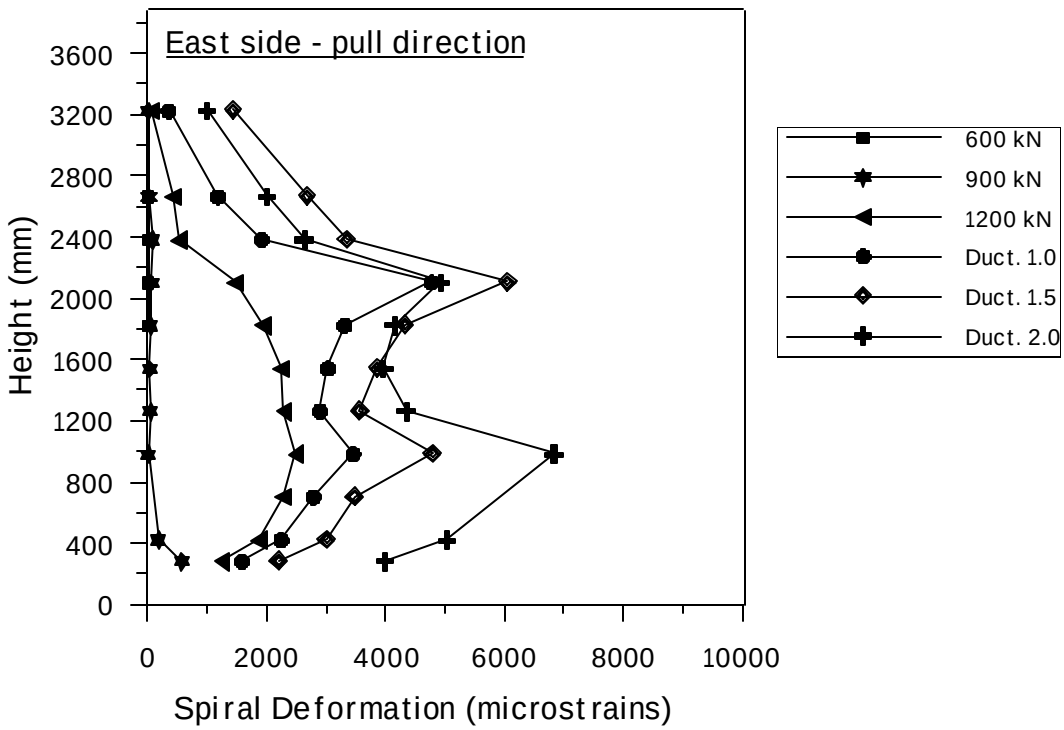

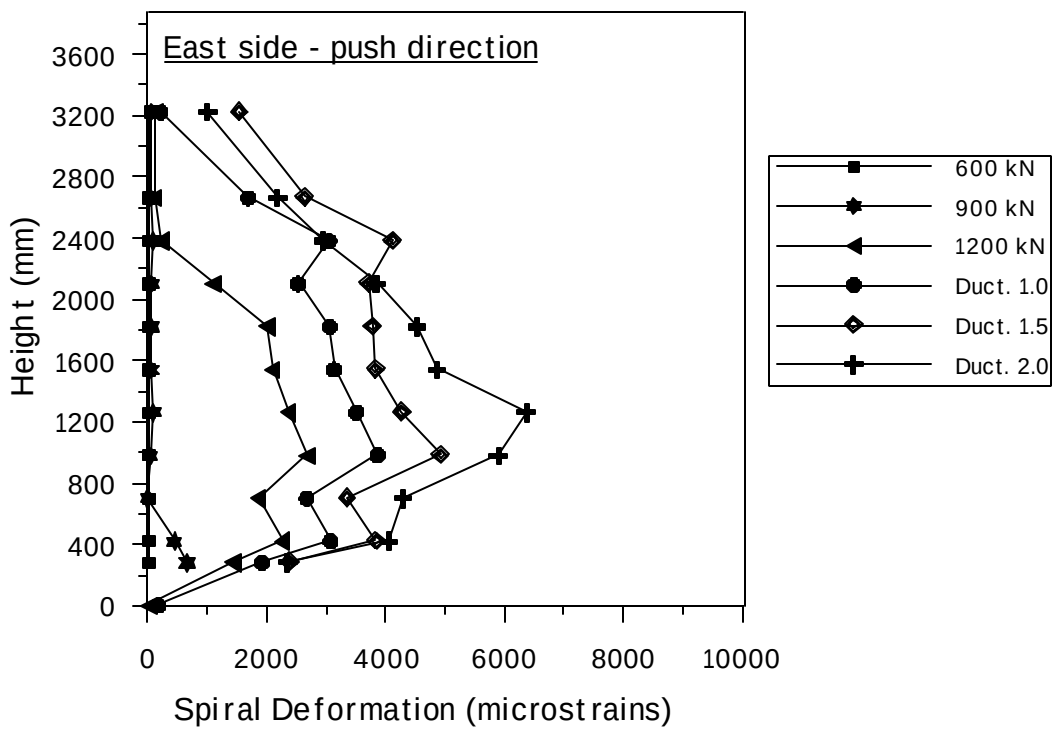

Figure 4.99 Unit HS3 Vertical Profiles of Spiral Strain on East Side

4.3.5.5 Section Longitudinal Strain Profiles

The distribution of the longitudinal strains over the section depth is analyzed in Figure 4.100 to Figure 4.105 for three different sections: one below the column base and two above the column base. The first section is at 102 mm below the column base, where it was observed that the longitudinal rebars strains in tension reached but did not exceed the yield point. The second section is at 152 mm above the base, where we it is expected to have reasonably accurate readings up to the later stages of testing. In this section, the profile was calculated based on the readings from 5 longitudinal bars. The third section, located at 609 mm above the column base is out of the predicted plastic hinge region, where only occasionally reaching the yield point in bars was found.

The longitudinal strain profile is obtained by plotting, for the same section, the strain values recorded along the north and south bars, located at extreme tension and compression sides of the unit, and the average value of the east and west gauges. For the section at 152mm above the base the same procedure was adopted in five (rather than three) different locations. The horizontal axis indicates the location of the gauges expressed as the distance from the section centroidal axis. The analysis of these three sections is carried out to provide a clear description of the region where inelastic flexural actions occurred. Different plots are provided for the push and pull direction, dividing into elastic and inelastic stages of testing. In the graphs two vertical dashed lines are provided in order to indicate the location of the inside face of the column wall. An additional continuous horizontal line is provided in the graphs to indicate the steel yield strain. As reported before, this type of steel has a well defined yield point at 2300$\mu\varepsilon$. In the first section (below the column base) there is an average compression depth of approximately 250 mm, slightly less than what was observed in the same section in previous units. In the second section (152 mm above the base) it is quite complex to evaluate the depth of the compression zone, but it should probably be around 400 mm. This is definitely more than what was observed in previous units due to the presence of a significantly higher axial load. It is also evident the lack of symmetry of the behavior in the push and pull directions.

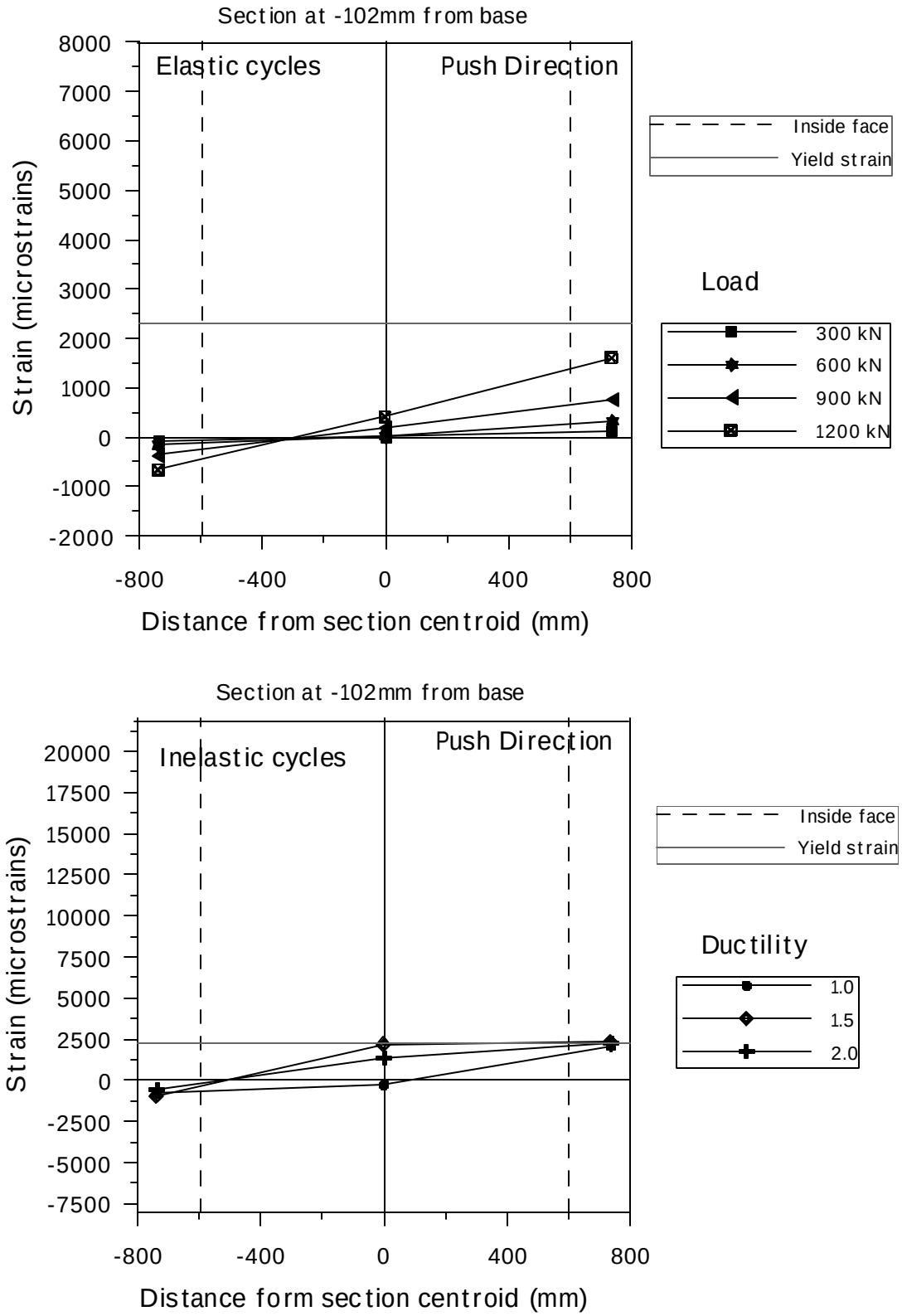

Figure 4.100 Unit HS3 Section Longitudinal Bar Strain Profiles 102 mm Below Base Section, Push Loading

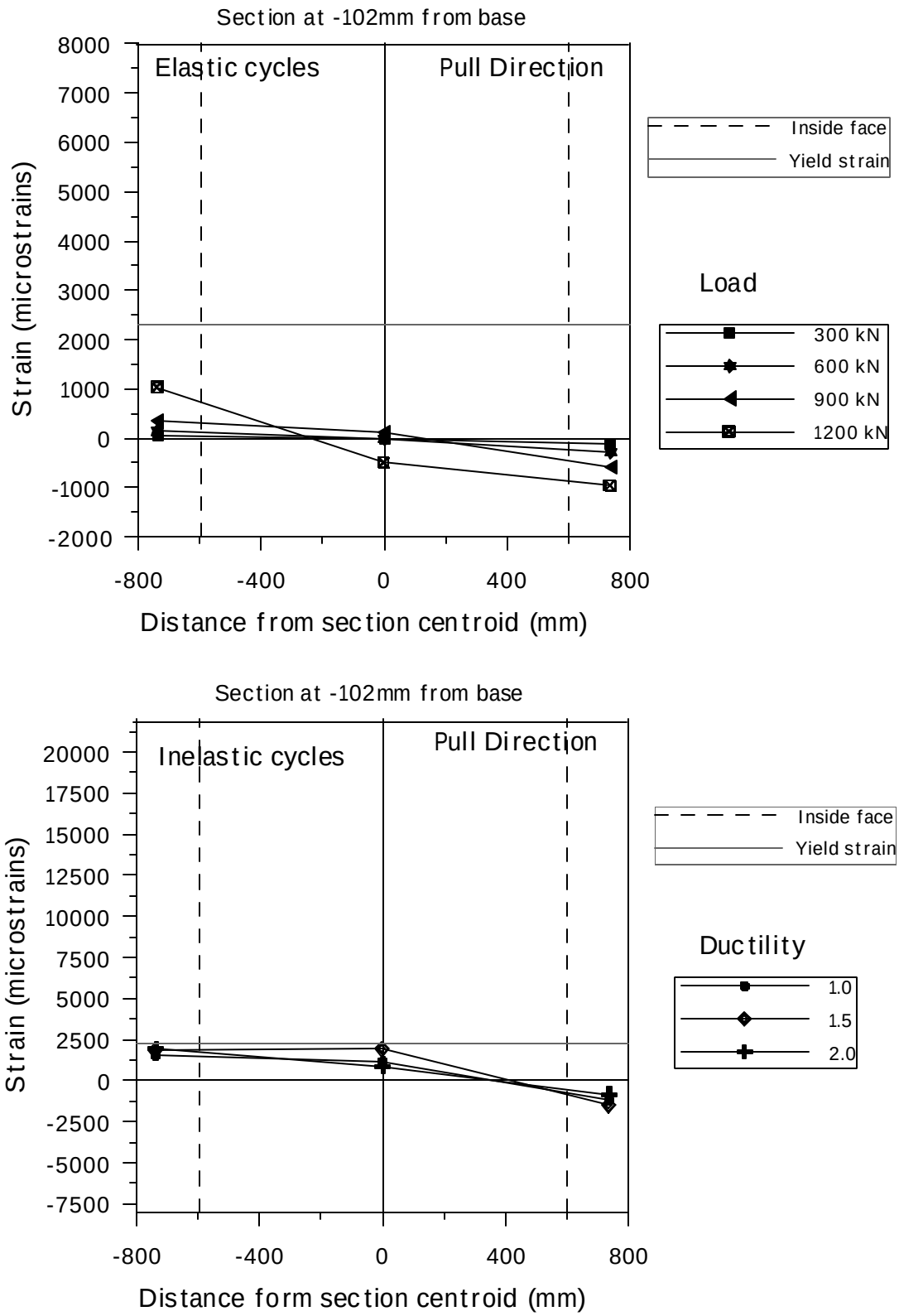

Figure 4.101 Unit HS3 Section Longitudinal Bar Strain Profiles 102 mm Below Base Section, Pull Loading

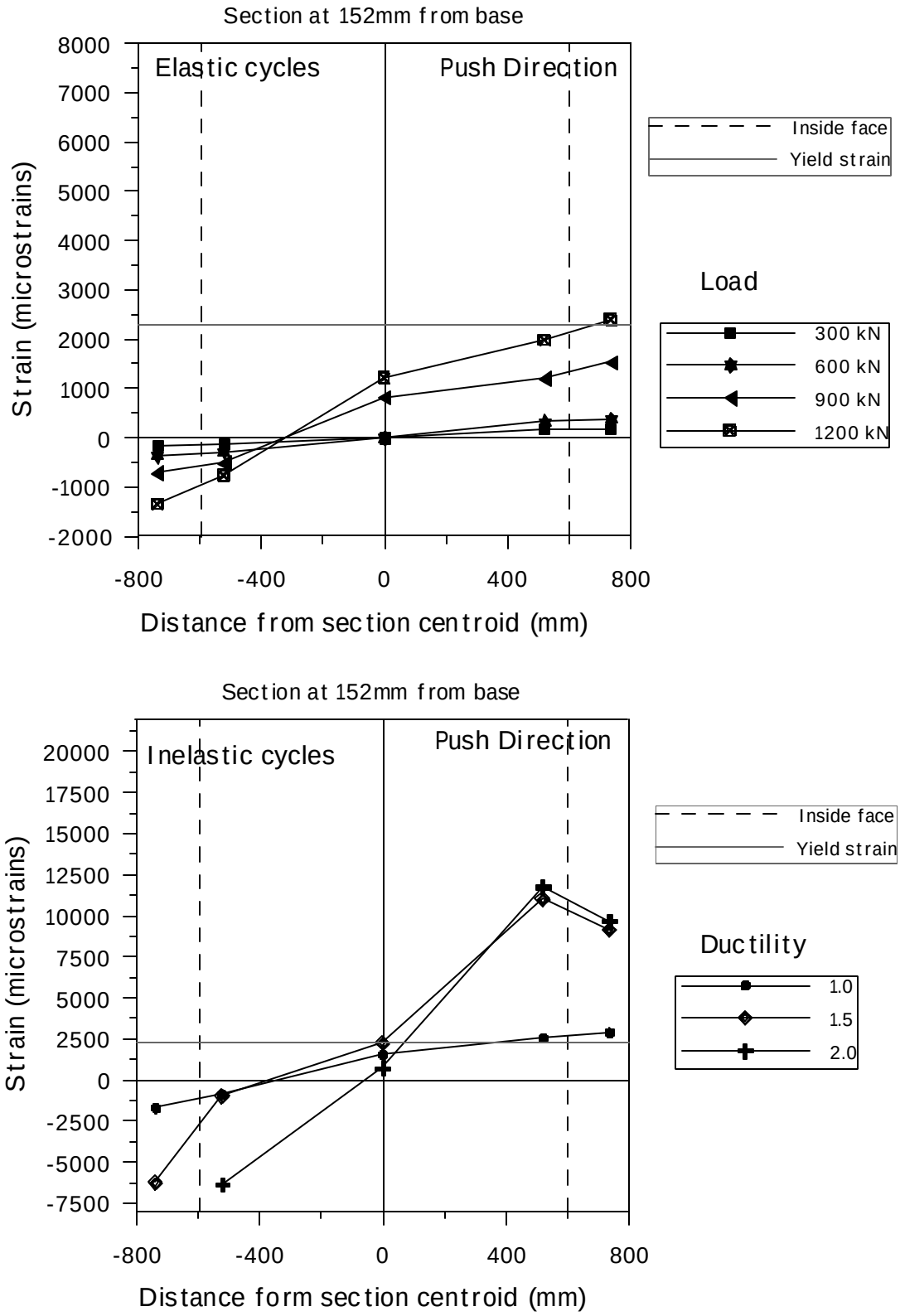

Figure 4.102 Unit HS3 Section Longitudinal Bar Strain Profiles 152 mm Above Base Section, Push Loading

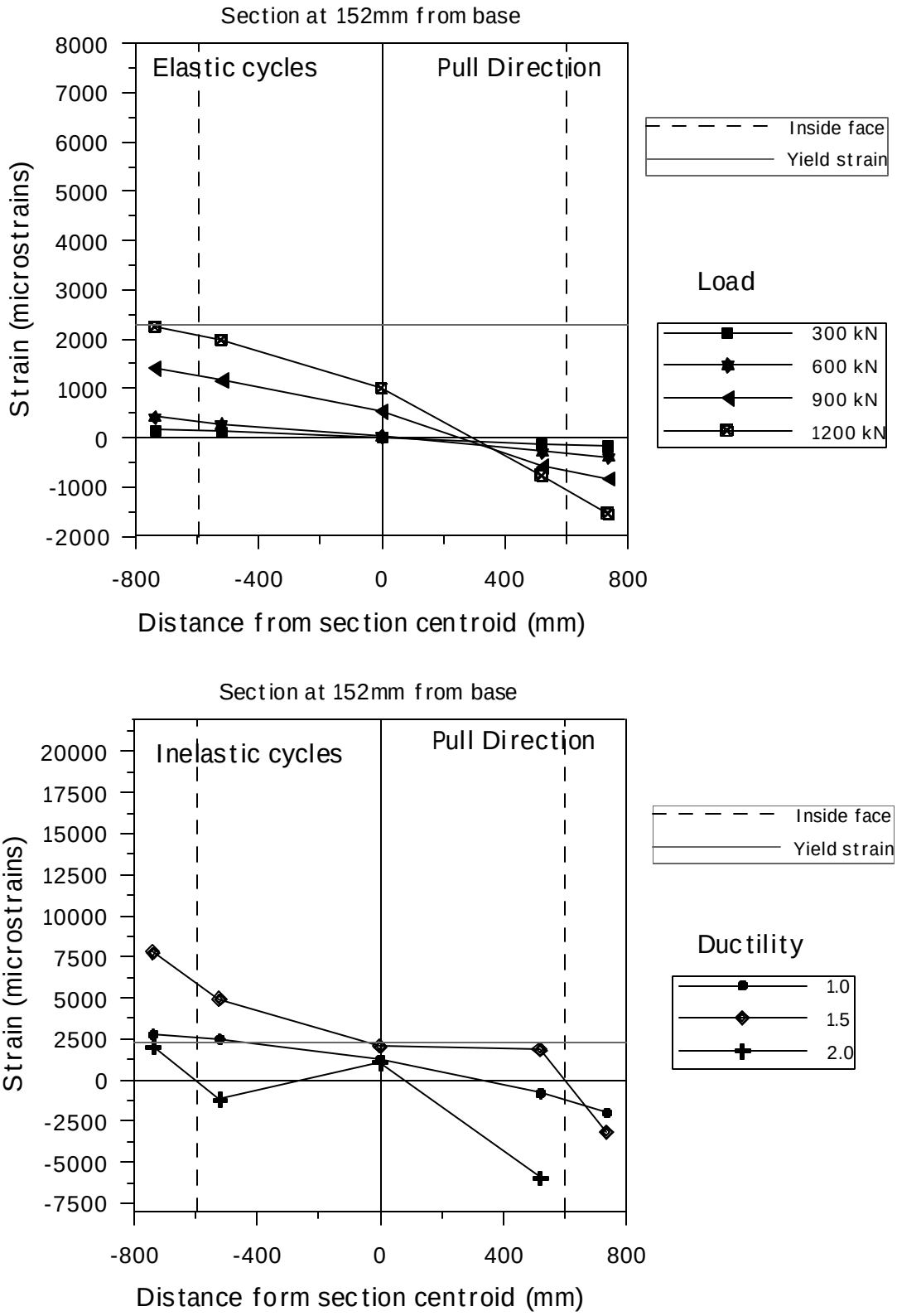

Figure 4.103 Unit HS3 Section Longitudinal Bar Strain Profiles 152 mm Above Base Section, Pull Loading

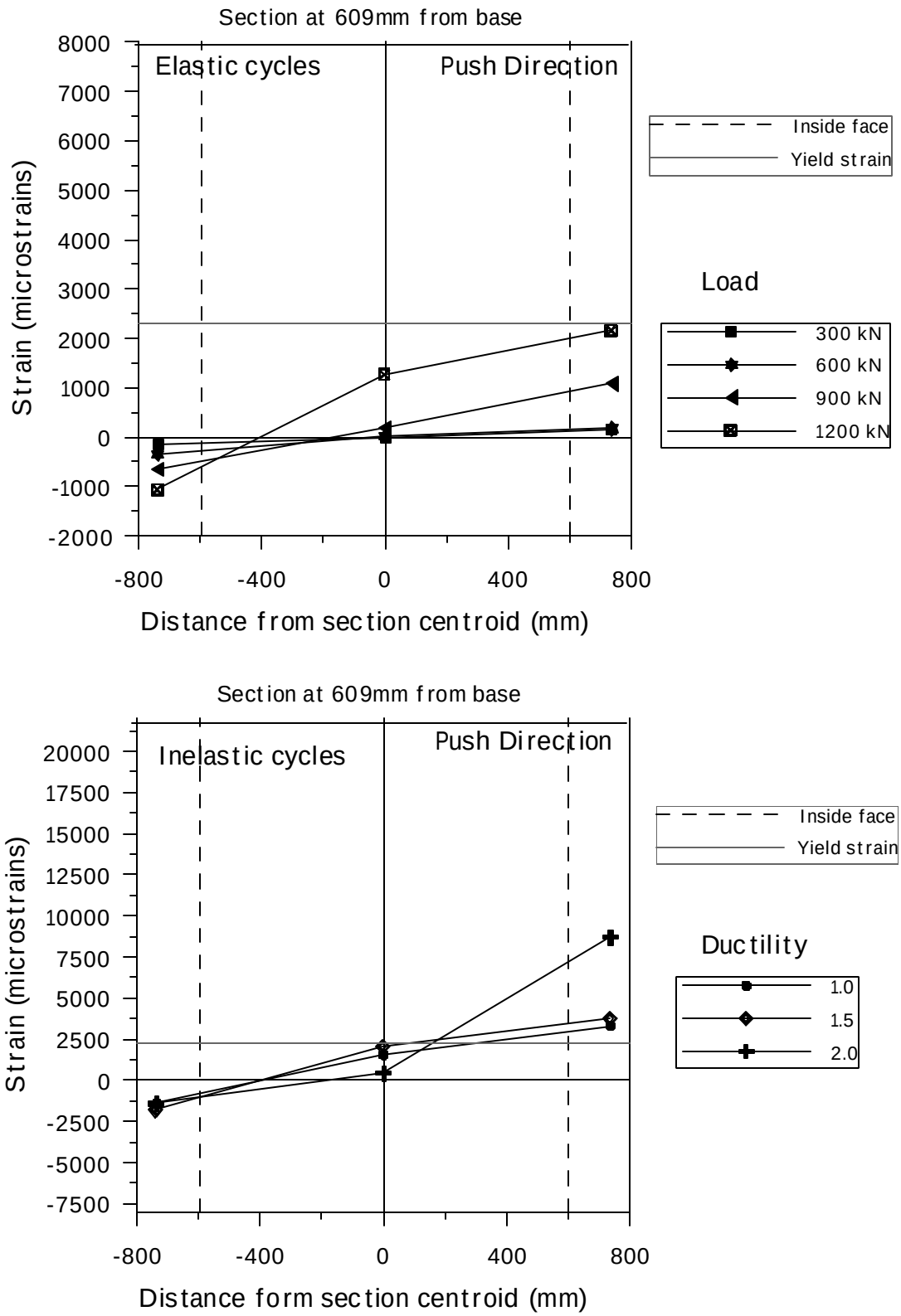

Figure 4.104 Unit HS3 Section Longitudinal Bar Strain Profiles 609 mm Above Base Section, Push Loading

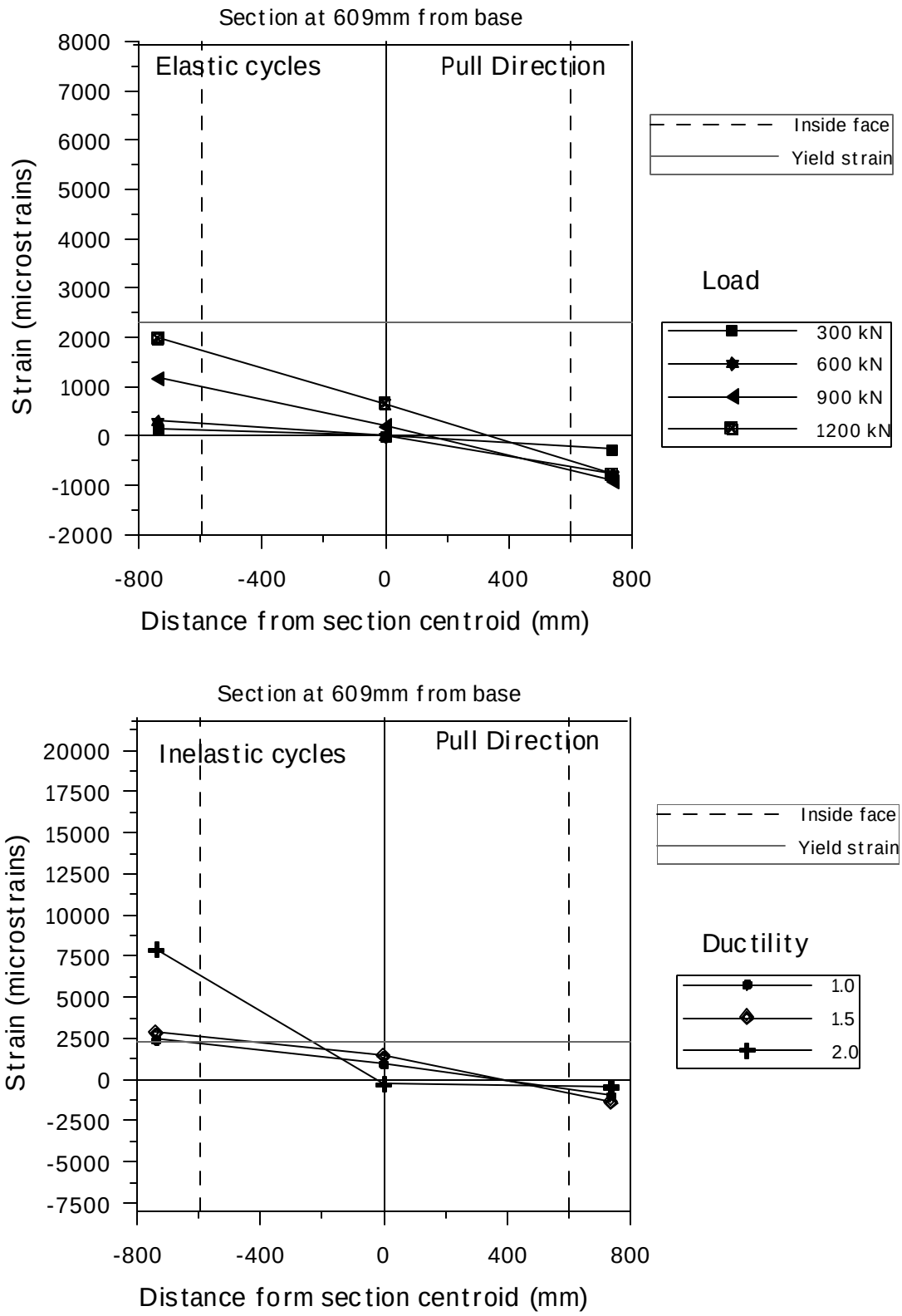

Figure 4.105 Unit HS3 Section Longitudinal Bar Strain Profiles 609 mm Above Base Section, Pull Loading

Very high compressive strains (up to -0.6%) are recorded in this section. These values should be treated with caution since at later stages of testing buckling occurred in this region. In the section at 609 mm above the base, the compression zone is significantly deeper than in previous units. This is because inelastic strains do not occur in this section and the compression due to the axial load keeps the neutral axis closer to the section centroid.

4.3.5.6 Section Transverse Strain Profiles

Transverse strains recorded on the spiral reinforcement are plotted as a function of the distance from the section centroid, with the same format used to describe the distribution of longitudinal strains over the section depth. In this unit there are five instrumented points over the section depth. As observed in unit HS1, maximum strains tend to occur towards the tensile part of the section instead that at column mid-depth, especially near the column base. Results are presented in Figure 4.106 to Figure 4.108 for three sections located respectively at 280, 700 and 1260 mm above the column base.

Looking at the bottom section (280 mm above the base), note that the behavior is very similar to that observed in unit HS1. The maximum strains occur at section mid-depth in earlier stages of testing, while they tend to occur towards the tensile part of the section as the flexural damage increases.

In the section located at 700mm above the base the maximum strains always occur at section mid-depth, while the strains in the tensile part of the section remain quite high. In the top section (1260 mm) above the base, the profiles are almost symmetric with respect to the section centroidal axis. Thus, it is confirmed what was observed in the unit HS1 that lower strains occur in the compressed part of the section in the region where significant flexural damage is present. This fact might suggest to review the way the confined properties of concrete are defined. In fact, from this experimental evidence it seems unconservative to calculate confined concrete properties based on the assumption

that the transverse steel reaches the yield stress everywhere in the section from the elastic range of response.

In plastic hinge region in fact, the stress in the transverse reinforcement never exceeds 160-170 MPa within the compressed part of the section. Hence the confining pressure might be significantly less than the assumed 800 kPa, and therefore the crushing strain might be less than 0.005.

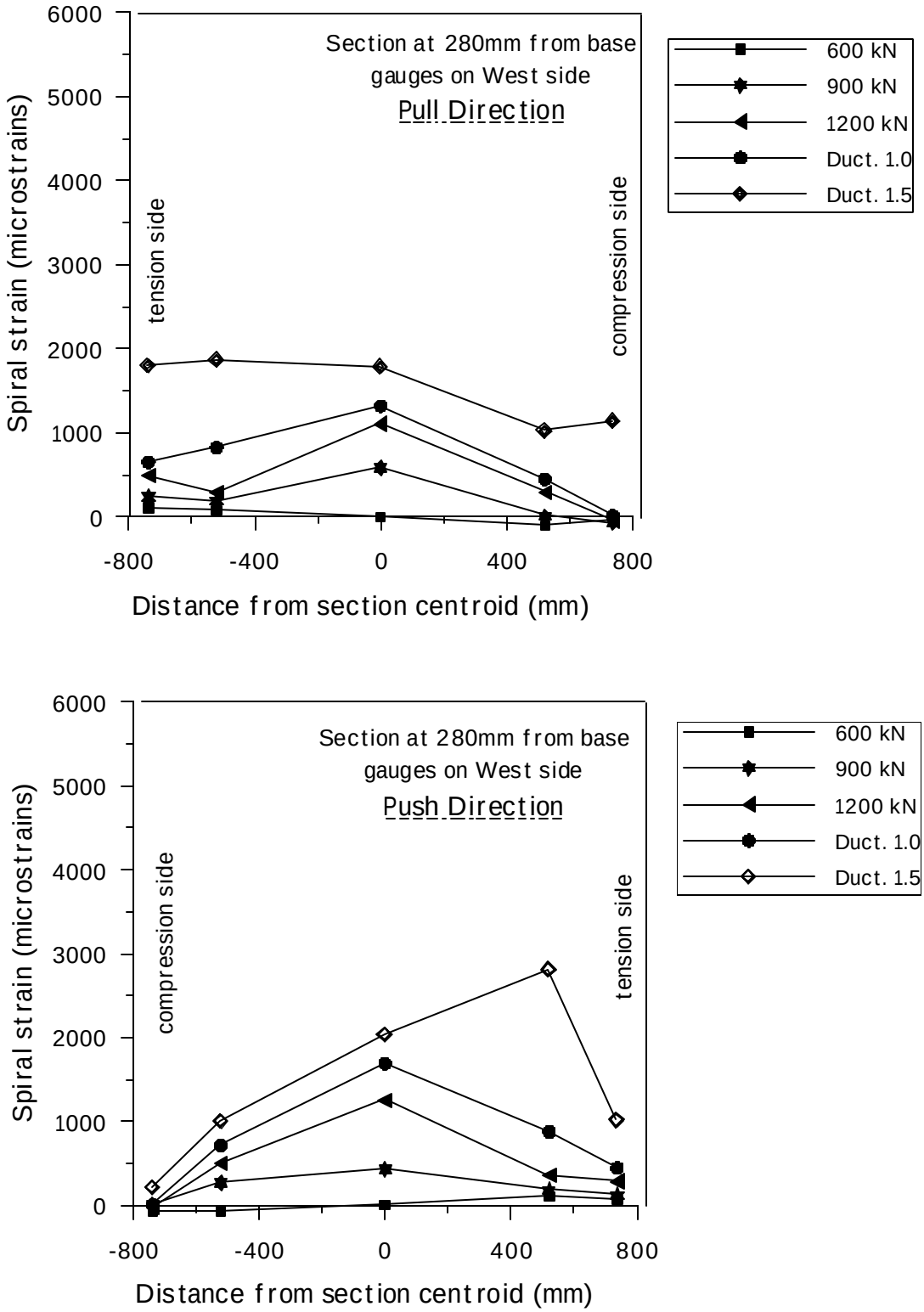

Figure 4.106 Unit HS3 Section Transverse Bar Strain Profiles 280 mm Above Base Section

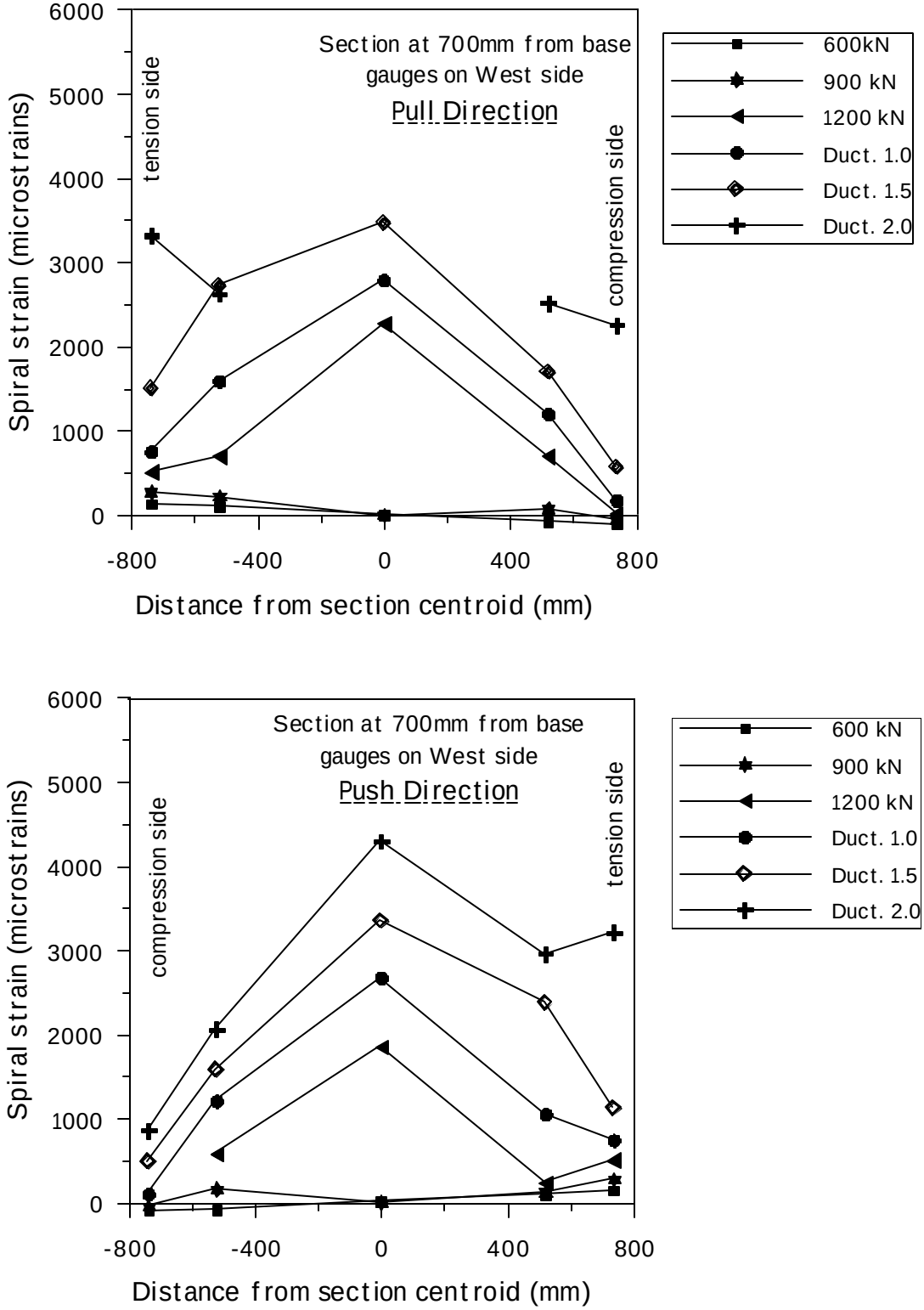

Figure 4.107 Unit HS3 Section Transverse Bar Strain Profiles 700 mm Above Base Section

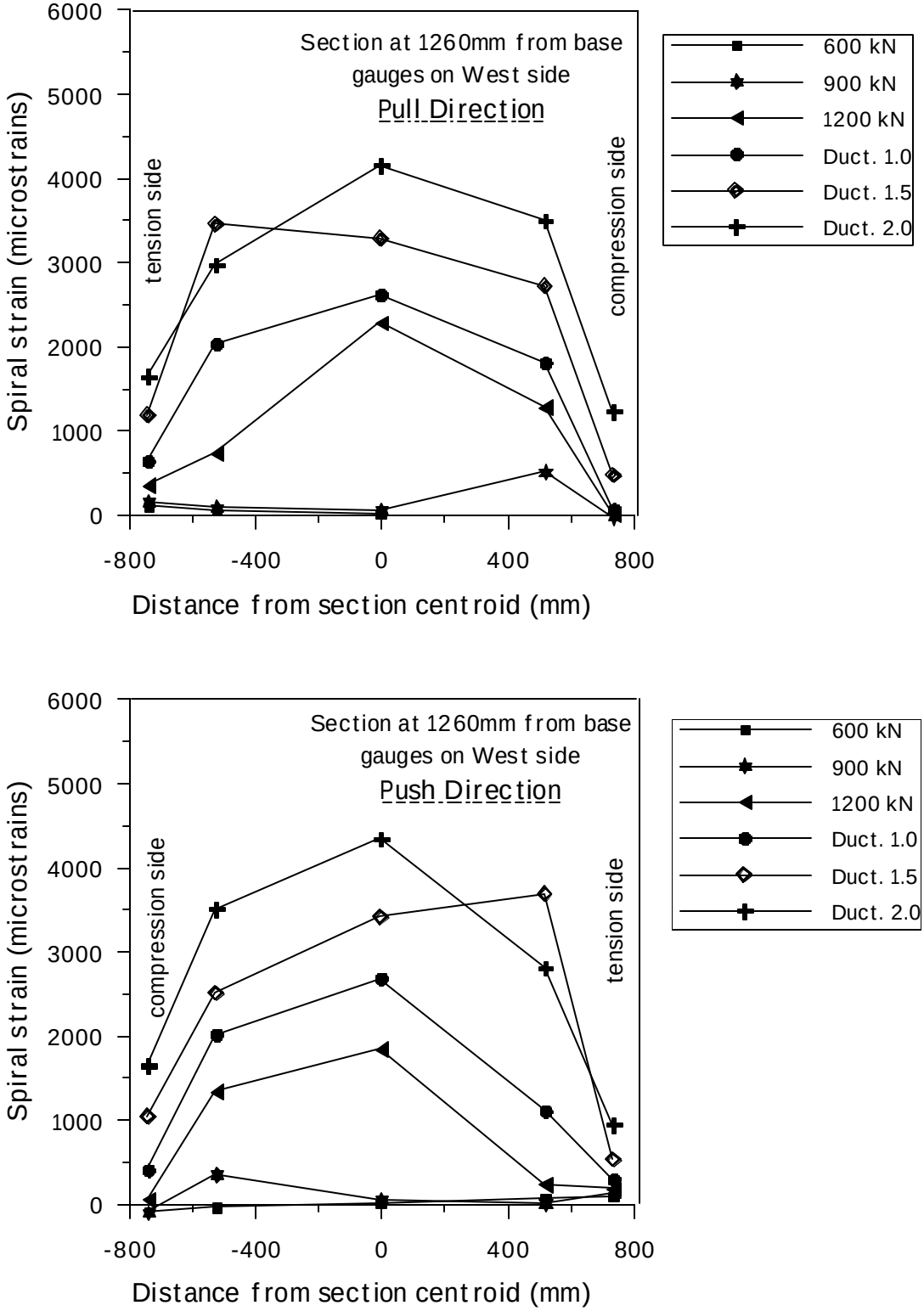

Figure 4.108 Unit HS3 Section Transverse Bar Strain Profiles 1260 mm Above Base Section

4.3.5.7 Section Shear Deformation Profiles

In the previous section it is observed that there is tendency for transverse strains to increase in the tensile part of the section where significant flexural damage is present. This fact was evident from the results of the first unit (HS1) as well. However, these deductions were made based on the readings of strain gauges. These latter might be affected by local cracking. In fact, a local increase in strain might be due to the presence of a shear crack near the gauge. In order to double check this aspect from a different perspective, profiles of the shear deformations over the section depth will be examined based on the readings from the small shear deformation panels. As commented above, these panels essentially give an indication of the average behavior of a portion of the reinforced concrete structure and are therefore not affected by local cracking. In fact, it was observed during the test that at least three cracks happened to occur within each of the instrumented panels (see Figure 4.109). This fact guarantees that the average behavior is well captured.

The shear deformation was calculated in each of the instrumented panels. The readings of these deformations indicate that the shear is carried by this particular structural system. The moment to shear ratio is 2.8 m in the bottom panel and 1.9 m in the top panel and we appreciate a substantial difference in the behavior. The maximum deformation is reached towards the section tensile side as shown in Figure 4.110 for the location of the bottom panel. The maximum deformation is reached exactly on the extreme tensile side as shown in Figure 4.111 for the location of the top panel. A symmetric behavior is shown in both push and pull directions. This fact confirms that shear deformations are concentrated where flexural damage is higher and consequently strains in the longitudinal and transverse reinforcement are higher.

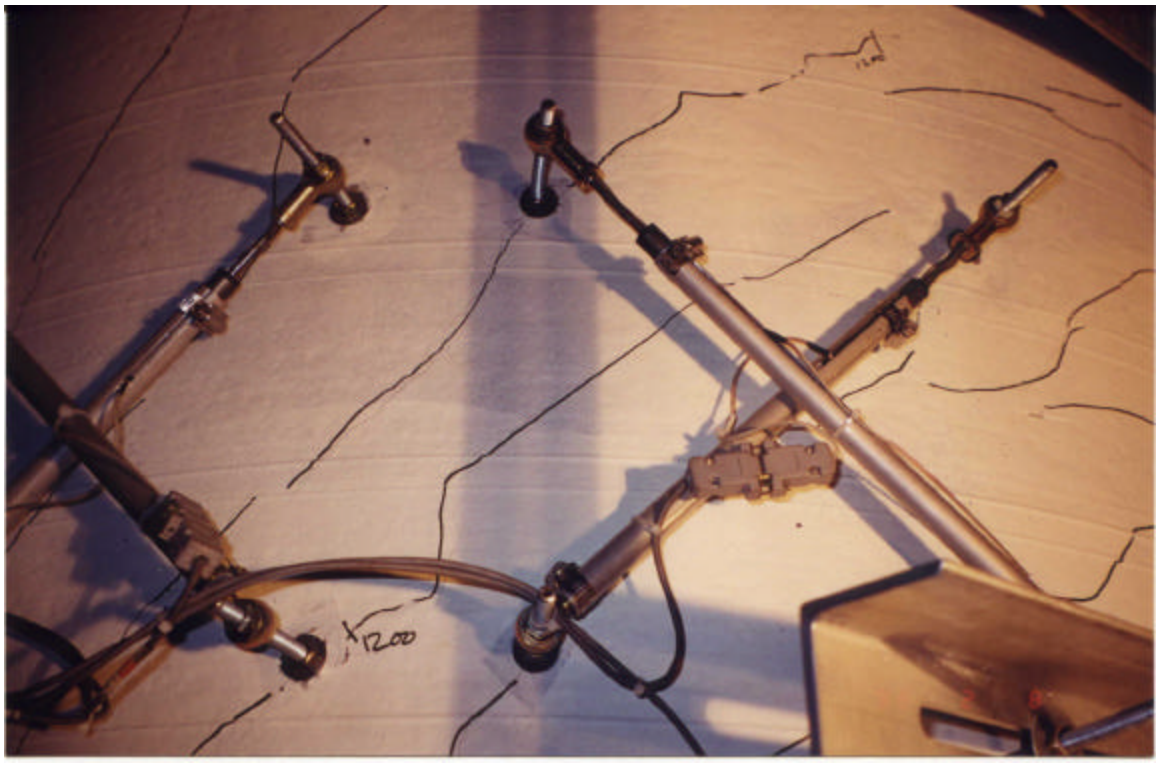

Figure 4.109 Crack Pattern in Small Instrumental Shear Panels

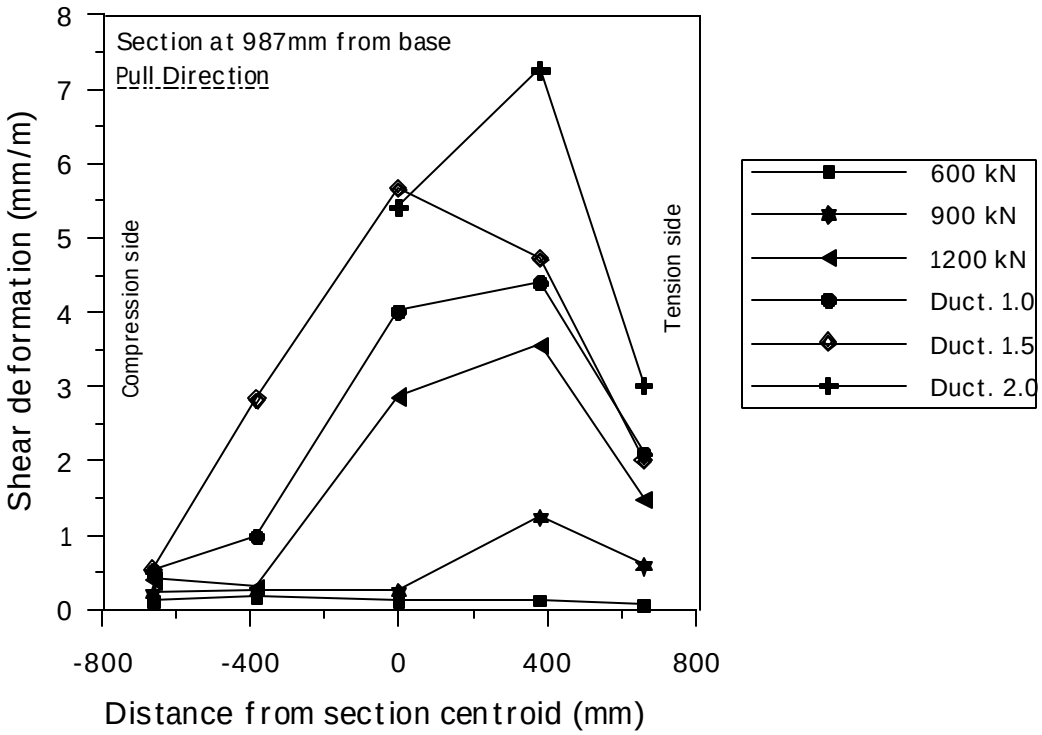

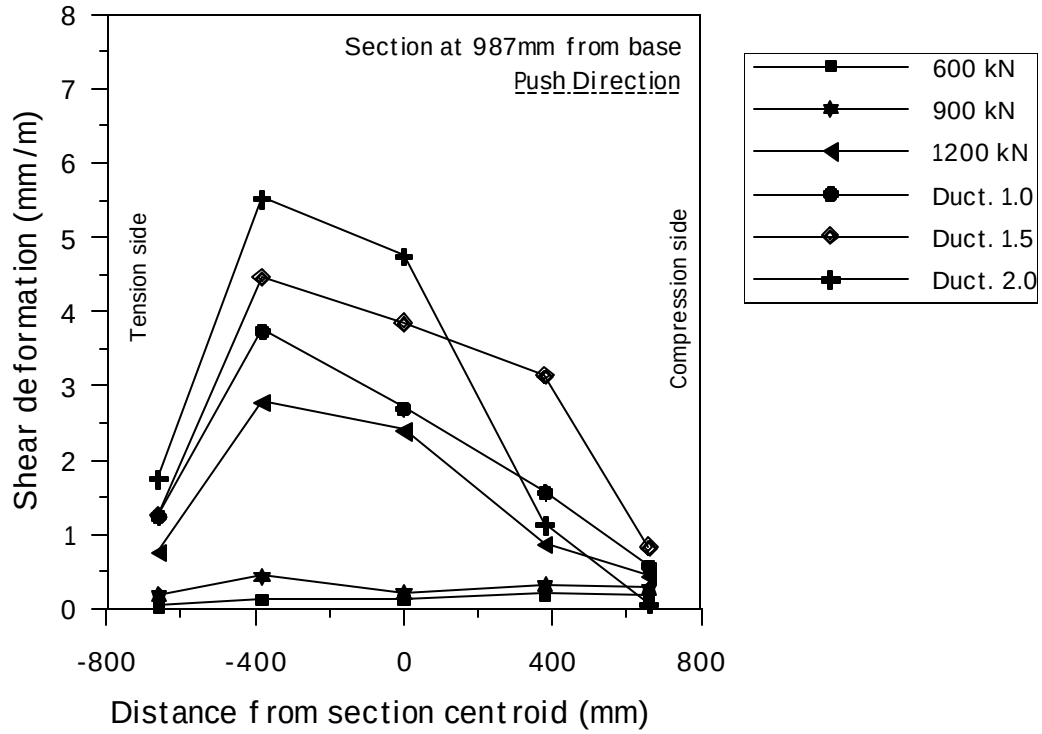

Figure 4.110 Unit HS3 Shear Deformation Measured by Small Shear Panels 987 mm Above Base Section

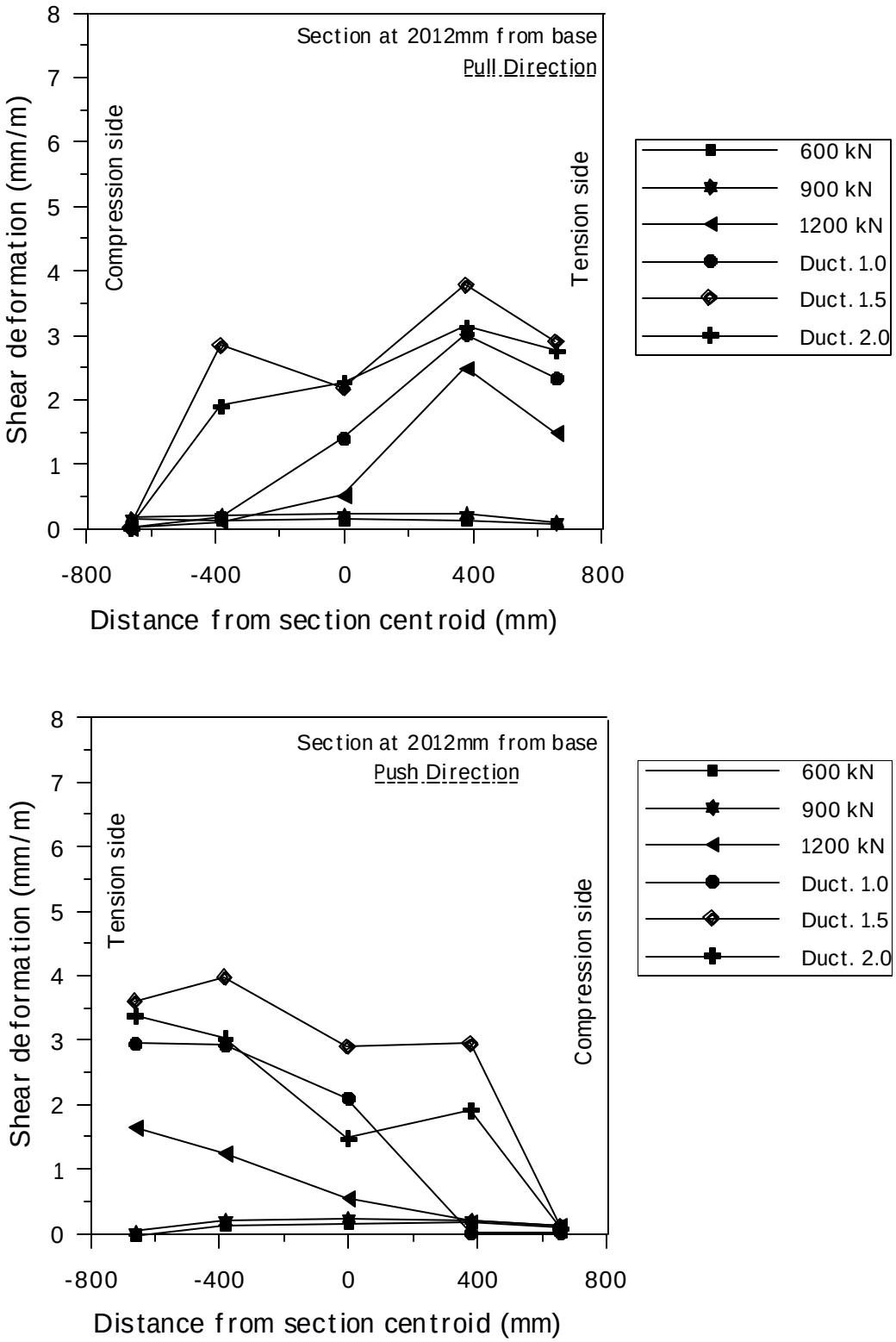

Figure 4.111 Unit HS3 Shear Deformation Measured by Small Shear Panels 2012 mm Above Base Section

4.3.6 Discussion

The response of this test unit indicated that a considerable loss of deformation capacity is attained when the axial load is significantly increased. The only difference between the units HS2 and HS3 was the axial load ratio (15% in HS3 instead of 5% in HS2). The deformation capacity of HS3 was 43% less than that of HS2. The experimental evidence has showed that simplified shear models cannot easily capture this type of shear failures, caused by concrete failure in diagonal compression. However, these models accurately predict the level of average strain in the transverse reinforcement as a function of flexural damage (see Figure 4.112). In the case of high axial compression it is important to check that before the ultimate shear capacity given by the transverse steel is reached, the member does not prematurely fail due to concrete capacity. In this regard, conservative assumptions have to be made for the properties of confined concrete. In general it appears that usual considerations tend to overestimate the concrete ability to resist compression when high principal tensile strains occur.

The use of shear strength models leads to satisfactory estimates of the behavior, provided a simple check is conducted on the maximum shear stress that the concrete can resist. In these models it is also confirmed that the axial load effect is properly taken into account when a separate component (as in the UCSD shear models) is used. Other models clearly underestimate the influence of axial load. This fact is very evident even in the elastic phase. A good prediction of the load required for the strain activation in the transverse steel was obtained by fully including the V_p component in the UCSD traditional shear model (evident from Figure 4.113). Concrete spalling in the inside face determines obviously a loss of strength but it is not necessarily the cause of failure. It confirms what was observed in the unit HS2. Concrete spalling in the inside face did not cause the unit to failure. Also, in this case failure was reached with concrete spalling in the outside face and longitudinal rebar buckling, not specifically by concrete spalling in the inside. Shear damage, as well as flexural damage, tends to be concentrated towards the tensile part of the section, where cracks have in average a larger width.

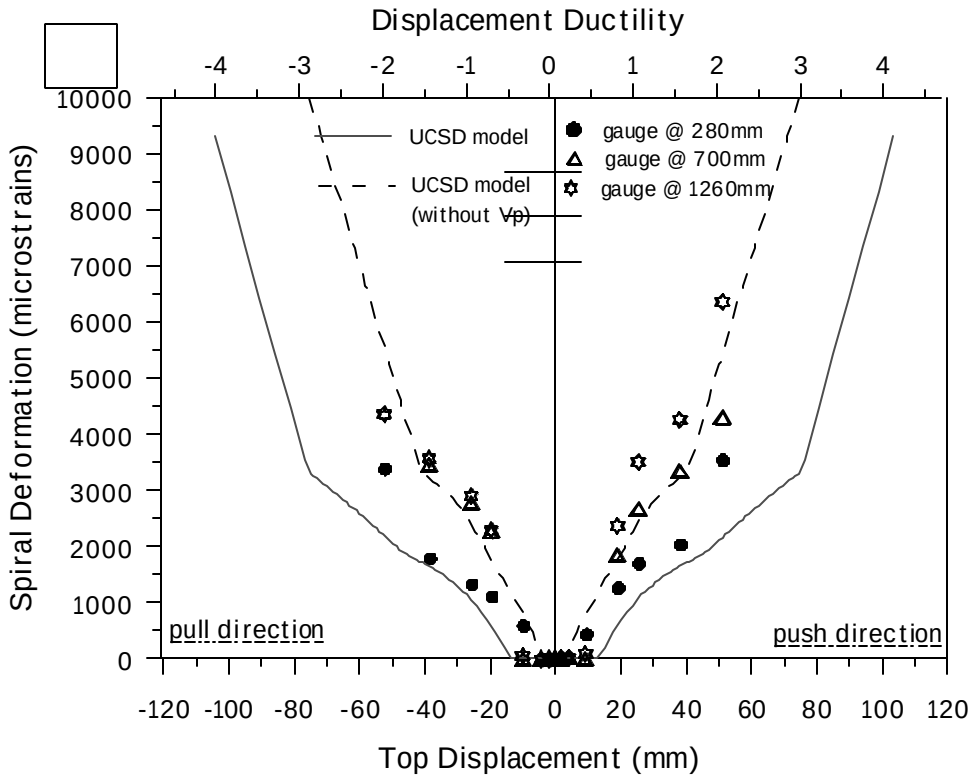

Figure 4.112 Unit HS3 Development of Spiral Strain with Increasing Top Development

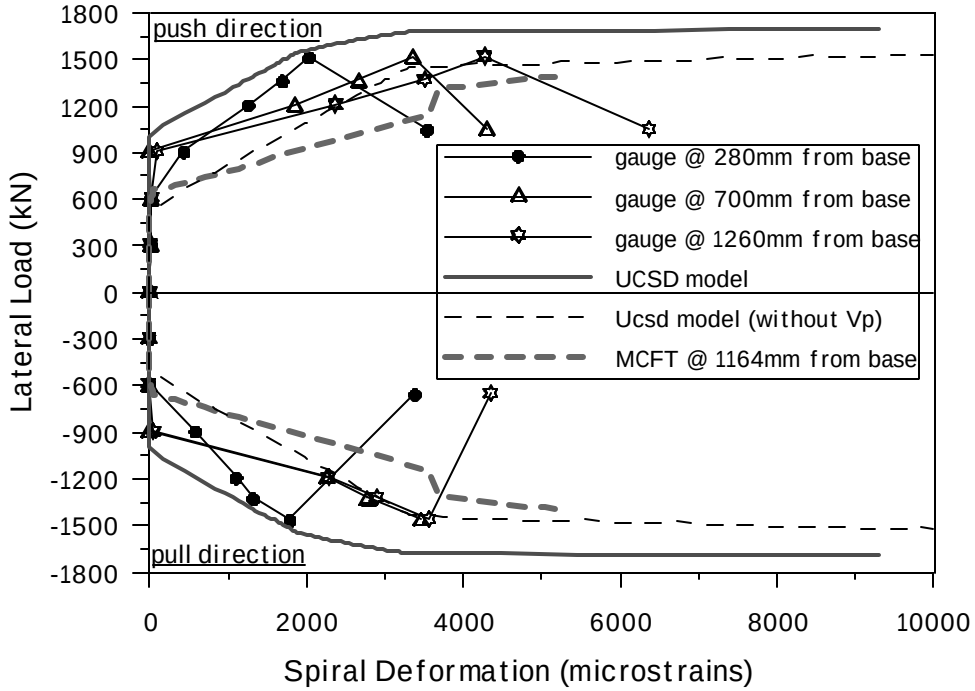

Figure 4.113 Unit HS3 Development of Spiral Strain with Increasing Lateral Load

5 SUMMARY AND CONCLUSIONS

Three units were tested in order to study the shear behavior of a thin-wall circular hollow column under cyclic loading. For all test units, the ratio of the shear span to the section diameter was selected to be 2.5, and the same amount of the transverse reinforcement D6 @70 mm corresponding to 0.35% volumetric ratio of transverse reinforcement was also provided. The unit HS1 was designed with a low flexural capacity in order to prevent a brittle shear failure. The relatively low longitudinal reinforcement ratio (1.4%) and axial load ratio (5%) ensured a good deformation capacity; the unit failed in flexural at displacement ductility of 6. The unit HS2 was designed with a higher longitudinal reinforcement ratio (2.3%) and axial load ratio (5%). The unit failed in a brittle flexural/shear failure mode at displacement ductility of 3. The unit HS3 was designed with a longitudinal reinforcement ratio (2.3%) but higher axial load ratio (15%). The deformation capacity was 43% less than that observed in the unit HS2, and due to the concrete failure the unit HS3 failed in shear at displacement ductility of 2. The top displacement contributed by the shear deformation was measured to be 20%, 30%, and 40% for the unit HS1 (Figure 4.16), HS2 (Figure 4.54), and HS3 (Figure 4.90), respectively.

The UCSD old model and UCSD new model were used to calculate the shear strength of the test units and compared with the design model of the ATC-32 and Caltrans Memo 20-4. It was found that the UCSD old model with the modification on the axial force component could predict the shear strength of a thin-wall circular hollow column (see Figure 4.48 and Figure 4.84). The UCSD new model slightly overestimated the shear strength and deformation capacity of the member, but other models clearly underestimated the shear strength. Based on the test results presented in the report, the following conclusions can be drawn:

(1) The ductility capacity of thin wall hollow column members depends strongly on the concrete confinement near the inside face.

(2) Low axial load ratio and low longitudinal reinforcement ratio as the unit HS1 ensure ductile behavior as the solid column, provided that the adequate transverse reinforcement is used.

(3) As a ductile hollow column as the unit HS1, the ATC-32 model and Caltrans M20-4 model underestimate the shear strength of the column (Figure 4.1). However, the UCSD model would be more appropriate to estimate the shear strength if considering the reduced axial force component, V_p (Figure 4.36).

(4) As a brittle/shear failure column as the unit HS2, the ATC-32 model and Caltrans M20-4 model also underestimate the shear strength of the column (Figure 4.37). The UCSD model is appropriate to estimate the shear strength if the full axial force component, V_p, is considered (Figure 4.74).

(5) As a brittle concrete failure as the unit HS3, the UCSD model slightly overestimates the shear strength (Figure 4.84), because the strength prediction is based on the yield of transverse reinforcement not concrete compression capacity. However other models clearly underestimate the influence of the axial load to the shear strength (Figure 4.75).

(6) Based on these three test results, simplified shear strength models, derived as a modification of the UCSD shear model, shows to predict the behavior with good accuracy. The axial load component in the shear strength estimation can be conservatively neglected in design for the circular hollow column.

(7) A wall thickness of 10% of the section diameter appears to be a conservative design choice and shows not to be a potential source of buckling for the concrete tube.

REFERENCES

(1) Applied Technology Council (1996), "Improved Seismic Design Criteria for California Bridges: Provisional Recommendations," *Report No. ATC-32*, Redwood City, California.

(2) Bentz, E.C., Collins, M. P. (1998), " Response 2000 – Reinforced Concrete Sectional Analysis using the Modified Compression Field Theory," – *Users manual*, University of Toronto, Canada.

(3) Caltrans Memo to Designers 20-4, Attachment B (1996), "Earthquake Retrofit Analysis for Single Column Bents".

(4) Collins, M.P., Vecchio, F.J. (1988), "Predicting the Response of Reinforced Concrete Beams Subjected to Shear using Modified Compression Field Theory," *ACI Structural Journal*.

(5) Paulay, T., Priestley, M.J.N. (1992), "Seismic Design of Reinforced Concrete and Masonry Structures," John Wiley and Sons, New York.

(6) Priestley, M.J.N., Kowalsky, M.J., Vu, N., Mc Daniel, C. (1998), "Comparison of Recent Shear Strength Provisions for Circular Bridge Columns," *Proceedings of the Fifth Caltrans Seismic Workshop*, Sacramento.

(7) Priestley, M.J.N., Ranzo, G., Kowalsky, M.J., Benzoni, G. (1996), "Yield Displacement of Circular Bridge Columns," *Proceeding of the Fourth Caltrans Seismic Workshop*, Sacramento.

(8) Tokyu Construction Company, (1998), "Test Notes on Hollow Bridge Columns," Unpublished report, Tokyo, Japan.

(9) Whittaker, D., Park, R., Carr, A.J., (1987), “Experimental Tests on hollow Circular Concrete Columns for Use in Offshore Concrete Platforms,” *Proceedings of the 3rd Pacific Conference on Earthquake Engineering*, New Zealand.

(10) Zahn, F.A., Park, R. and Priestley, M.J.N., (1990), “ Flexural Strength and Ductility of Circular Hollow Reinforced Concrete column without Confinement on Inside Face,” *ACI Structural Journal.*